Simulations et essais cliniques virtuels pour l'évaluation de la valeur clinique de l'angio-tomosynthèse par rapport à l'angio-mammographie

Ruben Sanchez de La Rosa

▶ **To cite this version:**

Ruben Sanchez de La Rosa. Simulations et essais cliniques virtuels pour l'évaluation de la valeur clinique de l'angio-tomosynthèse par rapport à l'angio-mammographie. Imagerie médicale. Université Paris Saclay (COmUE), 2019. Français. NNT : 2019SACLT046 . tel-02951607

HAL Id: tel-02951607
https://pastel.hal.science/tel-02951607

Submitted on 28 Sep 2020

HAL is a multi-disciplinary open access archive for the deposit and dissemination of scientific research documents, whether they are published or not. The documents may come from teaching and research institutions in France or abroad, or from public or private research centers.

L'archive ouverte pluridisciplinaire **HAL**, est destinée au dépôt et à la diffusion de documents scientifiques de niveau recherche, publiés ou non, émanant des établissements d'enseignement et de recherche français ou étrangers, des laboratoires publics ou privés.

NNT : 2019SACLT046

Thèse de doctorat

Simulations and virtual clinical trials for the assessment of the added clinical value of angio-tomosynthesis over angio-mammography

Thèse de doctorat de l'Université Paris-Saclay
préparée à Télécom Paris, Institut Polytechnique de Paris

École doctorale n°580 Sciences et technologies de l'information et de la communication (STIC)
Spécialité de doctorat : Traitement du signal et des images

Soutenance realisée le 16/12/19, par

Rubén Sánchez de la Rosa

Composition du Jury :

IRÈNE BUVAT Directrice de Recherche, CNRS (IMIV)	Présidente du jury
MICHEL DESVIGNES Professeur, Grenoble-INP (GIPSA-CICS)	Rapporteur
DAVID SARRUT Directeur de Recherche, CNRS (CREATIS)	Rapporteur
HILDE BOSMANS Professeur, KU Leuven (Medical Physics and Quality Assessment)	Examinatrice
CORINNE BALLEYGUIER Chef du Service Imagerie Diagnostique, Institut Gustave Roussy (Medical Imaging)	Invitée
ISABELLE BLOCH Professeur, Télécom Paris, Institut Polytechnique de Paris (LTCI)	Directrice de thèse
SERGE MULLER Directeur Scientifique, GE Healthcare (WHARe)	Co-directeur de thèse

Acknowledgment

This work was developed as a collaboration between GE Healthcare France and laboratory Laboratoire de Traitement et Communication de l'Information (LTCI), Télécom Paris. It is partially funded by the Association Nationale de la Recherche Technique (ANRT) under CIFRE grant $n^0$2016/0265.

I owe a sincere thank you to all the people who has helped and motivated me through the completion of my thesis. I would like to express my sincere gratitude to my thesis advisors Prof. Isabelle Bloch and Dr. Serge Muller. Isabelle, your motivation through all the big moments of this work as well as your insightful comments about the results I was obtaining at each step were fundamental from the beginning to the end, and I am sure they will continue to be indispensable for my future work. Serge, I will be always grateful for the trust you have placed in me, since my internship, along the PhD thesis, until my recent integration in the team for my future work. Discussion after discussion I learned how to go always further in my research and do not stay on the surface. To my scientific advisors, Dr. Ann-Katherine Carton and Dr. Pablo Milioni de Carvalho, because an enormous part of this work belongs to you. Ann-Katherine, if I write down all the "thank you" you deserve the resulting book will be longer than this work. Morning coffee was the best humanizing coffee. Pablo, thank you for all the scientific and technical discussions we had around the whiteboard of the open space, not just during this thesis, but since my internship. You always found/find the time for a good (and lengthy) discussion.

I would like to thank Prof. Michel Desvignes and Prof. David Sarrut for accepting to review this manuscript. Thank you for your the time you spent reading this work and your valuable comments. I would also like to thank the rest of my thesis committee for accepting being members of this thesis. All of your comments and insights will be the leading light for the future work related to this thesis.

I would also like to thank my fellow WHARe-mates, old and new: Giovanni, Sylvie, Laurence, Vivianne, Razvan, Zhijin, Andrei, Clement... as well as my dearest PhD mates at GE: Anna, Maissa and Karine (hard moments team), Aymeric, Emmanuelle, Ketan and Lucas. The rest of the people at GE: Jorge, Fabio, Clement, Charlotte, Alexis, Gwladys, and a long etcetera... As well as all the interns who worked with me since my arrival at GE (specially to Valentin and Matthieu). I cannot put the name of everybody, you are a lot!

I thank my mates at Telecom Paris: Guillaume, Clement, Helene, Sylvain, Christian... who welcomed me in the lab and accompanied me during the days I worked there.

Also, I have been lucky enough to have the perfect crew who supported me from the distance, either in Valladolid (Ana, Mongil, Dario, Ricardo, Villa, Luis, Federico, Badas, Carlos, Alex, Chuchi, Santiago), or in the world (Joaco, Sergi, Hugo, Matute, Lucia, Pedro, Alaitz, Luis, Maruel, Gonzalo, Fede, Javi, Guido). And of course, to the friends who were living the hard moments on live: Inigo, Sonia, Roque, Leire, Marc, Marina, Matthias, Charles, Victoria, Mikel, Mariana, Alicia, Javi, Gorka and Udane. I would like to write something special for each of

you, but I need to limit the acknowledgement section or nobody is going to continue reading. Without you I could not have done it. And Sebastian and Anna... What would I do all these years without you? Thank you so much.

Finally, I am infinitely grateful to all my family, especially my parents and my brother. For being always there, despite the kilometres (and the bad reception in the underground), at the other side of the phone, giving all their love and positive waves. No bad moments when you were there. To Paula, my love, for being there the crazy days (there were a lot!) to support me. It was a hard road this one we have travelled, but with you by my side I wouldn't mind to embark me on the most arduous journey.

Contents

Acknowledgment **1**

Abbreviations **6**

Resumé **9**

Introduction **23**

1 Context and motivation **25**
1.1 Contrast-enhanced X-ray imaging of the breast 25
1.1.1 Tumor angiogenesis 26
1.1.2 Contrast-Enhanced Digital Mammography 26
1.1.3 Contrast-Enhanced Digital Breast Tomosynthesis 28
1.1.4 Clinical protocol in contrast-enhanced X-ray imaging of the breast 29
1.2 Image simulation in virtual clinical trials 31
1.2.1 Simulation of the X-ray chain 33
1.2.2 Simulation of the breast 34
1.3 Mammography acquisition chain for CE X-ray imaging 37
1.3.1 Description of acquisition systems 37
1.3.2 Introduction to an analytic X-ray simulation platform: CatSim 39
1.3.3 Factors impacting the image quality 41
1.4 Conclusion 43

2 Improved realism in simulating X-ray imaging systems **45**
2.1 Frequency response of an X-ray system 45
2.1.1 Frequency response at the detector 47
2.1.2 Scattering processes 49
2.2 A novel approach in modeling X-ray scatter in X-ray imaging systems 51
2.2.1 General overview of our model 52
2.2.2 Introducing a parametric expression of the scatter transfer function . . . 53
2.2.3 Validation of the proposed parametric scatter transfer function 56
2.2.4 Simulation of scattered field in systems without anti-scatter grid 63

2.2.5 Conclusion . . . 67
2.3 Stochastic processes in a X-ray system . . . 70
2.3.1 Quantization ramp . . . 70
2.3.2 Electronic noise . . . 72
2.3.3 Quantum noise . . . 79
2.4 Memory processes in a X-ray system . . . 86
2.4.1 Modeling the lag in CEDBT sequences . . . 88
2.4.2 Experimental assessment of the lag . . . 90
2.4.3 Validation of the lag model . . . 93
2.5 Other simulated elements: focal spot size and shape, heel effect . . . 94
2.6 Conclusion . . . 96

3 A new modeling of realistic iodine contrast uptakes 101
3.1 Lesion classification in contrast enhanced X-ray breast imaging . . . 101
3.2 Simulation of mass-like contrast uptakes . . . 105
3.2.1 Shape . . . 106
3.2.2 Margin . . . 109
3.2.3 Contrast uptake distribution . . . 113
3.3 Combining contrast uptakes inside the breast texture . . . 116
3.4 Conclusion . . . 120

4 Generation of recombined and reconstructed images 121
4.1 Recombination of low- and high-energy images . . . 121
4.1.1 Recombination in simulated images . . . 125
4.1.2 Stochastic processes after material decomposition . . . 126
4.1.3 Frequency response after material decomposition . . . 131
4.1.4 Memory processes after material decomposition . . . 137
4.1.5 Validation of simulated recombined pairs . . . 139
4.2 Image reconstruction . . . 142
4.2.1 Reconstruction in digital breast tomosynthesis (DBT) . . . 142
4.2.2 Reconstruction in CEDBT . . . 146
4.2.3 Optimizing FBP for CEDBT clinical task . . . 149
4.3 Conclusion . . . 154

5 CEDBT system design improvements 157
5.1 Texture cancellation . . . 159
5.2 Parenchyma enhancement . . . 160
5.3 Detectability of contrast uptakes . . . 168
5.4 Cupping artifact in recombined images . . . 171
5.4.1 Evaluation of the cupping artifact magnitude and range . . . 173
5.4.2 Contrast uptakes in the presence of cupping artifact . . . 177

5.4.3 Discussion . . . 179
5.5 Conclusion . . . 181

6 A comparison of CEDBT and CESM potential clinical performance 183
6.1 Human reader study . . . 183
6.1.1 Definition of the dataset . . . 184
6.1.2 Acquisition system parameters . . . 189
6.1.3 Image evaluation . . . 190
6.1.4 Data analysis . . . 190
6.2 Results . . . 192
6.2.1 Detectability . . . 193
6.2.2 Characterization . . . 196
6.3 Conclusion . . . 199

Conclusion and perspectives 203

Publications 211

Appendix 213

A MRMC Studies 215
A.1 Evaluation of diagnostic systems . . . 215
A.1.1 Parametric approach . . . 215
A.1.2 Non-parametric approach . . . 218
A.2 Multiple Readers Multiple Cases (MRMC) . . . 220
A.2.1 Estimation of AUC: single-shot . . . 220
A.2.2 Building an average ROC . . . 222
A.2.3 Hypothesis test: DBM . . . 223
A.2.4 Increasing analysis performance with split-plot study design . . . 224

B Adjusting stochastic processes after material decomposition 227

Abbreviations

AUC	Area Under the Curve
AWGN	Additive White Gaussian Noise
bCT	breast Computed Tomography
BPE	Breast Parenchyma Enhancement
CE-MRI	Contrast Enhanced-Magnetic Resonance Imaging
CEBI	Contrast Enhanced Breast Imaging
CEDBT	Contrast-Enhanced Digital Breast Tomosynthesis
CESM	Contrast-Enhanced Spectral Mammography
CSA	Cascaded System Analysis
DBM	Dorfman-Berbaum-Metz
DBT	Digital Breast Tomosynthesis
EMD	Earth Moving Distance
EPR	Enhanced Permeability and Retention
ESF	Edge Spread Function
FBP	Filtered BackProjection
FFDM	Full Field Digital Mammography
FPF	False Positive Fraction
FT	Fourier Transform
HE	High Energy
IIR	Iterative Image Reconstruction
IQ	Image Quality
LE	Low Energy
LTI	Linear Time Invariant
MC	Monte-Carlo
MRMC	Multiple Reader Multiple Cases
MSE	Mean Square Error
MTF	Modulation Transfer Function
NPS	Noise Power Spectrum
OSTR	Ordered Subset Transmission Reconstruction
OTF	Optical Transfer Function
PSF	Point Spread Function
PTF	Phase Transfer Function
ROC	Receiver Operating Characteristic
SART	Simultaneous Algebraic Reconstruction Technique
SDD	Source to Detector Distance
SDNR	Signal Difference-to-Noise Ratio
SID	Source to Isocenter Distance

SNR	Signal-to-Noise Ratio
SPR	Scatter-to-Primary Ratio
TC	Texture Cancellation
TPF	True Positive Fraction
TV	Total Variation
VCT	Virtual Clinical Trial
WSS	Wide Sense Stationary

Resumé

Le cancer du sein est le type de cancer le plus commun, et l'une des principales causes de mortalité par cancer chez la femme. Le dépistage précoce réalisé avec la mammographie standard permet d'augmenter le taux de survie. Cependant, le diagnostic en utilisant cette technique est très affecté par les lésions situées dans des tissus de haute concentration glandulaire. De plus, certaines lésions du sein ne sont pas toujours visibles lors de l'examen. Ces problèmes ont conduit au développement de méthodes d'imagerie du sein par rayons X avec prise de contraste : angiomammographie (*Contrast Enhanced Spectral Mammography* ou CESM) et angiotomosynthèse (*Contrast Enhanced Digital Breast Tomosynthesis* ou CEDBT).

Ces techniques exploitent le processus biologique d'angiogénèse, c'est-à-dire la formation d'un nouveau réseau sanguin autour d'une masse tumorale. En particulier, la technique CESM utilise le même équipement que la mammographie standard pour obtenir des images projetées du produit du contraste (de l'iode) qui s'accumule dans le sein. Pour obtenir cela, deux images sont acquises après l'injection de l'iode avec deux spectres énergétiques différents, appelées image basse énergie (LE) et image haute énergie (HE). Plusieurs études ont prouvé que CESM offrait de meilleures sensibilité et spécificité que la mammographie standard. D'autres études ont démontré que CESM offrait une performance de diagnostic similaire à celle de l'imagerie par résonance magnétique avec prise de contraste (CE-MRI). Malgré tous ces bénéfices, CESM reste une imagerie de projection qui fournit des images bidimensionnelles du sein, avec superposition de tissus dans l'image finale. CEDBT cherche à résoudre ce problème en utilisant différentes positions de la source de rayons X, afin de reconstruire des coupes du contenu de l'iode qui s'accumule dans le sein, et de retrouver ainsi l'information tridimensionnelle perdue en CESM. Cependant, CEDBT est une technique très récente, qui n'est pas encore commercialisée, et sa valeur clinique par rapport à l'examen clinique actuel CESM n'est pas bien comprise. Les protocoles d'acquisition des deux techniques, CESM et CEDBT, sont illustrés dans la figure 1.

L'objectif de cette thèse est d'étudier les bénéfices cliniques de CEDBT comparé à CESM en termes de détection et de caractérisation des différentes prises de contraste présentes lors de l'examen clinique. Cependant, une telle évaluation nécessiterait une grande base de données de cas cliniques avec une représentation complète des prises de contraste, ainsi que la "vérité" (détection et caractérisation de référence) de chaque cas. De plus, notre étude présente un autre défi : au début de notre travail, nous ne disposions pas d'un prototype clinique CEDBT. Dans ce contexte, une étude clinique virtuelle peut constituer une solution pré-clinique. L'objectif de ce type d'études est de remplacer partiellement ou complètement les composantes impliquées dans une étude clinique réelle. La figure 2 représente les éléments qui peuvent être remplacés dans une étude virtuelle. Le réalisme nécessaire des composantes virtuelles dépendra de l'objectif de l'étude.

Par conséquent, à la place d'une vraie étude clinique, la nouveauté de notre travail réside dans l'évaluation des deux techniques, CESM et CEDBT, à l'aide de données simulées réalistes :

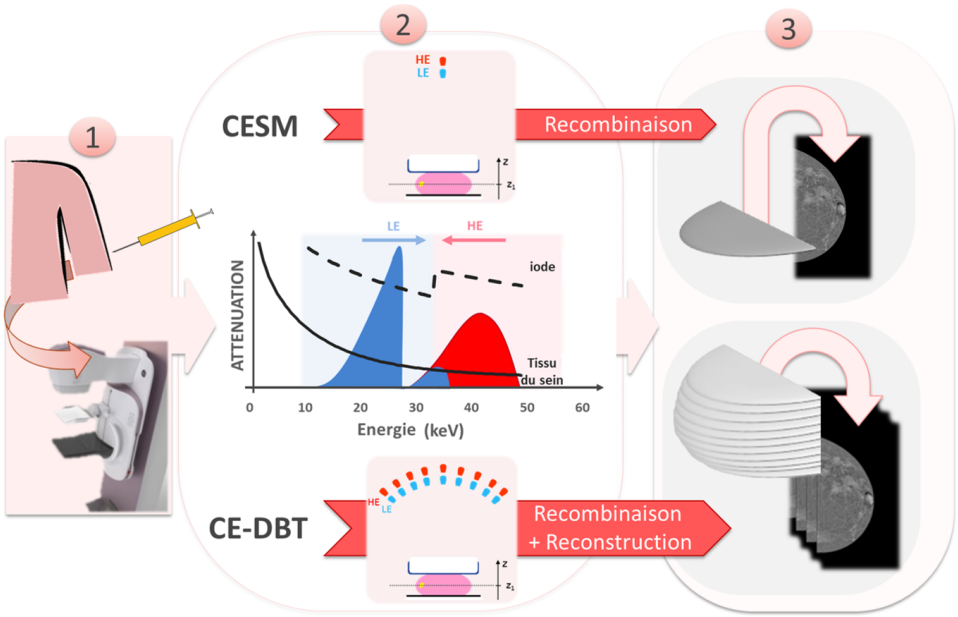

Figure 1: Protocole d'acquisition pour CESM et CEDBT. D'abord, un agent de contraste est injecté par voie intraveineuse dans le patient. Ensuite, des projections du sein sont acquises : une seule projection LE et HE au même instant pour CESM, et plusieurs projections LE et HE selon différents angles pour CEDBT. L'étape finale est le traitement des images acquises : recombinaison d'une seule image dans le cas de CESM, recombinaison et reconstruction d'un ensemble d'images dans le cas de CEDBT.

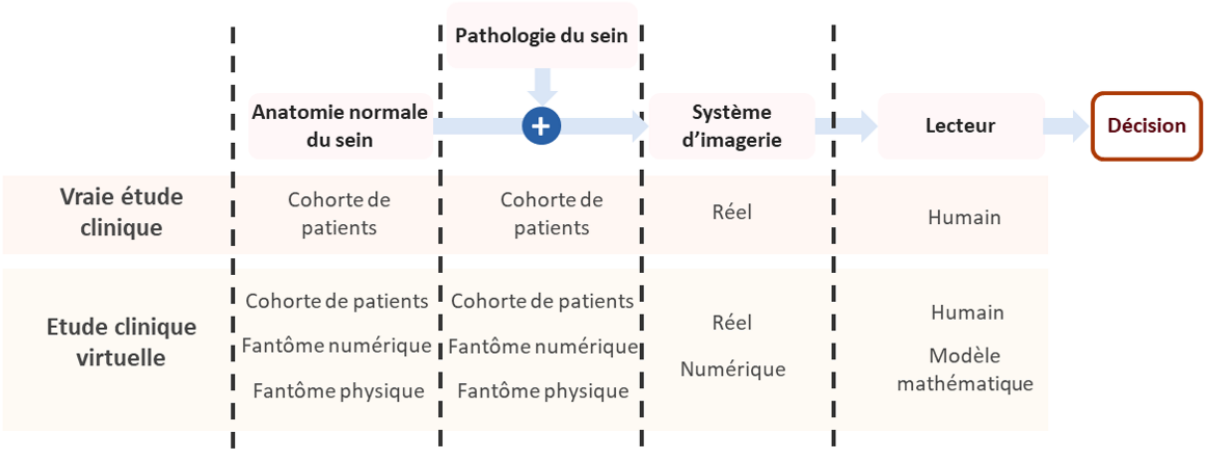

Figure 2: Composantes d'une étude clinique réelle et virtuelle. Les composantes d'une étude virtuelle peuvent être combinées selon les choix faits pour l'étude.

simulation de l'acquisition de projections d'un objet par un système d'imagerie par rayons X avec les propriétés des vraies acquisitions expérimentales, et modélisation de prises de contraste de type masse liées aux lésions mammaires, ainsi que la prise de contraste naturelle observée dans le parenchyme du sein. Une autre contribution porte sur l'amélioration de l'algorithme de reconstruction CEDBT pour améliorer la qualité des coupes reconstruites.

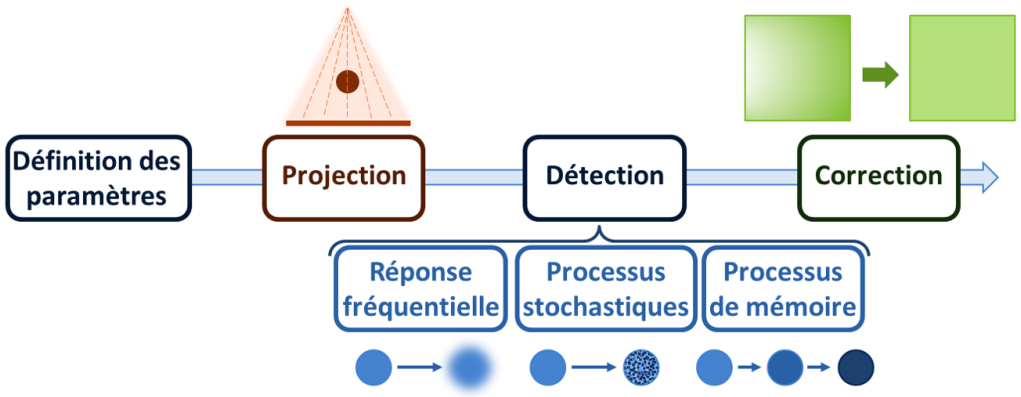

Figure 3: Étapes suivies dans la simulation d'une image finale générée par CatSim.

Dans les systèmes d'acquisition à rayons X, il y a plusieurs processus physiques qui contribuent à la génération de l'image finale. Au cours des deux dernières décennies, plusieurs approches ont été considérées pour simuler la chaîne d'acquisition. En particulier on trouve trois groupes bien différenciés: simulations par Monte-Carlo, analyse des système en cascade, et simulateurs analytiques. Dans notre travail nous avons opté pour utiliser CatSim, une plateforme de simulation analytique d'images tomographiques, initialement développée par des chercheurs du centre de recherche de General Electric. Cette plateforme a été adaptée dans un travail précédent pour générer des images de mammographie, mais n'était pas capable de reproduire la séquence d'acquisition utilisée en CEDBT, ni plusieurs phénomènes physiques d'importance majeure pour la génération des images réalistes de basse et haute énergie. En particulier, nos images simulées analytiquement sont générées en suivant trois étapes (figure 3): une étape de projection où le système calcule le rayonnement primaire en utilisant un algorithme de traçage de rayons qui prend en compte les coefficients d'atténuation linéaire μ du fantôme numérique choisi ; une étape de détection où le système incorpore des phénomènes physiques à l'image idéale obtenue dans l'étape précédente ; et une étape de correction géométrique de l'image finale. Toutes les contributions présentées dans cette thèse ont été axées sur l'étape de détection. Nous avons différencié trois types de phénomènes physiques à modéliser : les phénomènes qui modifient la réponse en fréquence du système de mammographie, les phénomènes qui introduisent une incertitude ou bruit dans l'intensité de chaque pixel mesuré, et le processus de mémoire qui tient compte de l'état précédent du système. Pour réduire la complexité de calcul de nos simulations, nous avons utilisé une approximation mono-énergétique des spectres poly-énergétiques utilisés pour les acquisitions expérimentales. Cette approche a déjà été utilisée auparavant dans d'autres études. De plus, chaque nouveau modèle inclus dans la plateforme de simulation a été adapté pour deux spectres donnés (de basse et haute énergies), les deux modalités d'intérêt (CESM et CEDBT) et deux systèmes de mammographie différents (Senographe Pristina et Senographe DS).

La réponse en fréquence du système dépend de cinq effets principaux : le mouvement du tube à rayons X lors de la séquence d'acquisition, la taille et la forme du point focal, le rayonnement diffusé des rayons X lors de la traversée du fantôme, le diffusé optique lors du passage par le scintillateur, et la taille ainsi que la forme des photodiodes dans le détecteur. Nous considérons une séquence d'acquisition "step-and-shoot" (rotation puis exposition) où il n'y a pas de flou introduit par le mouvement du tube. De plus, nous avons considéré un point focal uniforme

et carré, de taille $0.3 \times 0.3mm$. Nous avons modélisé la réponse en fréquence due à la taille et la forme de l'aire active des photodiodes comme une fenêtre carrée de taille $80\mu m \times 80\mu m$ correspondant à des éléments de détection de $100\mu m \times 100\mu m$ avec un facteur de remplissage de 64%. Pour modéliser la dégradation de la réponse en fréquence du système causée par le rayonnement diffusé, nous avons développé un modèle analytique non-stationnaire. Notre modèle a l'avantage de fournir une expression d'épaisseur d'objet continue du champ de rayonnement diffusé qui utilisaient les informations d'un ensemble réduit de mesures expérimentales. Nous avons évalué la performance de ce modèle pour reproduire le champ de rayonnement diffusé dans des systèmes avec et sans grille anti-diffusante. Les résultats montrent une bonne corrélation entre les acquisitions expérimentales et les acquisitions simulées dans des systèmes intégrant une grille anti-diffusante, et améliorant la fidélité des simulations obtenues précédemment en utilisant un noyau de diffusion stationnaire. En particulier, pour les simulations prenant en compte la grille anti-diffusante, nous avons constaté que notre méthode fournissait des erreurs quadratiques moyennes 3 fois, 20 fois et 59 fois plus faibles pour des fantômes de $25mm$, $50mm$ et $75mm$ d'épaisseur lorsque l'on considère les acquisitions à basse énergie, et des erreurs quadratiques moyennes 1 fois, 22 fois et 3 fois plus petites pour des fantômes de $25mm$, $50mm$ et $75mm$ d'épaisseur pour les acquisitions à haute énergie. Les simulations à basse énergie simulées pour lesquelles la grille anti-diffusante a été supprimée montrent également une bonne corrélation avec des acquisitions expérimentales. Cependant, notre modèle est limité par les processus physiques pris en compte dans notre simulation. Lorsque la contribution du champ de diffusion des rayons X est élevée (objets d'épaisseur supérieure à $50mm$), nous ne trouvons pas une bonne corrélation entre les simulations à haute énergie et les images expérimentales.

L'image numérique finale obtenue avec un système de mammographie réel est composée de plusieurs processus aléatoires, chacun suivant une distribution différente. Ces processus aléatoires composent ce que nous appelons habituellement le bruit, ce qui peut affecter l'interprétation d'une image ou la visibilité d'une lésion mammaire particulière. Nous avons identifié trois types de bruit que nous avons modélisés par la suite : le bruit de quantification, le bruit électronique et le bruit quantique. Les trois sources de bruit dépendent du système de mammographie utilisé.

Le bruit de quantification est introduit dans le détecteur lors de la conversion du signal analogique en signal numérique. Cette source de bruit peut être identifiée mathématiquement par une loi uniforme $u \sim \mathcal{U}(0, a)$, où a dépend du pas d'échantillonnage. Pour inclure ces effets dans notre plateforme de simulation, nous avons implémenté la même rampe de conversion que celle utilisée dans le système de mammographie réel. Nous avons validé que la liste des valeurs du signal disponibles est la même pour les images acquises et simulées.

Le circuit de détection est composé de plusieurs éléments, chacun d'eux produisant un ensemble hétérogène de bruits internes qui introduisent une fluctuation aléatoire ajoutée au nombre d'électrons générés. Puisque le bruit thermique est dominant dans nos applications [221], nous pouvons le modéliser en utilisant un bruit additif blanc gaussien [62, 108, 249] $\varepsilon(E, M) \sim \mathcal{N}(0, \sigma^2_{elec}(E, M))$, avec une variance qui dépend du spectre utilisé E (basse ou haute énergie) et de la modalité M (CESM ou CEDBT). Ce paramètre a été ajusté à partir des mesures expérimentales. Pour la validation nous avons choisi de comparer les histogrammes d'images expérimentales et simulées sans exposition de rayons X (sans photons qui arrivent au détecteur) en utilisant la distance EMD (*Earth Moving Distance*) normalisée. Pour tous les cas comparés nous avons trouvé que cette mesure est inférieure de 0,9% à la distance entre histogrammes des images expérimentalement acquises sans exposition de rayons X. La magnitude negligible de

cette mesure nous peremet de valider l'ajustement fait sur le parametre $\sigma^2_{elec}(E, M)$ ainsi que l'hypothèse d'un bruit additif blanc gaussien.

En mammographie, les photons de rayons X générés, ainsi que leurs interactions quantiques dans leur chemin vers les pixels du détecteur, suivent des processus aléatoires qui induisent une incertitude dans le signal qui arrive au détecteur [187, 195]. Ce signal aléatoire est ce que nous appelons du bruit quantique. Le nombre de photons arrivant au détecteur suit une distribution de Poisson $X \sim \mathcal{P}(\lambda)$ où λ est le nombre moyen de photons qui arrivent au détecteur. Notre objectif est d'avoir des images simulées de mêmes moyenne et rapport signal à bruit que les images expérimentales. Le flux de photons de notre chaîne de rayons X simulée n'est pas adapté au rendement du tube d'un système de mammographie donné. De plus, le modèle de Poisson n'inclut pas d'interactions quantiques supplémentaires telles que le bruit Swank [284] ou la génération aléatoire de rayons X fluorescents K [63]. Ces autres processus peuvent modifier la variance mesurée lors d'acquisitions expérimentales. Par conséquent, nous avons introduit deux paramètres expérimentaux G et K qui nous permettent d'obtenir des images simulées avec les mêmes moyenne et rapport signal à bruit que les images expérimentales. La valeur de ces paramètres dépendra du spectre et de la modalité utilisés. Nous avons validé notre modèle en réalisant 100 mesures de valeurs d'intensité d'image et de variance pour chaque spectre considéré en modifiant les paramètres d'acquisition. L'erreur d'estimation moyenne obtenue pour la valeur d'intensité d'image est de $0,04\%$ pour la basse énergie et de $0,01\%$ pour la haute énergie. L'erreur d'estimation moyenne obtenue pour le rapport signal à bruit est de $0,61\%$ pour la basse énergie et de $0,71\%$ pour la haute énergie. Ces pourcentages sont plus petits que la variance de l'intensité d'image et le rapport signal à bruit trouvés dans des images expérimentales acquises avec les mêmes spectre, fantôme et niveau d'exposition. Pourtant, ces résultats nous permettent de prouver la validitè de nos paramètres expérimentaux G et K.

Dans notre modèle analytique d'acquisition nous avons considéré aussi les processus de mémoire ou *lag*. Lorsque la séquence d'acquisition nécessite la génération de projections successives par rayons X d'un objet, comme c'est le cas dans la tomosynthèse, il reste un signal résiduel induit par les radiations incidentes antérieures qui est ajouté à l'acquisition présente [273, 282, 298]. Nous avons modélisé le *lag* comme un système linéaire et invariant en temps (LTI) avec une réponse impulsionnelle finie (FIR), dans lequel une sortie y à un instant donné n dépend de l'entrée x à l'instant n et des entrées antérieures multipliées par un facteur de mémoire α qui dépend aussi du temps : $y[n] = x[n] + \sum_{k=1}^{n-1} \alpha[k] \cdot x[n-k]$. Les facteurs $\alpha[k]$ ont été estimés à partir des mesures expérimentales pour des spectres à basse et haute énergie.

Dans la séquence d'acquisition CEDBT les projections à basse (y_{LE}) et haute énergies (y_{HE}) s'intercalent et on a :

$$\begin{cases} y_{LE}[n] = x_{LE}[n] + \sum_{k=1}^{n-1} \alpha_{LE}[2(n-k)] \cdot x_{LE}[k] + \sum_{k=1}^{n-1} \alpha_{HE}[2(n-k)-1] \cdot x_{HE}[k] + \varepsilon + u \\ y_{HE}[n] = x_{HE}[n] + \sum_{k=1}^{n-1} \alpha_{HE}[2(n-k)] \cdot x_{HE}[k] + \sum_{k=1}^{n} \alpha_{LE}[2(n-k)+1] \cdot x_{LE}[k] + \varepsilon + u \end{cases} \tag{1}$$

Pour valider le modèle nous avons comparé les moyennes des intensités des images issues des séquences d'acquisition expérimentales et simulées. Nous avons trouvé que les simulations du système Senographe Pristina étaient correctes et qu'elles restaient dans la plage de variabilité trouvée dans les mesures expérimentales avec une erreur inférieure à $0,32\%$. Dans le cas du Senographe DS, notre modèle n'offre pas le même précision, avec une erreur maximale qui va jusqu'à 2%. Malgré ces limites, pour les objectifs de notre travail, nous avons considéré que notre modèle offrait une estimation raisonnable du *lag*.

Le modèle analytique final de nos simulations est finalement égal à :

$$\Gamma(I)[n,E] = G(E)\cdot\mathcal{P}\{K(E)\cdot(T_P(E)+T_S(E)\cdot SPR(t,E))I_0(E)\cdot e^{-\sum_{i=1}^{n_{mat}}\mu_i(E)t_i}\} \\ *h_T(t,E)*h_{det}$$

$$\begin{cases} I_{Final}[n,LE] = & \Gamma(I)[n,LE]+\sum_{k=1}^{n-1}(\alpha_{LE}[2(n-k)]\cdot\Gamma(I)[k,LE])+ \\ & \sum_{k=1}^{n-1}(\alpha_{HE}[2(n-k)-1]\cdot\Gamma(I)[k,HE])+\varepsilon+u \\ I_{Final}[n,HE] = & \Gamma(I)[n,HE]+\sum_{k=1}^{n-1}(\alpha_{HE}[2(n-k)]\Gamma(I)[k,HE])+ \\ & \sum_{k=1}^{n}(\alpha_{LE}[2(n-k)+1]\cdot\Gamma(I)[k,LE])+\varepsilon+u \end{cases} \quad (2)$$

L'influence de tous ces éléments est déterminante dans la détection et la caractérisation d'une prise de contraste. La réponse en fréquence d'un système détermine la visibilité de certaines caractéristiques qui peuvent être importantes pour décrire un type de lésion spécifique, au point de manquer toute la prise de contraste. Le bruit de fond réduit le rapport signal à bruit de l'image acquise, augmentant ainsi la probabilité de ne pas détecter de structures fines appartenant à la lésion voire la lésion elle-même. Enfin, l'incrément de l'intensité de signal à travers les différentes projections de la séquence d'acquisition en raison du *lag* peut produire des images recombinées inexactes, introduisant de fausses prises de contraste.

Bien qu'il existe plusieurs exemples de modèles développés pour simuler les caractéristiques représentatives des lésions du sein observées sur des images mammographiques [21, 88, 256], il existe un nombre très limité d'ouvrages présentant des modèles physiques ou virtuels reproduisant les caractéristiques des prises de contraste présentées dans des images à rayons X avec prise du contraste du sein [77, 122, 175]. Motivés par les données cliniques introduites dans les travaux de Dromain [77], nous avons concentré nos efforts sur le développement de modèles tridimensionnels correspondant à la variabilité complète des prises de contraste de type masse. Les prises de contraste de type non-masse, qui constituent l'autre groupe principal de prises de contraste présentes en CESM, n'ont pas été abordées dans ce travail. Ces prises de contraste n'ont pas été prises en compte en raison du peu d'information clinique existante sur leurs caractéristiques tridimensionnelles.

D'abord, il n'existe actuellement aucun lexique établi pour caractériser les prises de contraste observées sur les images par rayons X cliniques. Nous avons mené une revue de la littérature des travaux publiés concernant les caractéristiques des prises de contraste observées dans les images cliniques du CESM et avons identifié les principales différences avec l'ACR BI-RADS® établi pour CE-MRI. Ce travail nous a conduit à la définition d'une série de caractéristiques pouvant être considérées pour caractériser différentes prises de contraste (table 2). Nous avons ensuite développé des modèles capables de mélanger toutes les caractéristiques possibles pour les prises de contraste du type masse du lexique défini précédemment. Les lésions générées sont composées par agrégation de plusieurs surfaces analytiques, chacune associée au même coefficient d'atténuation linéaire ou à des coefficient différents. Notre modèle est entièrement géométrique, sans tenir compte des caractéristiques biologiques induites par l'angiogénèse tumorale. De plus, nous n'avons pas évalué le réalisme des images finales en les comparant à un ensemble de données de résultats réels. Malgré ces limites, cette stratégie nous permet de générer des images approximatives plus réalistes et, par conséquent, nous pouvons les utiliser pour mener une étude afin d'évaluer la capacité des systèmes d'imagerie à fournir des images permettant une caractérisation précise de la lésion. L'étude de modèles permettant de générer des prises de contraste du type non-masse est laissée pour des travaux futurs. Enfin, ces substituts des prises de contraste de type masse peuvent être insérés dans un modèle de texture du sein voxélisé [180]. Ce modèle a

Tableau 2: Caractéristiques considérées pour les prises de contraste du type masse et non-masse existantes dans des images par rayons X du sein avec prise de contraste.

Masse		**Non-masse**	
Forme	Ronde	Distribution	Focale
	Ovale		Linéaire
	Irrégulère		Segmentée
Marge	Circonscrite		Régionale
	Indistincte		Régions Multiples
	Spiculée	Distribution de contraste	Diffuse
Distribution de contraste	Homogène		Homogène
	Hétérogène		Hétérogène
	Prise en Anneau		Regroupée
	Sans contraste		Anneaux regroupés
			Sans contraste

été modifié pour fournir la prise de contraste naturelle du parenchyme du sein observé dans des images cliniques. Peu d'études ont inclus des prises de contraste de type masse dans le contexte de la prise de prise de contraste naturelle du parenchyme [38, 77].

Nous avons montré que le choix d'une des expressions de recombinaison proposées dans la littérature n'est pas trivial. Le choix de la soustraction logarithmique [25, 28] ou une combinaison polynomiale [152, 234] aura un impact sur le bruit, la résolution fréquentielle et le *lag* de l'image recombinée finale. Dans notre cas, nous étions limités par la nature de nos simulations mono-énergétiques. Par conséquent, nous avons appliqué une soustraction logarithmique aux images simulées à basse et haute énergies. Comme nous voulions fournir des images d'iode équivalentes aux images expérimentales, avec la même détectabilité des lésions, nous avons modifié le rapport signal à bruit des projections fournies par la plateforme de simulation, avec une erreur inférieure à 1%. Nous avons analysé aussi la réponse fréquentielle des images recombinées avec une soustraction logarithmique en utilisant la formulation développée par Richard and Siewerdsen [249]. Les résultats démontrent que la réponse en fréquence de l'image recombinée dépend de la composition de l'objet d'intérêt, c'est-à-dire du niveau de la concentration d'iode de la prise de contraste et de la composition glandulaire de son voisinage. Nous avons aussi évalué l'impact de l'effet de mémoire ou *lag* dans la recombinaison des paires d'images successives issues de la séquence d'acquisition CEDBT, et la différence produite par le choix des algorithmes de recombinaison. En particulier, sur des simulations du système Senographe Pristina, la différence entre les intensités de signal lors d'une recombinaison en utilisant une soustraction logarithmique et une combinaison polynomiale est inférieure à 2, ce qui représente une prise de contraste surfacique égale à $0,05 mg/cm^2$.

En ce qui concerne les algorithmes de reconstruction pour CEDBT, la reconstruction par rétroprojection filtrée (*Filtered BackProjection* ou FBP) [134] entraîne, par rapport aux méthodes telles que SART [235], OSTR [186] et autres, une augmentation du bruit dans les hautes fréquences et des prises de contraste à peine visibles, dues à une image peu contrastée. Au lieu de rechercher des approches de reconstruction complètement nouvelles, nous avons envisagé la modification du filtre utilisé dans FBP pour surmonter ces deux limites. Les prises de contraste présentes sur CEDBT, information utile, sont plus grandes que les structures observées dans la tomosynthèse. Par conséquent, les structures que nous devons reconstruire appartiennent à la bande des basses fréquences du spectre spatial qui est presque rejetée par le filtre utilisé dans

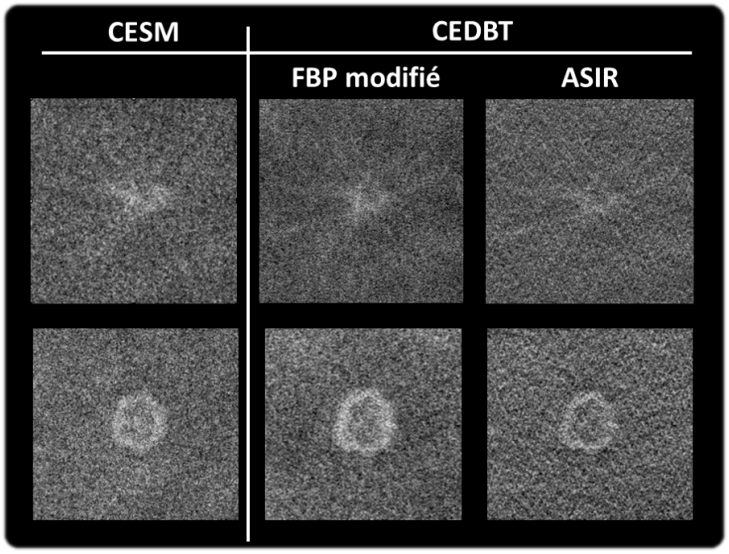

Figure 4: Comparaison des images simulées avec une prise de contraste spiculée et une prise de contraste en anneau pour CESM et la coupe centrale CEDBT reconstruite avec FBP en utilisant notre filtre modifié et la méthode de reconstruction itérative ASIR.

FBP. Motivés par les possibilités d'amélioration de la mise en œuvre de FBP développé par Zhou et al. [315], nous avons optimisé la forme du filtre rampe appliqué aux projections pour prendre en compte cette hypothèse. Nous avons également envisagé différents filtres de régularisation afin de réduire le bruit dans les hautes fréquences, qui ne fournit aucune information clinique. Nous avons observé que le filtre proposé offre un rapport signal à bruit des prises de contraste renforcé par rapport à ASIR, une méthode de reconstruction itérative standard commercialisée pour la tomosynthèse. Notre méthode préserve également les structures fines appartenant aux masses mammaires qui doivent être visibles dans les images CEDBT (figure 4).

Nous avons comparé la qualité des images des prototypes CEDBT à partir du Senographe DS et du Senographe Pristina à l'aide de notre plateforme de simulation. De cette façon nous pouvons analyser les bénéfices que les améliorations de la conception du système pendant plus de dix ans ont apporté sur les images de CEDBT. En particulier nous avons centré notre étude sur l'impact de l'effet mémoire, ou *lag*, ainsi que l'effet du rayonnement diffusé. La séquence d'acquisition du Senographe Pristina est optimisée pour réduire l'effet du *lag* et le système incorpore une grille anti-diffusante pour réduire la contribution du champ de rayons X diffusés. Ce n'est pas le cas dans le système Senographe DS. Ce système souffre d'une augmentation importante du signal dans des images de basse et haute énergies successives à cause du *lag*. De plus, le système n'incorpore pas une grille anti-diffusante lors de l'acquisition des projections CEBT et, par conséquent, les images acquises comportent une contribution significative des rayons X diffusés.

Tous nos résultats ont montré que le système Senographe Pristina permet une meilleure annulation de la texture de fond que dans les images recombinées du Senographe DS. En même temps, le Senographe Pristina garantit une meilleure représentation de la prise de contraste naturelle observée dans le parenchyme du sein et une meilleure détectabilité des prises de contraste dans des lésions mammaires. Nous avons également montré que même dans des conditions où il n'y a pas d'effet mémoire, l'annulation de la texture dans les acquisitions faites avec le

Senographe DS restait d'une qualité inférieure à l'annulation fournie par les images recombinées du Senographe Pristina. Cela peut être lié à la contribution plus élevée des rayons X diffusés dans les acquisitions du Senographe DS.

L'absence de grille anti-diffusante dans le Senographe DS aggrave également l'apparition d'artéfacts dits de cupping dans l'image recombinée, en introduisant une augmentation du signal parallèle au bord du sein, ce qui peut être confondu avec des prises de contraste réelles. Nous avons montré que ces artéfacts sont presque absents dans les images recombinées en considérant une grille anti-diffusante qui réduit l'influence du champ diffusé. De plus, le champ diffusé n'influence pas seulement l'artéfact de cupping, mais également le contraste absolu des prises de contraste. Ce contraste absolu peut changer en fonction de la position de la prise de contraste le long du sein. L'intégration d'une grille anti-diffusante nous permet de fournir des résultats plus quantitatifs tout en augmentant la spécificité des prises de contraste, car nous n'introduisons pas de fausses prises de contraste sous la forme d'artéfacts de cupping.

L'objectif principal de notre travail était d'évaluer la valeur clinique ajoutée de CEDBT par rapport à CESM. Notre plateforme de simulation nous permet de réaliser une étude clinique virtuelle en évaluant les performances de détectabilité et de caractérisation de CESM et CEDBT. Dans cette perspective, nous avons simulé 105 cas CESM et 105 cas CEDBT comprenant diverses lésions couvrant tout le spectre de caractéristiques défini par l'ensemble de descripteurs que nous avons utilisés (figure 5). Nous avons également généré 40 cas CESM et 40 cas CEDBT supplémentaires sans lésion. L'ensemble complet d'images simulées a été évalué par cinq ingénieurs de GE Healthcare, experts en imagerie mammographique, qui devaient répondre au questionnaire suivant pour chaque cas évalué :

Questionnaire 1.

Q1 : Il y a une lésion ? (Oui / Non)

Q2 : Quelle est la forme de la lésion masse ? (Ronde / Ovale / Irrégulière)

Q3 : Quel est le descripteur le plus adapté pour définir ses marges ? (Circonscrites / Indistinctes/ Spiculées)

Q4 : Quel est le descripteur le plus adapté pour définir la distribution de sa prise de contraste ? (Homogène / Hétérogène / Anneau)

Pour chaque question : Quel est votre niveau de confiance ? Pas confiant du tout / Pas confiant / Confiant / Très confiant.

L'analyse de leurs réponses avec des outils utilisés dans la littérature [99, 104] nous a permis d'estimer les courbes ROC (caractéristique de fonctionnement du récepteur) pour la détectabilité et la caractérisation, ainsi que de calculer leurs aires sous la courbe (AUC). Les courbes ROC moyennes, qui prennent en compte la réponse de tous les lecteurs, sont calculées à l'aide de la méthode proposée par Chen et al. [50]. Les AUC moyennes et les écarts-types correspondants sont calculés à l'aide de l'estimateur "one-shot" introduit par Gallas [103]. La différence statistique des AUC pour CESM et CEDBT a été estimée avec la méthode de Dorfman-Berbaum-Metz (DBM) [126] pour une analyse des courbes ROC multi-lecteurs à un niveau de signification de 0,05. Pour éviter un biais lié à l'apprentissage de la base de données (tous les lésions ovales sont circonscrites, par exemple), nous comparons uniquement chacune des caractéristiques globales du lexique (forme, marge et prise de contraste) à des lésions partageant les deux autres caractéristiques (table 3). Ce groupement réduit le nombre d'images évaluées par modalité pour

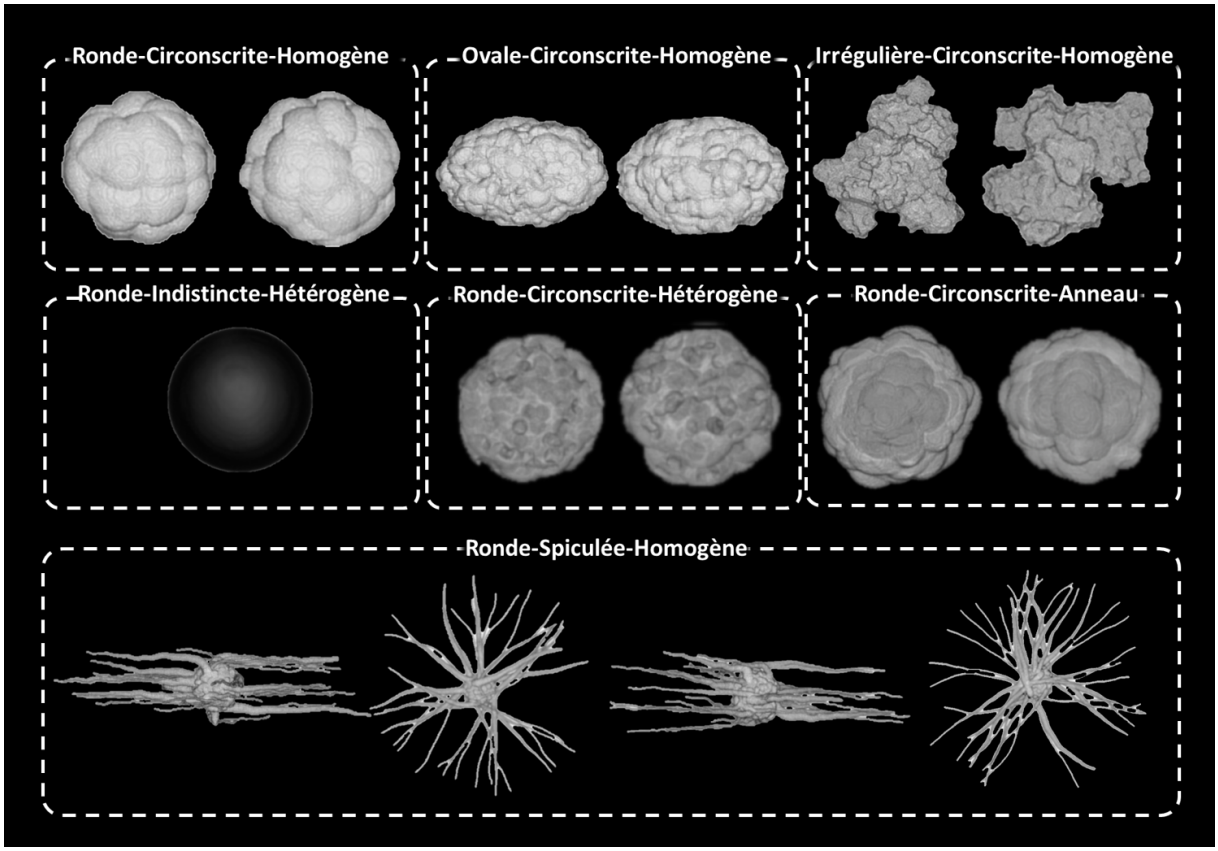

Figure 5: Exemples de modèles tridimensionnels créés en tant que substituts de lésions pour inclure des prises de contraste dans les images simulées.

Tableau 3: Lésions regroupées en catégories pour éviter un biais d'apprentissage lors de l'évaluation de la base de données des cas simulés.

Analyse de	***Lésions générées***		
Forme	ronde-circonscrite-homogène	ovale-circonscrite-homogène	irrégulière-circonscrite-homogène
Marges	ronde-circonscrite-homogène	ronde-spiculée-homogène	ronde-indistincte-homogène
Prise de contraste	ronde-circonscrite-homogène	ronde-circonscrite-hétérogène	ronde-circonscrite-anneau

chaque caractéristique à 45 cas (15 images contenant la caractéristique à évaluer et 30 contenant d'autres caractéristiques). De plus, nous avons également classifié les lésions en deux classes, malignes et bénignes, en fonction de leurs caractéristiques. Les lésions qui sont irrégulières, spiculées, indistinctes, hétérogènes ou en anneau sont classifiées comme malignes, tandis que les autres sont classifiées comme bénignes. Ce regroupement augmente le nombre d'images évaluées par modalité, CESM et CEDBT, et la classe, maligne et bénigne, à 135 cas.

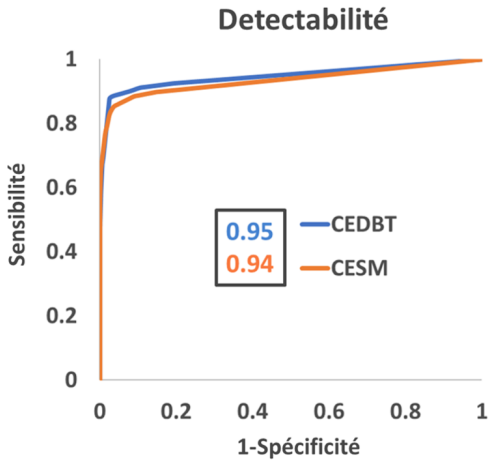

Figure 6: Courbes ROC et ses AUC respectives pour la tâche de détectabilité. Les valeurs de l'AUC sont basées sur l'ensemble des lecteurs et cas simulés pour CESM et CEDBT.

Nous avons constaté dans notre étude que la détectabilité globale était similaire pour CESM et CEDBT ($AUC_{CESM} = 0,94$ et $AUC_{CEDBT} = 0,95$ avec $p\text{-}value = 0,52$, figure 6). Cependant, nous avons remarqué que les lésions spiculées, ovales et irrégulières avec des concentrations plus faibles en iode étaient mieux détectées dans CEDBT. Nous pouvons conclure que, grâce à la disponibilité de plusieurs plans en CEDBT, le lecteur peut mieux dissocier les informations appartenant au cœur de la prise de contraste des lésions et prises de contraste du fond anatomique.

En ce qui concerne la caractérisation des prises de contraste, la forme et la distribution du contraste ont été mieux caractérisées sur les coupes reconstruites de CEDBT que dans les images de CESM (figure 7). Cela peut s'expliquer par le fait que CEDBT distribue les informations 3D dans plusieurs plans, ce qui permet au lecteur de suivre les structures sur les différentes coupes. La caractérisation des marges des lésions a été trouvée similaire sur CEDBT et CESM. Nous supposons que cela peut être attribué à la présence d'artéfacts hors focale (*non-focal artifacts*) dans les coupes reconstruites.

Dans le tableau 4, nous présentons les valeurs des AUC correspondant à chaque courbe ROC ainsi que les résultats du test DBM pour chaque caractéristique. Une différence significative a été observée pour les prises de contraste ovales ($p\text{-}value < 0,01$). Cette différence statistique significative provient probablement des informations tridimensionnelles fournies par CEDBT dans ses coupes multiples. Les formes ovales parallèles à la trajectoire des rayons X ont été interprétées comme rondes dans les projections de CESM, tandis que les lecteurs ont réussi à observer l'élongation de la prise de contraste à travers les différentes coupes fournies par CEDBT.

L'analyse statistique a montré que, malgré la tendance de supériorité de CEDBT sur CESM que l'on peut observer sur les courbes ROC pour la plupart des caractéristiques testées, seule la différence en termes d'identification des masses ovales a été prouvée statistiquement significative en faveur de CEDBT. Cela pourrait être dû à la taille réduite des échantillons pris en compte pour chaque caractéristique dans notre base de données (45 cas pour chaque caractéristique analysée). Pour augmenter la taille des échantillons, nous avons regroupé les cas en deux classes, maligne et bénigne, en fonction des attributs des prises de contraste. Cela nous permet d'avoir un échantillon de 135 cas pour évaluer chaque classe. Les courbes ROC pour chaque classement sont illustrées sur la figure 8, et dans le tableau 5 nous présentons la

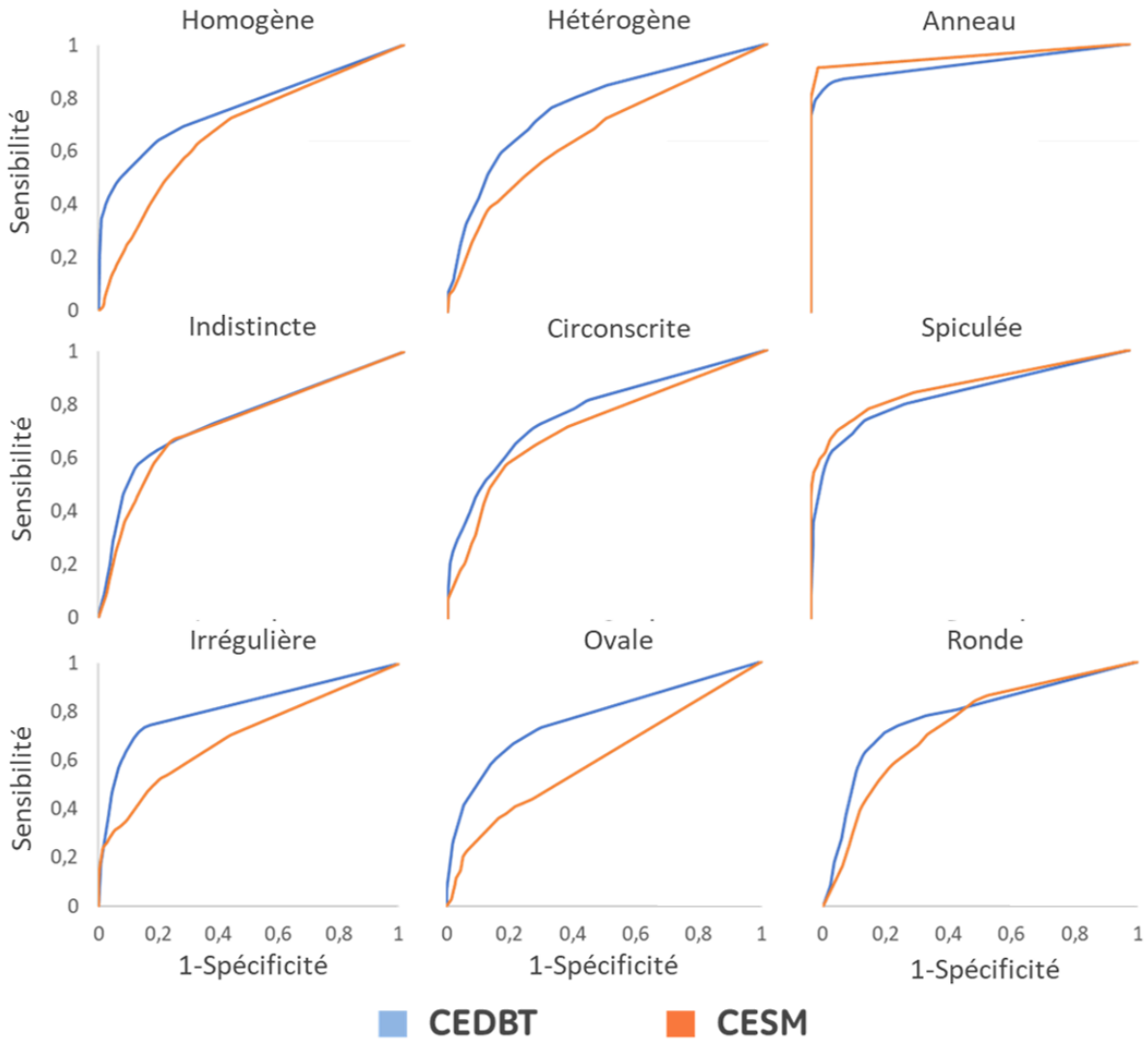

Figure 7: Caractérisation des courbes ROC moyennes des cinq lecteurs, pour CEDBT et CESM. De haut en bas : descripteurs pour la distribution de la prise de contraste, les marges, et la forme de lésions.

valeur des AUC correspondant ainsi que les résultats du test statistique DBM. En rassemblant nos cas, nous pouvons observer une nette supériorité de CEDBT par rapport à CESM en termes de performance clinique consistant à différencier les lésions malignes des lésions bénignes ($p\text{-}value = 0,009$ dans le groupe malin et $p\text{-}value = 0,003$ dans le groupe bénin).

Cependant, nous avons augmenté l'importance de nos résultats au prix d'une perte de spécificité. Nous ne pouvons pas indiquer quelles sont les caractéristiques individuelles qui sont les mieux perçues CEDBT. Par conséquent, un meilleur dimensionnement de l'étude pourrait être nécessaire pour trouver une différence plus importante entre les deux modalités. Dans ce contexte, le concept d'une étude en parcelles divisées discuté par Obuchowski et al. [223] pourrait aider à améliorer la puissance statistique de notre étude.

Dans cette étude, nous n'avons pas évalué l'impact de CEDBT sur l'analyse des prises de contraste de type non-masse, en raison de la complexité de la simulation de telles structures.

Tableau 4: Analyse des AUC obtenues pour différent caractéristiques. Les résultats ont été calculés en utilisant l'estimateur de l'AUC "one-shot" [103]. Les différences statistiques entre les valeurs d'AUC ont été calculées en utilisant la méthode DBM [126]. Les différences significatives sont indiquées en vert (p-*value* $< 0,05$).

		AUC (one-shot) *CESM*	**AUC (one-shot)** *CEDBT*	*p-value* **(BDM)**
Forme	*Ronde*	0.73±0.06	0.78±0.04	0.40
	Ovale	0.60±0.06	0.77±0.04	0.002
	Irrégulière	0.69±0.06	0.82±0.07	0.07
Marges	*Circonscrite*	0.72±0.05	0.77±0.09	0.40
	Spiculée	0.86±0.05	0.84±0.08	0.26
	Indistincte	0.73±0.03	0.75±0.03	0.96
Prise de contraste	*Homogène*	0.68±0.06	0.77±0.06	0.19
	Hétérogène	0.67±0.06	0.77±0.07	0.18
	Anneau	0.95±0.03	0.92±0.03	0.33

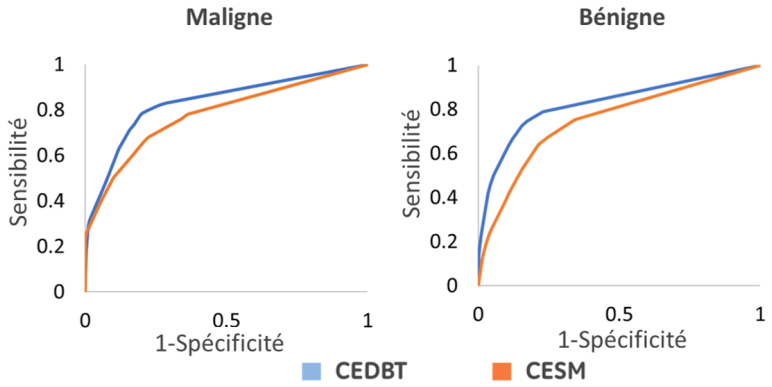

Figure 8: Caractérisation des courbes ROC pour les catégories maligne et bénigne.

Nous nous attendons à ce que la supériorité démontré de CEDBT par rapport à CESM soit également atteinte pour les prises de contraste de type non-masse à cause de leur compléxité morphologique, et leur évaluation sera au centre des études futures.

En résumé, nos contributions ont fourni les outils informatiques nécessaires pour réaliser une étude clinique virtuelle pertinente qui compare les performances cliniques de CESM et de CEDBT. Nous avons amélioré le réalisme d'une chaîne de simulation d'acquisition d'images par rayons X en intégrant plusieurs processus qui n'ont pas été pris en compte dans la littérature jusqu'à présent. Par ailleurs, nous avons créé une plateforme de simulation totalement originale pour créer des substituts virtuels pour les prises de contraste qui prend en compte les informa-

Tableau 5: Analyse des AUC obtenues pour la caractérisation de la malignité.

	AUC (one-shot) *CESM*	**AUC (one-shot)** *CEDBT*	*p-value* **(BDM)**
Malign	0.78±0.03	0.83±0.03	0.009
Benign	0.75±0.03	0.83±0.02	0.003

tions cliniques de CESM. Nous avons effectué une analyse analytique sur l'impact de l'algorithme de recombinaison sur les différents processus présents dans la chaîne d'acquisition des images par rayons X. Nous avons amélioré les performances actuelles de la reconstruction par FBP, en augmentant la détectabilité des prises de contraste dans CEDBT. Nous avons effectué une analyse approfondie des progrès techniques de CEDBT. Enfin, nous avons établi une étude virtuelle pour évaluer la detectabilité et la caractérisation des prises de contraste du type masse sur CESM et CEDBT. Notre évaluation a conclu que CEDBT présente une certaine valeur ajoutée clinique par rapport à CESM, avec une détection améliorée des prises de contraste spiculées et une meilleure caractérisation des signes malins et bénins.

Introduction

Breast cancer is the most common type of cancer developed by women all over the world, as well as the second cause of death by cancer in developed countries and first cause in developing countries [98]. The general trend to an increased survival is correlated with the improvement of screening protocols and systems, as well as a better diagnosis of the cancer at early stage. Standard mammography represents a fundamental solution for early screening of breast cancer, associated with a more favorable survival rate [56]. However, mammography, due to its 2D nature, has two main drawbacks. A dense glandular tissue composition can mask the tumorous lesions existing in the breast, interfering with the diagnosis or even making the lesion impossible to detect. Moreover, some types of breast lesions are not visible in mammography due to the nature of the lesion [198]. To overcome these difficulties, new efforts are needed to improve early detection and diagnosis, to achieve a larger reduction of the mortality.

Due to the tumor angiogenesis triggered by malignant tumors, contrast enhanced methods is one possible solution to address the problems of standard mammography. Currently, Contrast Enhanced Magnetic Resonance Imaging (CE-MRI) is the standard method used in screening of high-risk women and the most sensitive technique for detection and characterization of breast cancer, assessment of local extent of the disease, evaluation of treatment response, and guidance for biopsy and localization. However, this technique is expensive and time consuming. MRI scanners have a low availability, and they cannot be used to detect microcalcifications which are the only findings associated with some early stage breast cancers. On the other hand, Dual-Energy Constrast Enhanced Spectral Mammography (CESM) uses the same technology as standard mammography to retrieve a projection of the iodine content flowing in the breast, delivering contrast-enhanced mammography images. However, the projected nature of the CESM images, as in standard mammography, makes it difficult to analyze 3D information, in contrast to CE-MRI. Contrast Enhanced Digital Breast Tomosynthesis (CEDBT) uses different positions of the X-ray source to acquire a number of different projections of the breast and reconstruct slices of the analyzed breast, in an attempt to show-up the information not visible in a single CESM projection. However, its incremented clinical value, compared to the current CESM exam, is still not well understood [53].

The goal of this work is to compare the clinical benefits of CEDBT over CESM in terms of detection and characterization of the diverse contrast uptakes appearing in clinical exams, taking as starting point the analysis of mass-like enhancements performed by Dromain [77]. Also, we seek to optimize the performances of CESM and CEDBT to compare the full potential of both applications. The novelty of our proposal lies in the evaluation of both techniques using realistic simulated data (X-ray projections, lesions and breast anatomy), including several elements in the simulation chain based on empirical data that, to our knowledge, have never been considered in virtual X-ray contrast-enhanced imaging studies. This procedure helps us having more control

of the study and, consequently, improving the understanding of the clinical differences between CEDBT and CESM. The document is structured as follows.

In Chapter 1, we introduce the starting point of our discussion: the current position and advancements made in X-ray contrast-enhanced imaging systems for breast imaging, as well as the main advantages and limitations between CESM and CEDBT considered today. Then, we show the collective effort pursued nowadays to perform pre-clinical studies using computational tools instead of traditional clinical trials. In this context, we present the current offer of virtual surrogates for the X-ray acquisition chain, the breast anatomy and the breast lesions.

In Chapter 2, we present CatSim (Computer Assisted Tomographic Simulator), an analytic simulation platform conceived in the late 2000's at GE Global Research Center (CT and X-ray Laboratories, Niskayuna, NY, USA) [66] to simulate tomographic images. This platform was later adapted to generate images according to the topology and physical characteristics of mammography [208]. Our work consists in improving the realism of the low and high energy simulated images. In order to simulate clinically relevant results, we must introduce new elements for more realism, achieving simulated images with the same characteristics and quality as real images. This latter requirement is essential to have a faithful and reliable comparison of CESM and CEDBT.

In Chapter 3, we address the modeling of iodine-enhanced breast masses from several geometrical primitives. Our intention is to create, and combine as needed, the various morphological characteristics encountered in clinical practice, providing a large dataset of three-dimensional lesions representing breast masses. Additionally, we will work at representing the remaining anatomical texture observed in clinical contrast enhanced breast images, leveraging an already existent breast texture model developed by Li et al. [180]. Our objective is to integrat all these elements in the X-ray simulation platform.

In Chapter 4, we will focus on the assessment of the existing recombination algorithm. Frequency, stochastic, and memory processes are dependent on the recombination choice. Our goal is to study the impact of different recombination algorithms on the final properties of the recombined image. We will also work at optimizing the reconstruction algorithm for CEDBT to our clinical task.

In Chapter 5, we compare CEDBT for two different systems, Senographe DS and Senographe Pristina, to analyze the different elements of the imaging chain, how they affect the image quality, and how the impact of these factors may be reduced by technology to improve clinical results.

Finally, in Chapter 6, we present a Virtual Clinical Trial (VCT) comparing the clinical performance of CESM and CEDBT to detect and characterize mass-like contrast uptakes. We expect that the results of this study may help in the future creation of clinical protocols evaluating contrast-enhanced X-ray images of the breast.

Chapter 1

Context and motivation

In this chapter we present the clinical context of this work: the different X-ray contrast-enhanced imaging systems for the breast. To this end, we introduce the biological processes contributing to tumor development and how this is related to the vascular structure inside the breast. This will lead us to the main principles allowing us to visualize unusual concentrations of blood vessels and, therefore, depict different breast lesions. We also expose the still existing needs and requirements to further improve the detection and characterization of breast tumors in the existing X-ray contrast-enhanced imaging systems. At the same time, we present the components involved in a Virtual Clinical Trial (VCT), and how they can be used to provide an evaluation of different imaging techniques, through the simulation of the real elements composing a clinical study. Finally, in the conclusion of this chapter, we define the goals of the work and the organization of this work.

1.1 Contrast-enhanced X-ray imaging of the breast

Contrast-enhanced breast imaging (CEBI) refers to the acquisition techniques that, using a contrast agent introduced into the vascular system of the patient, benefit from the angiogenesis process to highlight the presence of potential tumoral growths inside the breast. Because of their increased contrast between normal breast tissue and possible findings, CEBI systems are expected to improve detection, localization and characterization of breast tumors compared to digital mammography. Despite this, their purpose is different from that of conventional mammography or breast tomosynthesis.

Nowadays, CEBI techniques focus on high risk screening, diagnosis and staging of breast lesions [18, 198]. For these tasks, 3D contrast-enhanced magnetic resonance imaging (CE-MRI) is the current standard of care in most of clinical environments. The acquisition protocol of this technique demands that a pre-contrast image is acquired before the injection of the gadolinium chelates, and several images are acquired during the few minutes following the contrast injection. The preinjection image is then substracted from the post injection images to deliver contrast-enhanced MRI images [164, 163, 201].

However, an effort of the scientific community has been made to demonstrate the value of X-ray based techniques as alternative methods with similar functional information, sensitivity, higher specificity, and less background enhancement [90, 91, 179, 189], improving the accessibility of the exam, the user experience, at a lower cost [230, 277]. These X-ray contrast-enhanced imaging systems for the breast will be the focus of this thesis.

1.1.1 Tumor angiogenesis

Tumor angiogenesis is the process by which a disordered vascular structure is formed around a tumor in growing phase. This development of new vessels from pre-existing ones is triggered when the tumor reaches a diameter larger than $1mm$. At this moment, the lump suffers from hypoxia symptoms as tumors need to consume more oxygen to grow, but limited by the vascular distribution surrounding them. The lump then secretes various growth factors to stimulate the creation of a new vascularization. During this step, a main difference appears between normal angiogenesis, that takes place for example during fetal growth, and tumor angiogenesis. In malignant tumors, the maturation phase during which the cell differentiation occurs does not take place, producing a highly disordered architecture of new vessels crossing and feeding the tumor. Furthermore, the enhanced permeability and retention (EPR) effect produces an increased permeability of the blood vessels generated around lumps, allowing some nano-particules, flowing in the blood stream, to diffuse into the tumor [101, 109, 296].

The basis of contrast enhanced techniques is to take advantage of this biological process. As a consequence, when a suitable contrast medium is injected in the blood flow of the patient, there is an accumulation of contrast through the mass, improving its contrast over the background and increasing its depiction and, therefore, its diagnosis. Two X-ray based techniques can be considered in this group: Contrast Enhanced Spectral Mammography (CESM) and Contrast Enhanced Digital Breast Tomosynthesis (CEDBT).

1.1.2 Contrast-Enhanced Digital Mammography

As described before, Contrast Enhanced Spectral Mammography (CESM) exploits the angiogenesis process, delivering highly contrasted mammography images, with contrast uptakes pointing to suspicious masses in the breast. This is performed thanks to the difference between the linear attenuation coefficients of the breast tissues (mainly adipose and glandular, as described by Cooper in [59]) and the iodine contrast agent injected into the vascular system of the patient. The iodine presents a K-discontinuity at 33.17 KeV. Consequently, two mammograms can be acquired using different energy spectra: a Low-Energy (LE) image with characteristics similar to standard mammography and a High-Energy (HE) image, taking advantage of the iodine incremental attenuation of photons with energy higher than 33.17 KeV. This difference between X-ray attenuation of iodine and breast tissues at low-energy and high-energy is exploited to cancel the contrast of tissues in regions without iodine through the combination of the two mammograms. This technique is known as dual-energy subtraction [177], and it is described more in detail in Chapter 4. Therefore, CESM generates an image that represents the quantity and distribution of the contrast agent along the breast, showing only regions with iodine uptakes [65, 227, 277]. The CESM acquisition sequence is illustrated in Figure 1.1.

Regarding the clinical benefits, several studies have proved the superiority of CESM over *Full-Field Digital Mammography (FFDM)* in terms of sensitivity and specificity, improving the detection, extent assessment and diagnosis of tumorous lesions [189, 190, 228, 288]. This improvement motivated the work of Lobbes et al. [183]. With 113 cases and two readers, they demonstrated the effectiveness of CESM as a consistent problem-solving tool to address the inconclusive results found in screening mammography images. Later, Lalji et al. [167] confirmed these results in a larger population of 199 cases and a panel of 10 radiologists with different CESM experience. Later on, Fallenberg et al. [92] studied the impact of CESM evaluations on detectability compared to FFDM depending on breast density. Using 107 cases, among which 56% were categorized as having a high breast density, CESM showed an increased sensitivity

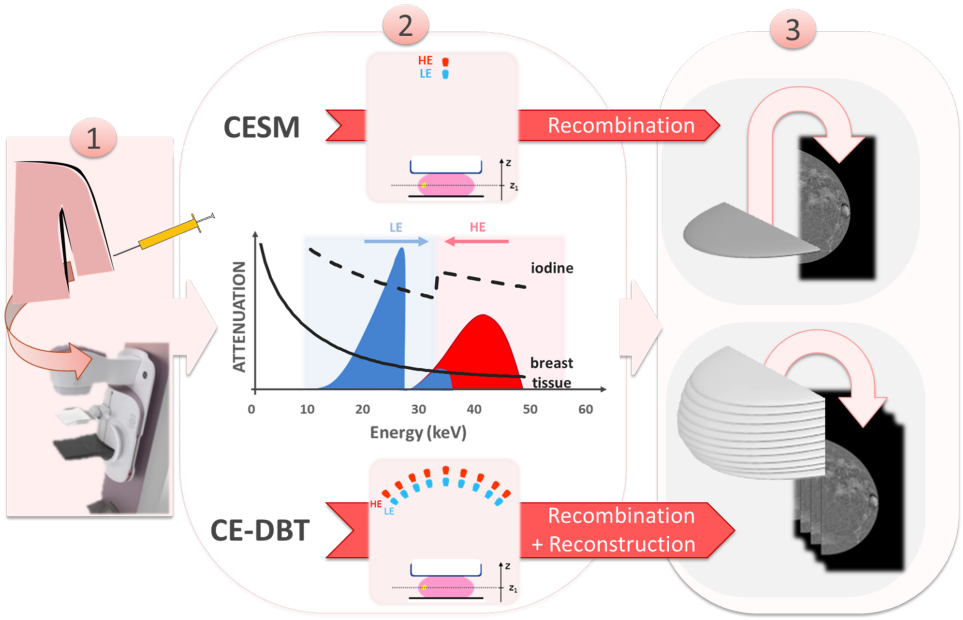

Figure 1.1: Acquisition protocol for CESM and CEDBT. First, the contrast agent is intravenously injected into the patient. Then the breast is imaged: single LE and HE projections at the same angle for CESM, and multiple LE and HE projections at different angles for CEDBT. The last step is the processing of the acquired images: recombination of the single pair in the case of CESM, the recombination and reconstruction of all the pairs of images in the case of CEDBT.

of 16.8% compared to FFDM (94.7% against 77.9%, respectively). In a more recent study, Mori et al. [213] imaged 143 breasts using both FFDM and CESM, among which 90.2% were considered as having a high density. In this work, CESM showed an increase in sensitivity of 32.8% compared to FFDM (86.2% against 53.4%, respectively). In addition, low-energy CESM images provide similar information for FFDM images, avoiding to perform additional mammography acquisitions to patients who were scheduled for a CESM exam, reducing the total Average Glandular Dose (AGD) [166].

Compared to *breast CE-MRI* protocols, CESM offers similar diagnostic performance, with similar sensitivity and higher specificity [179, 188]. In particular, Fallenberg et al. [90] studied the correlation between the tumor size measurements provided by FFDM, CESM, CE-MRI and post-operative histology. In this work, both techniques, CESM and CE-MRI, showed no significant difference to the breast cancer size obtained in histopathology. In an independent study, Lobbes et al. [184] showed also a high correlation between the size measures using CESM, CE-MRI and histopathology, obtaining Pearson's correlation coefficients (PCC) above 0.9 ($p\text{-}value < 0.0001$). Besides that, a reliable breast cancer extension assessment is critical when monitoring the Neoadjuvant Therapy (NAT) response. This type of therapy is applied to advanced, big cancerous growths, in order to reduce their size before surgery [182]. Iotti et al. [140] showed high correlated measurements between CESM and MRI of the lesion sizes before (0.96), during (0.94) and after (0.76) treatment. Similarly, Patel et al. [229] compared the residual tumor size after treatment, proving that both, CESM ($p\text{-}value = 0.009$) and CE-MRI ($p\text{-}value = 0.01$), had a good correlation with the size of the pathology measured after surgery. Another domain where CE-MRI is currently the standard is the screening of high-risk patients, due to the

reduced sensitivity of mammography over this population [232]. Phillips et al. [230] evaluated the preference of high-risk patients regarding CESM and CE-MRI. CESM was chosen over CE-MRI by a large percentage of the women participating in the study (79%) if both techniques share the same sensitivity. In their study, Fallenberg et al. [91] performed the evaluation of 155 patients using FFDM, CESM and CE-MRI. From this population, 88 women had dense breasts, each of them with at least one tumorous growth. In these conditions, CESM and CE-MRI had no significant differences in terms of Area Under the Curve (AUC), sensitivity and specificity (see Appendix A for more information about the statistical tools to evaluate clinical performance).

Despite all the benefits mentioned above, CESM remains a projection technique, as standard mammography, providing 2D images of the breast. Even with intravenous contrast enhancement, at projection, all the overlaying breast tissues enhanced by the contrast uptake are superposed in the final image. This may affect the detections, measurement and characterization of cancerous lesions [69]. An example of CESM clinical images is shown in Figure 1.2.

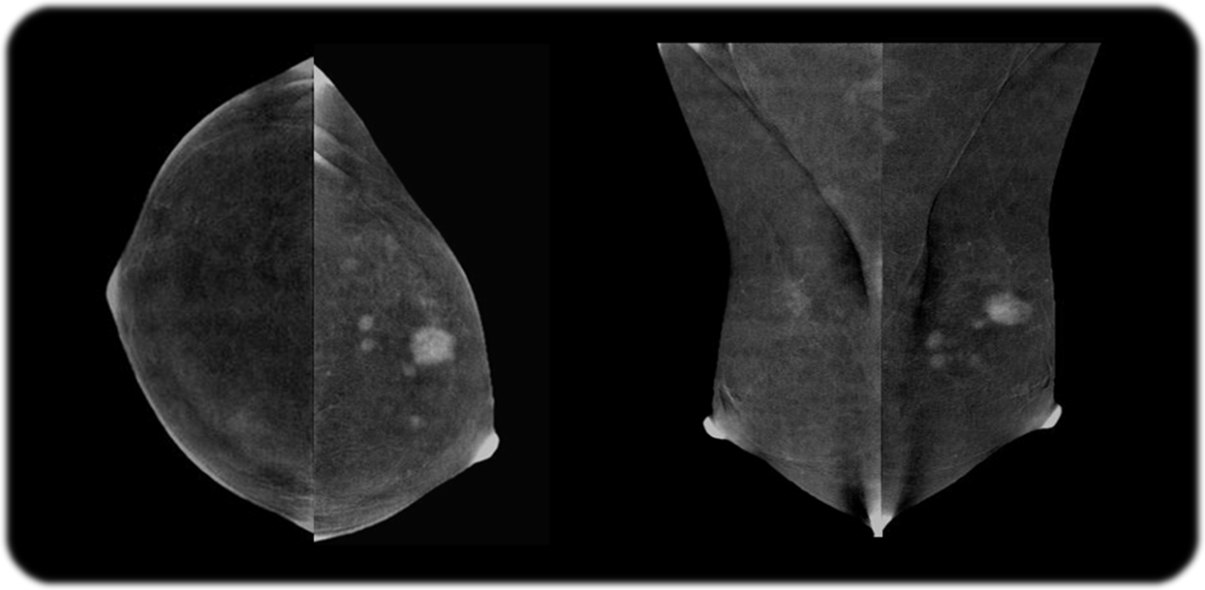

Figure 1.2: Example of CESM clinical images (Images courtesy of Dr. Clarisse Dromain, Gustave Roussy – Villejuif, France).

1.1.3 Contrast-Enhanced Digital Breast Tomosynthesis

Contrast Enhanced Digital Breast Tomosynthesis (CEDBT) relies on the same hypotheses as for CESM. This technique also uses LE and HE mammograms to obtain, through their combination, a representation of the contrast medium injected to the patient. However, this technique uses an acquisition sequence similar to conventional digital breast tomosynthesis (DBT), where different projections are acquired at multiple gantry positions, in a delimited angle range. Subsequently, these projections are reconstructed to produce a series of tomographic slices through the breast. In CEDBT, LE and HE projections are acquired at different angles, so they can be recombined and reconstructed, to generate several breast slices containing information about the iodine content in a specific region of the total breast thickness. The different reconstruction techniques are further developed in Chapter 4. The CEDBT acquisition sequence is illustrated in Figure 1.1.

CEDBT attempts to combine the benefits from CESM and DBT, enhancing the conspicuity and contrast of cancerous lesions. Therefore, CEDBT is expected to improve detectability, localization and characterization of suspicious masses [49]. However, due to the technical complexity required for CEDBT acquisitions, there is only a reduced collection of published clinical works. Consequently, its incremented clinical value, compared to the current CESM exam, is not still well understood. In a preliminary study, Carton et al. [39] showed the clinical feasibility of dual energy CEDBT providing similar information to MRI for a single imaged malignant lesion. Later, Hill et al. [125] performed a proof of concept in rabbits, comparing the results observed in CEDBT reconstructed slices to the histopathology. In parallel, Gavenonis et al. [107] evaluated the characterization of 10 lesions in a population of 8 patients using CEDBT, FFDM and MRI. The results indicated a similar performance of CEDBT compared to MRI, characterizing as malignant 7 out of 8 lesions. A larger study was performed by Chou et al. [53] where 185 patients and a total of 225 lesions were evaluated before biopsy. In this work, three readers scored the probability of malignancy for each case reviewing the available modalities in the following order: FFDM, DBT, CESM, CEDBT and CE-MRI. The additional information contained in the contrast enhanced modalities was evaluated by computing the averaged AUCs. CESM (0.878), CEDBT (0.892) and CE-MRI (0.897), were found to be superior to FFDM (0.740) and DBT (0.784). Moreover, no statistical difference was found between these three modalities ($p\text{-}value < 0.05$). More recently, Huang et al. [134] published a preliminary report from an ongoing clinical feasibility study. In their work, a total of 11 malignant lesions were evaluated by two readers using CESM and CEDBT. A 5 point scale comparative score for contrast enhancement and margin identification between the two modalities was given for each case. Their results indicate a better margin characterization of CEDBT compared to CESM, while detectability may be compromised because CEDBT offers less contrast-enhancement in its in-focus planes than CESM.

At this moment, CEDBT shows some clinical benefits compared to CESM, including the three dimensional information as for MRI and the spatial resolution of DBT, which may increase lesion characterization compared to CESM. However, there are still several elements to be considered for an appropriate comparison between both modalities. The complexity of its associated acquisition sequence increases the consequences of some physical effects in the X-ray chain, degrading the quality of the projections [41]. Moreover, the methods used for the reconstruction of CEDBT slices may affect detectability and characterization of the enhanced lesions [266]. In Figure 1.3, we show some slices of an early clinical CEDBT prototype.

1.1.4 Clinical protocol in contrast-enhanced X-ray imaging of the breast

In clinical studies, several factors may affect the final lesion assessment made by the radiologist. In particular, the evaluation of contrast-enhanced mammography images share the inherited visual analysis performed in CE-MRI, and also the characteristics observed in standard mammography. Radiologists have defined a series of visual criteria which must be considered for clinical assessment. The study and better understanding of these criteria can help us to provide a more deep insight of the possible advantages of CEDBT over CESM.

Presence, type and intensity of artifacts.

An artifact is defined as a spurious contrast uptake in the recombined image, that cannot be attributed to breast tissue parenchyma, skin contour, axillary anatomical structures, calcification, foreign object, or enhancing lesion in breast parenchyma or lymph node. It is typically introduced into the final image as a consequence of the hypotheses considered in the recombi-

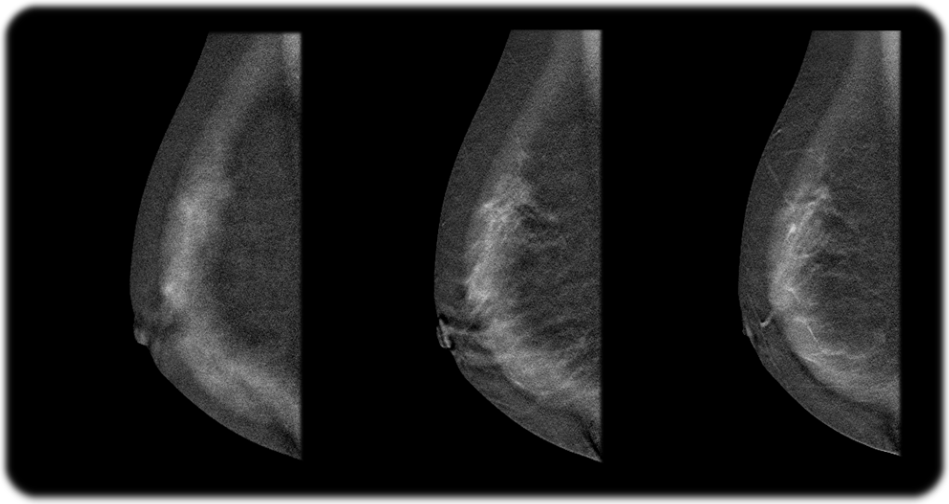

Figure 1.3: CEDBT slices from early prototype, just for illustration.

nation algorithm, such as stationarity of X-ray physic phenomena, subsequent projections of a still object, and a simplification of the elements composing the breast tissue (see Chapter 4 for further clarifications on the hypotheses introduced in image recombination).

Several types of artifacts have been identified as common findings in the recombined images, grouped into five categories [17, 304] (Figure 1.4):

- Rim or breast-within-breast artifact: this undesired enhancement is characterized by a whiter "arc"-shaped region parallel and near the breast edge.
- Low-frequency artifact: it can be described as a white intensity gradient coming from the pectoral muscle region and spreading onto the breast surface.
- Skin-line artifact: this enhancement is observed over the skin contour and the nipple, causing a fine white line in the breast edge.
- Ripple artifact: it is defined by parallel black and white lines covering the breast region where the parenchyma is present.
- Negative contrast enhancement artifact: these "fake" enhancements are identified as blacker areas over the breast surface.

Detectability and intensity of the contrast uptakes in the recombined images.

Some recent studies have related the intensity of the visualized contrast uptakes to the malignancy of the findings [290]. Consequently, CESM and CEDBT acquisitions need to be qualitatively consistent and offer an intensity of the contrast uptake related to the real iodine concentration. By doing that, we can fulfill also another requirement: visually differentiate contrast uptakes with different iodine concentrations.

Lesion characterization.

The characterization of the lesions, as they are identified, is based on the ACR BIRADS descriptors (type of lesion, shape, borders and internal enhancement) [76]. A more detailed description of these characteristics and how they are interpreted by radiologists is given in Chapter 3.

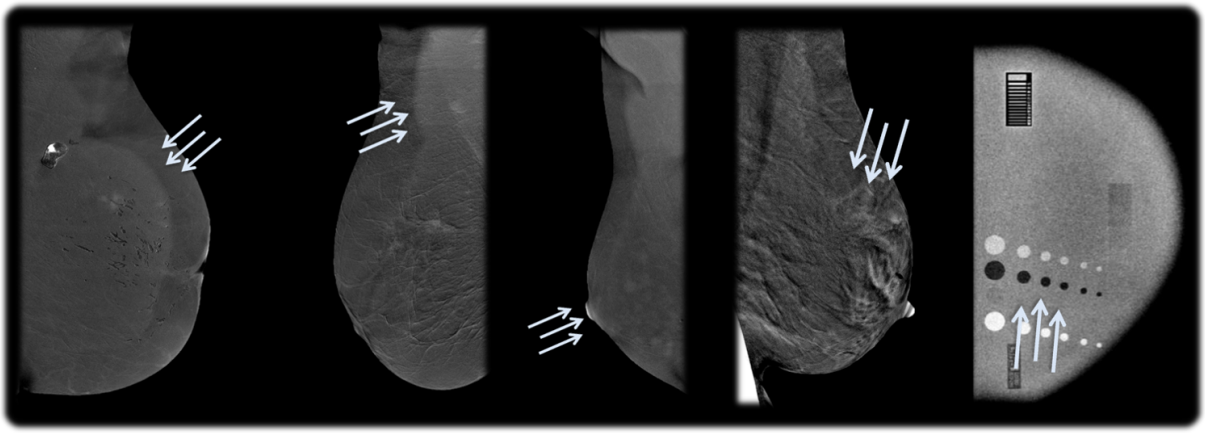

Figure 1.4: From left to right: breast-within-breast, low-frequency, skin-line, ripple, and negative contrast enhancement artifacts in CESM images.

Evaluation of Breast Parenchyma Enhancement (BPE).

BPE is a well-known phenomenon first observed in CE-MRI, which is common in all contrast enhanced breast imaging modalities [165]. This effect refers to normal fibroglandular breast tissue affected by the contrast uptake after intravenous injection. In particular, in CESM recombined images, BPE appears as a background enhancement uncorrelated to the presence of a lesion [231]. However, it is not an undesired phenomena, as recent studies suggested to include the degree of the BPE intensity as a possible new breast cancer risk factor [265]. Moreover, it has been shown that there is a substantial agreement between the level of BPE observed on CESM and MRI images [278]. Several studies have demonstrated that the ratio of false-positive cases increases when a moderate or marked BPE is present [11, 55, 71]. Finally, BPE must also be considered as a factor reducing the detection and characterization of breast lesions due to its masking effect [287, 293].

Contribution of the low image to diagnosis.

CESM acquisitions only show contrast enhanced tissues. Consequently, some important signs of malignancy which do not absorb any contrast uptake may be not present, such as microcalcifications. Despite this, the quality of low energy images from CESM acquisitions is not inferior to a standard Full Field Digital Mammography, giving similar diagnostic information. Furthermore, clinicians recommend using this additional information in the assessment of the recombined image [23, 166].

1.2 Image simulation in virtual clinical trials

The assessment of new systems, tests, treatments or acquisition methods (including algorithms) is driven by clinical trials, where a human research is performed to measure their safeness and effectiveness. Clinical trials is the conventional approach to assess the performance of novel mammography techniques, and compare them to its presumed concurrence, when standard quality metrics are not enough to evaluate their clinical benefits. However, such evaluations are often expensive, lengthy and burdensome. Moreover, access to ground truth is not always available. This may interfere with the reliability of the results when performance of two or more novel techniques are compared.

Virtual clinical trials (VCT) refer to computational tools helping to simulate a clinical trial. VCT has been established as a pre-clinical alternative to real clinical trials due to their cost and time-consuming conditions [157, 197]. Therefore, over the last years, an increased number of publications have implemented VCT routines to evaluate different clinical tasks [8, 86, 111]. As shown in Figure 1.5, in VCT we can model the healthy and diseased patient and the acquisition chain, as well as the image evaluation performed by the radiologists. This workflow can be used to provide a quantitative and objective analysis of the advantages of a new imaging technique. The components of a VCT can replace entirely or partially any of the elements involved in a real clinical trial. In this context, the human cohort of patients can be substituted by anthropomorphic physical or digital breast phantoms which imitate the anatomical content of real breasts. We can also introduce inside those phantoms different breast lesion surrogates portraying the wide variability of characteristics observed in clinical environments. The imaging system can be replaced by an X-ray simulation platform that realistically models the image acquisition process. Finally, simplified visual tasks and radiologist scoring can be also modeled using mathematical observers to reduce reading time.

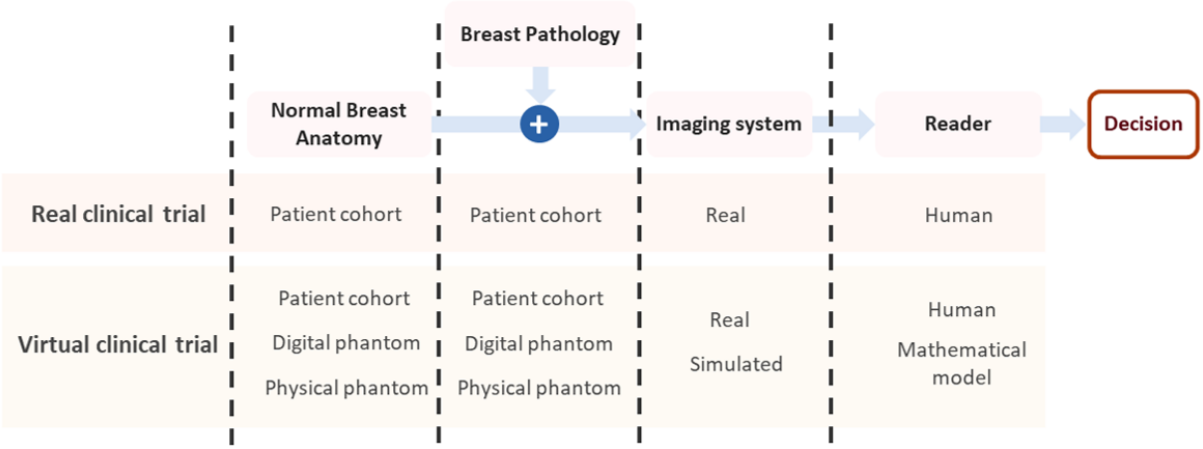

Figure 1.5: Components of a real and virtual clinical trials. The components of VCT can be combined depending on the choices made for the study.

As shown in Table 1.1, the main limitations of VCT are the realism of the results provided by the simulated environment and the choice among the different elements composing the VCT. These two constraints depend on the clinical protocol to be evaluated, which must be defined beforehand. On the one hand, the realism level needed in VCT tools depends on the goal of the study. For instance, physical and digital breast models reproduce the anatomical breast content with different levels of detail, from large scale structural elements to local details describing small regions of interest. Furthermore, due to the challenge involving the simulation of certain physic phenomena or/and some components in the real acquisition systems (e.g. anti-scatter grid), the image simulation platforms may replicate them using different realism levels. On the other hand, there is an inherent trade-off when choosing among the available VCT tools which must be analyzed in advance. For instance, while the physical breast phantoms available today do not reproduce a large variability of anatomical structures, digital phantoms offer us the opportunity of simulating a larger database of different cases. Therefore, if the goal of the study is to assess clinical feasibility, physical phantoms may be sufficient for VCT evaluation. However, larger VCT may need the adoption of digital phantom models. Similarly, the realism

needed in the simulated acquisition platform depends on the metric to be evaluated and how each of the physical processes of the X-ray chain may affect the results.

Table 1.1: Advantages (✓) and disadvantages (✗) of real clinical and virtual clinical trials.

	Time	Cost	Variability	Realism	Choice of study elements
Clinical Trial	✗	✗	✗	✓	✓
VCT	✓	✓	✓	✗	✗

Some VCT studies have been already performed to evaluate the characteristics of CESM and CEDBT. Bliznakova et al. [20] developed a complete mammography simulator to demonstrate the feasibility of dual-energy subtraction mammography. Dromain published in her PhD [77] preliminary results of a simulated comparison between CESM and CEDBT. In her work, three readers evaluated simulated images of different contrast uptakes inside anthropomorphic phantoms, resulting in a similar characterization and detectability for both modalities.

1.2.1 Simulation of the X-ray chain

In X-ray acquisition systems there are numerous physic processes contributing to the final image generation. Over the last two decades, a considerable amount of work presented different approaches to anticipate the quality of future radiography systems using digital replicas. These approaches reproduce the physic phenomena using diverse numerical tools. They can be categorized into three distinct groups: Monte-Carlo (MC) simulations, Cascaded System Analysis (CSA), and analytical simulators.

Monte-Carlo simulations

MC algorithms have been largely adopted in the literature, alone [93, 94] or in combination with analytical models [306], to simulate medical applications employing iodinizing radiation. These simulation platforms use the known probability distributions of particle interactions and a discretized setting to model the physical phenomena throughout the acquisition chain. The probability distributions are sampled using MC algorithms to compute the distance between interactions with the medium, the energy loss and angular deflection in the interactions, and the generation of secondary particles. This approach can be used to accurately simulate X-ray projections of an digital phantom. However, a large amount of particle trajectories need to be simulated to converge to the actual solution [7]. To overcome this disadvantage, more sophisticated algorithms based on mathematical tools [57] or new hardware architectures [5] have been developed. These improvements have provided powerful and efficient simulation tools [6]. Moreover, large VCT studies have been published using this approach [8]. Despite these advancements, this technique requires massive computational resources. In addition, some elements of the X-ray system, such as the movement of the anti-scatter grid, can be very complex to be included efficiently into MC simulations.

Cascaded System Analysis

Beside MC simulations, CSA theory was developed to provide quality metrics depending on the parameters of a particular imaging system. The mathematical framework was originally proposed by Rabbani and Van Metter [237, 238], where each of the physical processes triggered by photon interactions in a X-ray chain are divided into two groups: gain or scatter stages. In their work these authors describe the statistical properties (i.e. mean, variance and covariance) of the signal distribution at the output of each one of these stages, helping to represent a whole complex system as a serial cascade of simpler stages. This linear model was continued

by Cunningham [61]. In his work, various parallel paths are included to describe more complex processes in X-ray imaging. This same approach was adopted by a large number of studies [211, 248, 274, 313]. CSA has the benefit of being completely analytical, however, it only works under conditions of wide sense stationary (WSS) noise processes [206]. This hypothesis is no longer true when we need to simulate the X-ray projection of a full object, as the input is non-homogeneous.

Analytic simulations

However, regardless the stationary constraint introduced by CSA models, some analytic tools adopted the essence of linear cascaded modeling to reproduce X-ray images [66, 85, 87, 108, 305]. These frameworks are based on the pioneer simulations of Van Metter [294], where an input random signal representing a noisy version of the primary field is transmitted through various linear cascaded stages, similarly to CSA. In this approach, two main phases are distinguished: ideal image formation or projection phase, and image degradation or detection phase. In ideal image formation, the simulator needs to know the spectrum and geometry used by the system. Then, a ray-tracing algorithm is used to compute the number of photons arriving at each pixel of the detector after crossing the object, following the Beer-Lambert law [172, 272] (for more information about the image formation in X-ray systems see [144]). This process generates an image which represents the ideal primary field. In other words, an image with perfect resolution, contrast, and without any noise or artifact. Secondly, in the image degradation phase, as in CSA, several gain and blurring stages are applied to the ideal primary field, in order to introduce the noise, blur, and scatter level of the real acquisition system. All these stages are mathematical models of the real processes which intervene in the X-ray chain, and help to produce images with similar properties to the experimental ones: resolution, contrast and noise, among others.

However, to our knowledge, there is no available analytic simulation tool capable of simulating a complete CEDBT sequence and, therefore, the development of a simulation tool capable of this type of simulations will be one of the goals of this work.

1.2.2 Simulation of the breast

In VCT the human patients can also be replaced by virtual or physical surrogates representing the morphological features of the woman breast and the described lesions which may appear in symptomatic patients. Consequently, in this section we present the different models described in the literature to generate realistic breast anatomical textures, and some of the breast findings with morphological characteristics as observed in clinical practice.

Breast anatomy

The anatomical complexity of the breast has motivated the development of several techniques to simulate the texture observed in X-ray breast images.

First, breast texture models have benefited from the parametric formulation of the mathematical random field theory [289]. These models were originally used to create bidimensional intensity representations of realistic FFDM images [24, 32], and they were further developed to generate three-dimensional volumes resembling the background anatomical breast texture [245, 181]. Hill et al. [123] used a double-layered clustered lumpy background (CLB) with modified layers to include the iodine appearance in mammographic images. More precisely, iodine was added to one layer with long linear structures representing the breast vascularity, and into a second layer with finer structures representing the parenchyma. The advantages of random field breast texture models lie in their parametric nature. Different simulated textures can be obtained from a simple random model by sampling the parameters defining the model. Moreover, the statistics properties of the model can be analytically derived and used in theoretical

performance studies, such as detection performance of human observers [34]. However, these models have also some limitations. In particular, these models offer a restricted morphological variability, as well as a lack of realism, when they are compared to clinical breast images.

In a different manner, instead of seeking a mathematical description of the characteristic texture of clinical mammograms, anthropomorphic breast phantoms are three-dimensional models simulating the arrangements of large, medium and small anatomical structures inside the breast. Depending on the methodology employed to simulate this anatomical complexity, three categories can be distinguished:

- In model-based phantoms, the simulated anatomical structures consist of several geometric elements defined by mathematical primitives. For instance, the compartmental nature of adipose and glandular breast tissue is usually represented by stochastic tessellations using simple primitives such as spheres, ellipsoids, or Voronoi diagrams. Other structures such as the breast ductal network can be included into the model using also simple geometric elements. Finally, such models can be sampled using multi-resolution meshes [37, 196] or voxelized structures [10, 46, 191, 233, 309]. Carton et al. [38] also included the effect of iodine uptake in fibroglandular tissue. In their work, they assigned attenuation coefficients corresponding to homogeneous mixtures of fibroglandular tissue and different iodine concentrations to the mesh objects representing the fibroglandular tissue. The main drawback of these models is the lack of mathematical tractability as they are not dependent on a fixed, well defined, mathematical model.

- Empirical-based phantoms employ clinical data or high-dose breast computed tomography of mastectomy specimens to create an anatomical breast simulation. The different structures are extracted and classified from these data using a segmentation algorithm. Afterwards, each of the segmented volumes is associated with the corresponding anatomical properties. Furthermore, these volumes can be modified through image morphing [130] or surface deformation [178] to obtain a larger variability of breast tissue compositions. Kiarashi et al. [158] proposed a segmented model with dynamic representation of the contrast uptake to assess the parenchyma enhancement in CESM images. Elangovan et al. [84] created an anthropomorphic phantom with glandular texture obtained using segmented DBT volumes. However, these models are limited by the efficiency of the applied segmentation algorithm. Moreover, empirical-based phantoms provide only a restricted range of different breast textures.

- The goal of hybrid phantoms is to combine the benefits of random field breast texture models, model-based phantoms and empirical-based phantoms. Three-dimensional random fields describing the background fibroglandular and adipose distribution can be combined with geometric primitives representing other anatomic structures [22, 170]. Similarly, empirical data can also be added to include higher-frequency breast structures [51]. Li et al. [180] proposed a hybrid methodology to create three-dimensional tractable mathematical models of the breast texture. This phantom is generated using random field processes described by parameters based on segmented clinical data.

All the three-dimensional models presented before can be included in the simulation platforms discussed in Section 1.2.1 to obtain realistic mammography simulations, or fabricated as a physical object to be imaged by a real imagery system [199].

Breast lesions

Similarly, to assess lesion detectability and characterization, virtual and physical models of pathological findings described in different breast modalities have been developed. Traditionally, three-dimensional physical geometrical inserts, such as spheres of different diameter ranges to represent microcalcifications and masses, and linear structures to represent architectural distortions, have been used to measure the pre-clinical performance of FFDM and DBT assessing findings [220, 247, 302]. However, the variability of morphological characteristics available in these phantoms is extremely reduced. To overcome this constraint, digital models have been proposed to offer a more variable spectrum of mammography masses. Within this category, we can distinguish two different approaches. First, the analytic characterization of breast findings appearance in real images produces a parameter space which can be randomly sampled to produce synthetic findings [15, 225, 264].

Otherwise, breast findings can be simulated using three-dimensional mathematical objects. These simulations can be integrated into a simulated breast texture and projected with a X-ray simulation platform to obtain mammographic images. Bliznakova et al. [21] simulated regular shaped breast abnormalities, as round, lobular and elongated findings, using simple geometrical primitives such as spheres, ellipsoids and cylinders. Furthermore, they also proposed a 3D random walking algorithm to generate voxelized irregular shaped findings. Similarly, Ruschin et al. generated bidimensional representations of irregular shaped masses to include them sin real mammograms using a simplified random-walk algorithm [256]. This procedure was adopted by several authors later to generate three-dimensional solid masses with irregular margins [108, 128, 242]. In addition, Rashidnasab et al. introduced a variant to random walk methods by growing irregular solid structures from a defined nucleus using diffusion limited aggregation [88, 243]. Simulation models of spiculated masses have also been proposed. Sisternes et al. [276] included tubular shapes growing from random points of a central mass created with a Gaussian random sphere model. These tubular structures are concatenated iteratively with different diameters, lengths, orientations and bifurcations to generate spiculated structures. The realism of the model was validated later [67]. More recently, Elangovan et al. [83] used a different approach. In their study, they segmented spiculated structures from annotated landmarks in real DBT slices, and adapted them to the surroundings of other mammographic and tomographic images through a distortion model, improving the blending realism.

While there are several examples of models developed to simulate the representative features of breast lesions as they are observed in mammographic images, there are a very limited number of works introducing physical or virtual models which reproduce the features of the contrast uptakes presented in vascular breast X-ray imaging (see Chapter 2). Typically, contrast uptakes are represented as disks or spheres in physical phantoms so they can be used for image quality analysis and system optimization in CESM systems [175, 226]. Hill et al. [122] developed a physical phantom with representative geometrical inserts to evaluate the quality of CESM images. Four contrast uptake types (i.e. smooth, spiculated, rim and ductal) were reproduced using simple geometrical forms such as spheres and cylinders. Even with this simplicity, this phantom can be used for detection sensitivity studies as well as discrimination and classification test to help CESM performance assessment. Dromain [77] presented in her thesis five different types of simulated contrast uptakes: smooth, irregular, spiculated, rim and ductal. These virtual shapes were created through local modifications of the surface of geometrical primitives and they were used to study the classification performance of CEDBT and CESM.

Other models considering the kinetics of contrast agent propagation in different tissues have been proposed. Kiarashi et al. [158] presented a virtual phantom where they included rounded inserts using the model described in [45]. Similarly, Caballo et al. [36] developed a model for

contrast enhanced CT considering the perfusion kinetics of the contrast medium, and including a segmented lesion from a CT exam. These last models can be used for lesion detection, but the lack of a complete representation of the lesion descriptors observed in clinical images excludes their use from characterization tasks.

Motivated by the clinical data introduced in the work of Dromain [77], we will concentrate our efforts in the development of three-dimensional models corresponding to the complete variability of mass-like contrast uptakes. Non-mass like enhancements, the other type of contrast-uptakes present in vascular breast X-ray imaging, were not addressed in this work due to the scarce clinical information about the exact three-dimensional patterns followed by these uptake distributions and, therefore, the corresponding significant complexity of the required models. A more detailed insight of mass-like and non-mass-like enhancements is given in Chapter 3.

1.3 Mammography acquisition chain for contrast-enhanced X-ray imaging

The requirements of mammography systems allowing contrast-enhanced X-ray imaging are different from those that only provide single energy acquisitions. Based on the discussion in Section 1.2 on VCT, to develop virtual components allowing for a pertinent evaluation, we need to identify the characteristics of such systems. At the same time, we have to evaluate the current state of our X-ray simulation platform of choice, CatSim, to identify the missing elements. Finally, we recapitulate all the factors which may impact the image quality of low- and high-energy mammography images and, therefore, which may interfere in the study of CESM and CEDBT performance.

1.3.1 Description of acquisition systems

As illustrated in Figure 1.6, a full-field digital mammography (FFDM) system can be characterized by the nature of the X-ray tube, the filters used to shape the spectra, the presence (or not) of an anti-scatter grid, the type of detector and the elements composing it, and the geometry of the acquisition sequence [246]. We can distinguish three different types of acquisition sequences (Figure 1.7):

- 2D: as in standard mammography, a projected bidimensional image is acquired. In the case of CESM, low- and high-energy projections are acquired for the same tilt of the X-ray tube.
- 3D: as in DBT, several projections are acquired for different tube angles. In the case of CEDBT, at each tube angle a pair of low- and high-energy images is acquired.
- Static 3D: in this acquisition sequence the system acquires the same number of projections as in the 3D mode, but with the tube angle fixed at zero degree for all acquisitions.

In particular, in this work, we are interested in two different FFDM systems: Senographe DS and Senographe Pristina (GE Healthcare, Chicago, IL, USA). In Figure 1.8 we present the two mammography systems. The first of them went to business in 2004, and the latter in 2017:

- Senographe DS: the system is equipped with a Mo and Rh dual-track X-ray tube, and Mo, Rh and Cu μm-filters. Three target-filter combinations are allowed for the low-energy

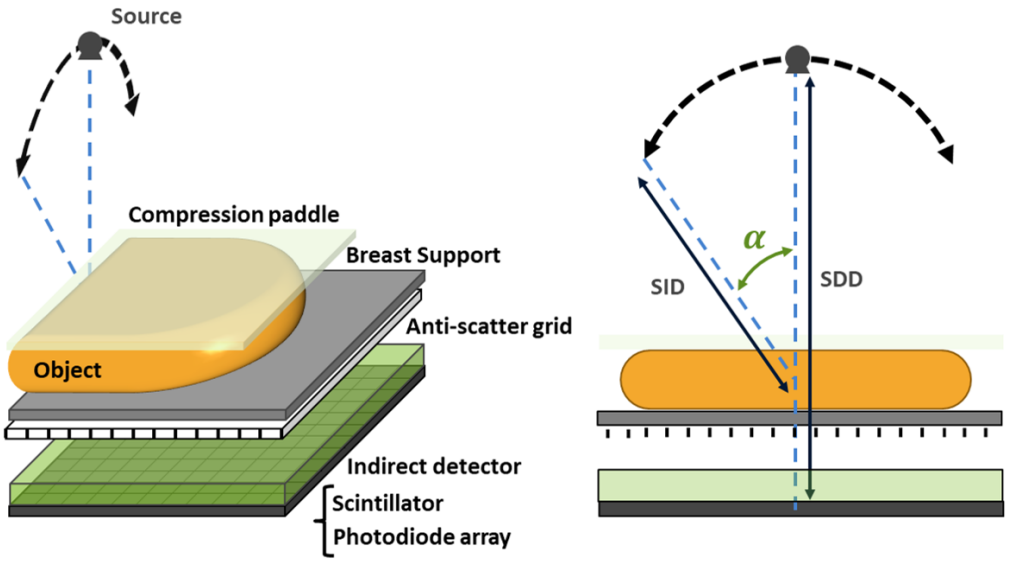

Figure 1.6: Elements composing a mammography system and its geometry. SDD and SID are the acronyms of source to detector distance and source to isocenter distance, respectively.

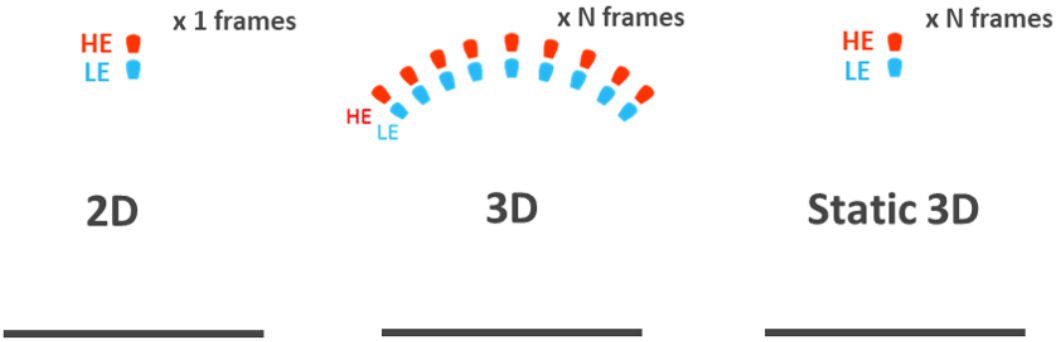

Figure 1.7: The three types of acquisition sequences available in a mammography system.

acquisitions: Mo-Mo from 22 kVp to 40 kVp, Mo-Rh from 22 kVp to 40 kVp and Rh-Rh from 22 kVp to 40 kVp. Two other target-filter combinations are allowed for the high-energy acquisitions: Mo-Cu between 40 kVp and 49 kVp, and Rh-Cu between 40 kVp and 49 kVp. The system is equipped with a CsI:Ti indirect conversion detector. The detector is formed by an array of $0.1 \times 0.1mm$ squared shaped pixels, with an area fill factor equal to 0.64. Full field images have a total size of $192 \times 230mm$. The system is not equipped with an anti-scatter grid in tomosynthesis mode. The airgap between the breast support and the detector is 23 mm, the source to detector distance (SDD) is 660 mm, and the source to isocenter distance (SID) is 616.76 mm. The tomosynthesis sequence is composed of 15 projections within an aperture of $\alpha = 12.5°$.

- Senographe Pristina: the system is equipped with a Molybdenum (Mo) and Rhodium (Rh) dual-track X-ray tube, and Mo, Silver (Ag) and Copper (Cu) μm-filters. Two target-filter combinations are allowed for the low-energy acquisitions: Mo-Mo from 22 kVp to 40 kVp and Rh-Ag from 22 kVp to 40 kVp. Two other target-filter combinations are allowed for the high-energy acquisitions: Mo-Cu from 40 kVp to 49 kVp, and Rh-Cu from 40 kVp to

49 kVp. The system is equipped with a CsI:Ti indirect conversion detector. The detector is formed by an array of $0.1 \times 0.1mm$ squared shaped pixels, with an area fill factor equal to 0.64. Full field images have a total size of $239.4 \times 285mm$. Additionally, the system has an anti-scatter grid with a grid ratio equal to 11:1 and 67 lines cm^{-1}) [159]. The airgap between the breast support and the detector is 23 mm, the source to detector distance (SDD) is 660 mm, and the source to isocenter distance (SID) is 616.76 mm. The tomosynthesis sequence is composed of 9 projections within an aperture of $\alpha = 12.5°$.

Figure 1.8: Two photos of the systems to be replicated in our simulation platform. Left: a Senographe DS system. Right: a Senographe Pristina system.

All the characteristics of these two systems need to be reproduced by our X-ray simulation platform.

1.3.2 Introduction to an analytic X-ray simulation platform: CatSim

Originally, CatSim was a 3rd generation CT simulator created to simulate projection images [66]. However, plenty of other functionalities and options have been included over the years [209], thanks to the collaboration of an enlarged community of researchers and developers across GE Global Research Center, GE Healthcare and other external collaborators. The different virtual elements of the X-ray chain are included in the platform as switchable modules coded in Matlab, plus a shared library written in C++ to improve the performance of certain tasks (e.g. ray-tracing), making the insertion of new models for physical processes easier.

As in other analytic simulation platforms of the X-ray chain, we can distinguish two phases to generate a mammographic image: ideal image formation or projection and image degradation or detection.

- In the image formation phase, the user can define a specific topology, spectrum choice (monoenergetic or polyenergetic), focal spot (size and shape), flat and bowtie filtering, digital phantoms (defined as analytic, mesh or voxelized structures), and detector geometry (pixel and array size). A ray-tracing algorithm applies a discrete approximation of the Beer-Lambert law to define the number P of X-ray photons arriving at the detector position

$[x, y]$ after traversing the object for the discrete energy bin E:

$$P[x, y, E] = I_0[E] \exp\left(- \sum_{i=0}^{n_{mat}} \mu_i[E] t_i[x, y] \right) \tag{1.1}$$

where n_{mat} is the number of different materials crossed by the X-Ray, I_0 is the output spectrum from the tube, μ_i is the energy-dependent attenuation coefficient for material i, and t_i the material thickness crossed from the source position to the detector position $[x, y]$.

- Afterwards, several cascaded stages modeling the physical phenomena of the X-ray chain can be applied to the deterministic signal P. In particular, there are two different types of phenomena related to the acquisition system and the acquisition parameters: the frequency response of the system and the statistics of the photon generation and interactions, as well as the random processes intrinsic to the detector electronics. Furthermore, if we consider the acquisition sequence of CESM and CEDBT we should also include time dependent effects because of the successive exposures. The particular physical processes involved in these three stages and their mathematical approximations included in the simulation platform will be explored in Sections 2.1, 2.3, and 2.4.

The X-ray spectra used in dual-energy mammography are polyenergetic. Discrete versions of the complete mammography spectra at the tube output have been used before for VCT studies [8, 86]. However, this procedure increases the computation complexity. As shown in Equation 1.1, when a polyenergetic spectrum is used, we need to compute a full image per energy bin. To reduce the computation time, an equivalent monochromatic spectra can be used [38, 180, 307]. In this dissertation we have used a monochromatic spectrum, with a total energy equivalent to the real spectrum. This simplifies Equation 1.1 into:

$$P[x, y] = I_0 \exp\left(- \sum_{i=0}^{n_{mat}} \mu_i t_i[x, y] \right) \tag{1.2}$$

To compute the linear attenuation coefficients μ_i, CatSim includes material files and energy-dependent Photoelectric, Compton and Rayleigh interaction database developed by members of the Geant4 Collaboration.

As in real acquisition systems, we can also consider a third step included inside the CatSim image generation: the gainmap correction. Gainmap correction allows compensating for the static defects of the detector caused by lithography. At the same time, it provides an attenuation of the geometrical effects of the conical beam after image acquisition (i.e. before image display). In this work, all our images, experimental and simulated, were corrected following a customized gainmap correction strategy:

$$\begin{aligned} I^T_{gainmap}[x, y] &= \frac{1}{5} \sum_{i=1}^{5} I^i_{gainmap}[x, y] \\ I_{corr}[x, y] &= I_{raw} \frac{\max_{[x', y'] \in S}(I^T_{gainmap}[x', y'])}{I^T_{gainmap}[x, y]} \end{aligned} \tag{1.3}$$

where $I^i_{gainmap}$ are images of a specific flat phantom, which are acquired with the same tube voltages, target/filter combinations as for the test object, I_{raw} and I_{corr} are the acquired images

of interest before correction and after gainmap correction, $[x, y]$ is the position of each pixel and S is the image support. Throughout this work, we will specify the type of phantom used for the gainmap in each set-up.

In Figure 1.9, we show a summary of the steps required for the simulation of a mammography image using CatSim. All the contributions made in this work are focused on the detection step.

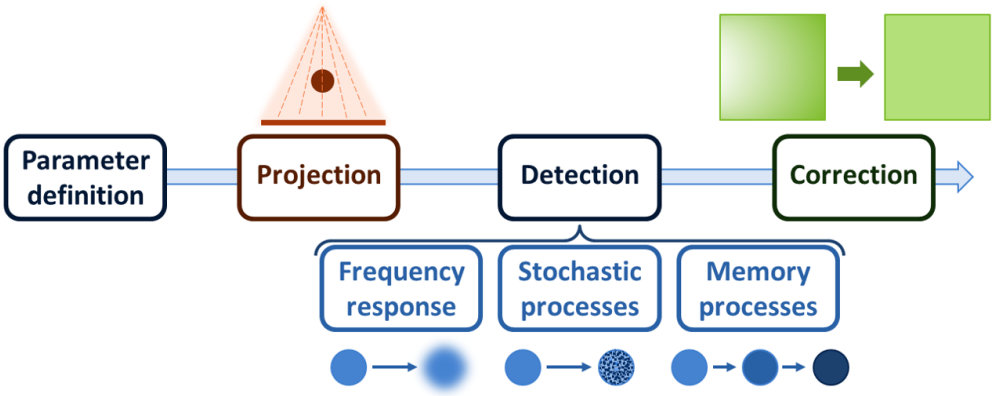

Figure 1.9: Steps followed in the simulation of the final images generated by CatSim.

To include a virtual object to be projected, CatSim allows three different types of phantom definitions:

- Analytic surfaces: the object is defined by the accumulation of several geometric primitives such as spheres, ellipsoids, cylinders and cones, among others. Such objects are defined by the position of their center and their different geometrical properties. Each surface contains its own linear attenuation coefficient associated with a given chemical composition.
- Polygonal meshed surfaces: the object is composed of several triangular facets defined by the position of their vertices. As in analytic surfaces, each meshified surface contains its own linear attenuation coefficient associated with a given chemical composition.
- Voxelized objects: the phantom is defined as a cube divided by a regular grid. This grid defines a set of voxels, each containing its own linear attenuation coefficient associated with a given chemical composition.

1.3.3 Factors impacting the image quality

As we have already introduced, the legitimacy of a study performed as a VCT depends on the realism of each of its components. From the clinical criteria for vascular breast X-ray imaging presented in Section 1.1.4, we can identify the parameters of the imaging chain impacting the clinical evaluation. This list can guide us through the development of our simulation platform, indicating which elements have necessarily to be realistically reproduced. Thus, we can distinguish three main root causes impacting Image Quality (IQ), and, consequently, the assessment of a recombined image:

- **Acquisition:** each of the components involved in all the steps from the electrons generation and acceleration in the X-Ray tube to the final digital data at the detector output

are fundamental in the information available to the processing algorithms and, therefore, to the clinician. We can distinguish three elements associated with this process:

  - Image acquisition system: the physical components of the acquisition chain. We need to describe the cumulative impact of these elements on the final characteristics of the digital image retrieved from the system.
  - Image acquisition parameters: the input values (kVs, mAs, tube filter) also influence the quality of our low- and high-energy images.
  - Image acquisition sequence: the timing and different phases of the acquisition influence the results of each recovered image [124].

  In Chapter 2 we investigate which elements of the acquisition must be modeled to guarantee a fair comparison between CESM and CEDBT.

- **External factors:** we call external factors all those elements that are not fixed by the system or the posterior image processing, and that will be different for each acquisition. More precisely we can find the following two factors:

  - Patient (physiology and motion): the breast composition (glandularity, BPE occurrence and lesion morphology) has a direct influence on the detection and characterization of possible findings, as well as the breast motion during and between high and low energy acquisitions.
  - Operator (iodine and paddle compression): the iodine distribution and the breast thickness deformation caused by the compression of the paddle may imply different quality losses in the final image.

  These factors will be addressed in Chapter 3.

- **Processing:** after retrieving the image from the acquisition system, the data are processed before final presentation to the clinician. This process includes three stages:

  - Raw image correction: just after acquisition, the image shows several imperfections such as the presence of the lithography pattern, bad pixel responses, or non-uniform exposure due to conical beam. Before showing the image to the user, these imperfections are corrected using previous images acquired in a controlled environment. These corrections may introduce image deformations and inconsistencies depending on the applied method.
  - Dual Energy recombination: the recombination algorithm making use of the low- and high-energy images to give an image of the iodine contrast has a direct impact on the assessment of the findings in the image.
  - Reconstruction: this step only concerns the reconstructed CEDBT slices. Several artifacts are introduced in the images during this process because of the partial sampling inherent to tomosynthesis acquisitions.

  These factors will be addressed in Chapter 4.

1.4 Conclusion

In this chapter, we have presented two X-ray vascular techniques for the breast: CESM and CEDBT. Their description was followed by a summary of current clinical studies involving the analysis of both modalities. We found that these studies provide very promising results and, therefore, that both techniques show an important contribution to breast lesion detection, as well as to the diagnosis of cancerous growths. However, while CESM has been proposed as a potential alternative of CE-MRI for breast cancer diagnosis at a lower cost [91], the incremented clinical value of CEDBT is still not well understood [53].

The aim of this dissertation is to compare the performance of CESM and CEDBT, and, at the same time, to understand the main factors which may impact the clinical evaluation for both modalities. The focus of our research is to analyze the capacity of each modality to detect and categorize correctly each of the descriptors for mass-like contrast uptakes, leaving the analysis of non-mass enhancements, due to their clinical complexity, to future research studies. In particular, we aim to compare the visual features of the mass-like contrast uptakes distinguished in the results of each modality to the actual characteristics of the ground truth. In other words, we explore the potential clinical benefits provided by the acquisition sequence of tomosynthesis applied to vascular breast X-ray imaging.

To allow for such a comparison, we need a large and representative database of breast lesions inserted in diverse heterogeneous backgrounds, along with their complete three dimensional description: their morphological characteristics and contrast uptake distribution. Furthermore, to evaluate the advantages and limitations of each method, according to the technology available today, we focus our study on the performance of both acquisition techniques given a specific set of characteristics related to a commercial system (Senographe Pristina™, GE Healthcare). This system is able to acquire standard mammography images as well as DBT, and CESM recombined images. However, CEDBT is not yet possible.

VCT offers a suitable framework to overcome these limitations. As we have introduced in Section 1.2, several publications have already used VCT to answer clinical questions and evaluate different imaging techniques. The simulation of the X-ray chain and the breast pathologies seems a relevant solution to the unavailability of a CEDBT system and the lack of a complete database of characterized lesions. However, the existing architecture cannot simulate the complete CEDBT sequence, nor the contrast uptakes appearing in contrast enhanced mammographies.

Consequently, before providing an analysis of CESM and CEDBT clinical performance, we need to develop the tools and models which will help us to perform a VCT. To this end, we evaluated the characteristics of two commercial mammography systems (Senographe DS™and Senographe Pristina™, GE Healthcare) and the current state of the analytic X-ray simulation platform we chose.

Chapter 2

Improved realism in simulating X-ray imaging systems

After the discussion in Chapter 1, in this chapter we focus on the development of an analytical simulation platform to model the main physical processes in a X-ray imaging system which can affect the evaluation of CESM and CEDBT cases. To this end, we describe the main changes we introduce into the CatSim simulation platform. Each of the changes increases the realism of low- and high-energy simulated images. For each new simulated physical phenomenon, we present the following:

- A description of the phenomenon, the technical background, why it is important for the image quality, and how it has been modeled in other published implementations.
- An explanation of the model we propose. Each model must deliver an analytic approximation of the physical phenomenon.
- A detailed description of the set-up and parameters needed to obtain the parameters of our model.
- The validation process, and a detailed description of the set-up to prove the validity of our model and the obtained results.
- A conclusion, explaining the goodness of our model and the guidelines to improve it in future work.

It is important to note that the proposed models are not system specific. In other words, they are based on physical phenomena shared by diverse mammography systems. However, we characterized the low- and high-energy images of the tomosynthesis and mammography sequences of a particular Pristina system, and the tomosynthesis sequence of a particular Senographe DS system. For a more detailed description of each of the physical processes involved, the reader is referred to [144].

2.1 Frequency response of an X-ray system

In the ideal image formation phase formulated in Chapter 1 (see Equation 1.1), we have considered the X-ray acquisition chain as an imaging system with an ideal modulation transfer

function (MTF), providing a perfect spatial resolution. However, this is not true in real acquisition systems, where several effects degenerate the total spatial resolution of the final image. In particular, we can distinguish five main effects having an impact on the resolution: the motion of the tube while the system is acquiring an image, the size and shape of the focal spot, the X-ray scatter in the phantom, the optical scatter in the scintillator, and the size and shape of the photodiodes at the detector.

Following the mathematical principles introduced by Metz and Doi [206], we consider that the X-ray acquisition chain is a linear time-invariant (LTI) system. In this type of systems, the spatial properties of the final image can be completely described by a particular transfer function h, or a cascade of several transfer functions. By convention, this analysis ignores any statistical effect in the image acquisition process. Therefore, the transfer function is applied to noise-free images. The statistical properties of the final images can be analyzed independently using the theory of stochastic processes (see Section 2.3).

In optical systems, this transfer function is called the Point Spread Function (PSF), and fulfills the following property:

$$\int_{-\infty}^{\infty}\int_{-\infty}^{\infty} h(x,y)dxdy = 1 \tag{2.1}$$

Therefore it does not contribute to the total gain of the imaging system. The output of an LTI system is computed as:

$$I(x,y) = P(x,y) * h(x,y) \tag{2.2}$$

where I contains the spatial properties of the final image, and P corresponds to the ideal image formation The same analysis of LTI systems can be performed in the frequency domain. The equivalent function of the PSF in the frequency domain is called Optical Transfer Function (OTF):

$$OTF(\nu_x,\nu_y) = \mathcal{F}\{h(x,y)\} \tag{2.3}$$

where $\mathcal{F}\{\cdot\}$ symbolizes the Fourier Transform (FT). Then:

$$\mathcal{F}\{I\}(\nu_x,\nu_y) = \mathcal{F}\{P\}(\nu_x,\nu_y)\cdot OTF(\nu_x,\nu_y) \tag{2.4}$$

However, the OTF is usually described by the combination of its modulus, the Modulation Transfer Function (MTF), and its phase, the Phase Transfer Function (PTF):

$$OTF(\nu_x,\nu_y) = MTF(\nu_x,\nu_y)\cdot e^{jPTF(\nu_x,\nu_y)} \tag{2.5}$$

Commonly, we consider that the PSF is real and even:

$$\begin{cases} \mathrm{Im}(h(x,y)) = 0 \\ h(-x,-y) = h(x,y) \end{cases} \tag{2.6}$$

where $\mathrm{Im}(z)$ denotes the imaginary part of z. When this is true, by the properties of the FT, the resulting OTF is real and even, so the PTF can be equal only to 0 or π. In practical applications, the OTF is considered strictly positive, so:

$$\mathcal{F}\{I\}(\nu_x,\nu_y) = \mathcal{F}\{P\}(\nu_x,\nu_y)\cdot MTF(\nu_x,\nu_y) \tag{2.7}$$

which means that we can completely describe the frequency response of a system, and therefore its spatial response, if we know its total MTF.

Going back to the five main effects having an impact on the resolution, we can model each of these effects by their impulse response and estimate the total resolution as the convolution of all these components:

$$I = P * h_{motion} * h_{fs} * h_{scat} * h_{scint} * h_{det} \tag{2.8}$$

where I is the final image, h_{motion} the impulse response due to the movement of the tube while shooting X-rays, h_{fs} the impulse response introduced by the focal spot shape and size, h_{scat} the impulse response due to quantum interactions across the object being imaged, h_{scint} the impulse response representing the quantum interactions occurring in the scintillator which produce an additional scattering, and h_{det} the impulse response associated with the detector pixel shape and size. In this model, the acquisitions are further assumed to be performed in an ideal step-and-shoot mode, with no blur introduced from tube motion ($h_{motion} = 1$). According to what we have established before, this is equivalent to:

$$\mathcal{F}\{I\} = \mathcal{F}\{P\} \cdot MTF_{fs} \cdot MTF_{scat} \cdot MTF_{scint} \cdot MTF_{det} \tag{2.9}$$

In this section, we present our contribution to the models of scattering and detection included in CatSim.

2.1.1 Frequency response at the detector

When arriving at the detector, the spatial distribution of luminescent photons is continuous. However, the active surface area of the photodiodes composing the detector array integrates and discretizes this distribution. In Figure 2.2a we illustrate the geometry of a detector photodiode. This geometry is shared by the Senographe DS and Senographe Pristina systems. Assuming a uniform sampling and a rectangular active area, we can compute the discrete distribution of photons D integrated at each detector position $[i, j]$ from the continuous distribution of photons P as:

$$D[i,j] = \int_{i\cdot T_s - \frac{\Delta_x}{2}}^{i\cdot T_s + \frac{\Delta_x}{2}} \int_{j\cdot T_s - \frac{\Delta_y}{2}}^{j\cdot T_s + \frac{\Delta_y}{2}} P(x,y)dxdy \tag{2.10}$$

where T_s the spatial sampling distance, and $\Delta_x \times \Delta_y$ the size of the active area, with $\Delta_x \leq T_s$ and $\Delta_y \leq T_s$.

This expression is equivalent to:

$$D[i,j] = (P * h)(i \cdot T_s, j \cdot T_s) \tag{2.11}$$

where

$$h(x,y) = \begin{cases} 1, & if -\frac{\Delta_x}{2} \leq x \leq \frac{\Delta_x}{2}, -\frac{\Delta_y}{2} \leq y \leq \frac{\Delta_y}{2} \\ 0, & otherwise \end{cases} \tag{2.12}$$

and its Fourier transform is equal to the bi-dimensional cardinal sine function:

$$H(\nu_x, \nu_y) = sinc\left(\frac{\nu_x}{\Delta_x}, \frac{\nu_y}{\Delta_y}\right) \tag{2.13}$$

Following this, we can separate our implementation into two phases: convolution with the pixel shape function and sampling. However, as shown in Equation 1.1, the main disadvantage of virtual environments is that we can only generate a discrete version of $P(x, y)$. To overcome

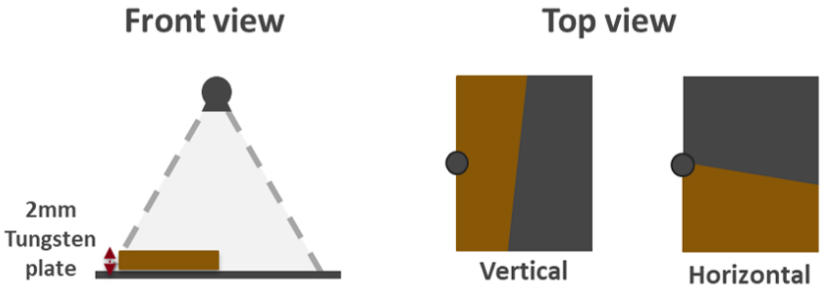

Figure 2.1: Setup of our simulation to validate the frequency response at the detector.

Table 2.1: Operational point used for the validation of the frequency response at the detector.

	Simulated	
	LE	**HE**
Spectrum	23keV (monoenergetic)	34keV (monoenergetic)
Target/Filter	Rh/Ag	Rh/Cu
Exposure	36mAs	110mAs
Gainmap	50mm PMMA	50mm PMMA

this limitation we can generate an oversampled discrete version of $P(x, y)$ we name $P[m, n]$, with pixel size $\Delta_{over} \ll \min(\Delta_x, \Delta_y)$, and, after convolution, decimate our image, leading to:

$$D[i, j] = (P * h)\left[i \cdot \frac{T_s}{\Delta_{over}}, j \cdot \frac{T_s}{\Delta_{over}}\right] \tag{2.14}$$

where $\frac{T_s}{\Delta_{over}}$ is the chosen oversampling factor which must be an integer. This factor is critical: if it is too big it reduces the timing performance of the simulation, but if it is too small it can introduce aliasing artifacts.

This formulation can be adapted for other pixel shapes modifying the impulse response $h[m, n]$. In our particular case, we approximate the real active area of the photodiodes by a discrete square of size M, smaller than the sampling factor ($\Delta_x = \Delta_y = \Delta = M \cdot \Delta_{over}$). Consequently, we can define the response of our pixels as:

$$h[m, n] = \begin{cases} 1, & if\ 0 \leq m \leq M-1,\ 0 \leq n \leq M-1 \\ 0, & otherwise \end{cases} \tag{2.15}$$

In particular, in our implementation, we chose $M = 4$, $T_s = 100\mu m$, $\Delta = 80\mu m$ and $\Delta_{over} = 20\mu m$.

The validation of our simulation was performed using the set-up illustrated in Figure 2.1 and the operational point described in Table 2.1. In these simulations, we only model the response of the detector, so the only processes considered are the projection, the shape of the detector pixel, and the gainmap correction. From these acquisitions, the Modulation Transfer Function (MTF) of the system can be obtained by measuring the Edge Spread Function (ESF), as described by Jones [145]. This technique is described in more detail in Section 2.1.2. We compared the resulting vertical and horizontal MTF to the theoretical curve corresponding to Equation 2.13.

We present the results in Figure 2.2b. As we can observe both curves, vertical and horizontal, are almost identical to the theoretical function, with a Mean Square Error (MSE) smaller than

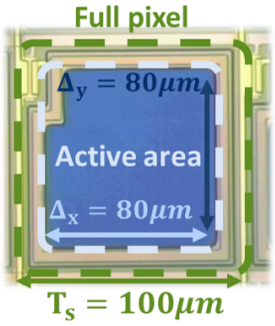

(a) Real shape of detector element.

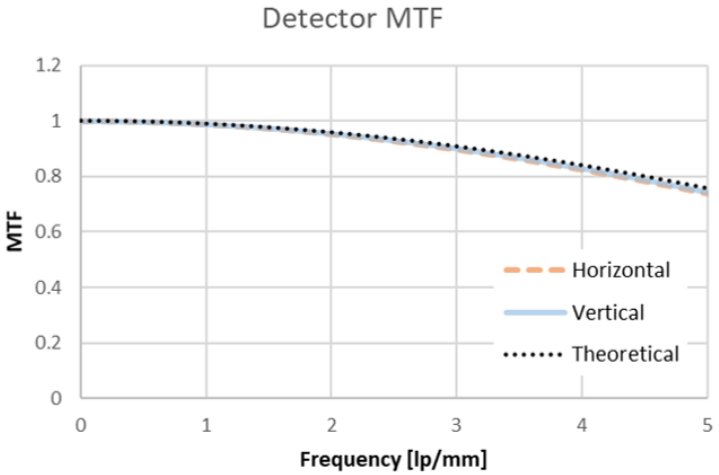

(b) Comparison between the frequency response of simulated images and the theoretical detector element response. Vertical and horizontal curves are identical for low- and high-energy acquisitions. Consequently, we only drew the low-energy MTF.

Figure 2.2: Spatial distribution and simulated frequency response of an element composing the photodiode array in the detector.

0.0001. One main problem of our approach is that the detector element is not perfectly square. As the reader can notice, in Figure 2.2a, we show the real geometry of an individual photodiode, and there is a small incision in the top left corner of this element. This incision affects the frequency response of the total detector response. In this work, we consider that the impact of this deformation may be negligible compared to the scatter effect and the optical scatter of the scintillator (described in Section 2.1.2). However, further investigations may be of interest to quantify the impact of this incision in the final frequency response of the whole system.

2.1.2 Scattering processes

One of the key elements in computer simulation of realistic X-ray systems is to generate the X-ray scatter field and include it into the simulated images. The final signal arriving to the detector is composed of two components: the primary and the scatter radiations. The primary component, generated by the photo-electric absorption process, provides the useful radiological image information. Otherwise, X-ray scatter is referred to as the X-ray photons that are deflected from their original travel direction due to interaction with electrons, mainly in the breast, on their way to the image detector. The relation between these two components has been traditionally quantified using the scatter-to-primary ratio (SPR). This figure defines the relative signal contribution of the scattered intensity S, compared to the primary intensity P:

$$SPR = \frac{S}{P} \tag{2.16}$$

where S is the energy provided by the scatter field at some point of the detector, and P is the energy delivered by the primary field at the same point of the detector.

Scattered radiation and its effects in X-ray breast imaging have been largely studied during the last two decades [27, 80, 185, 301, 241]. The scatter signal can be interpreted as a noise

source, reducing the image contrast and Signal-to-Noise Ratio (SNR) of the acquired images, and consequently, degrading the image quality [216]. In breast X-ray modalities such as breast Computed Tomography (bCT) and Contrast Enhanced Spectral Mammography (CESM), scattered radiation may impair image quality by introducing cupping artifacts and reducing the accuracy of the iodine quantification. Several simulation approaches have been developed to characterize scattered radiation and its impact on image quality. One of the first approaches was developed by Dance et al. [64] for mammography, where the quantum interactions of photon particles from the source to the detector were simulated using a Monte Carlo (MC) algorithm to measure the scatter to primary ratio for various detector types, breast sizes, and photon energies. Several studies adapted this strategy to different X-ray breast imaging modalitites [52, 68]. However, full MC simulations are computationally expensive, which reduce their practical use. To address this issue, convolution-based methods to estimate the scattering field from the primary X-ray images have been proposed [27, 301]. In these articles, the X-ray imaging system was modeled assuming parallel beam geometries, which is not representative of current breast X-ray imaging systems using cone-beam geometries.

With the cone-beam geometry, the length of the X-ray path from X-ray source to detector depends on the position of the detector element. Consequently, the distance traveled by X-rays in a constant-thickness object is not uniform over all the radiated surface of the detector. This is of utmost importance at the edge of breast projections. This geometry implies a spatial non-stationarity or non-uniformity of the scatter radiation. Therefore, Diaz et al. [72] recently developed a method using a pre-computed library of scatter kernels, determined from MC simulations, considering different breast thicknesses, air gaps and source projection angles. The use of pre-computed scatter kernels significantly reduces the simulation time of an image. However, a scatter kernel library offers a discrete version of the scatter field for different object thicknesses. To overcome this constraint, a narrow discretization step must be considered so the coarseness of the approximation can be reduced. Following this, the library proposed by Diaz et al. is composed of 100 kernels for each considered glandularity, projection angle, and air gap length. The large extension of this library, associated with the need of MC simulations to generate each scatter kernel, makes the method time consuming and computationally expensive.

Another approach, first proposed by Ducote et al. [81] and further developed by Leon et al. [176], is to compute the scatter kernels using experimental measures directly acquired from a real mammography system. In their work, these authors adopted the mathematical continuous description of the scatter kernel introduced by Seibert et al. [269], established originally to characterize the veiling glare in fluoroscopy. This scatter kernel models the typical X-ray spreading of direct detectors (i.e. without scintillator transforming the X-ray photons into luminescent photons). For a point source arriving at the detector, the spreading originated after traversing an object is given by the expression:

$$h(r) = \frac{\delta(r)}{r} + \frac{\rho}{(1-\rho)2kr} e^{-sr/k} \tag{2.17}$$

where r is the radial distance from the scattered X-ray position to the center of the point source, ρ is proportional to the portion of the signal which is scattered, k represents the spatial influence of the scatter, and the Dirac function $\delta(r)$ indicates the part of the signal which is not scattered. The radial expansion of the X-ray is described by the inverse relationship $1/r$. The values of ρ and k depend on different characteristics of the system. Leon et al. [176] defined both values as

a polynomial surface depending on the object thickness t and the chosen tube peak energy E:

$$\rho = \alpha_0 + \alpha_1 t + \alpha_2 E + \alpha_3 t^2 + \alpha_4 tE + \alpha_5 E^2 + \alpha_6 t^3 + \alpha_7 t^2 E + \alpha_8 tE^2 \tag{2.18}$$

$$k = \beta_0 + \beta_1 t + \beta_2 E + \beta_3 t^2 + \beta_4 tE + \beta_5 E^2 + \beta_6 t^3 + \beta_7 t^2 E + \beta_8 tE^2 \tag{2.19}$$

where the value of the coefficients $\alpha_0, ..., \alpha_8$ and $\beta_0, ..., \beta_8$ were fitted from different measures of the scatter kernel. In particular, these values were obtained from a reduced number of breast equivalent thicknesses (2, 4, 6, and 8 cm), 5 different tube potentials (24, 26, 28, 30, and 34 kVp), and 4 tube target and filter combinations with and without anti-scatter grid. For each of these conditions, the scatter kernel of a specific system was measured using the beam-stop method [268]. In this method, a series of radiopaque disks with different diameters are positioned over the scattering medium with the desired thickness. Then, the signal in the center of the disk shadow is measured. With all the measurements performed for the different diameters of the disks, the scatter signal for different distances can be extrapolated. Consequently, in their work, Leon et al. proposed 5 measures using lead disks with different radii (2.3, 2.9, 3.6, 5.5 and 7.5 mm) plus one without any object in the beam path to compute the Signal-to-Primary Ratio (SPR). In total, 960 measures were needed to obtain the final scatter kernel expression.

Due to the complexity of the beam-stop method, as well as the high number of measures required to fit the scatter kernel curve, other methods to measure the scatter kernel of a system have been proposed. In particular, the scatter kernel can be derived from the Edge Spread Function (ESF), as described by Jones [145]. This measure, largely studied and adopted for different X-ray systems [60, 31, 42], proved to offer a high accuracy while reducing the complexity of the set-up necessary to acquire the scatter kernel [27]. Salvagnini et al. [258] compared the performance of different set-ups to measure the system MTF to the results obtained from Monte Carlo simulations. The method introduced by Jones showed a slightly higher estimation error for the computation of the SPR. However, it is still recommended as an alternative method to measure the MTF of a mammographic system.

2.2 A novel approach in modeling X-ray scatter in X-ray imaging systems

In this section, we propose a simple, fast and effective method to model the X-ray scatter in simulated mammography images. We estimate a scatter kernel as a continuous function dependent on the object thickness and detector element position, considering a cone-beam geometry. To this end, we use experimentally acquired images on a commercially available mammography system equipped with an anti-scatter grid. Our method uses the characteristic ESF of the system relieving partially the burdensome tasks introduced by a high number of required acquisitions and a complex set-up. Additionally, our method extends the methods proposed by Ducote et al. [81] and Leon et al. [176] for indirect detectors, proposing a new analytic formula for the scatter kernel, proving to be better adapted for indirect detectors. To validate our approach we compared simulated images using our thickness dependent scatter model to experimentally acquired images. Additionally, we show the improvement that this approach suppose against a more traditional stationary additive scatter model, where only the stationary optical scatter (glare) and the average signal intensity of the simulated image are adapted.

2.2.1 General overview of our model

The signal intensity measured in an image detector includes both primary and scatter components (see Figure 2.3). Even if a system is equipped with an anti-scatter grid, some part of the scattered X-ray quanta arrive at the detector, causing image degradation [159]. Optical scatter, also called glare, refers to the optical photons that are deflected from their original travel direction due to interaction with electrons in the image detector scintillator. As presented in the introduction, the primary and the scatter components are commonly quantified through the SPR.

The spatial degradation generated by the different scattering processes can be characterized by multiple point spread functions (PSF) [269, 26], depending on the system topology, the acquisition parameters and the physical components forming the X-ray imaging system, as well as the object being imaged. Equivalently, the scattering process can be defined in the frequency domain by different modulation transfer functions (MTF) [145]. Considering the total frequency of the system only in one direction, and before energy integration, we can express the image projected on the detector as:

$$\hat{I}(\nu) = \mathcal{F}\{P \cdot e^{-\mu t}\}(\nu) \cdot (T_P \cdot H_G(\nu) + T_S \cdot SPR(t) \cdot H_S(\nu, t) \cdot H_G(\nu)) \cdot H_{det}(\nu) \tag{2.20}$$

where $\hat{I}$ is the Fourier Transform (FT) of the image incident on the image detector, ν is the one-dimensional frequency, $\mathcal{F}\{P \cdot e^{-\mu t}\}$ is the FT of the attenuated primary field, H_G is the MTF of the optical scatter process in the detector scintillator, H_S is the MTF of the X-ray scatter process mainly occurring in the breast before detector incidence (including the impact of the grid on spatial resolution), H_{det} is the frequency response introduced by the pixel shape of the detector, T_P is the transmission of primary X-rays through the anti-scatter grid, T_S is the transmission of scattered X-rays through the anti-scatter grid, SPR is the ratio between the scattered X-ray fluence and the primary X-ray fluence incident on the image detector when the anti-scatter grid is not present, and μ and t are the linear attenuation coefficient and the thickness of a material traversed by X-rays, respectively.

The contributions of H_G and H_S can be combined in a single MTF H_T, leading to the following reformulation of Equation 2.20 as:

$$\hat{I}(\nu) = \mathcal{F}\{P \cdot e^{-\mu t}\}(\nu) \cdot (T_P + T_S \cdot SPR(t)) \cdot H_T(\nu, t) \cdot H_{det}(\nu) \tag{2.21}$$

with:

$$H_T(\nu, t) = \frac{(T_P + T_S \cdot SPR(t) \cdot H_S(\nu, t)) \cdot H_G(\nu)}{T_P + T_S \cdot SPR(t)} \tag{2.22}$$

The associated scatter kernel in the spatial domain can be computed using the inverse Fourier Transform of Equation 2.22.

In this work, $H_T(\nu, t)$ was experimentally assessed in images of uniformly thick test objects of various thicknesses using low- and high-energy spectra on a commercially available breast X-ray imaging system. These experimental results allowed us to derive a continuous analytic expression of $H_T(\nu, t)$ as a function of the test object thickness. The analytic expression was then integrated in an X-ray image simulation platform to generate images, containing primary and scatter components, of numerical test objects with non-uniform thickness. In other words, a spatially non-stationary scatter process was simulated. A schema of the proposed method is presented in Figure 2.4, and details are provided in the next section.

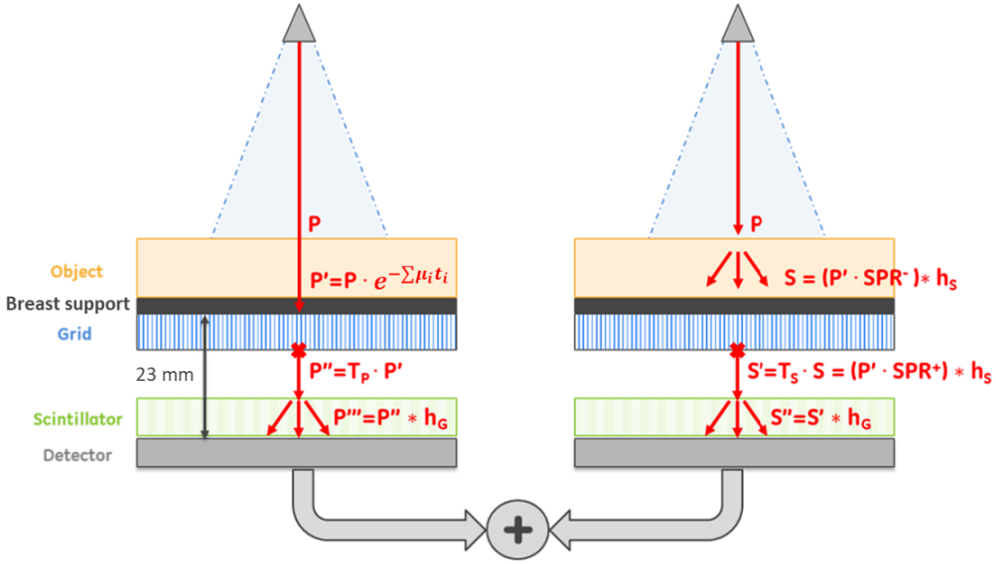

Figure 2.3: Schematic representation of primary and secondary quanta generated in the X-ray chain, where P is the primary field incident on the object, P' is the primary field after the object, P'' is the remaining primary field after the anti-scatter grid, P''' is the remaining primary field after the scintillator, S is the scatter field generated after traversing the object, S' is the remaining scatter field after the anti-scatter grid, S'' is the remaining scatter field after the scintillator, SPR^{-} is the Scatter-to-Primary Ratio before the anti-scatter grid, SPR^{+} is the Scatter-to-Primary Ratio after the anti-scatter grid, h_S is the scatter spreading caused by the quantum interactions inside the object, h_G is the scatter spreading caused by the optical interactions inside the scintillator, T_P represents the fraction of the primary field which passes through the anti-scatter grid, and T_S represents the fraction of the scatter field that is not absorbed by the anti-scatter grid.

2.2.2 Introducing a parametric expression of the scatter transfer function

Scatter kernels were experimentally estimated using the edge technique [60]. This technique can be used to retrieve not only the SPR but also the spatial spreading of scatter, assessed by the edge spread function (ESF), and its frequency response, assessed in the MTF, using only one measurement. A radio-opaque sheet of tungsten (phantom test device according to IEC 62220-1 [138]) with a polished edge was successively imaged on top of PMMA plates of various thicknesses t covering the entire detector (as shown in Figure 2.5). The PMMA plates were 25, 50 and 75 mm thick. The choice of the positioning of the radio-opaque sheet was carefully chosen based on preliminary experiments performed in our laboratory. Due to a non-perpendicular incident X-ray beam at the polished edge (cone-beam geometry), we ensured that no primary X-rays were incident under the radio-opaque sheet and that geometric image blur at the polished edge did not impact our measurement accuracy. We also ensured that the detector area covered by the radio-opaque sheet was large enough to allow for an accurate measure of the low-frequency scatter contribution (see Figure 2.6). The tungsten edge was positioned nearly parallel to the chest-wall direction (angle of approximately 3 to 5 degrees) covering $5cm$ of the detector in the chest-wall-nipple direction. This position allows us to retrieve the MTF perpendicular to the grid septa and, therefore, to acquire the unidirectional frequency response presented in the

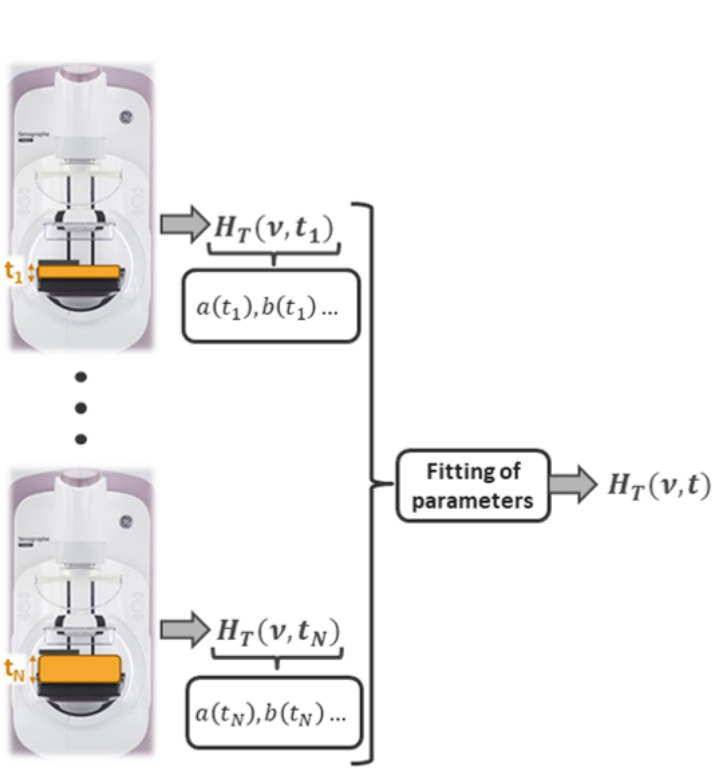

(a) From a few experimental acquisitions (N small) we generate a continuous thickness expression of the scatter field.

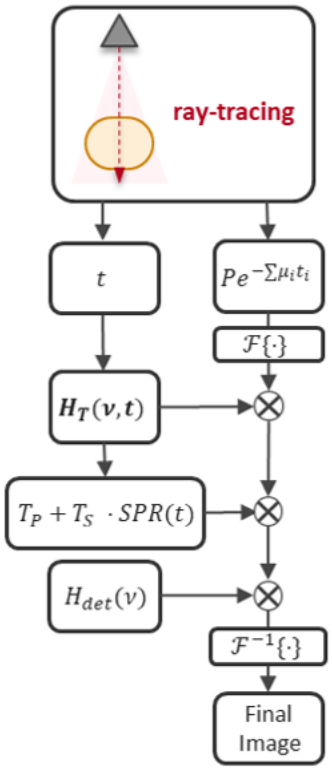

(b) The continuous expression is introduced in the simulation platform to recreate the scatter field depending on the local thickness of the projected test object.

Figure 2.4: Tow steps schema of the method proposed to simulate images including a non-stationary scatter field.

introduction of Section 2.1. As mentioned above, PMMA plates were used as test objects since it has been shown that they allow to reasonably well mimic breast tissue attenuation and scatter properties.

Low- and high-energy images of the PMMA plates with the tungsten sheet on top were acquired using the 34kVp Rh-Ag and 49 Rh-Cu target-filter combinations. Images were acquired in manual acquisition mode. The selected mAs values were close to the parameters obtained when imaging the PMMA plates alone in automatic exposure setting mode.

The gainmap correction proposed in Section 1.3.2 of Chapter 1 reduces the noise (average of several images) and the geometric factor (only $2mm$ of Al) introduced by the gainmap images.

The over-sampled ESFs and corresponding MTFs were computed using the software tool developed by Kao et al. [151]. With this tool, an over-sampled ESF, i.e. ESF sampled with a higher frequency than the limited resolution given by the pixel size, is determined from individual ESFs computed along the tungsten edge inside the selected ROI. The ROI is chosen for each case so as to contain the complete tail of the ESF. Then, the MTF is computed as the Fourier transform of the derivative of the over-sampled ESF, i.e. $MTF = \mathcal{F}\left\{\frac{d}{dx} ESF(x)\right\}$. The ROI

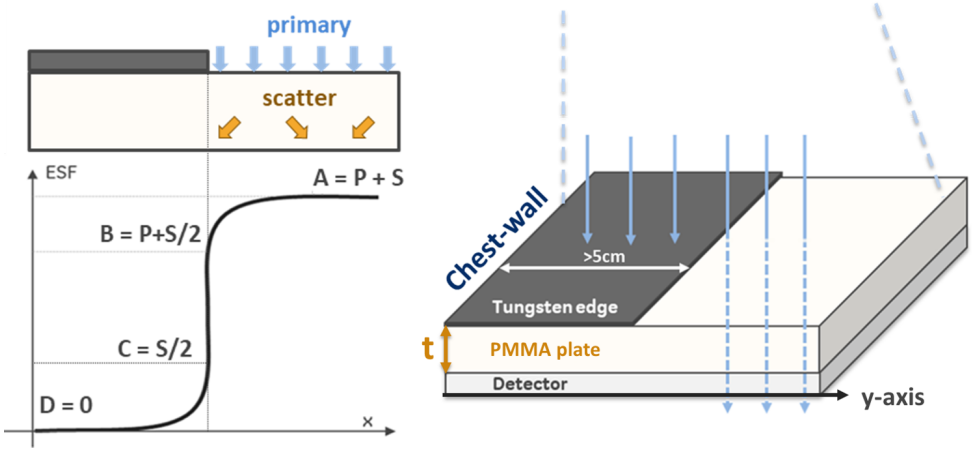

Figure 2.5: Schema of the resulting Edge Spread Function (ESF) and the experimental set-up.

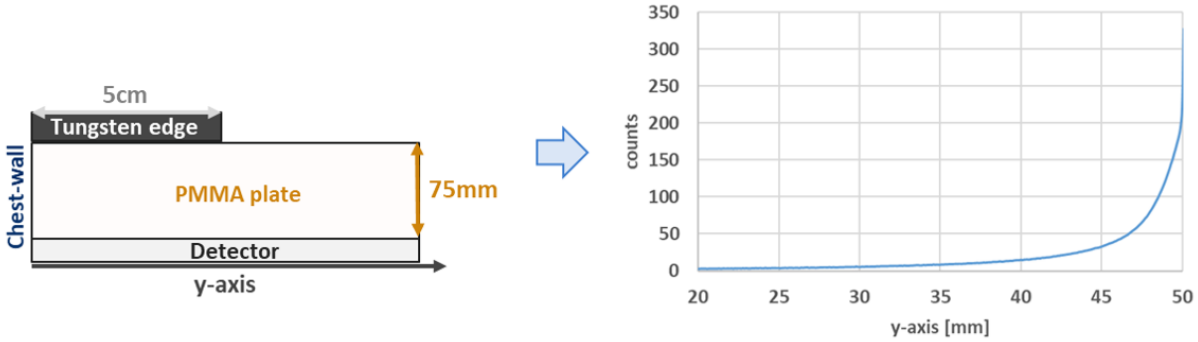

Figure 2.6: Worst case example of scatter effect with anti-scatter grid. Low-energy acquisition to estimate the scatter kernel at $75mm$. As we observe, the $5cm$ between the chest-wall and the end of the tungsten edge is large enough to consider all the scattering effect in our estimation.

widths allowed for at least 100 individual ESFs, and the chosen ROI heights verified that the end of the ESF tails inside our ROI had a decay smaller than 0.1%.

As illustrated in Figure 2.5, the resulting over-sampled ESFs, which depend on the PMMA plate thickness, can be measured to retrieve the SPR, as well as the total MTF of the system:

$$\begin{aligned} SPR(t) &= \frac{2 \cdot (ESF_A(t) - ESF_B(t))}{2 \cdot ESF_B(t) - ESF_A(t)} \\ MTF_{edge}(\nu, t) &= \mathcal{F}\left\{\frac{d}{dx} ESF(x,t)\right\}(\nu) \end{aligned} \tag{2.23}$$

where $ESF_A = Scatter + Primary$ and $ESF_B = \frac{Scatter}{2} + Primary$, $\mathcal{F}$ denotes the FT, and t is the thickness of the chosen PMMA plate.

Next, the experimentally assessed MTFs were analytically expressed using three previously proposed fitting models (sum of Gaussians, sum of Exponentials, sum of Lorentzians [102, 42]). The scatter model proposed by Ducote et al. [81] for direct detectors was included in our comparison, and adapted to include into their formulation the analytical expression of the optical glare as a fixed multiplying function in the frequency domain. The optical glare was measured using the edge technique described in this section, but with no PMMA plate in the field of view.

The resulting MTF of the optical glare was fitted following a sum of two Lorentzians functions, according to the work of Carton et al. [42]. We also propose a new rational expression to fit the MTF. After the evaluation of the shape given by the acquired MTFs, two types of magnitude decays were differentiated. At lower frequencies, the MTF frequency drop is fast and it can be approximated by an inverse third degree polynomial function. At higher frequencies, the MTF decay is slower and it can be modeled by a first degree polynomial. Additionally, the resulting rational function can supply three other requirements: no real root for any frequency, maximum magnitude equal to one, and monotonic frequency decay with $\lim_{\nu\to\infty} MTF(\nu) = 0$.

The five models of MTF considered in our study are defined in the frequency domain as:

$$H_{Gaussian}(\nu,t) = \frac{a_g(t)}{\sqrt{2\pi c_g(t)^2}} e^{0.5(|\nu|-d_g(t))^2/c_g(t)^2} + \frac{b_g(t)}{\sqrt{2\pi f_g(t)^2}} e^{0.5(|\nu|-g_g(t))^2/f_g(t)^2} \tag{2.24}$$

$$H_{Exponential}(\nu,t) = a_e(t)e^{-c_e(t)(|\nu|-d_e(t))} + b_e(t)e^{-f_e(t)(|\nu|-g_e(t))} \tag{2.25}$$

$$H_{Lorentzian}(\nu,t) = a_l(t)\frac{1}{1+(\frac{\nu}{b_l(t)})^2} + (1-a_l(t))\frac{1}{1+(\frac{\nu}{c_l(t)})^2} \tag{2.26}$$

$$H_{Ducote}(\nu,t) = \left(a_d(t) + \frac{b_d(t)}{\sqrt{1+(2\pi c_d(t)\nu)^2}}\right) H_{Glare}(\nu) \tag{2.27}$$

$$H_{Rational}(\nu,t) = \frac{a_r(t)|\nu| + b_r(t)}{|\nu|^3 + c_r(t)|\nu|^2 + d_r(t)|\nu| + b_r(t)} \tag{2.28}$$

where $H_{Glare}(\nu)$ represents the MTF of the optical glare, and a_g, a_e, a_l, a_d, a_r, b_g, b_e, b_l, b_d, b_r, c_g, c_e, c_l, c_d, c_r, d_g, d_e, d_r, f_g, f_e, d_g, and d_e are all parametric continuous functions of the material thickness traversed by the X-rays t. To estimate these functions (i.e. $a(t)$), we use the experimentally acquired MTFs H_{acq}. A sample point of the parametric continuous functions of a specific MTF model for a certain thickness t_i can be computed as:

$$\hat{a}(t_i) = \arg\min_{a(t_i)} \sum_{\nu} \left(H_{acq}(\nu,t_i) - H_T(\nu,t_i)\right)^2 \tag{2.29}$$

where $\hat{a}(t_i)$ is a sample of $a(t)$ at thickness t_i, $H_{acq}(\nu,t_i)$ is the experimental measure of the MTF at thickness t_i, and $H_T(\nu,t_i)$ represents each of the MTF models presented in Equations 2.24 to 2.28 at thickness t_i. Then, the goodness of each MTF model for each thickness can be evaluated using the Mean Square Error (MSE) between the acquired MTF and the MTF model. For example, if we consider $H_T(\nu,t_i) = H_{Rational}(\nu,t_i)$:

$$MSE_{H_{Rational}}(t_i) = \sum_{\nu} \left(H_{acq}(\nu,t_i) - \frac{a_r(t_i)|\nu| + b_r(t_i)}{|\nu|^3 + c_r(t_i)|\nu|^2 + d_r(t_i)|\nu| + b_r(t_i)}\right)^2 \tag{2.30}$$

Finally, the parametric continuous functions $a(t)$ can be obtained from linear interpolation of the sampled points $\hat{a}(t_i)$.

2.2.3 Validation of the proposed parametric scatter transfer function

The set-up shown in Figure 2.7 illustrates the problem derived from the cone-beam geometry at the edges of an object. A 50mm PMMA plate is placed parallel to the chest-wall, with a radio-opaque edge placed over it and covering half of the detector. At the object edge, the geometry of the acquisition creates a "shadow zone". This zone is characterized by an abrupt decrease of

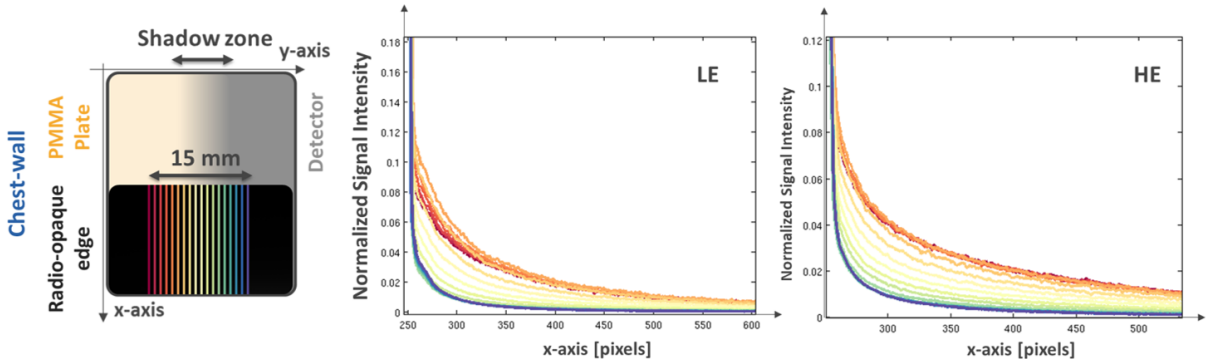

Figure 2.7: Experimental acquisitions in a Senographe Pristina system showing the scatter behavior at the abrupt edge of a 50mm thick PMMA test plate. We measured the vertical profiles in a $15mm$ region centered at the PMMA edge. Therefore, each line in the drawing (left) and the graphs (middle and right) represents the part of the normalized ESF below the radio-opaque edge for the two spectra considered in this study. As we can observe, the scattered signal varies along the shadow zone where the length of the path inside the test object traversed by the X-rays is suddenly reduced.

the length of the X-ray path traversing the object. Due to this effect, we can observe several different scattering spreads in the transition region, depending on the traversed thickness.

To validate the realism improvement of the thickness dependent scatter model over an **additive scatter model** where a unique scatter kernel is used over all the image, we use the set-up illustrated in Figure 2.8. A PMMA plate covers the entire detector in the direction parallel to the chest wall and $50mm$ in the direction perpendicular to the chest wall. In this set-up, the length traversed by the X-rays is similar to the thickness of the scatter plate at the chest wall side and decreases to zero at the physical edge of the phantom. The additive scatter kernel approach considers the same kernel extent independently of the traversed X-ray path length, while our method introduces a different scatter kernel for each traversed X-ray path length. The experiment was repeated for three PMMA thicknesses, i.e. 25, 50 and $75mm$.

Since the maximum spatial extent of the computed scatter kernels was $50mm$, a $50mm$ distance from the chest wall edge of the detector was considered enough for our measures. This minimal distance allows us to simulate images with enough scatter build-up inside the uniform projected object area. Signal intensities were evaluated along a $55mm$ long profile perpendicular to the chest-wall. To reduce the impact of noise, signal intensities were averaged across several rows (Figure 2.8 - vertical average of the rectangular ROI called "Profile" in middle figure insert).

Acquired MTFs and fitting functions

A comparison of the MSE between the MTFs derived from image acquisitions and their fits with the different considered functions in Equations 2.24-2.28, is presented in Figure 2.9. To illustrate the main limitations of each expression, we show in Figure 2.10 the optimal fit for each of the functions over the MTF acquired at low-energy spectra for a $50mm$ PMMA plate. We observe that, while the Lorentzian, the Rational and the expression proposed by Ducote et al. preserve the low-frequency drop, this is not true for the exponential and Gaussian functions. This is the main reason of their high MSE errors among all the energies and thicknesses we analyzed. Consequently, the exponential and Gaussian functions were discarded from our study. The sum of Lorentzian functions, as well as the expression proposed by Ducote et al., seemed to match correctly the acquired MTFs over all the range of thicknesses and spectra used in this

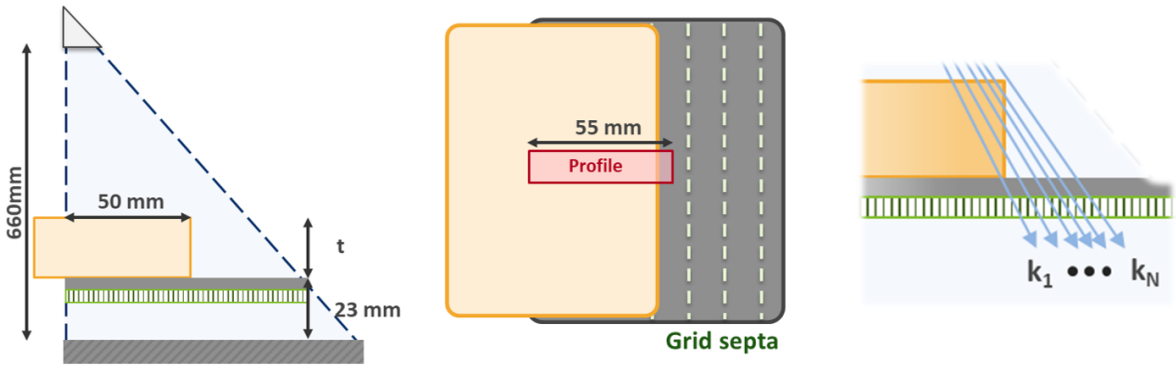

Figure 2.8: Set-up for PMMA edge with thickness t. Left: Side view of the system. Middle: Top-down representation of the elements placed over the detector and the region of interest used for validation. Right: Schema of the X-ray paths when traversing the object at different thicknesses. Each of the kernels, represented by $k_1 \dots k_N$, are related to the traversed PMMA thickness of each X-ray path. Considering this, the scatter spreading of k_1 is larger than k_N.

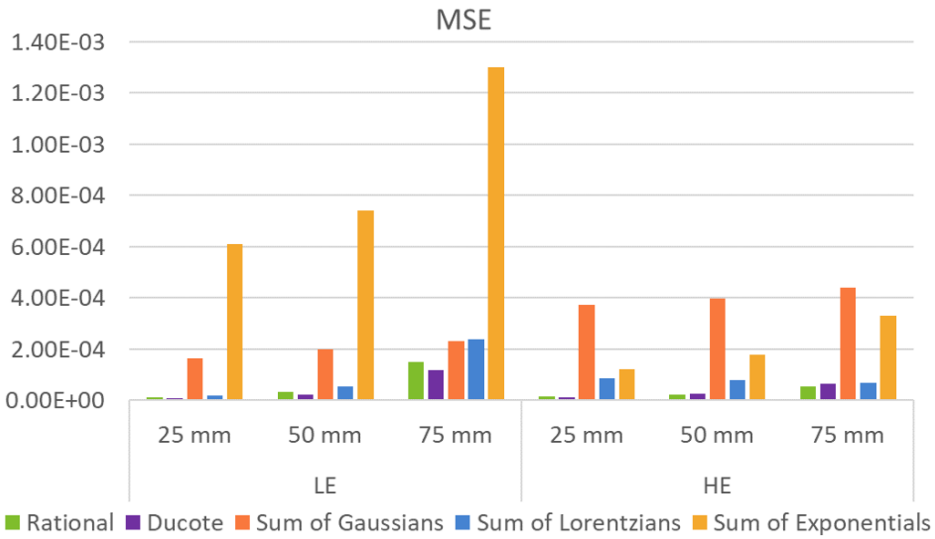

Figure 2.9: Mean Square Error for different fitted analytical functions.

study, with a similar MSE as the one of the rational function. However, in Figure 2.10, we find a slight difference at the low-frequency drop. Our rational function fits better this region of the MTF. We can better appreciate the consequences of this difference in the spatial domain. In Figure 2.11, we present the ESFs of a low-energy image for a $25mm$ PMMA plate, where we clearly observe this spatial difference. We observe that the summation of Lorentzians follows a linear decay in logarithmic domain, and the ESF produced by the expression proposed by Ducote et al. is slightly inferior to the acquired ESF. By contrast, our rational approximation of the experimental MTF offers a better representation of the experimental ESF in a real system, improving the fidelity of our simulations.

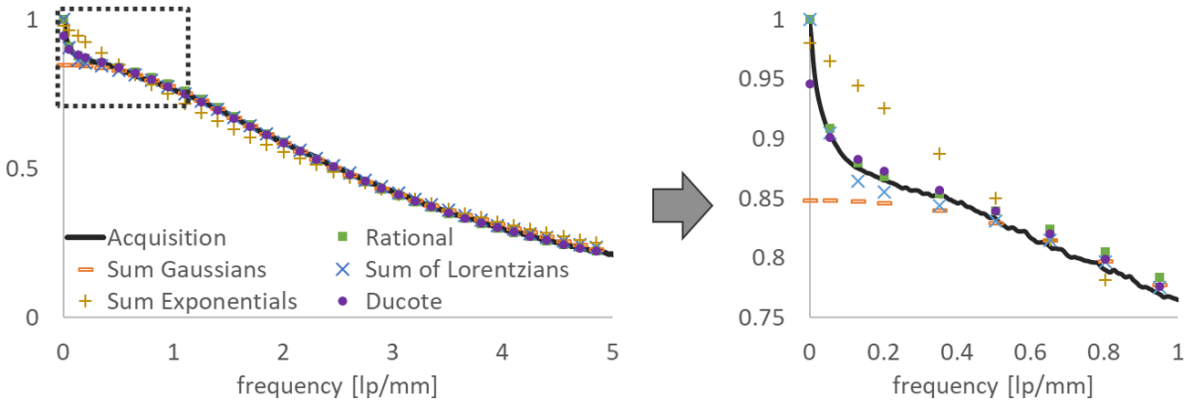

Figure 2.10: Comparison between different analytic MTF expressions for a low energy image of a $50mm$ PMMA plate.

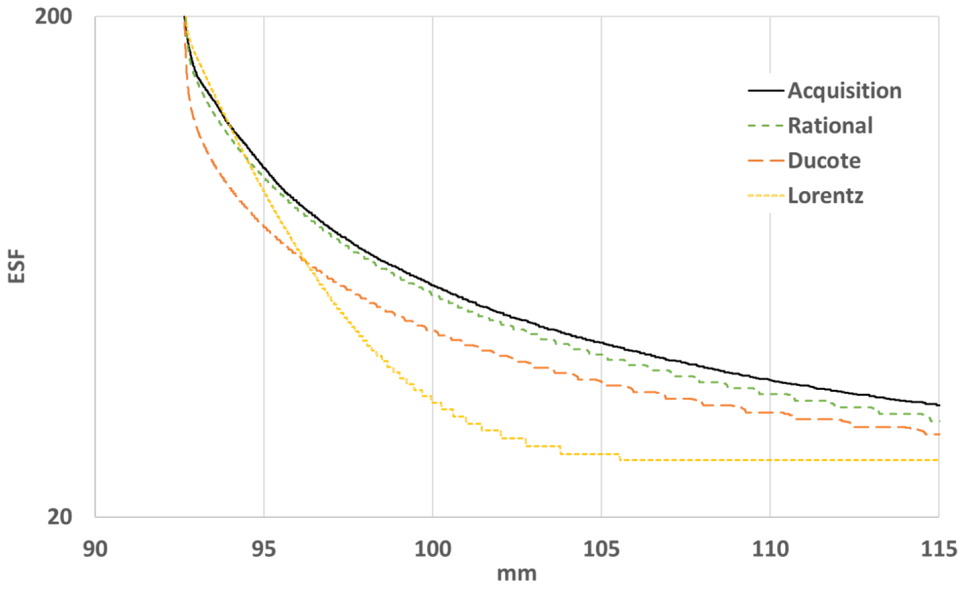

Figure 2.11: ESFs for a 25mm scatter plate acquired and simulated using the low-energy spectra using the summation of Lorentzians approximation, the function introduced by Ducote and our proposed rational function. Note that the y-axis is in logarithmic scale.

Each of the acquired MTFs was the approximated by H_T (rational function), described in Section 2.2.2. Results are presented in Figure 2.12. We can see that the proposed analytic expression (Equation 2.28) is well adapted to all thicknesses and spectra considered in this work.

Extrapolated MTFs

From the fitted MTFs at $t = 25$, 50 and $75mm$, we obtained three values for each of the coefficients $a_r(t)$, $b_r(t)$, $c_r(t)$, and $d_r(t)$, for both energies (Table 2.2). In Figure 2.13 we show that a linear extrapolation of these coefficients is well adapted to the values obtained.

The continuous thickness expression H_T presented in Equation 2.28 allows us to approximate the total MTF of the system for any other object thickness. This is illustrated in Figure 2.14. As

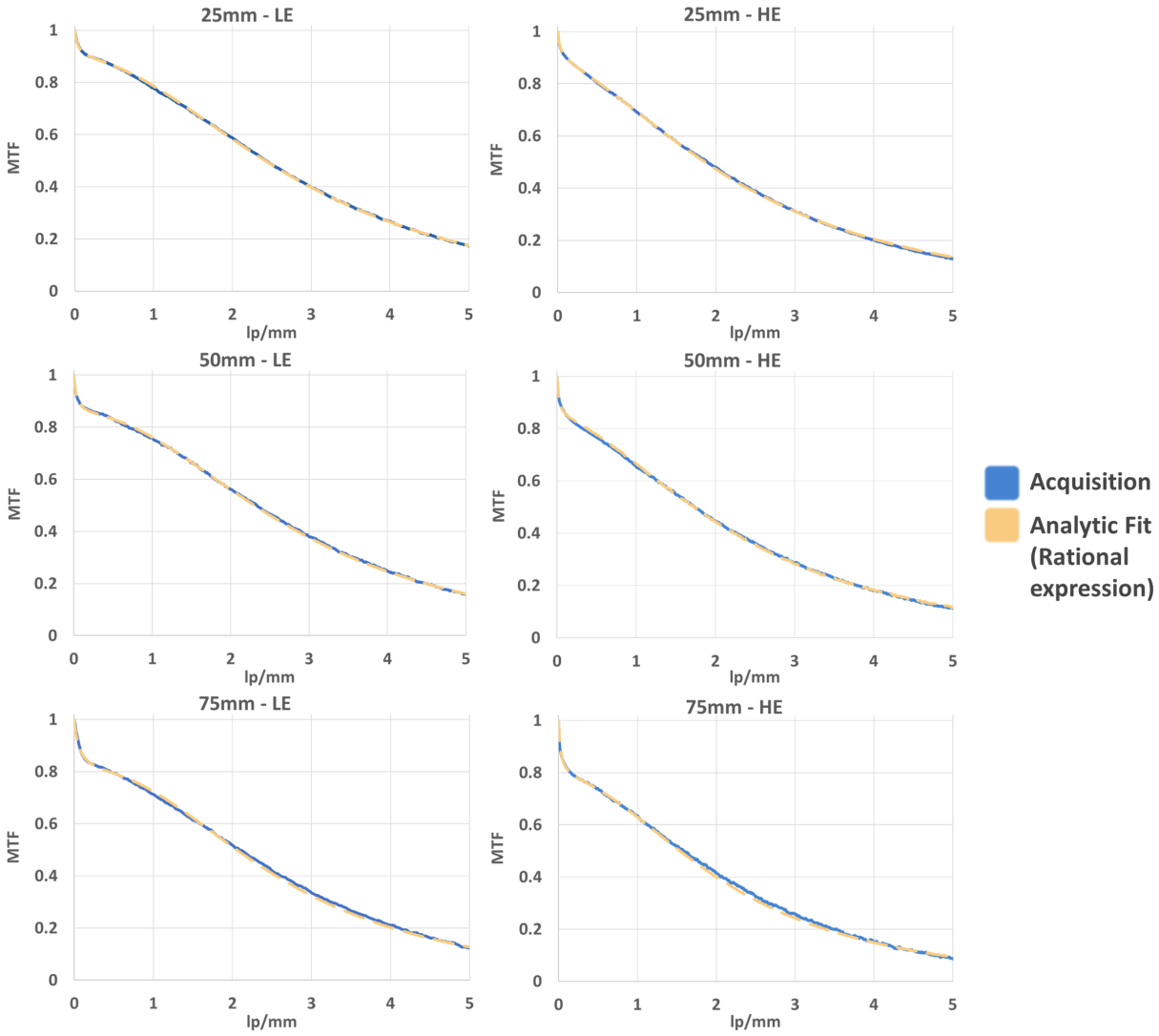

Figure 2.12: Computed and fitted MTFs for all combinations of energies and thickness used in our experimental set-up.

Table 2.2: Coefficients of the rational analytic MTF expression for the three thicknesses used. We show also the goodness of the linear fit for each of the coefficients.

	LE				**HE**			
	25	50	75	R-square	25	50	75	R-square
a	7.92	6.73	4.73	0.98	6.84	5.55	4.25	1.00
b	0.40	0.32	0.26	0.99	0.29	0.20	0.13	1.00
c	0.09	-0.23	-0.53	1.00	1.11	0.72	0.30	1.00
d	8.98	8.07	6.2	0.96	7.77	6.70	5.45	1.00

we observe, for the chosen range of represented thicknesses (i.e. $0 - 80mm$), the low-frequency drop due to scatter field smoothly increases with the thickness, as desired.

This effect is directly reflected in the SPR of our simulations. In Figure 2.15 we show the SPRs obtained from simulated images. The increasing slope of the SPR function of our

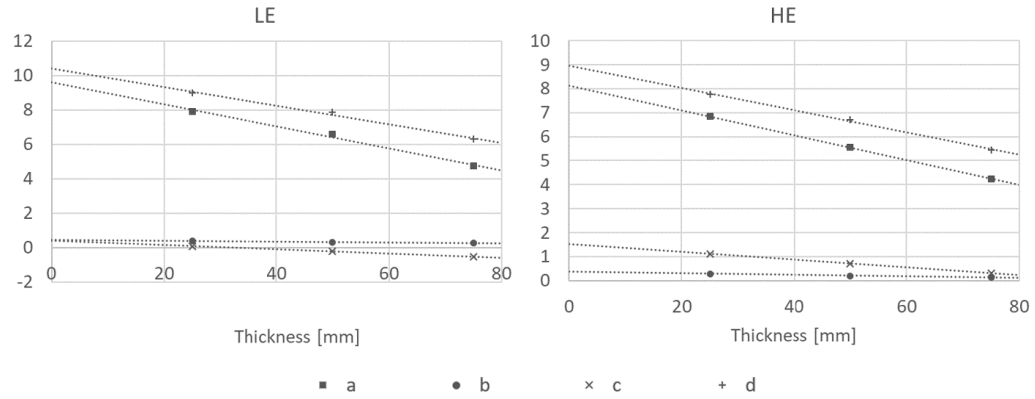

Figure 2.13: Linear fit for coefficients of generalized MTF expression for low- and high-energy images.

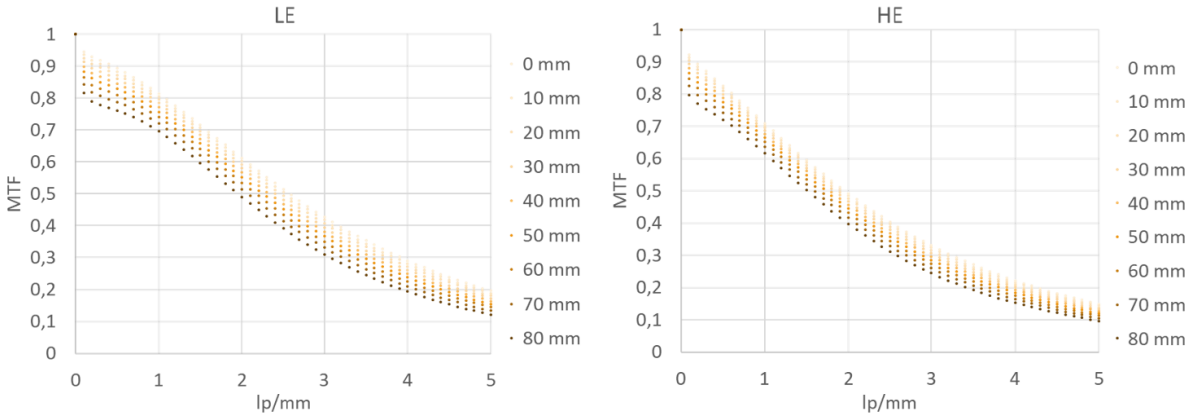

Figure 2.14: MTFs generated with generalized expressions depending on thickness from 0 to 80 mm for low- and high-energy acquisitions.

simulations is well correlated to the SPRs of our experimental measures in the real acquisition system. Furthermore, in Table 2.3 we present the errors between the measured SPRs in real acquisitions and simulated images. The absolute error is 0.005 for the LE and 0.008 for the HE images. Salvagnini et al. [258] showed a maximal error difference of 24% between the measures using the edge method and the values found in Monte Carlo simulations, and a 4% error between repeated measures of the SPR using the edge method. However, note that due to our anti-scatter grid, the range of SPRs in both simulated and acquired images is considerably smaller than in other references [29, 258]. This could explain the slightly higher percentage error we find in our simulations.

Validation results

As described in the introduction of this section, and following the setup of Figure 2.8, we compared the results of real system acquisitions and two types of simulations: one using an additive scatter model, and another one using a new thickness dependent scatter model.

To compare acquired and simulated profiles in PMMA edge phantoms, we normalized the signal intensity profiles to the mean value inside the uniform area of the imaged plate. These profiles are shown in Figure 2.16, and the MSE between them in Table 2.4. The use of the

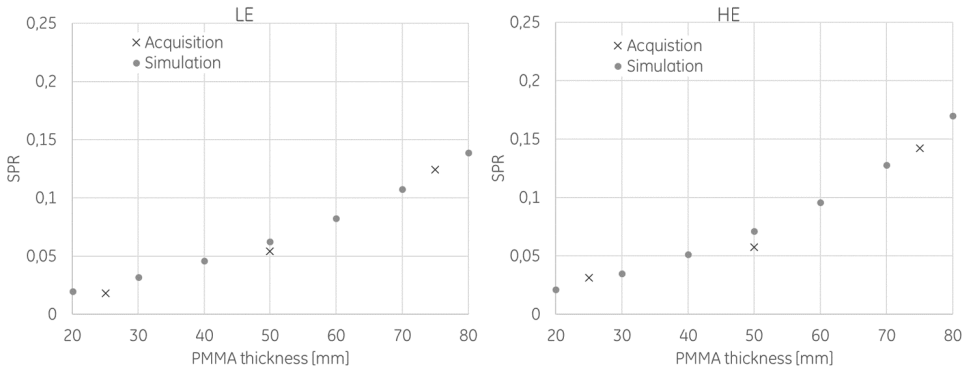

Figure 2.15: Scatter-to-Primary ratios from acquisitions at 25, 50 and 75mm against the values obtained from simulated images for thickness from 20 to 80mm.

Table 2.3: SPR measures in experimental acquisitions and simulated images.

	Thickness [mm]	**Acquisition**	**Simulation**	**Percentage Error**	**Absolute Error**	**Mean Error**
LE	25	0.018	0.025	41.6%	0.007	0.005
	50	0.054	0.062	14.8%	0.008	
	75	0.124	0.123	1.2%	0.001	
HE	25	0.034	0.028	17.6%	0.006	0.008
	50	0.058	0.071	22.4%	0.013	
	75	0.142	0.148	4.4%	0,006	

thickness dependent scatter kernels is needed in thick phantoms, as the edge profile is no longer shaped by pure geometrical effects but by a combination of the scatter field and the geometry of the conical beam. As we can see, for small thicknesses we do not observe a large difference of MSE between both algorithms and both spectra. However, in thicker objects we notice that our algorithm provides always an error which is inferior to the additive scatter. Besides, we have found a stable MSE in LE images measured for all the range of studied thicknesses, however, the same is not true for HE images. This may be caused by the non-linearities only present when using the high-energy spectrum, such as K-fluorescence or Swank noise, which are not considered in the numerical chain. Despite this, the MSE and shape of the profiles are still acceptable. In Figure 2.17, we show an example of the simulated images using the additive scatter and the thickness dependent models (low-energy images using the set-up presented in Figure 2.16 with a 75mm thickness PMMA plate). These images were generated considering that the scatter kernels are isotropic. As we can observe in the difference profile, even if the phantom is uniform and the only thing we change for their generation was the scatter kernel, both images do not share any common region with the same intensity.

Finally, in terms of computation time, in all our simulations we used Catsim running on Matlab in a system with an Intel® Xeon Silver® 4114 CPU @ 2.2GHz. A couple of simulated acquisitions (i.e. low- and high-energy images of the 50mm PMMA plate) with size 1000×1000 pixels took approximately 3.4 minutes when our thickness dependent scatter kernel was used, compared to 2.2 minutes when the stationary kernel was used. This slight increase in computer time is perfectly acceptable and does not prevent the method to be used in practice.

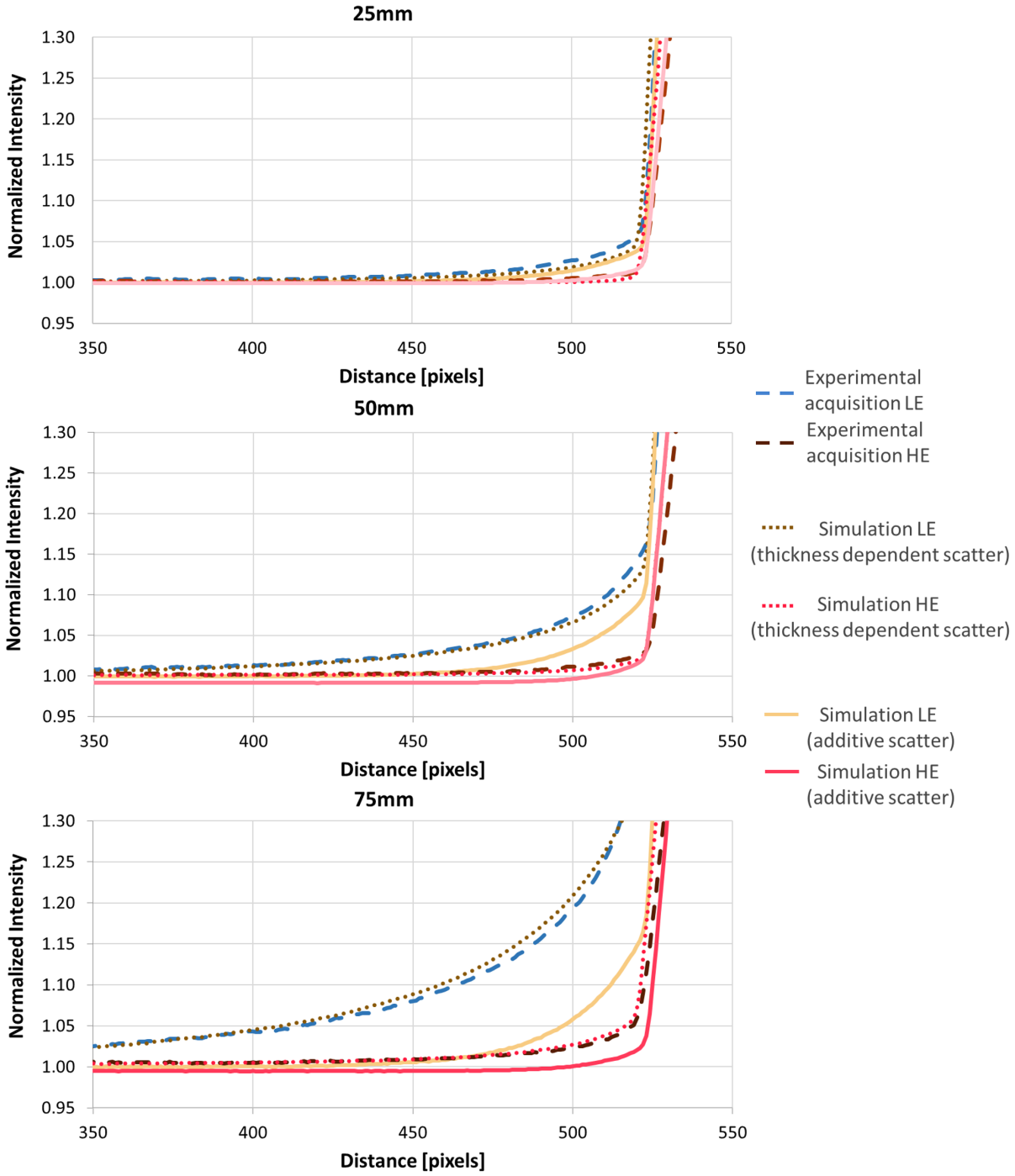

Figure 2.16: Experimental and simulated (additive and thickness dependent scatter models) low- and high-energy profiles in PMMA edge phantoms.

2.2.4 Simulation of scattered field in systems without anti-scatter grid

In Section 2.2.3, we have validated the performance of our method for mammography systems with anti-scatter grid. Although the simulation of the X-ray scattered field is necessary to provide realistic simulated images, in these systems, the contribution of the X-ray scattered field to the

Table 2.4: MSE between the experimentally acquired edge profiles and our simulations using the proposed thickness dependent scatter and only the scintillator stationary scatter kernel.

	LE			**HE**		
	25	**50**	**75**	**25**	**50**	**75**
thickness dependent scatter	2.6e−5	2.5e−5	8.8e−5	5.4e−6	1.1e−5	5.3e−4
additive scatter	7.2e−5	5.0e−4	5.2e−3	5.2e−6	2.4e−4	1.7e−3
additive/thickness error ratio	2.8	20.0	59.1	1.0	21.8	3.2

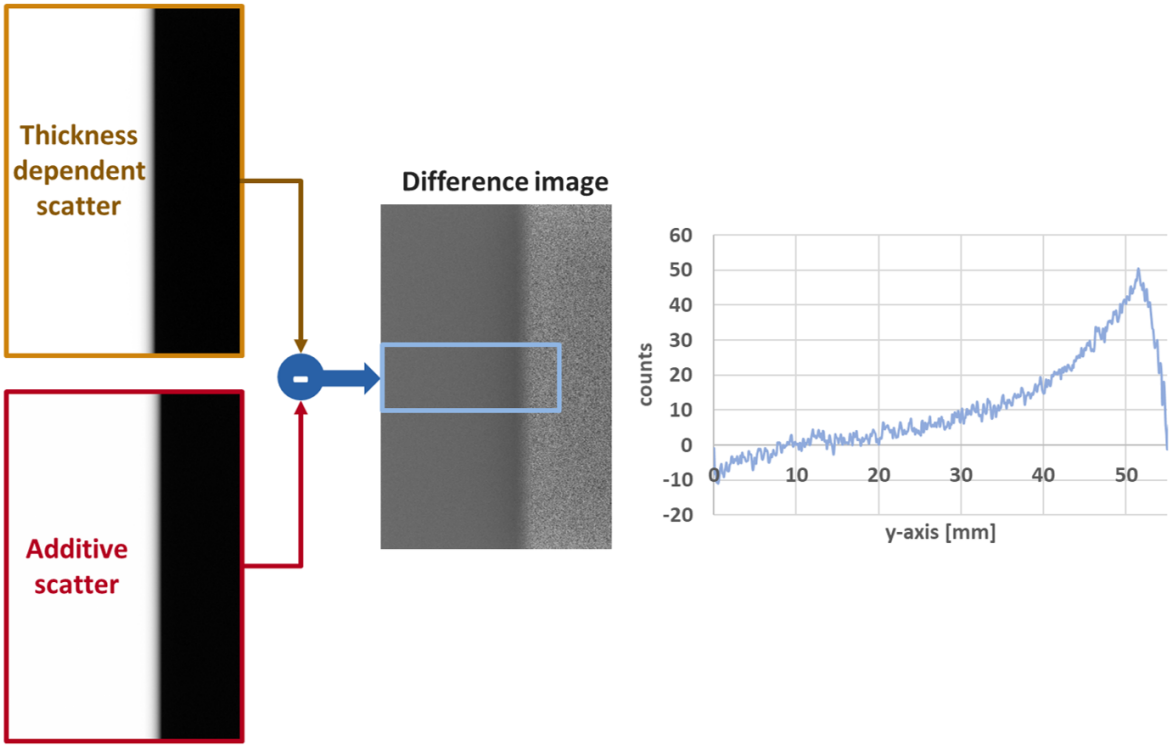

Figure 2.17: Example of simulated low-energy images with the same set-up as the one described in Figure 2.8 for $t = 75mm$ using both approaches (thickness dependent scatter and additive scatter model). The difference image and a horizontal profile of this difference is also displayed to show the improvement already commented in Figure 2.16.

total signal intensity is very small. Therefore, as showed in Figure 2.14, the difference between the scatter kernels for a large range of thicknesses is rather narrow (MTF drop at low-frequencies from 0.92 to 0.79 for 0 and $75mm$, respectively).

In this section, we analyze the potential of our approach when we have a higher X-ray scatter field contribution and, therefore, a notable difference between the scatter kernels for different thicknesses. More precisely, we want to know if the developed model is capable to estimate the thickness dependent scatter kernel $H_T(\nu, t)$ for a mammography system without anti-scatter grid, considering low- and high-energy acquisitions.

To this end, we performed all the steps proposed in Sections 2.2.1, 2.2.2 and 2.2.3 but replacing the experimental acquisitions by new ones obtained without an anti-scatter grid. This means that all the acquisitions presented in this section were performed with the same Senographe Pristina described in Section 1.3.1 of Chapter 1 but removing its anti-scatter grid.

Acquired MTFs and fitting functions

The first step is to obtain samples $\hat{a}_r(t_i)$, $\hat{b}_r(t_i)$, $\hat{c}_r(t_i)$ and $\hat{d}_r(t_i)$ of the coefficients $a_r(t)$, $b_r(t)$, $c_r(t)$ and $d_r(t)$ for different thicknesses t_i. In Section 2.2.2, we showed that three experimental measures of the MTF at t_i =25, 50 and 75mm were enough to obtain a thickness dependent scatter kernel for mammography systems with an anti-scatter grid. However, we found that this is no longer true when the system does not have an anti-scatter grid. A linear extrapolation of the sampled coefficients $\hat{a}_r(t_i)$, $\hat{b}_r(t_i)$, $\hat{c}_r(t_i)$ and $\hat{d}_r(t_i)$ for the thickness range between 0 and 25mm is not enough in this case. This is presumably due to the higher MTF variability for different thicknesses when the anti-scatter grid is removed. To solve this, it is necessary to add an additional sample at 0mm.

Consequently, we measured four different MTFs: one without any test object over the detector ($t_i = 0mm$) which corresponds only to the optical glare, and three more measures using the same PMMA plates and set-up we presented in Section 2.2.2 (t_i =25, 50 and 75mm). Each of these curves was approximated by the rational function introduced in Equation 2.28. The measured MTFs and their corresponding fitted rational functions are illustrated in Figure 2.18. As we can observe, these curves offer a higher variability of the MTF low-frequency drop than the ones presented in Figure 2.12 due to a higher scatter contribution (MTF drop at low-frequencies from 0.95 to 0.44 for 0 and 75mm, respectively).

In Table 2.5 we present the MSE of each fit, computed with Equation 2.30. We confirm that the analytic curves for the MTFs fit well the experimentally acquired MTFs. The worst case was found for the MTF at 0mm in high-energy acquisitions. The characteristics of this curve (almost linear at low-frequencies) makes it difficult to be replicated by the rational expression we introduced.

Extrapolated MTFs

Using Equation 2.29 and the fitted MTFs at t_i = 0, 25, 50 and 75mm, we can obtain four samples for each of the coefficients $a_r(t)$, $b_r(t)$, $c_r(t)$, and $d_r(t)$. In the case of a system without anti-scatter grid, we found that a third degree polynomial was suitable to adapt our thickness dependent expression $H_T(\nu, t)$ for the range of thicknesses considered in this work (0 to 75mm). In Figure 2.19, we illustrate each of the polynomial curves for each coefficient and spectra. Also, in Table 2.6, we present the values of each coefficient at each thickness and spectra.

We found that the coefficient c in low-energy MTFs is always equal to zero. This could be caused by the particular additional scattering processes in high-energy acquisitions that does not occur in low-energy acquisitions, such as the K-fluorescence [61, 314].

Finally, we followed the steps proposed in Section 2.2.2. Each polynomial thickness dependent expression $a_r(t)$, $b_r(t)$, $c_r(t)$, and $d_r(t)$ was introduced in our final thickness dependent scatter kernel $H_T(\nu, t)$ for low- and high-energy simulations.

Validation results

Using the procedure introduced in Section 2.2.3 and the set-up presented in Figure 2.8, we performed the validation of these new thickness dependent scatter kernels which consider a detector without anti-scatter grid. In particular, we compared the profiles perpendicular to the chest-wall of experimentally acquired images (same thicknesses for the PMMA plates as in Section 2.2.3: 25, 50 and 75mm) to the profiles measured in simulated images using the thickness dependent scatter kernels.

In Figure 2.20, we illustrate the difference between the profiles of experimentally acquired and simulated images. The corresponding MSE is given in Table 2.7.

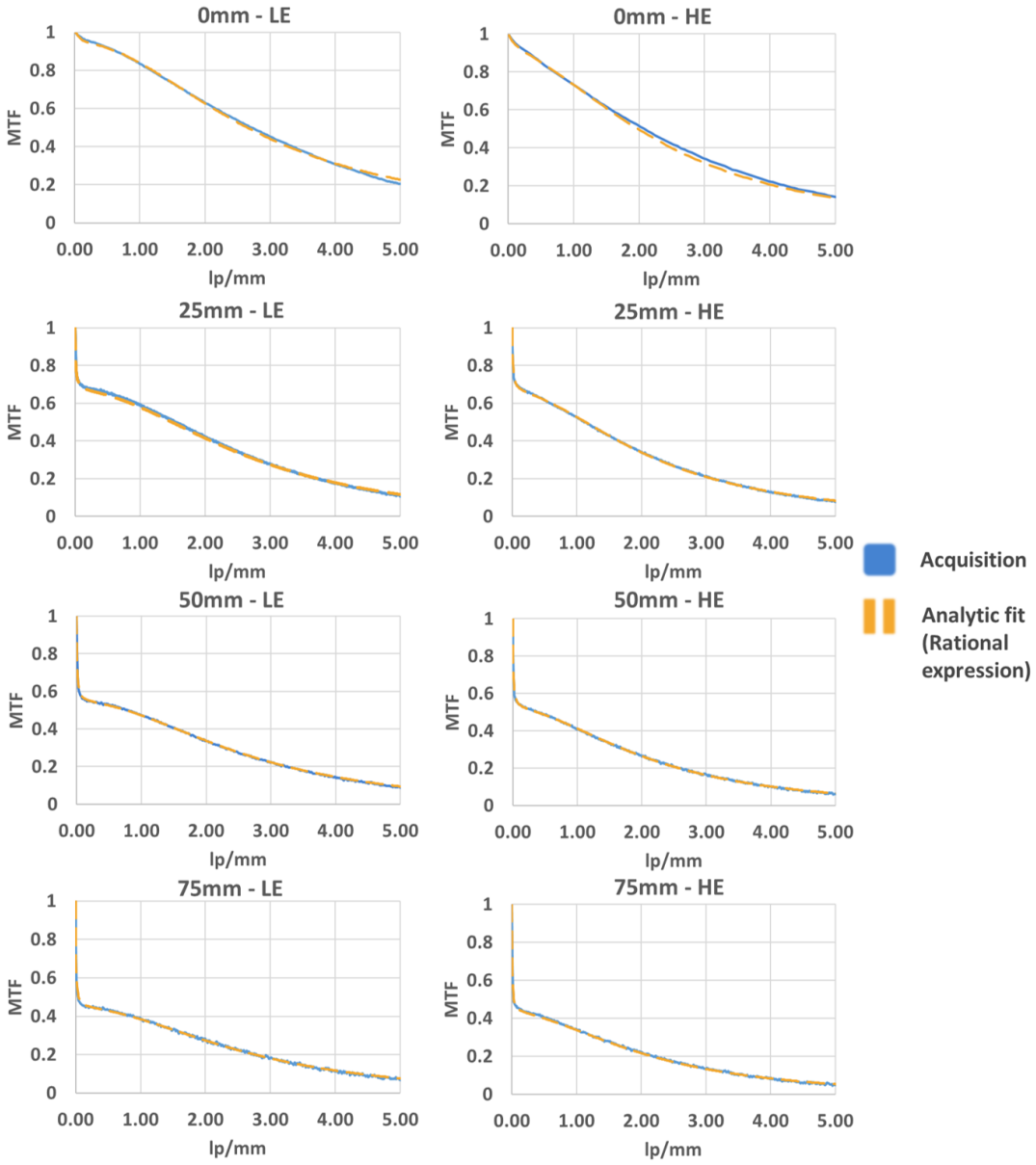

Figure 2.18: Low- and high-energy MTFs measured in a system without anti-scatter grid for different X-ray scattering fields (different object thicknesses) and their corresponding fitted function with the expression given in Equation 2.28.

Table 2.5: MSE between measured MTFs and fitted curves using the expression given in Equation 2.28 for different thicknesses and spectra.

	Thickness $[mm]$			
	0	**25**	**50**	**75**
LE	3.61e−5	6.3e−5	2.0e−5	3.3e−5
HE	2.26e−4	1.2e−5	1.0e−5	2.2e−5

We observe that, while in low-energy images the simulated profiles are well adapted to the different experimental measures, this is not the case in high-energy acquisitions. In high-energy

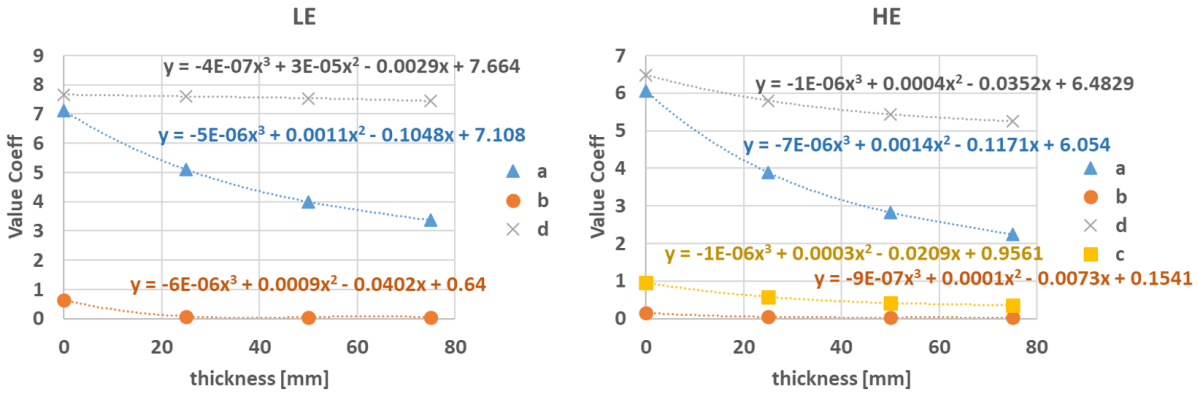

Figure 2.19: Third degree polynomial fitting using each of the sampled coefficients $a_r(t)$, $b_r(t)$, $c_r(t)$ and $d_r(t)$ for low- and high-energy MTFs. .

Table 2.6: Coefficients of the rational analytic MTF expression for the four thicknesses used in a Senographe Pristina without grid.

	LE					**HE**				
	0	25	50	75	R-square	0	25	50	75	R-square
a	7.11	5.10	4.00	3.37	1.00	6.20	3.89	2.83	2.25	1.00
b	0.64	0.08	0.05	0.05	1.00	1.00	0.05	0.03	0.03	1.00
c	0.00	0.00	0.00	0.00	1.00	0.72	0.58	0.42	0.36	1.00
d	7.66	7.60	7.54	7.44	1.00	7.00	5.80	5.44	5.26	1.00

profiles we obtain an acceptable simulation at $25mm$, however we observe an increased difference for thicker PMMA plates. This limitation of our approach could be related to the aforementioned K-fluoresce [61, 314], which is only present in high-energy acquisitions and it is not considered in our simulations.

To assess the relevance of the results obtained with our thickness dependent scatter kernel, and the realism improvement they suppose, we simulated the same set-up as before (Figure 2.8) but using a binary mask (Figure 2.21). In other words, we split our image in two halves (with and without test object presence), and we applied the MTFs for 25, 50 and $75mm$ when the X-ray beams traverse the 25, 50 and $75mm$ PMMA plates, respectively, and the MTF at $0mm$ when the X-ray beams do not intersect with the projected object. The results of these simulations are illustrated in Figure 2.22.

Comparing these results to the curves presented in Figure 2.20 we appreciate the noticeable improvement provided by our thickness dependent scatter kernel, even if our model seems limited to reproduce the behavior in high-energy simulated images.

2.2.5 Conclusion

In this work we proposed a new methodology to introduce into an analytic X-ray simulation platform the scattered field of an X-ray mammography acquisition system. This new procedure has the advantage to provide a continuous object thickness expression of the scattered field using the information of a reduced set of experimental measures. With this method we can quickly adapt the results of our simulation platform to the available systems, and generate

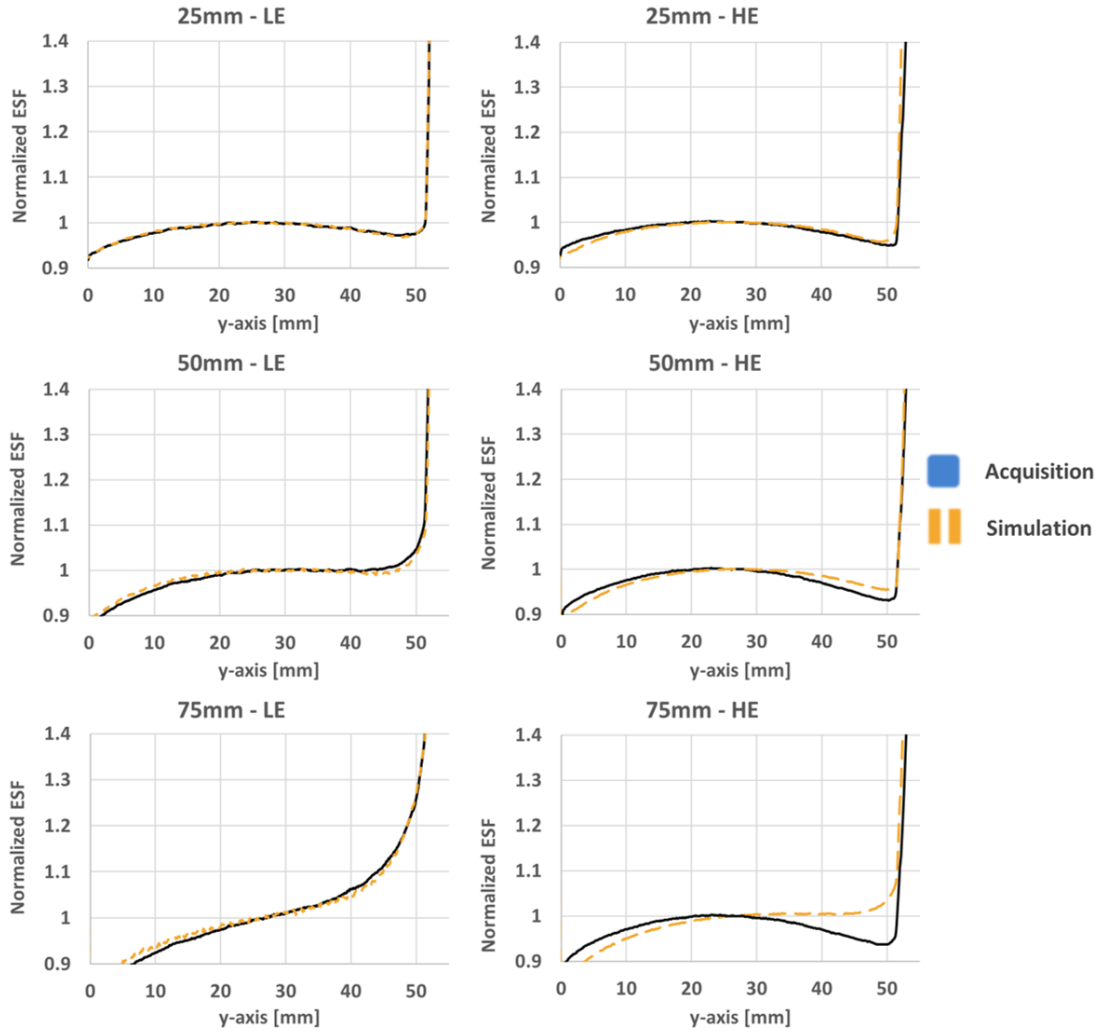

Figure 2.20: Profiles from experimentally acquired and simulated images as described in the set-up presented in Figure 2.8.

Table 2.7: MSE between the profiles of experimentally acquired and simulated images presented in Figure 2.20.

	Thickness [mm]		
	25	**50**	**75**
LE	4.56E-05	5.02E-05	1.12E-04
HE	5.70E-05	2.44E-04	1.30E-03

simulated images in a reduced time. The performance of our method was evaluated for X-ray mammography acquisition systems with and without anti-scatter grid.

Results show a good correlation between experimental acquisitions and simulated ESFs in systems which incorporate an anti-scatter grid, improving the fidelity of simulations previously obtained using a stationary scatter kernel. In particular, for simulations considering the anti-scatter grid, we found that our method provides a $3\times$ (at $25mm$), a $20\times$ (at $50mm$) and a $59\times$ (at $75mm$) improvement for low-energy acquisitions and a $1\times$ (at $25mm$), a $22\times$ (at

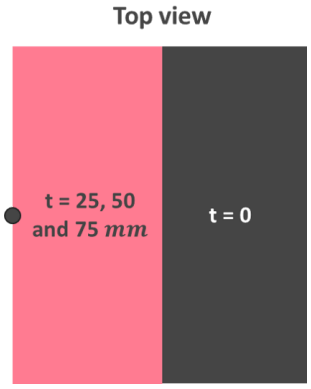

Figure 2.21: Binary mask applied to the two MTFs simulations. We consider that the image is splitted in two halves: presence and absence of the projected object.

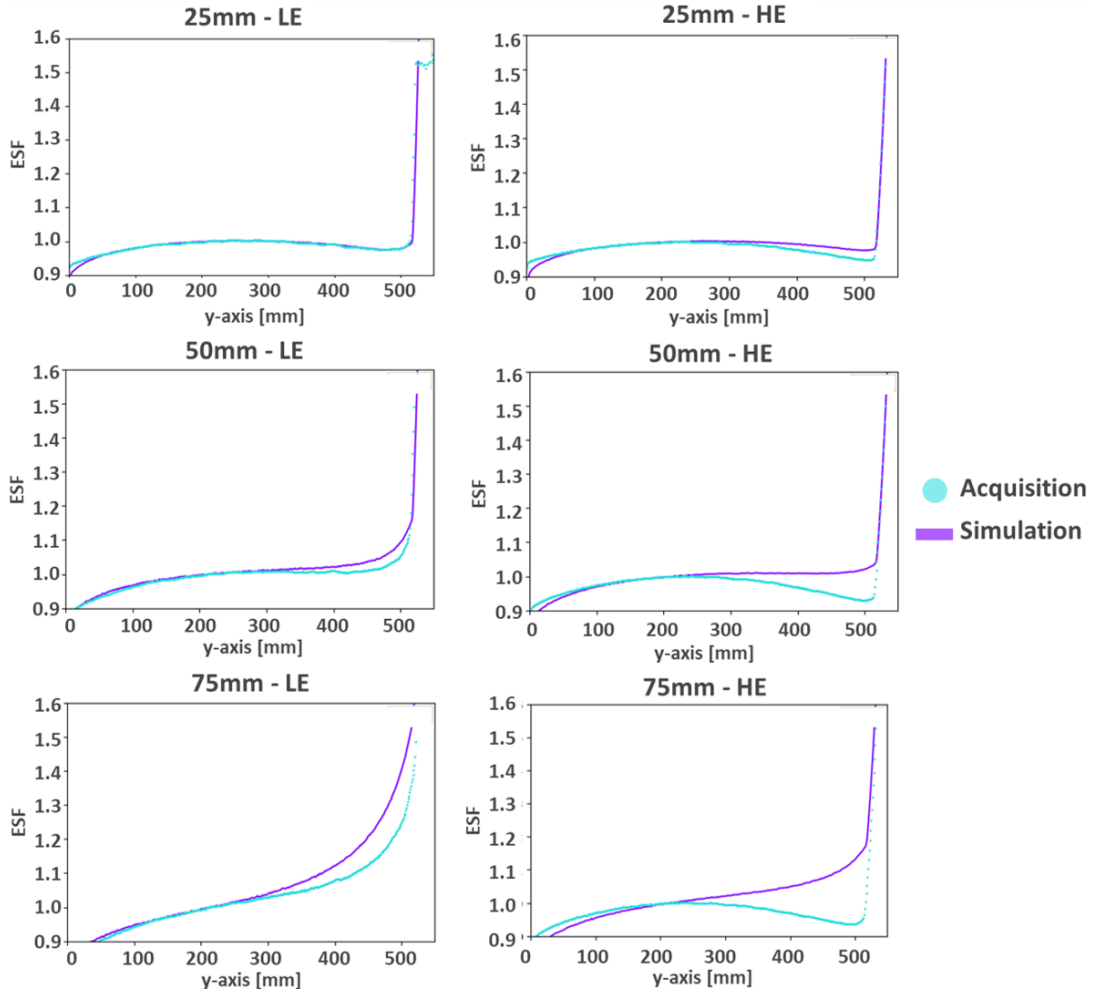

Figure 2.22: Results of the two MTFs simulations for all the PMMA thicknesses and spectra.

$50mm$) and a $3\times$ (at $75mm$) improvement for high-energy acquisitions. Low-energy simulated images of systems where the anti-scatter grid was removed also show a good correlation to experimental acquisitions. However, our model is limited by the physical processes considered in

our simulation. When the contribution of the X-ray scatter field is high (objects with thickness higher than $50mm$), we do not find a good correlation between high-energy simulated and experimental images.

This methodology provides a tool to adapt and simulate the frequency response of available acquisition systems and quickly iterate over different image quality tests to compare them. In terms of the workload needed before setting-up the proposed algorithms, the stationary scatter kernel needs one unique measure of the MTF of the system, while our thickness dependent kernel needs two supplementary measures. This only adds a small time previous to the simulations.

Moreover, as we provided a continuous expression of the scatter field depending on the object thickness, our methodology enables to study how different modifications of this expression impact the global performance of the system, providing useful information for future mammography acquisition systems

This work could be further developed in several directions. First, we could analyze the effect of the experimental number of points needed to obtain a good representation of $H_T(\nu, t)$ in the desired range of thicknesses. Secondly, as we have commented previously, the simulations presented here considered an isotropic scattered field, using the frequency response of the system in the direction tangent to the anti-scatter grid lines. This must be generalized to adapt the real anisotropy of the scatter field present in real systems. The MTF parallel to the grid-lines could be additionally measured to provide a two-dimensional anisotropic MTF combining both measures. Moreover, anisotropic scatter fields could impact on the phase response of the mammography system (see Section 2.1). Thirdly, the acquisition and simulation experiments were performed using an homogeneous object, however the scatter level depends on the composition of materials traversed by the X-ray and various compositions should be tested. Other effects induced by the conical geometry also affect the shape of scatter kernels. In particular air gap at the object exit is also spatially dependent, while this study considered it as a stationary effect. These elements will be the subject of further studies. Finally, to improve the realism of high-energy simulated images when there is no anti-scatter grid, the model needs to be modified to consider additional physical processes which are particular to high-energy acquisitions.

2.3 Stochastic processes in a X-ray system

The final digital image obtained with a mammography system is composed of several random processes, each of them following a different distribution. These random processes compose what is usually called noise, which may affect the interpretation of an image, or the visibility of a particular breast lesion. In this section we present the different stages we included in CatSim to model these processes.

2.3.1 Quantization ramp

Once the transistors of the detector have been charged thanks to the arriving optical photons, the electronics of the detector is in charge of transforming the analogical signal to digital bytes, so it can be interpreted by the computer. This process includes two main steps:

- Integration: through a charge integrator, electrons are transformed into “analogic” counts. More precisely, the image at this step is a continuous version of the final image presented to the user.

- Quantization: an analogical/digital converter discretizes the continuous information to transform the "analogic" counts into digital counts, introducing an error term. This step will be the focus our investigation.

Model

Quantization is the last stage of the acquisition chain, where each input value in the continuous range is associated with a fixed discrete value. Consequently, the quantization step is defined by its discretization step. If this step is the same for all the possible input values, the quantization is said to be linear. Alternatively, non-linear quantizers use smaller steps in common input signal levels, and increase the gaps where the signal input is less likely to occur, to reduce the impact of discretization. The implementation of the quantization stage can be directly done in our simulation platform following the description of the detector parameters provided by the manufacturer. The documentation and details about the digital ramp implemented in a Senographe DS and a Senographe Pristina has been studied before implementation. For both systems, the ramp is composed by a linear and a non-linear part, however, a GE confidential disclosure protects the details of the quantization ramp and it will not be reproduced here.

To model the noise introduced by this stage, we consider simple linear quantizers. In linear quantization, when the amplitude of the continuous signal is much larger than the size of the quantization step, the introduced error is not significantly correlated to the input signal, and it can be approximated by a uniform distribution:

$$u \sim \mathcal{U}(a, b) \tag{2.31}$$

where a and b depend on the quantization step and how the approximation is performed, from continuous to discrete values. In our case, the quantization step is adapted to the intensity of the input continuous signal. However, with the purpose to describe analytically the noise introduced by this stage, we consider a fixed quantization step a and the quantization function is defined as:

$$Q(x) = a \cdot \left\lfloor \frac{x}{a} \right\rfloor \tag{2.32}$$

Consequently, our quantization noise can be modeled as:

$$u \sim \mathcal{U}(0, a) \tag{2.33}$$

Acquisitions and simulations

In order to evaluate the validity of our implementation, we use the set-up illustrated in Figure 2.23a for the acquisitions and the simulations. A projection of a PMMA slanted phantom allows us to acquire an image including the full dynamic of the ramp. In other words, a full histogram with all the possible values which can be obtained from our system.

The ramp parameters depend on the system (Senographe DS or Senographe Pristina) and acquisition mode (tomography or standard 2D mammography). Consequently, both systems and modes need to be considered. Different exposure levels were used, so we could have access to the whole dynamic available in the acquisition system (signal from 0 to 16384). Because we need to access all the values available by the quantization ramp after acquisition, no gainmap was applied. The operational point for each system is shown in Tables 2.8 and 2.9. An example of the simulated images is illustrated in Figure 2.23b.

Validation

The images, acquired and simulated using the set-up presented before, include the quantization "holes" attributed by our ramp. Consequently, to validate our implementation, we verified

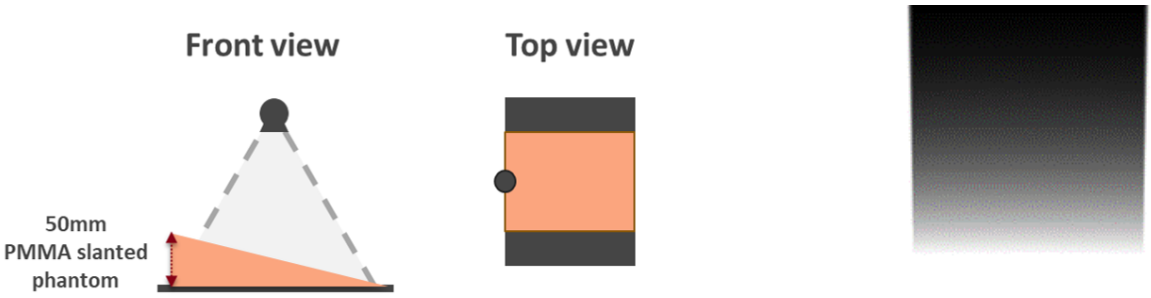

(a) Set-up used for simulations and real acquisitions to validate the implementation of the quantization ramp in the simulator. This procedure was identical for the Senographe DS and Senographe Pristina systems, and the tomography and standard 2D acquisition modes.

(b) Example of a Senographe Pristina-like simulated image using a replica of the slanted phantom.

Figure 2.23: Procedure to validate the quantization ramp implementation.

Table 2.8: Operational point used for the validation of the quantization ramp for the **Senographe Pristina** system. The exposure values were divided by the number of low- and high-energy expositions in the tomography mode.

	LE		**HE**	
	Real	*Simulated*	*Real*	*Simulated*
Spectrum	34kVp	23kVe (monoenergetic)	49kVp	34keV (monoenergetic)
Target/Filter	Rh/Ag	Rh/Ag	Rh/Cu	Rh/Cu
Exposure	Various mAs	Various mAs	Various mAs	Various mAs
Gainmap	No gainmap	No gainmap	No gainmap	No gainmap

that the list of available signal values is the same in acquired and simulated images, for both modalities and mammography systems.

2.3.2 Electronic noise

The detector circuitry is composed of several elements, each of them producing a heterogeneous collection of internal noise: thermal, flicker, shot, burst... These noise sources are completely independent of the number of luminescent photons captured by the photodiodes, but are nonetheless dependent on the detector integration time. Although they are not related to image formation, they introduce a random fluctuation added to the number of electrons consid-

Table 2.9: Operational point used for the validation of the quantization ramp for the **DS** system. The exposure values were divided by the number of low- and high-energy expositions.

	LE		**HE**	
	Real	*Simulated*	*Real*	*Simulated*
Spectrum	28kVp	20keV (monoenergetic)	49kVp	39keV (monoenergetic)
Target/Filter	Mo/Mo	Mo/Mo	Rh/Cu	Rh/Cu
Exposure	Various mAs	Various mAs	Various mAs	Various mAs
Gainmap	No gainmap	No gainmap	No gainmap	No gainmap

ered to generate the final digital value assigned to each image pixel. The relative importance of electronic noise to the total noise increases in low exposure acquisitions such as in CEDBT [314].

Siewerdsen et al. [274] introduced each of the components affecting electronic noise separately as several independent random sources added to the total variance of their CSA model, each of them following a different statistical distribution. Mackenzie et al. [193] separated the effects of electronic noise from the total Noise Power Spectrum (NPS) of the acquisition chain, using it to fit and generate the electonic effect of simulated images [83]. Beside these exceptions, even if electronic noise is generated by a compendium of numerous, heterogeneous, and independent sum of noise sources, we can consider the hypothesis that the influence of thermal noise [221] is dominant for our applications. This noise source can be characterized by an Additive White Gaussian Noise (AWGN) in standard applications [244]. This approximation of the total electronic noise has been largely adopted [62, 108, 249] and it is the approach proposed in this dissertation.

Model

We model the electronic noise as a random signal following a Gaussian distribution added to the simulated image before the detector ramp. Although this signal is independent of the X-ray exposition, the noise magnitude included in the image depends on the time the detector spends acquiring the image. In other words, the electronic noise variance is directly related to the integration time, which may vary slightly among the low- and high-energy acquisitions. Moreover, the value of resistors, capacitors, operational amplifiers, among others, are dynamically assigned depending on the modality of the acquisition, mammography or tomosynthesis, and, consequently, CESM or CEDBT. Considering all this, we model the electronic noise as a random signal following a normal distribution of zero mean, and standard deviation dependent on the energy and the modality of the acquisition:

$$\varepsilon(E, M) \sim \mathcal{N}(0, \sigma^2_{elec}(E, M)) \tag{2.34}$$

where E is the energy of the acquisition (i.e. low- or high-energy) and M the modality (i.e 2D or 3D). Consequently, at this moment, our image formation model is described by the following equation:

$$y = x + \varepsilon + u \tag{2.35}$$

where y is the final acquired image, x is the image after the projection and filtering phase, ε the electronic noise model presented in Equation 2.34, and $u \sim \mathcal{U}(0, a)$ is the quantization noise presented in Section 2.3.1.

To find the parameters and adapt our electronic noise model, we need to be capable of measuring ε in real acquisitions. Thanks to a specific set-up experimentation we can isolate the quantum noise from acquired images. However, our images will continue to be contaminated by the error induced in the quantization step:

$$y_0 = \varepsilon + u \tag{2.36}$$

where y_0 is an acquired pixel value without X-ray exposure.

Considering that both effects are additive and independent of each other, the total variance of the pixel value in an acquisition without X-ray exposure $\sigma^2_{y_0}$ is the sum of the variances of both noise sources. Therefore, the variance of the electronic noise σ^2_{elec} can be formulated as follows:

$$\sigma^2_{elec} = \sigma^2_{y_0} - \sigma^2_u \tag{2.37}$$

where $\sigma_u^2 = \frac{a^2}{12}$ is the known variance of our quantization noise.

There is one last thing we must also consider in our model. Real systems include several pre-processing steps before presenting the image to the user. After the image has been acquired, the system performs an offset correction to remove the fixed pattern structures of the detector originated by the litography process during manufacturing [244]. This process is characterized by the following equation:

$$I_{offset_{corrected}} = I_{raw} - \sum_{i=1}^{N} \frac{I_{offset_i}}{N} \tag{2.38}$$

where $I_{offset_{corrected}}$ is the image after the offset correction, I_{raw} the image acquired directly from the detector, $I_{offset_i} = \varepsilon + u$ each of the correction images the detector acquires automatically before X-ray exposure, and N is the number of correction images used. This last parameter depends on the modality and energy of the acquisition.

Considering that the electronic noise of subsequent acquisitions is not correlated, the total variance associated with the image presented to the reader can be modeled as:

$$\sigma^2_{offset_{corrected}} = \frac{N+1}{N}\left(\sigma^2_{elec} + \frac{a^2}{12}\right) \tag{2.39}$$

This leads us to our final equation to estimate the electronic noise variance of a single acquisition:

$$\sigma^2_{elec} = \frac{N}{N+1}\sigma^2_{offset_{corrected}} - \frac{a^2}{12} \tag{2.40}$$

Acquisitions and simulations

To calibrate our model we need several measures of σ^2_{elec} for different acquisition parameters. The calibration of the model must be done using a system readout with the unique presence of the electronic noise. This means that we have to avoid any charge in the photodiodes. The set-up proposed for this calibration is illustrated in Figure 2.24a. A steel sheet is placed on top of the detector, covering it completely. The thickness of this sheet allows us to completely attenuate the X-rays within the energy and exposure range used in this experiment. Consequently, this set-up avoids any incident X-ray affecting the detector, and the unique signal present in the detector is the electronic noise.

We acquired several images considering the parameters which may impact the electronic noise magnitude: manually selected mAs, low- and high-energy spectra, tomosynthesis and 2D modalities, and Senographe Pristina and Senographe DS systems. The operational point for each system is shown in Tables 2.10 and 2.11. All the automatic pre-processing corrections of the system were disabled to avoid non-expected error sources. Instead, to remove the static patterns in our acquisitions, we computed a customized offset correction using Equation 2.38 with parameter $N = 1$. More precisely, for each experimental acquisition used in this section, we acquired two subsequent images and subtracted them. The difference between the images before and after the manual correction is illustrated in Figure 2.24b. A centered ROI of size 700×700 pixels was chosen to measure the standard deviation.

The values of the standard deviation measured in the corrected images, $\sigma_{offset_{corrected}}$, are presented in Figure 2.25. Similarly, in Table 2.12, we show the values of the standard deviation for the electronic noise in a single acquisition, σ_{elec}. On the one hand, we observe that it is difficult to find a particular correlation between the standard deviation and the mAs. The

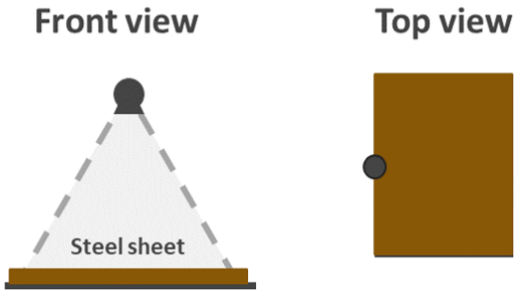

(a) Set-up used for simulations and real acquisitions to calibrate and validate our electronic noise model. This procedure was identical for the Senographe DS and Senographe Pristina systems, and the tomography and standard 2D acquisition modes.

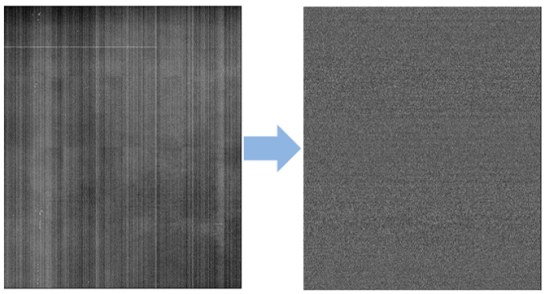

(b) Example of the acquired images, before and after the offset correction.

Figure 2.24: Procedure to validate the implementation of the electronic noise.

Table 2.10: Operational point used for the validation of the electronic noise model for the **Senographe Pristina** system. The exposure values were divided by the number of low- and high-energy expositions in the tomography mode.

	LE		**HE**	
	Real	*Simulated*	*Real*	*Simulated*
Spectrum	34kVp	23keV (monoenergetic)	49kVp	34keV (monoenergetic)
Target/Filter	Rh/Ag	Rh/Ag	Rh/Cu	Rh/Cu
Exposure	Various mAs	Various mAs	Various mAs	Various mAs
Gainmap	No gainmap	No gainmap	No gainmap	No gainmap

maximum increment of the standard deviation due to the mAs among our measures is approximately 1% of the total standard deviation of the electronic noise. On the other hand, we find that there is a real difference between the values of low- and high-energy 3D Senographe Pristina acquisitions. Consequently, for our implementation, we used the average values of the standard deviation presented in Table 2.12, which depend on the selected energy, modality, and system.

Validation

In the proposed electronic noise model, we supposed the dominance of an Additive White Gaussian Noise (AWGN) source. To prove the validity of this approximation we need to prove

Table 2.11: Operational point used for the validation of the electronic noise model for the **Senographe DS** system. The exposure values were divided by the number of low- and high-energy expositions.

	LE		**HE**	
	Real	*Simulated*	*Real*	*Simulated*
Spectrum	28kVp	20keV (monoenergetic)	49kVp	39keV (monoenergetic)
Target/Filter	Mo/Mo	Mo/Mo	Rh/Cu	Rh/Cu
Exposure	Various mAs	Various mAs	Various mAs	Various mAs
Gainmap	No gainmap	No gainmap	No gainmap	No gainmap

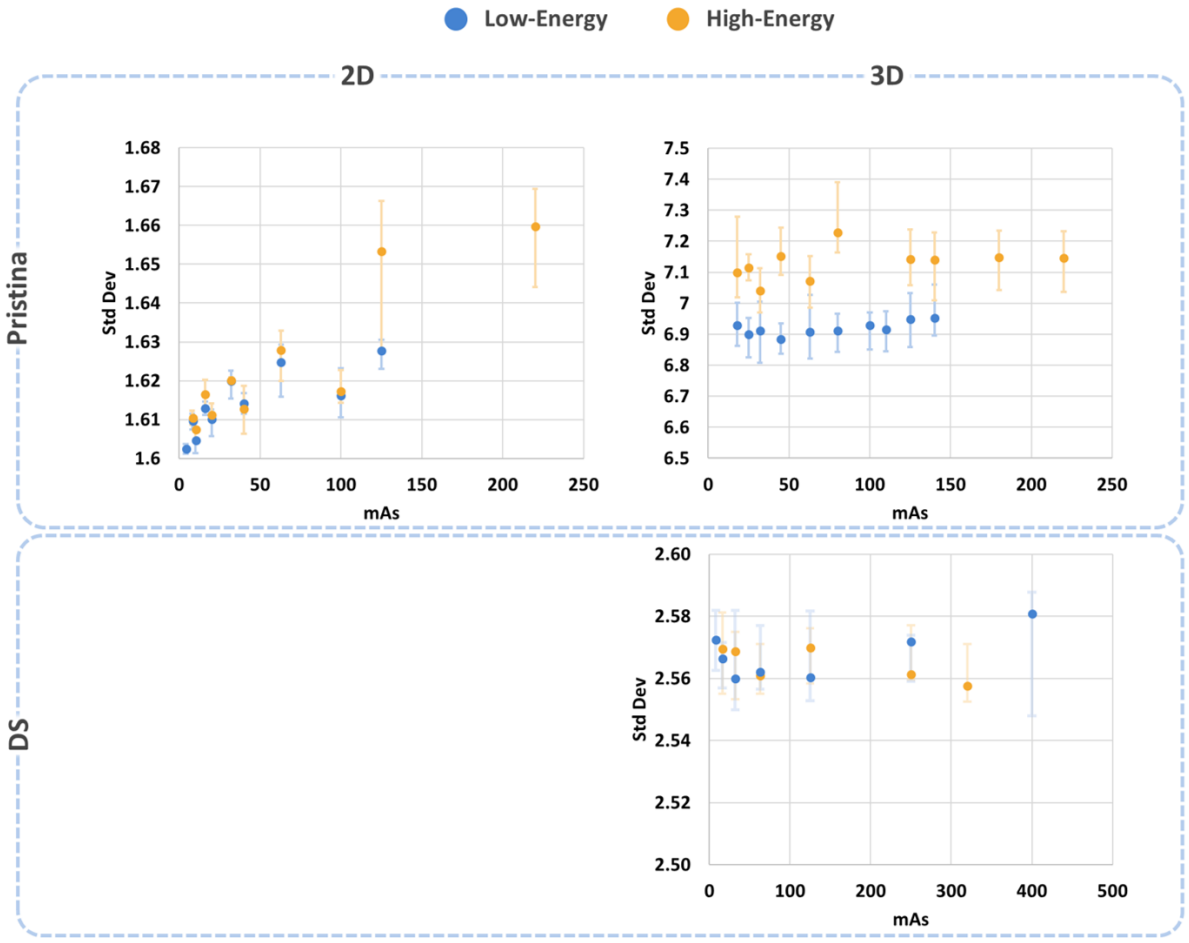

Figure 2.25: Average values of the standard deviation after correction, $\sigma_{offset_{corrected}}$, for five low- and high-energy 2D and 3D acquisitions for Senographe Pristina and Senographe DS systems. Error bars show the minimum and maximum measured values found for each series.

the whiteness and Gaussianity of our experimental acquisitions. On the one hand, we show in Figure 2.26 that the Normalized Noise Power Spectrum (NNPS) of two experimental acquisitions is considerably flat over all the spatial frequency band of interest, illustrating the whiteness of the electronic noise. On the other hand, Gaussianity is more difficult to prove. Experimental measures are polluted by quantization noise (i.e. a uniform distibution). The mild variance of electronic noise is similar to the variance of this quantization noise, preventing us from using a statistical test to prove the Gaussianity of our final results. To overcome this issue, and prove the validity of our results, we compare the distribution of our simulations to the real distribution found in experimental images.

Several measures were proposed to compare distributions (see e.g. [219, 236, 283]). Here, the validation of the electronic noise distribution was performed using the Earth Moving Distance (EMD) [255]. This measure can be used to compute the distance between two probability distributions or, as in our case, two histograms, providing a value of the effort needed to transform one of the histograms to match the other. Formulating this problem as a transportation problem, we formalize our two histograms as the signature $H = \{(\boldsymbol{n_1}, h_{\boldsymbol{n_1}}), ..., (\boldsymbol{n_p}, h_{\boldsymbol{n_p}})\}$ containing p bins with $h_{\boldsymbol{n_i}} \geq 0$, $\forall i \in \{1...p\}$, the signature $K = \{(\boldsymbol{m_1}, k_{\boldsymbol{m_1}}), ..., (\boldsymbol{m_q}, k_{\boldsymbol{m_q}})\}$ containing q

Table 2.12: Estimated standard deviation of the electronic noise, σ_{elec}, for different exposures, modalitites, energies and systems.

mAs	Senographe Pristina				Senographe DS	
	2D		3D		3D	
	LE	***HE***	***LE***	***HE***	***LE***	***HE***
4	1.09					
8	1.10	1.10			2.02	
10	1.10	1.10				
16	1.10	1.11			2.02	2.02
18			4.76	4.88		
20	1.10	1.10				
25			4.74	4.90		
32	1.11	1.11	4.75	4.84	2.01	2.02
40	1.10	1.10				
45			4.73	4.92		
63	1.11	1.11	4.75	4.86	2.01	2.01
80			4.75	4.98		
100	1.11	1.11	4.76			
110			4.75			
125	1.11	1.13	4.78	4.92	2.01	2.02
140			4.78	4.91		
180				4.92		
220		1.13		4.92		
250					2.02	2.01
320						2.01
400					2.03	
Average	1.10	1.11	4.75	4.91	2.02	2.02

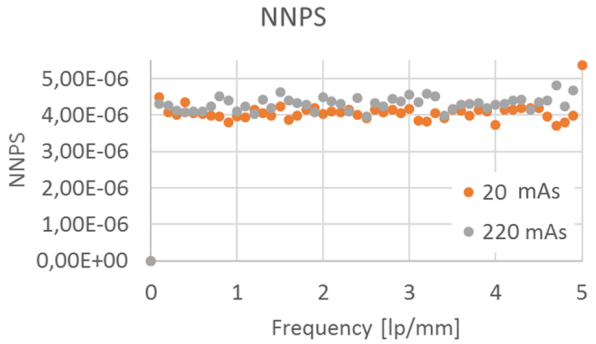

Figure 2.26: Normalized NPS of two experimental acquisitions using a low-energy spectrum in Senographe Pristina for two extreme expositions: 20 and 220 mAs.

bins with $k_{\boldsymbol{m_j}} \geq 0$, $\forall j \in \{1...q\}$, and we represent the distance between the bins $\boldsymbol{n_i}$ and $\boldsymbol{m_j}$ as d_{ij}. Knowing this, we compute the flow f_{ij} between bins $\boldsymbol{n_i}$ and $\boldsymbol{m_j}$ that minimizes the overall

cost $\sum_{i=1}^{p}\sum_{j=1}^{q} d_{ij} fij$, subject to the following constraints:

$$f_{ij} \geq 0 \quad , \ 1 \leq i \leq p, 1 \leq j \leq q \tag{2.41}$$

$$\sum_{j=1}^{q} f_{ij} \leq h_{\boldsymbol{n_i}} \ , \ 1 \leq i \leq p \tag{2.42}$$

$$\sum_{i=1}^{p} f_{ij} \leq k_{\boldsymbol{m_j}} \ , \ 1 \leq j \leq q \tag{2.43}$$

$$\sum_{i=1}^{p}\sum_{j=1}^{q} f_{ij} = \min\left(\sum_{i=1}^{p} h_{\boldsymbol{n_i}}, \sum_{j=1}^{q} k_{\boldsymbol{m_j}}\right) \tag{2.44}$$

Once we have computed all the flow elements f_{ij}, the EMD is defined as:

$$EMD(H,K) = \frac{\sum_{i=1}^{p}\sum_{j=1}^{q} d_{ij} fij}{\sum_{i=1}^{p}\sum_{j=1}^{q} fij} \tag{2.45}$$

In our case, we used the EMD to compare the intensity histograms of simulated and experimentally acquired images with the set-up shown in Figure 2.24a. However, the EMD presented in Equation 2.45 is not bounded. To provide a suitable error measure and quantify the percent error between the experimental distribution and the one of our simulations, we propose a normalized EMD, comparing the distance between two histograms to the maximum possible distance:

$$EMD_{norm}(H,K) = \frac{EMD(H,K)}{\max_{H',K'}(EMD(H',K'))} \tag{2.46}$$

When the histograms are normalized, i.e. $\sum_{i=1}^{p} h_{\boldsymbol{n_i}} = \sum_{j=1}^{q} k_{\boldsymbol{m_j}} = 1$, sharing the same bins $\boldsymbol{n_i} = \boldsymbol{m_i}$, $\forall i \in \{1...p = q = N\}$, and we use the norm L_1 for the distance d_{ij}, the EMD is equal to the match distance [270], which corresponds to the distance between the cumulative distributions:

$$EMD(H,K) = \sum_{s=1}^{N}\left|\sum_{g=1}^{s}\left(h_{\boldsymbol{n_g}} - k_{\boldsymbol{m_g}}\right)\right| \tag{2.47}$$

Considering the hypothesis above, we know that:

$$\max_{k\in\{1...N\}}\left|\sum_{g=1}^{s}\left(h_1[k] - h_2[k]\right)\right| = \begin{cases} 1, & \text{for } 1 \leq s \leq N-1 \\ 0, & \text{for } s = N \end{cases} \tag{2.48}$$

and, consequently:

$$EMD(H,K) \leq N - 1 \tag{2.49}$$

In the particular case when:

$$h_{\boldsymbol{n_i}} = \begin{cases} 1, & if\ i = 1 \\ 0, & otherwise \end{cases} \tag{2.50}$$

$$k_{\boldsymbol{m_j}} = \begin{cases} 1, & if\ j = N \\ 0, & otherwise \end{cases} \tag{2.51}$$

we obtain the bound of the EMD established in Equation 2.49, and consequently:

$$\max_{H',K'}(EMD(H',K')) = N-1 \tag{2.52}$$

Considering this, our normalized measure is expressed as follows:

$$EMD_{norm}(H,K) = \frac{\sum_{s=1}^{N}\left|\sum_{g=1}^{s}\left(h_{\boldsymbol{n_g}} - k_{\boldsymbol{m_g}}\right)\right|}{N-1} \tag{2.53}$$

In Figure 2.27 we show the normalized histograms for the simulated images after fitting the parameter σ_{elec} of our model. Each histogram is compared to its corresponding real acquisition. In Table 2.13 we present the value of the normalized EMD for each pair of these histograms. The visual similarity between histograms is confirmed by the mild value of the normalized EMD, inferior to 0.9% for all cases. In addition, the maximum value of the normalized EMD between different acquired sequences is bigger than the normalized EMD between a simulation and its corresponding acquisition (values between brackets in Table 2.13). Therefore, we considered that the hypotheses introduced in our electronic noise model are acceptable.

2.3.3 Quantum noise

In mammography, the generated X-ray photons, as well as their quantum interactions in their path to the detector pixels, produce several random processes: number of photons leaving the tube, number of photons passing through the object without being affected, number of photons captured by the detector, and number of light photons generated per captured X-ray photon [187, 195]. All these stages introduce unpredictability, as the final number of photons that actually participate in image formation can change between acquisitions. This random signal is what we call quantum noise.

The analytic quantum noise statistics have been extensively studied in CSA literature [62, 211, 248]. However, as introduced in Section 1.2.1, this analysis is incompatible with the synthetic generation of images where the projected object is non-homogeneous (i.e. the signal in the image is non-stationary). Otherwise, two different approaches have been introduced to include quantum noise in "noise-free" images. Both approaches fit the statistics of real mammography images:

- SNR fitting: these approaches adapt the mean and variance of the simulated images to deliver the same SNR as acquired images. Young et al. [307] simulated quantum noise by sampling the value of each pixel from a Gaussian distribution with a specific mean and variance adapted to the parameters of the detector. Similarly, Gong et al. [108] and Milioni [208] included the quantum noise into their simulations using a scaled Poisson distribution, modifying the mean pixel value and variance of the simulated noise to fit those characteristics of acquired images.

- NPS fitting: even if the previous approaches can replicate the mean variance of a real acquisition system, random gain and scattering processes of the X-ray chain introduce noise correlation. The ultimate consequence of this is that the variance becomes frequency dependent. Bath et al. [14] proposed a method for radiographic images, where images composed uniquely of white noise are filtered in frequency domain to be adapted to the acquired NPS. This same method was used for mammography images by Mackenzie et

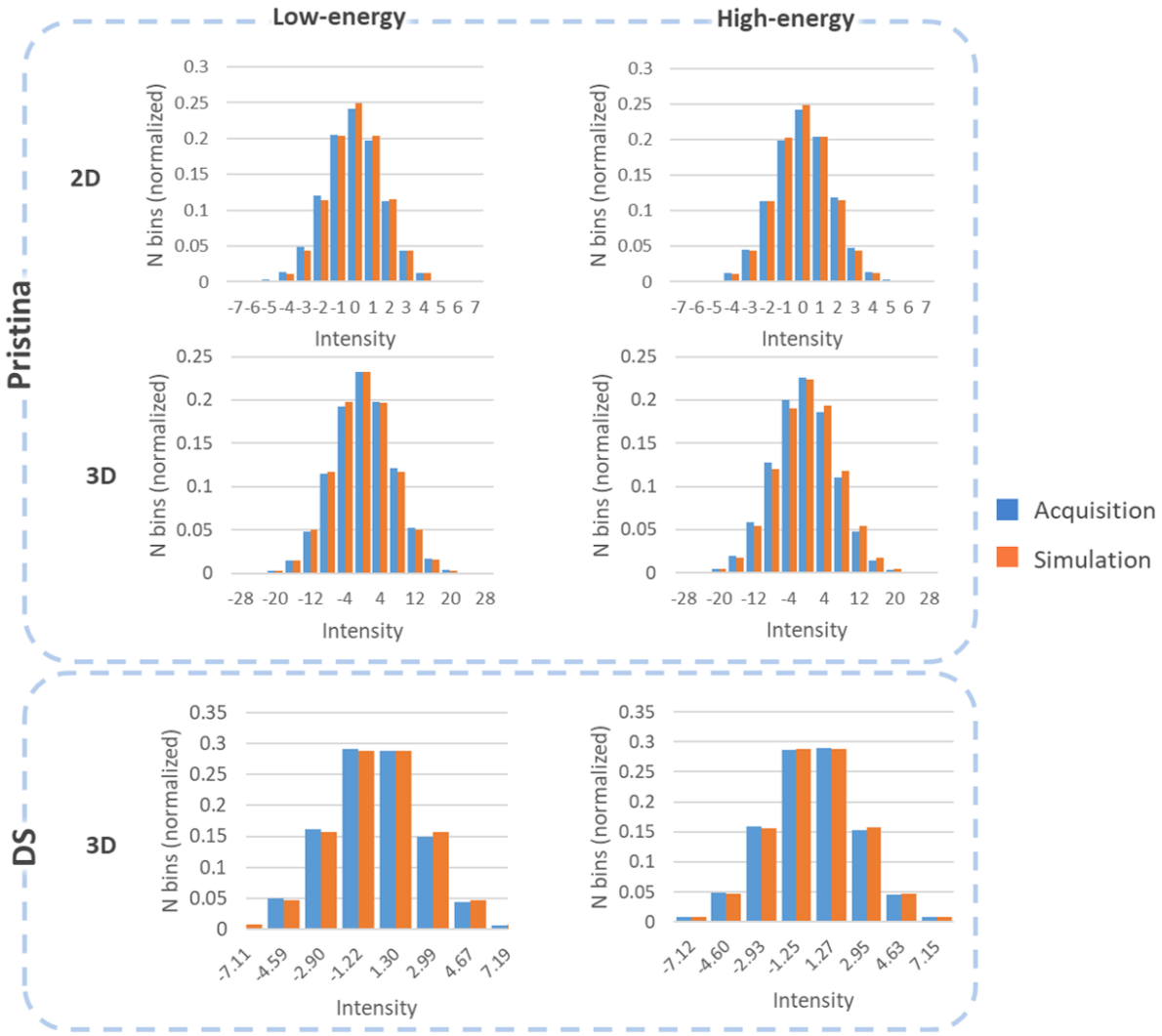

Figure 2.27: Comparison between histograms of acquired and simulated images without X-ray exposure. The EMD values for each pair of histograms is presented in Table 2.13.

Table 2.13: Normalized EMD between the histograms of acquired and simulated images of electronic noise, for different systems, spectra and modalities. Maximal normalized EMD between acquired series is also included between brackets for each combination of parameters.

Energy	**Senographe Pristina**		**Senographe DS**
	2D	**3D**	**3D**
Low-Energy	0.003 (0.005)	0.003 (0.008)	0.004 (0.053)
High-Energy	0.002 (0.002)	0.008 (0.010)	0.005 (0.040)

al. [192, 193]. In their work, they improved the method of Bath et al. [14] considering the rest of contributing sources to the total noise represented in the NPS (i.e. electronic, quantum, and structure noise).

In this work, we want to adjust the SNR of our simulated images to the SNR measured in acquired images. To accomplish this, we propose a simple parametrization of a Poisson process,

similar to the approaches of Gong et al. [108] and Milioni [208], which can be easily used to calibrate our simulation platform to the noise level of a specific mammography system.

Model

X-rays are composed of discrete photons. The probability of emitting k photons at the output of the X-ray tube during a definite amount of time follows a Poisson density function ($X \sim \mathcal{P}(\lambda)$):

$$Pr(X = k) = \frac{e^{-\lambda}\lambda^k}{k!} \tag{2.54}$$

where k is the number of occurrences of the event, and $\lambda = \Lambda \cdot T$ is the average number of events Λ per observation interval T.

Later on, some of these X-ray photons are absorbed by the objects they traverse in their path to the detector. Then, they turn into luminescent photons in the scintillator. The number of luminescent photons created depends on the scintillation efficiency. These consecutive stages, impacting the final number of electrons participating in the image formation, can be approximated by using several sampling processes modeled by a Binomial distribution with deterministic gain p_i ($Y_i \sim B(n, p_i)$):

$$Pr(Y_i = k \mid X = n) = \binom{n}{k} \frac{n!}{n!(n-k)!} p_i^k (1-p_i)^{n-k} \tag{2.55}$$

with p_i the probability of success of the i-th sampling stage, n the number of total events, and k the number of successful elements, in our case, the photons which survived the sampling process.

Considering the random X-ray photon generation and only one sampling stage (i.e. $i = 1$), we can establish through the law of total probability that:

$$\begin{aligned} Pr(Y_1 = k) &= \sum_{x=k}^{\infty} P(Y_1 = k \mid X = x) P(X = x) = \sum_{x=k}^{\infty} \binom{x}{k} \frac{x!}{k!(x-k)!} p_1^k (1-p_1)^{x-k} \frac{\lambda^x e^{-\lambda}}{x!} \\ &= \frac{p_1^k e^{-\lambda}}{k!} \sum_{x=k}^{\infty} \frac{1}{(x-k)!} (1-p_1)^{x-k} \lambda^x = \frac{(p_1\lambda)^k e^{-\lambda}}{k!} \sum_{x=k}^{\infty} \frac{(\lambda(1-p_1))^{x-k}}{(x-k)!} \end{aligned} \tag{2.56}$$

Applying the change of variable $s = x - k$ we get:

$$Pr(Y_1 = k) = \frac{(p_1\lambda)^k e^{-\lambda}}{k!} \sum_{s=0}^{\infty} \frac{(\lambda(1-p_1))^s}{s!} = \frac{(p_1\lambda)^k e^{-\lambda p_1}}{k!} \tag{2.57}$$

Therefore, the number of photons arriving at the detector also follows a Poisson distribution with characteristic parameter λ^T:

$$\lambda^T = \lambda \cdot \prod_{k=1}^{N} p_i \tag{2.58}$$

where N is the total number of sampling stages. Consequently, the final image $I_{L,H}$ acquired for a mono-energetic spectrum can be expressed as:

$$I_{L,H} = M \cdot Y_N + \varepsilon + u \tag{2.59}$$

where $I_{L,H}$ is the final digital low- or high-energy image, M the known total electronic gain, $Y_N \sim \mathcal{P}(\lambda^T)$ the random number of generated electrons, $\varepsilon \sim \mathcal{N}(0, \sigma_{elec}^2)$ the electronic noise

introduced in Section 2.3.2, and $u \sim \mathcal{U}(0, a)$ the quantization noise presented in Section 2.3.1. These two additional noise sources are uncorrelated to the quantum noise.

Let us consider the simulation platform. We presented in Equation 1.1 the average number of X-ray photons after traversing the imaged object. The average number of visible photons arriving at the detector can be computed including the efficiency of the scintillator. Instead of modeling each sampling stage as a Binomial distribution, we can use Equation 2.58 to model the parameter λ^T of the final image Y_N as follows:

$$\lambda^T = I_0 \cdot \prod_{k=1}^{n_{mat}} \left(e^{-\mu_k t_k}\right) \cdot \left(1 - e^{-\mu_{CsI} t_{CsI}}\right) \tag{2.60}$$

where μ_{CsI} and t_{CsI} are the linear attenuation coefficient and thickness of the CsI composing the scintillator.

In this dissertation, we want to obtain simulated images with the same mean and variance per pixel as those of experimentally acquired images for a given mammography system. This is defined by:

$$\begin{cases} \mathbb{E}\left\{I_{L,H}^{simu}\right\} = \mathbb{E}\left\{I_{L,H}^{acq}\right\} = \mu_{L,H}^{acq} \\ Var\left\{I_{L,H}^{simu}\right\} = Var\left\{I_{L,H}^{acq}\right\} = \left(\sigma_{L,H}^{acq}\right)^2 \end{cases} \tag{2.61}$$

where $I_{L,H}^{acq}$ is the low- or high-energy experimentally acquired pixel values and $I_{L,H}^{simu}$ is the low- or high-energy simulated pixel values.

The photon flux of our simulated X-ray chain is not adapted to the tube yield of a given mammography system. Moreover, the model presented in Equation 2.59 do not include additional quantum interactions such as the Swank noise [284] or the random generation of K fluorescent X-rays [63]. These other processes may modify the measured variance in experimental acquisitions. Therefore, to accomplish the equivalences presented in Equation 2.61, we introduce two empirical factors, K and G, with the only purpose of adjusting the mean pixel value and variance of our model to the experimental measures. These factors are included in Equation 2.59 for the simulated image as follows:

$$I_{L,H}^{simu} = M \cdot \frac{G}{K} \cdot Y_N^K + \varepsilon + u \tag{2.62}$$

where $Y_N^K \sim \mathcal{P}(K \cdot \lambda)$. Consequently, we can obtain the value of G and K from experimental acquisitions using Equation 2.61:

$$\begin{cases} \mu_{L,H}^{acq} = M \cdot G \cdot \lambda + \frac{a}{2} \\ \left(\sigma_{L,H}^{acq}\right)^2 = M^2 \cdot G^2 \cdot \frac{\lambda}{K} + \sigma_{elec}^2 + \frac{a^2}{12} \end{cases} \tag{2.63}$$

We introduce the following parameters:

$$\begin{cases} \mu_{L,H}^{acq_q} = \mu_{L,H}^{acq} - \frac{a}{2} \\ SNR_{L,H}^{acq_q} = \frac{\mu_{L,H}^{acq_q}}{\sqrt{\left(\sigma_{L,H}^{acq}\right)^2 - \sigma_{elec}^2 - \frac{a^2}{12}}} \end{cases} \tag{2.64}$$

where $\mu_{L,H}^{acq_q}$ and $SNR_{L,H}^{acq_q}$ are the experimental mean pixel value and SNR, respectively, before quantization and electronic noise addition. We can then compute each factor as:

$$\begin{cases} G = \frac{\mu_{L,H}^{acq_q}}{M \cdot \lambda} = \frac{\mu_{L,H}^{acq_q}}{\mu_{L,H}^{simu_q}} \\ K = \sqrt{\lambda} \cdot SNR_{L,H}^{acq_q} = \frac{SNR_{L,H}^{acq_q}}{SNR_{L,H}^{simu_q}} \end{cases} \tag{2.65}$$

where $\mu_{L,H}^{simu_q}$ and $SNR_{L,H}^{simu_q}$ are, respectively, the mean and SNR of the simulated pixel values without K and G correction and other additional noise sources (i.e. without electronic and quantization noise). Consequently, the mean value of the new distribution is only dependent on factor G, while the SNR of the simulated pixel values depends only on factor K.

Acquisitions and simulations

First of all, the quantum noise depends on several factors impacting X-ray energy fluence: material and thickness of imaged object, mAs and spectra used for the acquisition, as well as the acquisition system itself. Therefore, our G and K parameters may also depend on all these factors, and must be considered to fit our model.

Secondly, to obtain the parameters G and K, we must characterize the first and second order moments of the pixel value distribution. Instead of estimating these moments from several measures on a single pixel, we consider that the properties of the statistical distribution among the different pixels composing an image are the same. In other words, we consider that the statistic of the arriving quantum photons is identical within a specific ROI when traversing a uniform phantom.

Considering all this, our purpose is to measure the mean signal intensity and standard deviation of acquired images to validate and fit our model for the quantum noise. Consequently, two different set-ups were proposed.

The first of them was conceived to *validate* the hypothesis about the nature of the quantum noise made in the previous section. This is the purpose of the set-up illustrated in Figure 2.28a. In this set-up, several uniform plates of different materials are stacked one on top of the other so we can acquire an image for each combination of material and thickness. The materials used in the set-up are characterized by their equivalent content of glandular tissue. In other words, each phantom is made of a material with a linear attenuation coefficient equivalent to the same thickness of breast tissue with a certain glandular percentage. To this end, we use $1cm$ CIRS BR0 (0% glandular), CIRS BR30 (30% glandular), CIRS BR50 (50% glandular) and CIRS BR70 (70% glandular) plates, stacked in thicknesses from 1 to $5cm$. To consider also the influence of different X-ray exposures, we performed our experiment for several mAs levels and two spectra. In Table 2.14 we show the operational point for the acquisitions and simulations performed. This set-up was only performed on a Senographe Pristina system using the 2D mode.

Our second set-up was used to fit the parameters K and G of our model for a standard acquisition case which we could use from this point forward. The set-up was similar to the one already shown in Figure 2.28a, with the difference that we only placed a $5cm$ plate of CIRS BR50. This set-up was used for both systems (Senographe Pristina and Senographe DS) and acquisition modes (2D and 3D). The operational points for the Senographe Pristina and Senographe DS systems are respectively presented in Tables 2.15 and 2.16.

Validation

From our first set-up we obtained a total of 100 paired measures of the signal intensity and standard deviation in acquired and simulated images for both considered spectra. Then, each pair was used to fit a particular K and G couple. All cases were simulated again with the adapted quantum noise parameters. The difference between the quantum noise statistics before and after fitting the parameters K and G is illustrated in Figure 2.29.

As we observe, after setting the parameters G and K the distribution of the SNR and signal intensity is almost identical for the acquired and the simulated images. As we show in Table 2.17, the mean errors between acquisitions and simulations mean and SNR are less than 1%. This

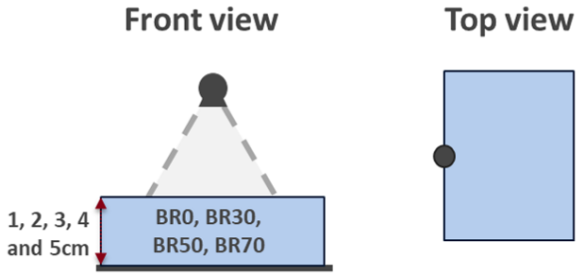

(a) Set-up used for simulations and real acquisitions to adapt the magnitude of the quantum noise in simulations. This procedure was identical for the tomography and standard 2D acquisition modes in the Senographe Pristina system. To calibrate the parameters K and G of the Senographe DS system we only used a $5cm$ PMMA phantom covering completely the detector.

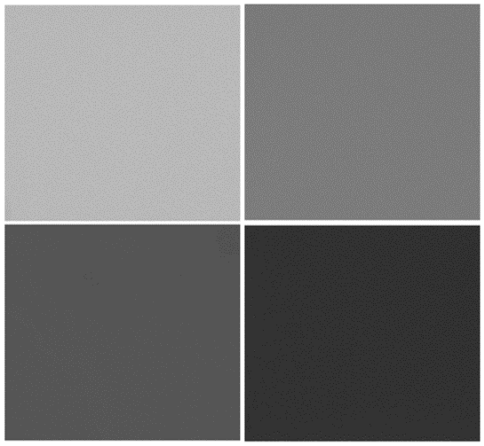

(b) Example of low-energy, $36mAs$, $3cm$ Senographe Pristina acquired images. Top left: BR0. Top right: BR30. Bottom left: BR50. Bottom right: BR70.

Figure 2.28: Procedure to validate the implementation of the quantum noise.

Table 2.14: Operational point used for the validation of the quantum noise model using a **Senographe Pristina** system.

	LE		**HE**	
	Real	*Simulated*	*Real*	*Simulated*
Spectrum	34kVp	23keV (monoenergetic)	49kVp	34keV (monoenergetic)
Target/Filter	Rh/Ag	Rh/Ag	Rh/Cu	Rh/Cu
Exposure	8, 16, 32, 45, 71 mAs	8, 16, 32, 45, 71 mAs	20, 32, 45, 71, 90 mAs	20, 32, 45, 71, 90 mAs
Gainmap	$2mm$ Al	$50mm$ PMMA	$2mm$ Al	$50mm$ PMMA

percentage is smaller than the mean and SNR variance found for real images acquired with the same set-up (same spectrum, phantom, and mAs level).

Also, it is easy to validate the appropriateness of our Poisson model for the quantum noise in the X-ray chain. If we plot the signal intensity of each acquisition and simulation against its variance (Figure 2.30), we find the expected linear relation matching the proposed model in Equation 2.59.

Table 2.15: Operational point used to fit the parameters K and G of our quantum noise model using a **Senographe Pristina** system. The exposure values were divided by the number of low- and high-energy expositions in the 3D mode.

	LE		**HE**	
	Real	*Simulated*	*Real*	*Simulated*
Spectrum	34kVp	23keV (monoenergetic)	49kVp	34keV (monoenergetic)
Target/Filter	Rh/Ag	Rh/Ag	Rh/Cu	Rh/Cu
Exposure	36mAs	36mAs	110mAs	110mAs
Gainmap	$2mm$ Al	$50mm$ PMMA	$2mm$ Al	$50mm$ PMMA

Table 2.16: Operational point used to fit the parameters K and G of our quantum noise model using a **Senographe DS** system. The exposure values were divided by the number of low- and high-energy expositions.

	LE		**HE**	
	Real	*Simulated*	*Real*	*Simulated*
Spectrum	28kVp	20keV (monoenergetic)	49kVp	39keV (monoenergetic)
Target/Filter	Mo/Mo	Mo/Mo	Rh/Cu	Rh/Cu
Exposure	110 mAs	110 mAs	320 mAs	320 mAs
Gainmap	50mm PMMA	50mm PMMA	50mm PMMA	50mm PMMA

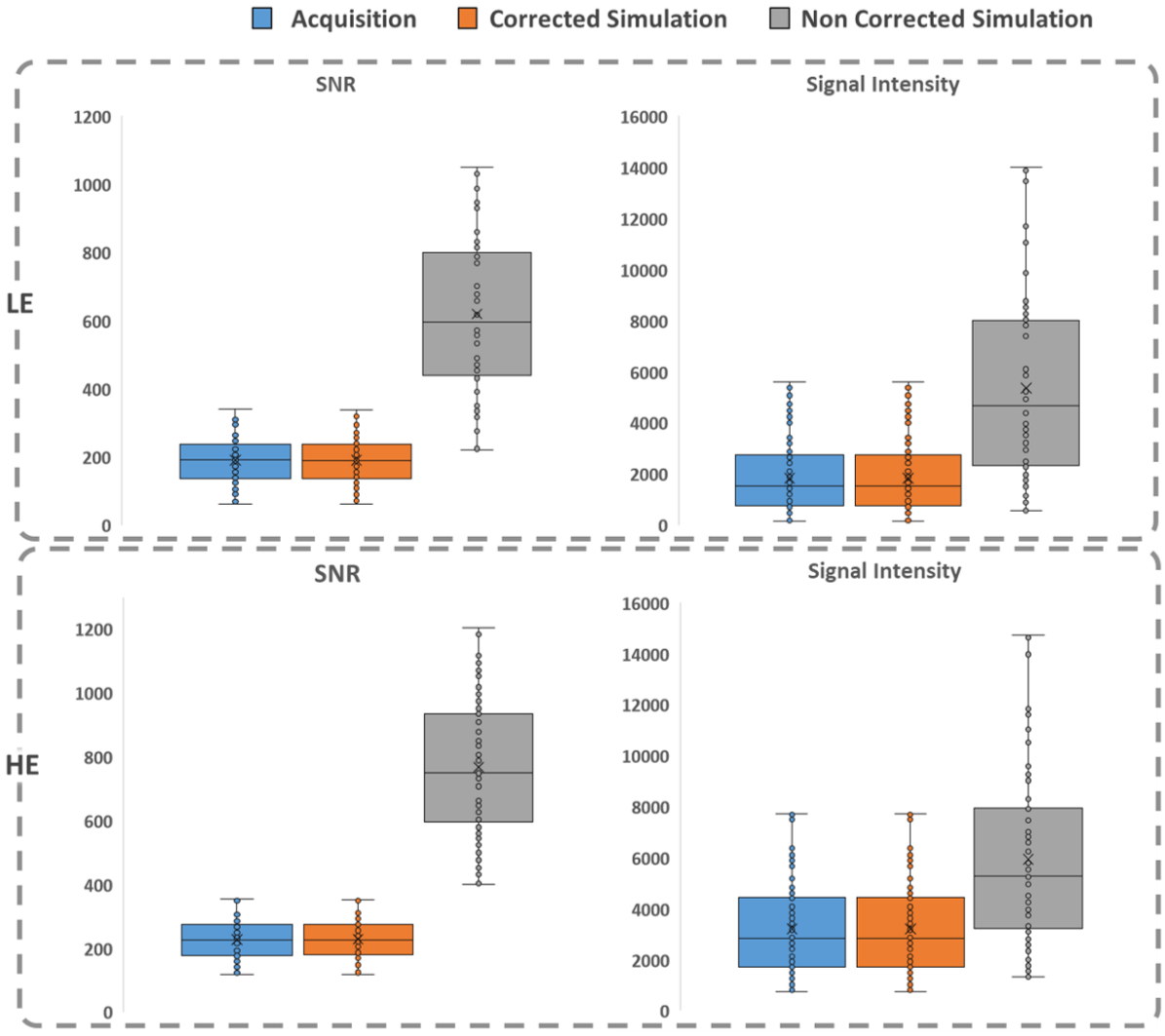

Figure 2.29: Comparison of the signal intensity and SNR between the acquired and simulated images before and after fitting the parameters K and G. For each collection of images we present the lower and upper extremes, the lower and upper quartiles, the median as an horizontal line and the average value as a cross.

From our second set-up, we found the values of K and G of a unique particular acquisition. The results are illustrated in Figure 2.31. In this case, we also found an estimation error smaller than 1% for all configurations (Table 2.18).

Table 2.17: Estimation error after image correction to adapt the quantum noise statistic.

	LE	HE
SI	$0.04\% \pm 0.05$	$0.01\% \pm 0.01$
SNR	$0.61\% \pm 0.5$	$0.71\% \pm 0.5$

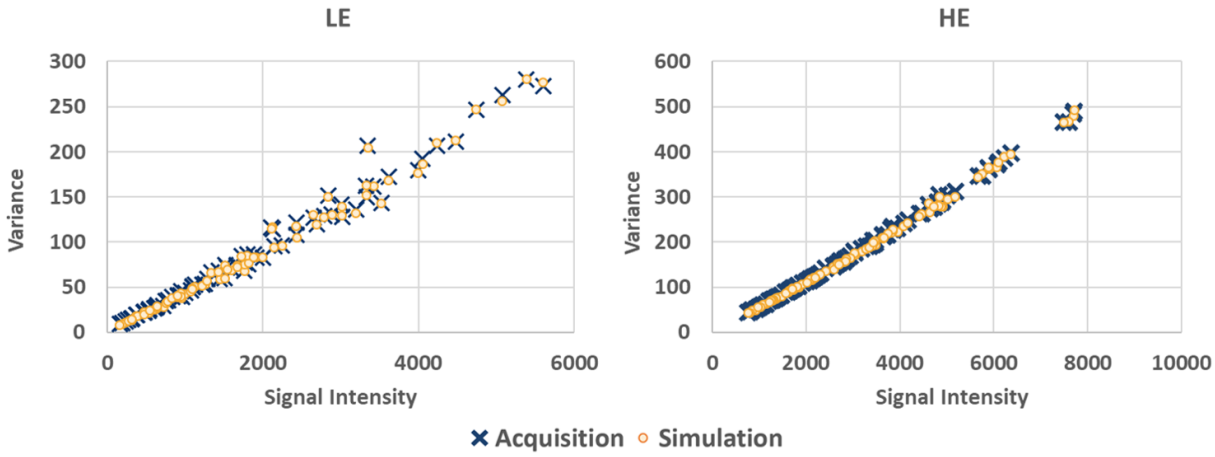

Figure 2.30: Signal intensity vs variance plot for each pair of acquired and simulated images considering all the factors presented in the set-up of Figure 2.28a and Table 2.14.

2.4 Memory processes in a X-ray system

When the acquisition sequence requires successive X-ray projections, or "frames", of an object from multiple views, as it is the case in tomosynthesis, a residual signal from previous incident radiations remains in the subsequent frames [273, 282, 298]. This memory (or lag) effect has three known sources:

- Scintillator afterglow: some of the X-ray photons arriving at the scintillator are not immediately leading to visible light. Instead, luminescent photons are emitted even after the scintillator excitation by X-ray photons is cut-off. This emission of optical photons follows an exponential decay of typically 1 to 10 milliseconds approximatively.

- Charge trapping: defects in detector material bulk and surface introduce energy states known as "traps". Electrons are retained in these energy states and are released over time. The amount of charges kept in trap states depends on trap density, illumination intensity, and current state of traps. The escape of electrons is exponential and depends on the trap energy at each instant. This is the main contributor to the lag effect.

- Charge transfer: charge readout is performed through a RC classical circuit, following an exponential discharge of the accumulated energy during acquisition. If the reading time is smaller than the RC constant, the transistor keeps an offset state before the next frame. This effect is typically small because integration time is greater than RC constant, and charge-integrating amplifiers are used in the readout (instead of voltage-integrators).

As shown by Carton et al. [41], this residual signal may have a big impact on iodine estimation in CEDBT slices when the acquisition sequence interleaves low- and high-energy images.

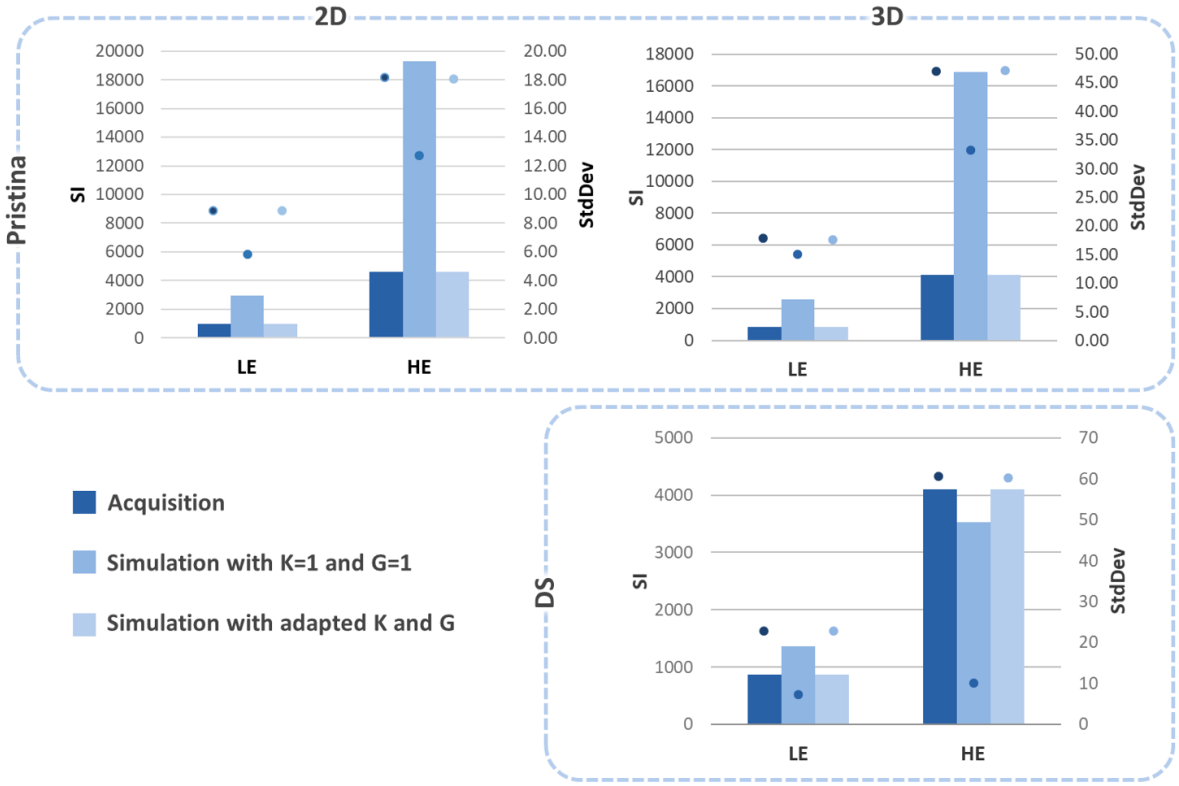

Figure 2.31: Values of the signal intensity and standard deviation before and after adjusting the value of the parameters K and G. The signal intensity of the acquired and simulated images, with and without adapted K and G parameters, is represented by bars with different shades of blue. Their standard deviation is represented by the dots (over the bars).

Table 2.18: Estimation error after image correction for a standard acquisition case.

	Senographe Pristina 2D		**Senographe Pristina 3D**		**Senographe DS 3D**	
	LE	***HE***	***LE***	***HE***	***LE***	***HE***
SI	0.14%	0.14%	0.13%	0.32%	0.01%	0.04%
SNR	0.25%	0.57%	0.88%	0.10%	0.12%	0.41%

The first model to simulate the lag effect in cone-beam computed tomography (CBCT) was introduced by Siewerdsen and Jaffray [273]. In their work, they considered the lag process as a discrete linear time-invariant (LTI) system where the output signal depends on the previous and current states of the input multiplied by the impulse response of the system, introducing a memory effect. This idea was also adopted by Hsieh et al. [129] to model the detector decay characteristics in CT. In their work, they propose a continuous LTI where the impulse response of the system is modeled by a multi-exponential function. This same idea was also used by Yang et al. [305] and Starman et al. [280]. Both works used the multi-exponential function presented by Hsieh et al. to fit the response of the detector at different frames and compute the coefficients of the impulse response of a discrete LTI.

The modalities investigated in this dissertation are considerably far from the time constraints of the methods proposed above (e.g., 15 frames per second in the publication presented by

Starman et al. [280]). Consequently, we are not interested in a continuous function modeling the time response of the detector. Instead, we will present a LTI system based on the same concepts, but using a series of experimental discrete coefficients. This stage will be only applied to 3D acquisition sequences.

2.4.1 Modeling the lag in CEDBT sequences

In our model we consider that the charge trapping effect only depends on previous illuminations of the detector and is independent of the current projection. Therefore, each subsequent projection depends on the image without lag plus all the previous images without lag. We define the lag process as a following Finite-duration Impulse Response (FIR) LTI system, leading to:

$$y[n] = \begin{cases} x[n] + \sum_{k=1}^{n-1} \alpha[k] \cdot x[n-k] & , \; if \; n > 1 \\ x[1] & , \; if \; n = 1 \end{cases} \tag{2.66}$$

where $n \in \{1...N\}$ is the frame number of the sequence and N is the total number of acquisitions of the sequence, $y[n]$ is the frame n with the lag already included, $\alpha[k]$ the lag coefficients of our impulse response, and $x[n]$ the frame n without lag.

We consider now that all the acquisitions without lag are the same $x[i] = x[j] \; \forall (i,j) \in \{1...N\}$. This is true, for example, when we acquire several frames of the same phantom at the same position and geometry and using the same acquisition parameter. In this particular case, the lag coefficients can be estimated from acquisitions as:

$$\hat{\alpha}[n-1] = \frac{y[n] - y[n-1]}{x[1]} \tag{2.67}$$

However, the residual signal due to the lag effect is independent of the electronic noise and the quantization. Therefore, Equation 2.67 produces a biased estimator $\hat{\alpha}[n]$. To compute an unbiased estimator, we need to consider three error sources included in our measure: quantum noise, electronic noise, and quantization error. These effects are added to our acquisitions as follows:

$$y[n] = \Gamma(x[n]) + \sum_{k=1}^{n-1} \alpha[k] \cdot \Gamma(x[n-k]) + \varepsilon + u \tag{2.68}$$

where $x[n] \sim \mathcal{P}(\lambda_n)$ represents the X-ray field of the frame n, $\varepsilon \sim \mathcal{N}(0, \sigma^2_{elec})$ the electronic noise introduced in Section 2.3.2, $u \sim \mathcal{U}(0,a)$ the quantization noise presented in Section 2.3.1, and $\Gamma(x)$ is a linear operator. Consequently, u, ε and $x[n]$ being mutually independent, and $\mathbb{E}\{x[i]\} = \mathbb{E}\{x[j]\} = \lambda$, $\forall (i,j) \in \{1...N\}$, our biased estimator is equal to:

$$\begin{aligned} &\hat{\alpha}[n-1] \\ &= \frac{\mathbb{E}\left\{\Gamma(x[n]) + \sum_{k=1}^{n-1} \alpha[k]\Gamma(x[n-k]) + \varepsilon + u\right\} - \mathbb{E}\left\{\Gamma(x[n-1]) + \sum_{k=1}^{n-2} \alpha[k]\Gamma(x[n-1-k]) + \varepsilon + u\right\}}{\mathbb{E}\{\Gamma(x[1]) + \varepsilon + u\}} \\ &= \frac{\Gamma(\lambda) + \sum_{k=1}^{n-1} \alpha[k]\Gamma(\lambda) + \frac{a}{2} - \Gamma(\lambda) - \sum_{k=1}^{n-2} \alpha[k]\Gamma(\lambda) - \frac{a}{2}}{\Gamma(\lambda) + \frac{a}{2}} = \frac{\alpha[n-1]\Gamma(\lambda)}{\Gamma(\lambda) + \frac{a}{2}} = \frac{\alpha[n-1]}{1 + \frac{a/2}{\Gamma(\lambda)}} \end{aligned} \tag{2.69}$$

where $\hat{\alpha}[n-1]$ is the biased estimator of the lag coefficients which does not consider the error sources, and $\alpha[n-1]$ is the unbiased estimator which considers the random processes of the

X-ray acquisition chain. We can observe that the electronic noise does not affect the estimation of the lag coefficients. Consequently, we can estimate the lag coefficients from experimental acquisitions as:

$$\alpha[n-1] = \left(1 + \frac{a/2}{\Gamma(\lambda)}\right) \cdot \frac{\mathbb{E}\{y[n]\} - \mathbb{E}\{y[n-1]\}}{\Gamma(\lambda)} \tag{2.70}$$

In CEDBT acquisition sequences, low- and high-energy acquisitions are interleaved. A low-energy acquisition is followed by a high-energy acquisition until all the frames have been acquired. This means that low-energy acquisitions x_{LE} correspond to odd frames $n = 1, 3, 5...$ and high-energy acquisitions x_{HE} correspond to even frames $n = 2, 4, 6....$ Once we have estimated the lag coefficients $\alpha_{LE}[n]$ and $\alpha_{HE}[n]$ for each energy using Equation 2.70, our final model for low-energy images is:

$$y_{LE}[n] = \begin{cases} x_{LE}[n] + \sum_{k=1}^{n-1} y^L[k] & , \; if \; n > 1 \\ x_{LE}[1] & , \; if \; n = 1 \end{cases} \tag{2.71}$$

where n is odd and

$$y^L[k] = \begin{cases} \alpha_{LE}[k] \cdot x_{LE}[n-k] & , \; if \; k \; is \; even \\ \alpha_{HE}[k] \cdot x_{HE}[n-k] & , \; if \; k \; is \; odd \end{cases} \tag{2.72}$$

While the final model for high-energy images is:

$$y_{HE}[n] = x_{HE}[n] + \sum_{k=1}^{n-1} y^H[k] \tag{2.73}$$

where n is even and

$$y^H[k] = \begin{cases} \alpha_{LE}[k] \cdot x_{LE}[n-k] & , \; if \; k \; is \; odd \\ \alpha_{HE}[k] \cdot x_{HE}[n-k] & , \; if \; k \; is \; even \end{cases} \tag{2.74}$$

According to this model we only need to find the values of $\alpha_{LE}[n]$ and $\alpha_{HE}[n]$ to adapt the characteristic memory process of the acquisition sequence. Therefore, to adapt and validate our model, we proceed in two steps. First, we provide the necessary elements to find the individual values of $\alpha_{LE}[n]$ and $\alpha_{HE}[n]$ for the low- and high-energy projections using Equation 2.70 (see Section 2.4.2). These memory terms are included in our simulation platform using the model described in Equations 2.71 and 2.73. Secondly, we validate our model by comparing the average signal measured in simulations to the average signal measured in acquired images (see Section 2.4.3).

Additionally, the analysis of the lag is closely related to the performance of the detector included in our system. In the following sections, we need to be cautious of the operational point used in the acquisitions. The detector of a mammography system has a defined dynamic, with minimum and maximum values tolerated by the detector. The detector saturation percentage S measures the level of the signal detected compared to the limitations of the detector. It is measured as:

$$S[n] = \frac{y[n] - SI_{min}}{SI_{max} - SI_{min}} \cdot 100 \tag{2.75}$$

where $y[n]$ is the signal detected, and SI_{min} and SI_{max} are respectively the minimum and the maximum signals endured by the detector. We have experimentally observed that the magnitude of the image lag depends on the saturation of the detector. This is illustrated with an example in Figure 2.32. As we can observe, for the same uniform phantom, the same geometry and the same spectrum, we obtain higher memory terms when we expose the detector with a higher signal (a higher mAs applied in the tube), and the detector is more saturated.

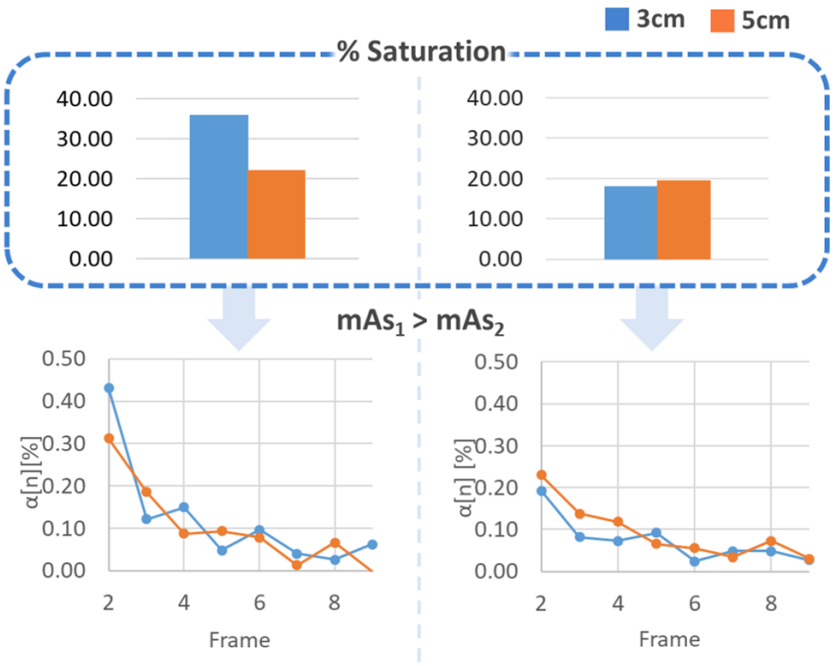

Figure 2.32: Example of the influence of saturation percentage on lag coefficients. 30 and 50mm thick BR50 plates were exposed with two different mAs values for the same high-energy spectrum on a Senographe Pristina system.

2.4.2 Experimental assessment of the lag

As established in Equation 2.70, the lag coefficients can be estimated using three different values: a which is the known quantization step of the quantization ramp, $\Gamma(\lambda)$ which is the average signal when there is no lag and $\mathbb{E}\{y[n]\}$ which is the output average signal with lag. In Figure 2.33 we illustrate the set-up used to retrieve all these measures and estimate the values of $\alpha_{LE}[n]$ and $\alpha_{HE}[n]$.

This set-up consists of a static 3D sequence including only LE and of only HE projections for CIRS BR0 (0% glandular) and CIRS BR50 (50% glandular) of three thicknesses: 30, 50 and 80mm. The images acquired with this set-up provide the necessary values presented in Equation 2.70: n is the ordered number of each frame, $\Gamma(\lambda)$ is the average value of the first frame which is not impacted by any lag effect (in our static set-up, all images without lag are the same), and $y[n]$ are the subsequent frames affected by the lag effect. To test the stability of the estimated lag coefficients, three independent static 3D sequences for each system and plate thicknesses were acquired. As we have shown in Section 2.4.1, we may appreciate higher lag coefficients for higher saturation percentage levels. However, in this study, we do not have modeled this dependency. Instead, to respect standard saturation percentage levels, the operational point for each acquisition was chosen according to the automatic exposure values assigned in the Senographe Pristina and Senographe DS systems, presented in Tables 2.19 and 2.20, respectively.

The results of the estimated lag coefficients for Senographe Pristina (Figure 2.34a) and Senographe DS (Figure 2.34b), and their corresponding saturation levels, are presented in Figure 2.34. We observe that the lag coefficients for Senographe DS are much higher than in Senographe Pristina. Furthermore, the lag coefficients for low-energy acquisitions in Senographe Pristina fluctuate around zero. This may be due to the negligible effect of lag over other effects,

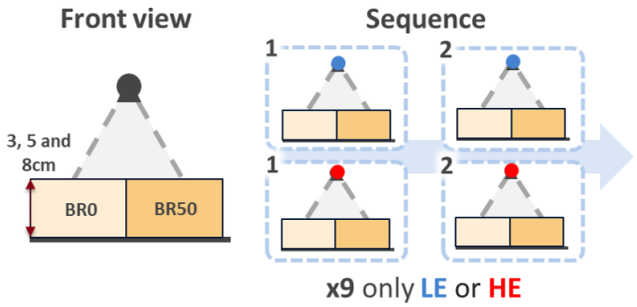

Figure 2.33: Set-up used to retrieve the estimated values of $\alpha_{LE}[n]$ and $\alpha_{HE}[n]$. We acquired 9 consecutive low- and high-energy projections in two independent sequences.

Table 2.19: Operational point used for lag fitting and validation using a **Senographe Pristina** system. The exposure values were divided by the number of low- and high-energy expositions in the 3D mode.

	LE		**HE**	
	Real	*Simulated*	*Real*	*Simulated*
Spectrum	26 (3cm) and 34 (5 and 8cm) kVp	23keV (monoenergetic)	49kVp	34keV (monoenergetic)
Target/Filter	Mo/Mo (3cm) and Rh/Ag (5 and 8cm)	Mo/Mo (3cm) and Rh/Ag (5 and 8cm)	Rh/Cu	Rh/Cu
Exposure	110 (3 and 5cm) and 250 (8cm) mAs	110 (3 and 5cm) and 250 (8cm) mAs	110mAs	110mAs
Gainmap	50mm PMMA	50mm PMMA	50mm PMMA	50mm PMMA

as standard variability between acquisitions. We also observed some extreme deviation in the high-energy acquisitions of the Senographe DS, illustrated by the error bars. This may be due to some instabilities in the X-ray tube and they are not a consequence of the lag. In any case, for our implementation, we have used the average lag coefficients from the three independent acquisitions. We have excluded from this average the extreme deviations and negative lag values, as they do not have any physical meaning.

The impact of higher memory terms on the acquired images is illustrated in Figure 2.35. As we can observe, in an acquisition sequence where low- and high-energy exposures are interleaved, the average signal of low-energy images in the Senographe DS is highly increased from the first

Table 2.20: Operational point used for lag fitting and validation using a **Senographe DS** system. The exposure values were divided by the number of low- and high-energy expositions.

	LE		**HE**	
	Real	*Simulated*	*Real*	*Simulated*
Spectrum	22 (3cm), 28 (5cm) and 32 (8cm) kVp	20keV (monoenergetic)	49kVp	39keV (monoenergetic)
Target/Filter	Mo/Mo (3 and 5cm) and Mo/Rh (8cm)	Mo/Mo (3 and 5cm) and Mo/Rh (8cm)	Rh/Cu	Rh/Cu
Exposure	110 (3 and 5cm) and 250 (8cm) mAs	110 (3 and 5cm) and 250 (8cm) mAs	320 mAs	320 mAs
Gainmap	50mm PMMA	50mm PMMA	50mm PMMA	50mm PMMA

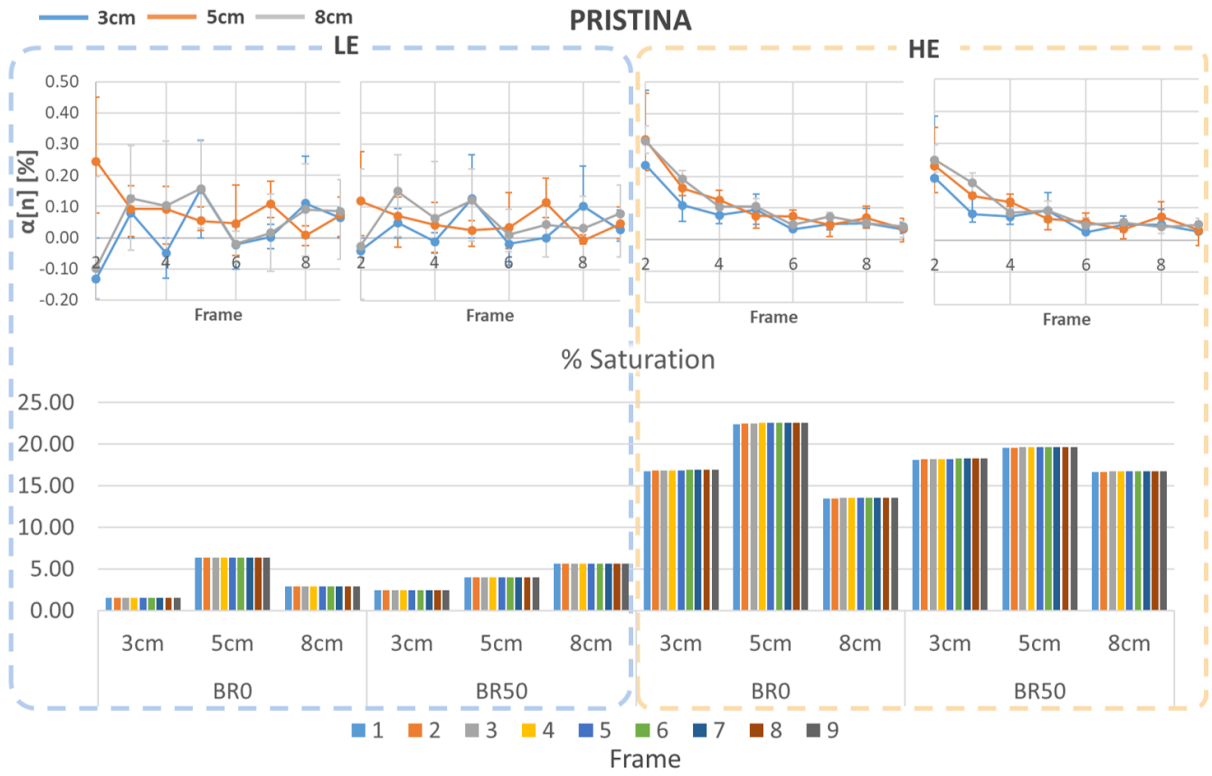

(a) Senographe Pristina lag coefficients.

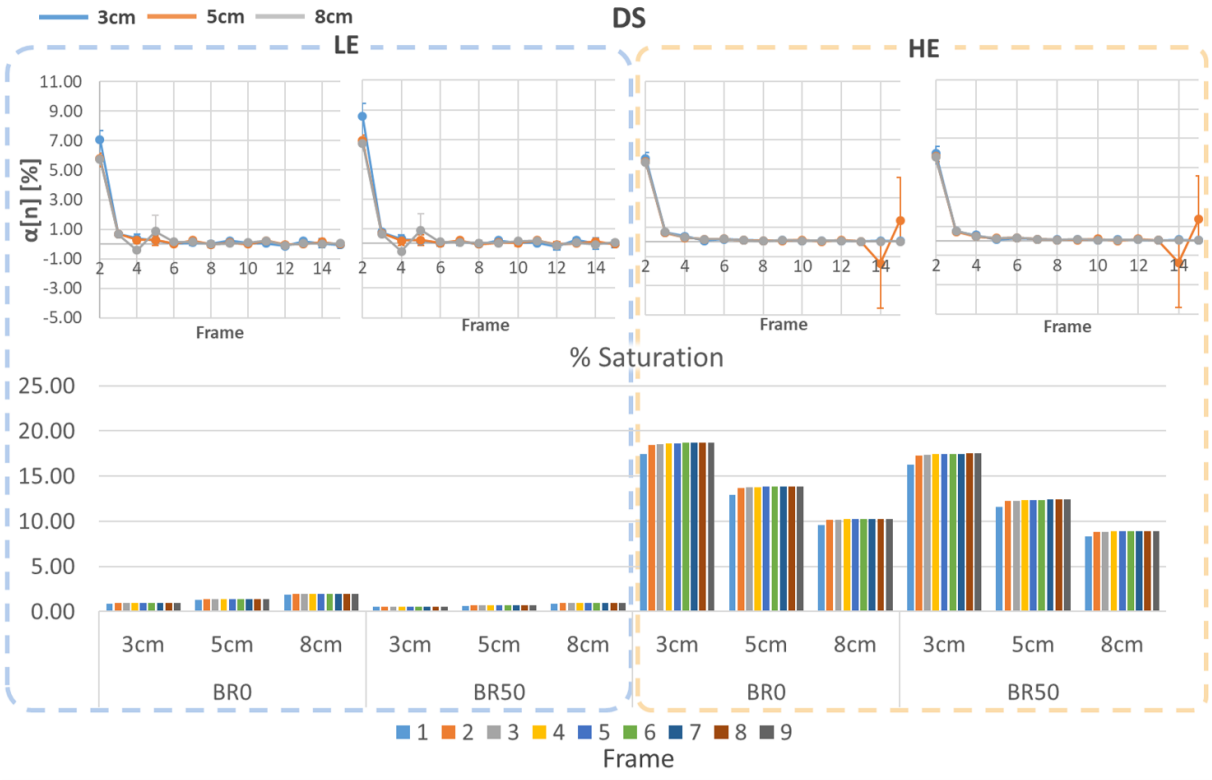

(b) DS lag coefficients.

Figure 2.34: Average lag coefficients computed from three independent acquisitions for Senographe Pristina and Senographe DS systems. Error bars show the maximum and minimum lag coefficients.

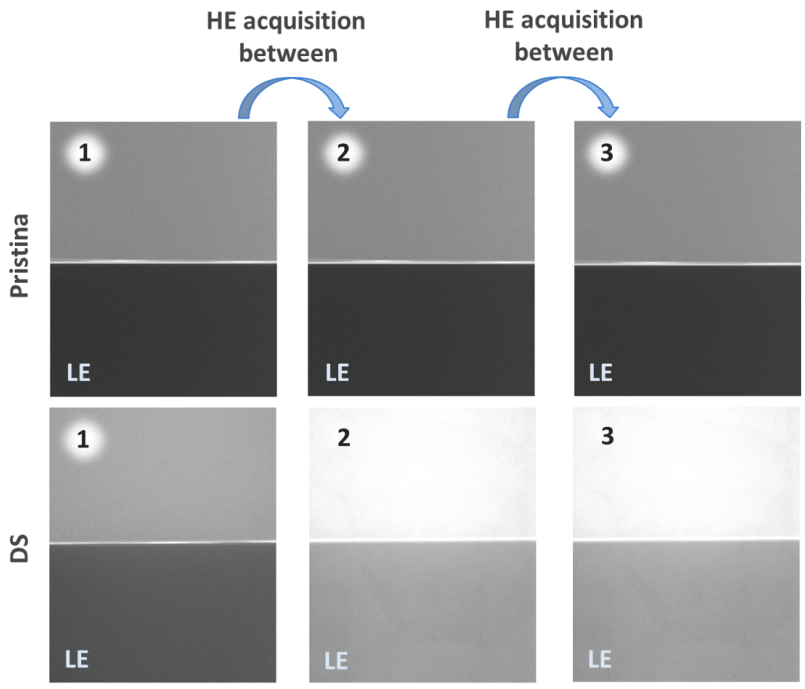

Figure 2.35: Example of the impact that lag has on low-energy images acquired in Senographe Pristina and Senographe DS systems. The set of images represented here correspond to the $5cm$ BR50 and BR0 plates. To illustrate the visual impact, the same windowing was applied to all images.

to the second frame, after the first high-energy image is acquired. This effect is less visible in Senographe Pristina acquisitions due to smaller memory terms in the more recent detector technology embedded in this mammography system.

2.4.3 Validation of the lag model

Once we have retrieved the lag coefficients $\alpha_{LE}[n]$ and $\alpha_{HE}[n]$, we can include them in our simulation platform following the model proposed in Equation 2.71 and 2.73 and generate interleaved simulated images. We need to validate that the average signal intensity of these interleaved simulations corresponds to experimental acquisitions of the CEDBT sequence.

In Figure 2.36, we illustrate the set-up used to validate the simulated images. The same set-up is used to retrieve the experimental acquisitions and the simulated images. The main difference between this set-up and the one described in Section 2.4.2 (Figure 2.33) is that low- and high-energy projections were interleaved during the acquisition sequence. In other words, we used a similar sequence to the one used in real CEDBT, where a low-energy exposure is followed by a high-energy one, until all projections are acquired. Three independent static 3D sequences for each system were acquired. We projected two uniform $50mm$ thick plates: CIRS BR0 (0% glandular) and CIRS BR50 (50% glandular). As the statistical properties of our simulations are controlled (the average signal is always the same), we only simulated one series per system and plate composition. Finally, the operational points presented in Tables 2.19 and 2.20 for experimental acquisitions and simulations were used.

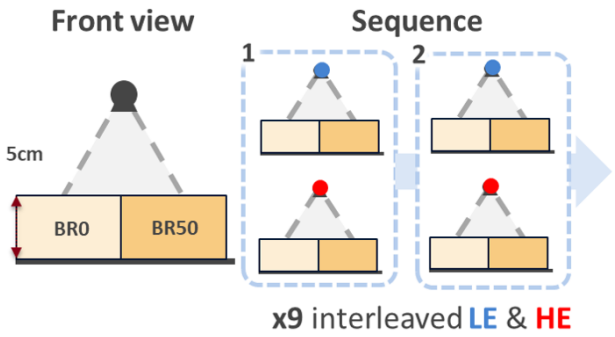

Figure 2.36: Set-up used to validate our memory model. We acquired 9 consecutive interleaved low- and high-energy projections.

The results of the validation are presented in Figure 2.37. Our goal is that the estimated values made by our model (the average signal of the simulated images) are always between the minimum and maximum average signal intensities measured in our three experimental series. This requirement is almost achieved for all the Senographe Pristina simulations. We only found an overestimation of the signal intensity equal to one in the case of low-energy acquisitions of the CIRS BR50 plate. In the case of the Senographe DS, our model does not offer the same precision. In Table 2.21 we extend these results, presenting the percentage errors between the simulated images using our lag model and the average of the three series acquired for each system and plate composition. For Pristina simulations, we found an error smaller than 0.32% for all the images, while the error for DS simulations is higher, attaining 2%.

These results show the limitations of our lag model. Several error sources need to be considered. First, we only evaluated three experimental series of images to estimate the values of $\alpha_{LE}[n]$ and $\alpha_{HE}[n]$, and, therefore, we may have not considered the complete variability of the lag coefficients. Secondly, our model considers that the lag effect behaves as a FIR LTI system where the output of previous frames (images with lag) does not impact the output of the current frame. However, this could not be true when the lag coefficients are high enough. We showed that the saturation of the detector can modify the value of the lag coefficients, so when the system is impacted by a substantial memory process, the saturation increases with each image with lag and, therefore, each previous frame. This is the case, for example, of the Senographe DS. Finally, we considered that the charge trapping effect as the main contributor of the lag effect and our model does not introduce any correlation with the scintillator afterglow or the charge transfer effects, which may cause other additional interactions over time.

2.5 Other simulated elements: focal spot size and shape, heel effect

We call focal spot the illuminated area of the anode surface receiving the electron beam from the cathode. This area, where the electrons strike the anode, have a specific size and shape, which is determined by the dimensions of the filament tungsten coil, the construction of the focusing cup, and the position of the filament in the focusing cup. The size of the focal spot in mammography, the modality of our interest, varies typically from 0.3 mm to 0.6 mm. The

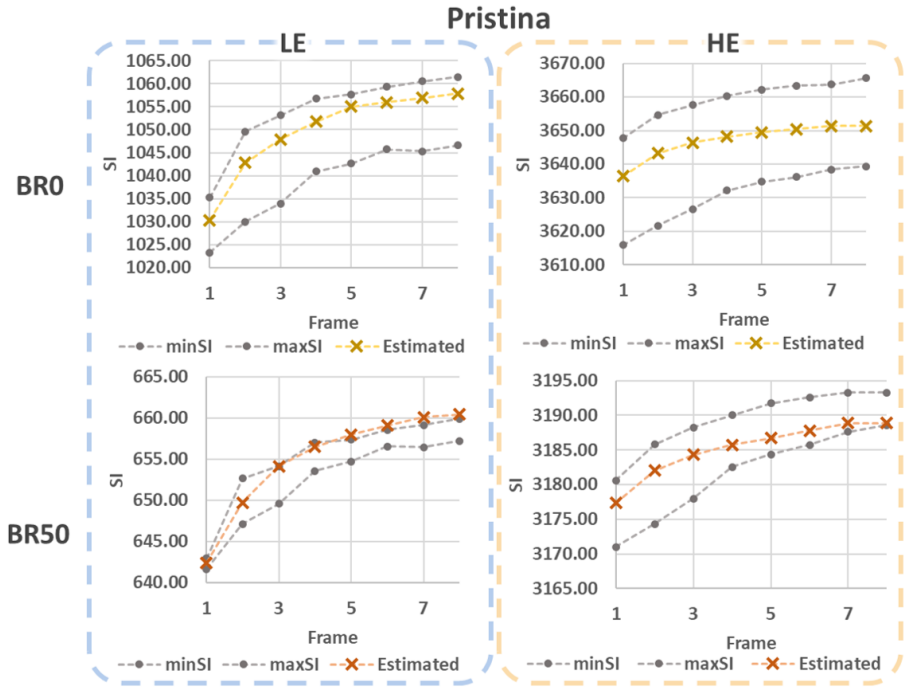

(a) Minimum and maximum signal intensities measured in our experimental series (50mm thick uniform BR0 and BR50 plate) using a Senographe Pristina compared to the estimation made by our lag model.

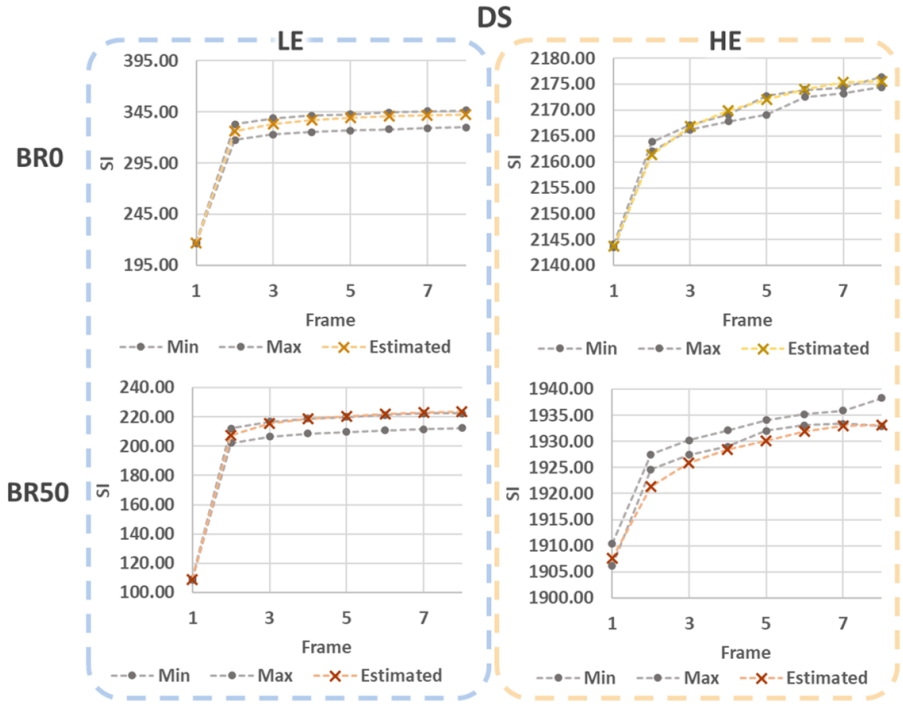

(b) Minimum and maximum signal intensities measured in our experimental series (50mm thick uniform BR0 and BR50 plate) using a Senographe DS compared to the estimation made by our lag model.

Figure 2.37: Estimation of low- and high-energy interleaved pairs using our lag model.

focal spot blur has been shown to impact the total system degradation [161, 257, 260]. In our simulation platform, we consider a finite, uniform focal spot with square size of 0.3×0.3mm.

Table 2.21: Percentage errors between the simulated images using our lag model and the average of the three series acquired for each system and plate composition.

	Pristina		**DS**	
Frame	**BR0**	**BR50**	**BR0**	**BR50**
1 (LE)	0	0	0	0
2 (HE)	0	0	0	0
3 (LE)	0	0.09	0.06	0.59
4 (HE)	0.02	0.01	0.08	0.22
5 (LE)	0.22	0.29	0.36	1.07
6 (HE)	0.01	0.01	0.01	0.13
7 (LE)	0.15	0.15	0.76	1.62
8 (HE)	0.05	0.05	0.06	0.08
9 (LE)	0.23	0.26	1.00	1.83
10 (HE)	0.09	0.07	0.04	0.13
11 (LE)	0.15	0.24	0.96	1.82
12 (HE)	0.09	0.06	0.04	0.10
13 (LE)	0.16	0.32	1.02	1.98
14 (HE)	0.12	0.07	0.07	0.06
15 (LE)	0.16	0.29	1.03	1.99
16 (HE)	0.17	0.14	0.02	0.08

The origin of the Heel effect is also originating from the tube anode, but it has a different nature. Part of the energy lost at the deceleration of electrons penetrating the anode is transformed in electromagnetic radiation (X-rays). As the penetration depth is different for each of the electrons arriving to the anode, the path of the X-ray photons inside the anode will be also different, so the final energy of the signal at the tube output will depend on the angle parallel and perpendicular to the chest-wall, introducing a low-frequency non-uniformity in the radiation received by the detector. As for our study we will use centered ROIs of a certain size smaller to the influence of this effect, we will not consider this element in our simulation platform, and, consequently, it has not been modeled.

2.6 Conclusion

We introduced in Section 1.2.1 of Chapter 1 several approaches to simulate an X-ray chain, with a special interest on the simulation of the mammography chain. Additionally, in Section 1.3.2 of the same chapter, we looked deeper into the elements composing an analytic X-ray simulator. However, we found that none of these approaches was capable to reproduce the complete CEDBT sequence required by the goals of this work.

In this chapter, we presented our contributions to the X-ray simulation chain. We adapted it to be capable of simulating realistic low- and high-energy image pairs, accordingly to the characteristics of CESM and CEDBT. To summarize, each of the individual stages described in the sections of this chapter can be combined in a single model for the simulation of low- and high-energy images (Figure 2.38). This final model is described by the following equations:

$$\begin{cases} I_{Final}[n, LE] = & \Gamma(I)[n, LE] + \sum_{k=1}^{n-1} y[k, LE] + \varepsilon + u \\ I_{Final}[n, HE] = & \Gamma(I)[n, HE] + \sum_{k=1}^{n-1} y[k, HE] + \varepsilon + u \end{cases} \tag{2.76}$$

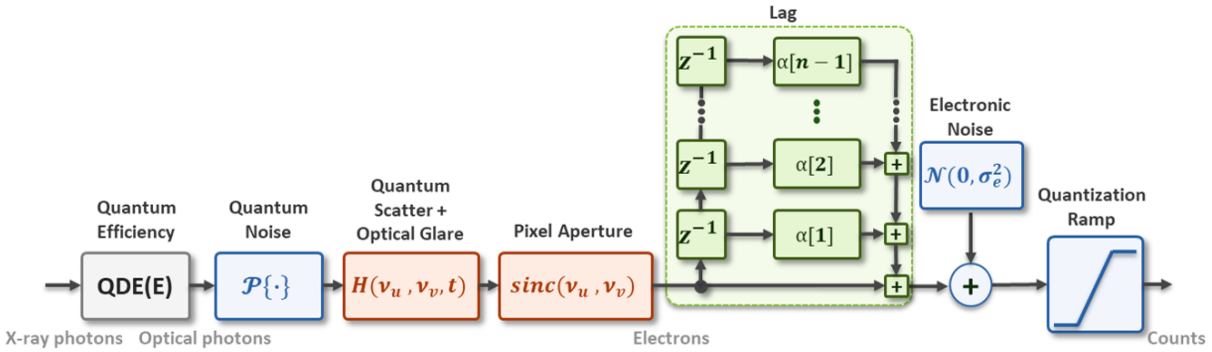

Figure 2.38: Block diagram of the contributions made in this work. In orange, the elements impacting the frequency response. In blue, the elements which consider the stochastic processes of the X-ray acquisition. In green, the memory process.

where

$$\begin{cases} y[k, LE] = \begin{cases} \alpha_{LE}[k] \cdot \Gamma(I)[n-k, LE] & , \; if \; k \; is \; even \\ \alpha_{HE}[k] \cdot \Gamma(I)[n-k, HE] & , \; if \; k \; is \; odd \end{cases} \\ y[k, HE] = \begin{cases} \alpha_{LE}[k] \cdot \Gamma(I)[n-k, LE] & , \; if \; k \; is \; odd \\ \alpha_{HE}[k] \cdot \Gamma(I)[n-k, HE] & , \; if \; k \; is \; even \end{cases} \end{cases} \tag{2.77}$$

and

$$\Gamma(I)[n, E] = G(E) \cdot \mathcal{P}\{K(E) \cdot (T_P(E) + T_S(E) \cdot SPR(t, E)) I_0(E) \cdot e^{-\sum_{i=1}^{n_{mat}} \mu_i(E) t_i}\} * h_T(t, E) * h_{det} \tag{2.78}$$

Our contributions to this model were focused on three axis. First, we provided the same frequency response as a real system, considering the impact of the scattered field for different thicknesses and the size of the detector pixel. Secondly, we included the different stochastic processes of the X-ray acquisition in the simulation chain to deliver an image sharing the same noise sources, same average signal intensity and SNR as an acquired image. Finally, we incorporated a memory term in the simulated acquisition sequence to emulate the lag effect appearing in real acquisitions.

The influence of all these elements is decisive in the detection and the characterization of a lesion. The frequency response of a system determines the visibility of certain characteristics that may be important to describe a specific type of lesion, to the point of missing the whole lesion. The background noise reduces the SNR of the acquired image, thus increasing the probability of missing fine structures belonging to the lesion or the lesion itself. Lastly, the increased signal intensity through the different projections of the acquisition sequence due to the lag may produce an inaccurate recombination of the low- and high-energy acquisitions, introducing false contrast uptakes.

Each of the models included in the simulated chain were adapted using empirical measures from a unique Senographe DS and Senographe Pristina system. The simplicity of the set-ups and validations proposed in this work allow future users to adapt each of the models following a clear workflow.

However, in our formulation, several hypotheses were considered to provide a practical implementation:

- Our thickness dependent scatter model was only validated in one direction, and was considered rotationally invariant. This is usually true in systems which do not incorporate an anti-scatter grid. However, due to the alignment of the grid septa, this is not true in Senographe Pristina, which is operating with an anti-scatter grid for both angio-mammography and angio-tomosynthesis (while Senographe DS does not implement any anti-scatter grid in angio-tomosynthesis mode). Therefore, this model could be further improved including also the thickness dependent MTF in the direction of the grid septa and combining both expressions in an anisotropic scatter kernel.

- Our quantum noise model is based on the known statistics of the photon fluence emitted by the X-ray tube. However, we considered the sampling quantum processes as a unique statistic gain stage defined by a uniform and deterministic gain parameter λ of a Poisson random distribution, while, in real systems, the efficiency of the scintillator is non-uniform and the conversion gain is also random. This last effect is known as Swank noise [284]. Also, other physical phenomena present in the scintillator, such as the random generation of K fluorescent X-rays [63], were not considered in our implementation. The simulation of these processes may be the focus of future research.

- Similarly, we also have a unique scattering stage, modeled by the kernel h_T. In Equation 2.76, we have located this kernel outside the Poisson process. This is not the real order of processes in the X-ray acquisition chain, where scattering and random processes are interleaved [274]. However, as we have decided to separate those processes in unique isolated stages, the kernel must be included after the Poisson distribution, introducing a similar spatial noise correlation to the observed in experimental images. Otherwise, we would obtain a flat Normalized Noise Power Spectrum (NNPS). We illustrate a schematic example of this in Figure 2.39. Therefore, the theoretical NNPS of our model is defined by:

  $$NNPS = |H_T \cdot H_{det}|^2 \tag{2.79}$$

  This is however not true in real X-ray acquisitions due to the effects in the scintillator described above. NPS fitting models, presented in Section 2.3.3, include an additive noise to alleviate this mismatch. We did not use this approach since the current additive noise models are uncorrelated to the local intensity value of the image, while this is not the case in experimental images.

- Another not considered effect is the structure noise. This noise source is associated with several factors, as fluctuations of the detector response over time and different sensitivity or linearity between pixels among others. Consequently, it is a noise source complex to measure and simulate. However, it can be mostly removed using simple gainmap correction.

- As we had discussed in Section 2.4.1, lag depends on detector saturation. This was not consider in our simulations, and it could introduce some bias compared to experimental acquisitions obtained using other acquisition parameters.

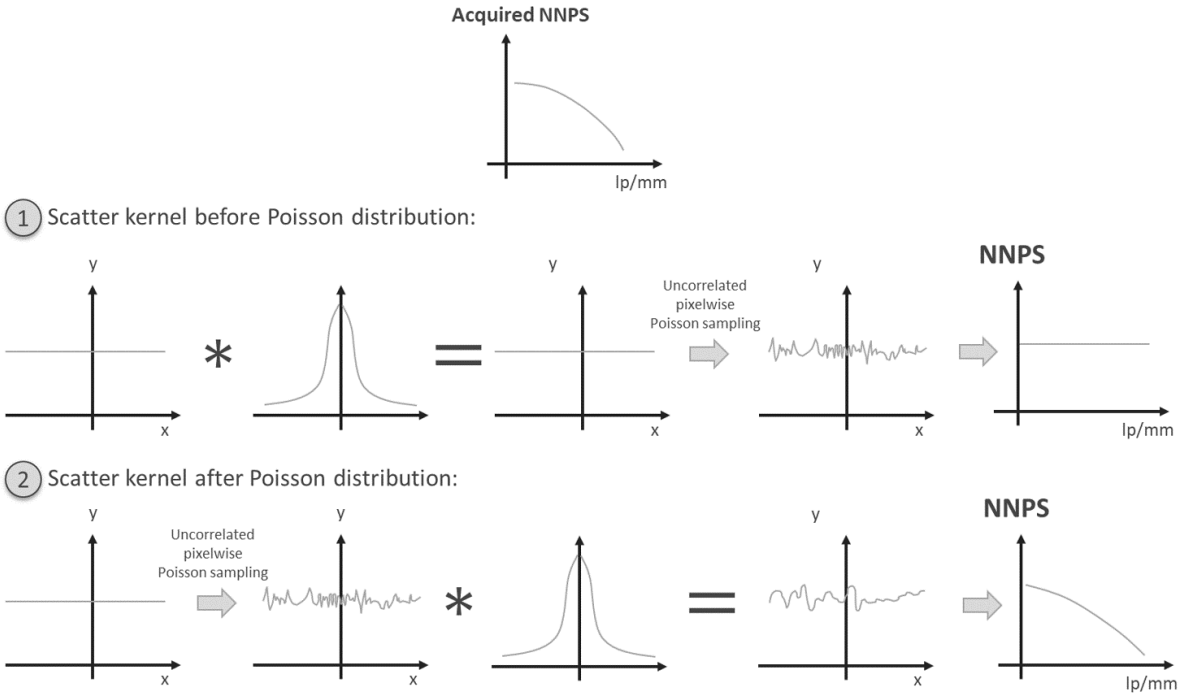

Figure 2.39: Impact of the chain order on the final spectrum of the quantum noise.

Chapter 3

A new modeling of realistic iodine contrast uptakes

In Chapter 2, we have developed several models to improve the realism of an analytical X-ray simulation platform and make it able to replicate the main characteristics of experimentally acquired images. To create images simulating clinical cases, we also need three-dimensional surrogates of clinical structures to be used as input to the X-ray simulation platform. While several virtual and physical models have been proposed for conventional mammography and tomosynthesis, within the scope of Virtual Clinical Trials (VCT) [21, 242, 256] (see Section 1.2.1), this is not the case for clinical contrast uptakes observed in contrast enhanced X-ray breast imaging. Only a limited number of studies used virtual surrogates of clinically relevant structures [77, 122]. The restricted variability of simulated clinical characteristics may impact the results obtained in these studies. One reason behind the absence of virtual models for contrast uptakes in X-ray breast imaging is the lack of a recognized universal lexicon defining the characteristics of the findings observed in such images, as it is the case for mammography. At the same time, as detailed in Section 1.1.4, Breast Parenchymal Enhancement (BPE) is an important effect to be considered in clinical studies for the evaluation of vascular breast X-ray images, due to its impact on lesion detectability and characterization. However, only a few studies have tried to simulate contrast enhanced X-ray images reproducing this effect [38, 123].

In this chapter, we present a review of the different characteristics evaluated in the literature to define contrast uptakes in CESM. Then, we develop a flexible framework to model virtual structures with these typical characteristics and generate surrogates of the findings found in clinical contrast uptakes. Afterwards, we introduce a previously developed anthropomorphic breast texture model. We describe how this texture can be modified so that we can simulate contrast enhanced X-ray images with different levels of BPE. Moreover, we propose a method combining the texture and the lesion models into a single simulated image. Finally, we conclude by discussing the main benefits and limitations of our models and their influence in a VCT study.

3.1 Lesion classification in contrast enhanced X-ray breast imaging

The term "lesion" refers to the general group of abnormal findings which can be found inside the breast by a radiologist during the analysis of an image acquired with any type of breast imaging

technique. This includes any kind of damage in the breast tissue, and any type of abnormality (including mass or non-mass structures). Among all the lesions found in a clinical environment, a tumor is a lesion characterized by a non-controlled inflammation or replication of tissues. The distinction between lesions produced by wounds or diseases, or by tumorous processes, is one of the main goals of clinical radiology. In clinical radiology, each finding is described by a series of visual descriptors, grouped in a lexicon, providing the necessary support to the subsequent lesion categorization and analysis. Therefore, the goal of any imaging technique is to provide a faithful representation of the characteristics defining the lesion.

To evaluate the quality of the images acquired by both CESM and CEDBT techniques, and their clinical benefits, we need to analyze the morphology and appearance of the contrast uptakes found in clinical images. The Breast Imaging Reporting and Data System® (BI-RADS®) initiative, supported by the American College of Radiography, has tried to standardize the reporting practice since 1980. This standardization of the adopted lexicon has two main purposes. On the one hand, it provides an accurate lesion description and characterization of the findings encountered by the radiologists. On the other hand, it improves the communication between different teams simplifying the management of subsequent proceedings. Till today, the ACR BI-RADS® has only included an ensemble of descriptors for findings that can be observed in conventional mammography, Contrast Enhanced Magnetic Resonance Imaging (CE-MRI) and ultrasound [35]. In particular, the CE-MRI BI-RADS® (5th edition, 2013) [76] divides contrast uptakes into three main classes: focus, masses and non-masses.

Focus is the category including all contrast uptakes with a diameter smaller than $5mm$ and, consequently, too small to be further characterized.

Masses is the category embracing the lesions which occupy a specific region in the three-dimensional space with diameter bigger than $5mm$. They can be described by their shape, margins and internal enhancement:

- To describe the ***shape***, a mass can be *round* or *oval*, if its envelope can be interpreted as a unique convex shape, such as a sphere or ellipsoid, respectively. If the global shape of the lesion cannot be properly described by the previous geometric primitives because it is defined by a more concave shape, then it will be described as *irregular*.
- The ***margin*** can be *smooth*, if the external envelope is perfectly sharp, or *irregular* if the edges are uneven or jagged. In the case of perpendicular linear structures surrounding their surface we will be talking of *spiculated* masses.
- The distribution of the ***internal enhancement*** can be either *homogeneous* if the contrast uptake is uniform, *heterogeneous* when some regions of the lesion are more contrasted than others, *rim enhancement* if the lesion crust is more enhanced than its nucleus, or *dark internal septa* if the contrast uptake is divided into several regions by negative contrasted walls.

Non-masses is the category containing the lesions without space-occupying characteristics. Non-masses structures are described by their pattern, enhancement distribution, and symmetry:

- A non-mass enhancement can be classified according to its ***pattern*** as either *focal* when the enhancement is very small and in a confined area, *linear* if it has a curvilinear structure that may not conform to a duct, *segmental* when it has a triangular or conical enhancement with its apex pointing to the nipple, *regional* if the enhancement involves a large volume

of tissue gathered in a specific geographic section of the breast, *multiple regions* when at least two geographic areas are affected by the contrast uptake, or *diffuse* if the contrast uptake is distributed uniformly throughout the breast.

- The ***enhancement distribution*** can be either *homogeneous* if the contrast uptake is enhanced uniformly, *heterogeneous* if it follows a non-uniform random pattern separated by normal enhanced areas, *clumped* when it is described as a cobblestone-like enhancement with occasional confluent areas, or *clustered ring* if the non-mass contrast uptake is constituted by a series of rim-like enhancements grouped in the same region.

- In MRI both breasts are imaged simultaneously. The enhancement ***symmetry*** of non-masses between the two breasts can be assessed, and lesions can be described as *symmetric* or *asymmetric*.

Several studies have used the CE-MRI BI-RADS® descriptors described above to characterize the contrast uptakes found in clinical CESM images and differentiate between malignant and benign breast lesions [19, 78, 90, 91, 143, 160, 254]. These studies conclude that the CE-MRI BI-RADS® lexicon can be applied to describe CESM findings, as discrepancies are uncommon and do not affect the malignancy degree associated with the lesion. However, other publications [77, 117, 150, 210] noticed that the standard CE-MRI BI-RADS® lexicon does not provide the same conclusions for certain observed findings in CESM, such as rim enhancements. Additionally, some of the findings described in the CE-MRI BI-RADS® have never been recognized in CESM images, such as dark internal septa. Because of these differences, several authors proposed some modifications to improve the analysis of CESM images. We can summarize their propositions in the following points:

1. Low-energy projection of CESM images proved to have similar clinical relevance to conventional mammography [166]. Consequently, the lexicon for contrasted mammography should consider the option of a lesion appearing in the low-energy acquisition, without counterpart in the recombined image. This enlarges the catalog of possible findings, including lesions that do not take any contrast after the injection phase.

2. Rim enhancement for mass-like findings and clustered ring for non-mass-like findings can be also found in CESM clinical images, however they have a different behavior. In CE-MRI, they represent an important descriptor to depict cancerous lesions, while in CESM it is considered as a controversial characteristic. This can be explained by the inability to exclude abscess cavities and infected cysts in the recombined radiographic images, increasing the number of wrong diagnoses based on this descriptor.

3. The description of mass-like enhancement margins should be adapted for CESM images, including a new differentiation between distinct, well-delimited lesion edges, and indistinct lesions, if their limits are ill-defined and it is difficult to evaluate the real extent of the mass, reducing the confidence level when measuring the biggest diameter size of this type of lesions.

4. Dark internal septa enhancements as a descriptor for the enhancement distribution of masses was never reported. This can be caused by the projected nature of CESM. The superposition of tissues after projection may hinder this type of findings. Therefore, we have not considered this characteristic in our work.

Table 3.1: Considered descriptors for mass-like and non-mass-like enhancements in contrast enhanced X-ray breast imaging.

Mass		**Non-mass**	
Shape	Round	Distribution	Focal
	Oval		Linear
	Irregular		Segmental
Margin	Circumscribed		Regional
	Indistinct		Multiple Regions
	Spiculated	Enhancement	Diffuse
Enhancement	Homogeneous		Homogeneous
	Heterogeneous		Heterogeneous
	Rim enhancement		Clumped
	No enhancement		Clustered ring
			No enhancement

5. Finally, in CESM each breast is imaged separately, making it impossible to analyze simultaneous localizations of lesions. Instead of characterizing the symmetry of the findings as in CE-MRI, in CESM it is recommended to use a laterality descriptor so a finding can be interpreted as unilateral (if it is present only in one of the breasts) or bilateral (if it is described in both breasts).

To our knowledge, due to the novelty of the technique, there are no publications about the lexicon which could be applied in CEDBT images. However, some publications have found it appropriate to use the CE-MRI BIRADS© to describe the contrast enhancement present in CEDBT clinical images [39, 53, 134]. In this dissertation, we will consider the modifications proposed above for both CESM and CEDBT images.

The descriptors considered for contrast uptake characterization in CESM and CEDBT are summarized in Table 3.1. It is expected that, because of their three dimensional complexity, non-mass enhancements could be better described in CEDBT volumes than in projected CESM images. However, also due to their complexity, they are more difficult to associate to specific, well-defined, structures, which is the case for mass-like enhancements. By contrast, mass-like enhancements are composed by simpler structures which have been well described. Additionally, the work of Dromain [77] provided a large amount of clinical data and information about the specific patterns of this type of contrast uptakes. For these reasons, in this work, we only focus on the assessment of mass-like enhancements through digital surrogates reproducing the features categorized in Table 3.1. Since they describe independent characteristics of the findings, the descriptors of each category can be combined to fully describe the lesion of interest. This leads us to the following problem: only considering mass-like enhancements, the combination of categories guiding the radiologist in the evaluation of new suspicious findings results into 36 different types of contrast uptakes. Consequently, independent models for each combination seems unattainable for the scope of this dissertation. Instead of that, we propose a new model of realistic iodine contrast uptakes which can combine all the features present in CESM images.

3.2 Simulation of mass-like contrast uptakes

As introduced in Section 1.2.2, there are just a few examples of contrast uptake models for contrast enhanced X-ray breast imaging. Melissa Hill et al. [122] developed a physical phantom with simple task-based test objects for CESM performance evaluation. The phantom incorporates solid iodinated plastic features with different clinically relevant iodine concentrations to test some of the main structures and morphology descriptors included in the CE-MRI BIRADS©. These plastic features are constituted of different simple geometrical volumes, such as spheres and cylinders. Dromain et al. [77] presented more realistic simulated lesions, including spiculated and irregular mass-like enhancement generated through local surface deformations.

These prior studies share similar problems when representing lesions in CESM images. First, some characteristics such as heterogeneity or indistinct margins are not represented. Furthermore, these models are feature oriented, and do not consider the combination of different characteristic patterns. In total, Hill et al. [122] provided physical models for three mass-like enhancements, while Dromain [77] modeled four types of mass lesions, which reduces drastically the variability of different findings that can be found in clinical CESM images. To better compare CESM and CEDBT imaging we need to be capable of representing the entire versatility of mass-like contrast uptakes (see Table 3.1).

In CatSim, a phantom is composed of enclosed surfaces, each of them containing the same or different materials associated with a linear attenuation coefficient. All the space that is not defined by these surfaces is considered to contain air. There are three possible types of surfaces: voxels, meshes or combination of analytic surfaces. When the selected surfaces are voxels, a part of the space, defined as a rectangular cuboid, is subdivided in a regular grid of smaller cubes. In the case of mesh, each surface is defined by a group of vertices, edges and triangular faces. Finally, the analytic surfaces are described by the equations defining simple geometrical objects such as spheres, ellipsoid or cones.

Each of these representations present some constraints that need to be considered. In the case of the voxel representation, CatSim only interprets binary volumes, which means that for a given material we need to define the entire voxelized volume identifying the voxels where the material needs to be placed. At the same time, the resolution of the final object will depend on the voxel size. In the case of triangular meshes, each closed mesh defines the envelope of a unique material. Therefore, the resolution of the object will be fixed by the number of triangular faces defining the surface. Finally, in analytic objects, each geometric primitive is associated with a material. Each geometric primitive constitutive of the lesion is read according to an ordered set, whereby the material attenuation coefficients of previously read primitives are overwritten by those of subsequent primitives. As this solution consists of continuous geometrical surfaces it has an unlimited resolution.

The lesions we want to simulate contain thin and fine structures, such as spicules and internal septas, which must be faithfully represented. Also, the chosen representation must provide an efficient solution to combine the different iodine concentrations and, consequently, different materials composing heterogeneous lesions. Therefore, voxel and mesh representations are less suitable for our purpose, as the required resolution and number of materials will result in a high amount of data we cannot manage. Conversely, the combination of several analytic surfaces provides a good trade-off between the required details in the desired lesions and the amount of data employed for their generation.

Following this, we created a software platform to generate mass-like contrast-enhancements exhibiting typical characteristics encountered in clinical CE-MRI and CESM imaging, according

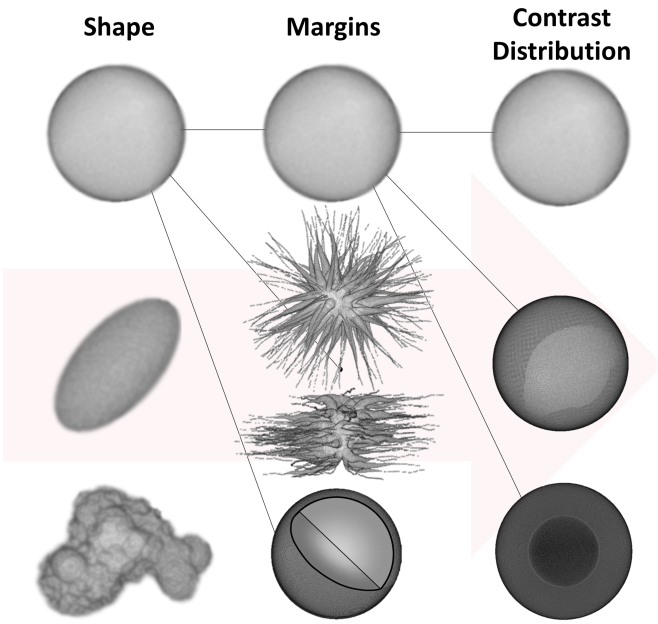

Figure 3.1: Three stages of the contrast uptake generator platform. 1) Generation of the structure defining the shape of the lesion. 2) Margin definition. 3) Contrast uptake distribution. For clarity purpose, in this figure we only represent the evolution of a spherical sharp mass-like enhancement, but other combinations of characteristics are possible.

to Table 3.1. Lesions are entirely defined by the concatenation of simple geometrical surfaces, and a material is assigned to each geometrical surface. In our work, we consider that contrast uptakes are composed of a homogeneous mixture of fibroglandular tissue and different iodine concentrations at constant volume. Consequently, the mass generation is performed in three steps: lesion shape, margins, and contrast enhancement distribution, as illustrated in Figure 3.1.

3.2.1 Shape

In this first step, we model the shape of the desired lesion according to the CE-MRI lexicon:

- Round and oval lesions are defined by a central sphere and ellipsoid, respectively.

- For irregular lesions, we create first a central spherical or ellipsoidal structure. Then, the surface is further deformed as follows. A configurable number of seed points is positioned on the sphere or ellipsoid surface according to a uniform distribution. There are several methods to sample an unbiased uniform distribution over a spherical surface [297]. We have chosen the following sphere point picking algorithm. Considering the uniform random variables $M \sim U(0,1)$ and $N \sim U(0,1)$, we generate random samples of the spherical coordinates ($\theta \in [0, 2\pi), \phi \in [0, \pi]$) as:

$$\phi = 2\pi m \tag{3.1}$$
$$\theta = \arccos(2n - 1) \tag{3.2}$$

where m and n are random values sampled from the distributions M and N respectively. Using these results, the Cartesian coordinates of the random point can be computed as:

$$x = r \cdot \sin(\phi) \cdot \cos(\theta) + x_0 \tag{3.3}$$
$$y = r \cdot \sin(\phi) \cdot \sin(\theta) + y_0 \tag{3.4}$$
$$z = r \cdot \cos(\phi) + z_0 \tag{3.5}$$

where r and (x_0, y_0, z_0) are, respectively, the radius and the center of the considered sphere.

If the original surface is an ellipsoid defined by its principal semi-axes lengths (a, b, c) oriented along the directions $(\vec{a}, \vec{b}, \vec{c})$, and center (x_0, y_0, z_0), we generate a uniform distribution over its surface using the Monte Carlo solution proposed by Williamson [300]. Two main phases are considered: generation of points following a biased distribution and rejection of some points to obtain the final unbiased uniform distribution. First, we generate a point using the sphere point picking algorithm presented before, and then we map it to the surface defined by the equation $f(x, y, z) = \frac{x^2}{a^2} + \frac{y^2}{b^2} + \frac{z^2}{c^2}$ (i.e. centered ellipsoid with its main axes aligned with the Cartesian axes):

$$x = a \cdot \sin(\phi) \cdot \cos(\theta) \tag{3.6}$$
$$y = b \cdot \sin(\phi) \cdot \sin(\theta) \tag{3.7}$$
$$z = c \cdot \cos(\phi) \tag{3.8}$$

where θ and ϕ are computed using Equations 3.1 and 3.2. However, when we apply this mapping, the isotropic small area dS considered in the sphere point picking algorithm is transformed in the small area dS' around the point (x, y, z) which is no longer isotropic. This generates a distortion of the point distribution density. To correct the distortion we can use the rejection-sampling method proposed by von Neuman et al. [217]. Then, for the surface defined by f and each point (x, y, z) we accept it when:

$$\frac{|\nabla f(x, y, z)|}{\max(|\nabla f(x, y, z)|)} \geq \zeta \tag{3.9}$$

where ∇ is the gradient operator and $\zeta \in (0, 1)$ is a uniformly distributed random number. This sampling considers the surface area dS' around the point (x, y, z), rejecting more points when the area is smaller. This process makes the point distribution density uniform. Finally, we translate and rotate the point following the center (x_0, y_0, z_0) and principal axis directions $(\vec{a}, \vec{b}, \vec{c})$ of the original ellipsoidal surface.

Each seed point is the center of a new sphere or ellipsoid. The orientation and size of the peripheral primitives are uniformly distributed. Their minimum and maximum size can be defined by the user. This process can be repeated several times to generate more complex structures.

This algorithm can be used for individual objects. However, when the structure is composed of n_{obj} objects with different surfaces S_j, $j \in [1...n_{obj}]$, and we need to place N points uniquely over the global envelope S_T, two issues arise: intersection between objects, and individual surfaces with different extensions. To overcome these problems we use the following iterative algorithm.

For each object j and each iteration i we generate n_{ij}^S points over the surface S_j following Equations 3.1 to 3.5 if the surface is a sphere, and Equations 3.6 to 3.9 if the surface is an

ellipsoid. The total number of points to generate at each iteration for all objects is:

$$P_i = \sum_{j=1}^{n_{obj}} n_{ij}^S \tag{3.10}$$

From this point distribution, we preserve all the points which lie on the intersecting surface $S'_j = S_T \cap S_j$. This means that we reject all the points placed inside the volume delineated by the total surface S_T. Consequently, only n_{ij}^{sel} points survive the process. The total number of selected points at each iteration for all objects is:

$$Q_i = \sum_{j=1}^{n_{obj}} n_{ij}^{sel} \tag{3.11}$$

where $0 \leq Q_i \leq P_i$. Our goal is to generate at each iteration the remainder points which were rejected in the previous iteration ($P_{i+1} = P_i - Q_i = N - \sum_{k=1}^{i} Q_i$), so, at the end of the iterative process, there are at least N points over the global envelope: $\sum_{k=1}^{\infty} Q_i = N + \varepsilon$, ε being a small fixed tolerable error related to the number of objects composing the global envelope.

The number of points generated for each object should depend on the area of the surface S'_j contributing to the area of the global envelope. The rejection process described before can be used to compute the Monte Carlo estimator of the surface ratio in object j which belongs to the global envelope of the structure:

$$r_{1j} = \frac{n_{1j}^{sel}}{n_{1j}^S} \tag{3.12}$$

We can update this estimator at each iteration:

$$r_{ij} = \frac{\sum_{k=1}^{i} n_{kj}^{sel}}{\sum_{k=1}^{i} n_{kj}^S} \tag{3.13}$$

Applying this ratio, we can compute the number of points to be generated per object j at each iteration i:

$$n_{ij}^S = \begin{cases} \max\left(\left\lceil \left(N - \sum_{k=1}^{i-1} Q_k\right) \frac{r_{i-1j}}{\sum_{q=1}^{n_{obj}} r_{i-1q}} \right\rceil, 0\right) & \text{, if } i > 1 \\ \left\lceil \frac{A(S_j)}{\sum_{q=1}^{n_{obj}} A(S_q)} \right\rceil \cdot N & \text{, if } i = 1 \end{cases} \tag{3.14}$$

where A is the area operator. Considering all the objects and the ceil operator, we obtain the following range of generated points at each iteration:

$$N - \sum_{k=1}^{i-1} Q_k \leq P_i \leq N - \sum_{k=1}^{i-1} Q_k + n_{obj} \tag{3.15}$$

and consequently:

$$0 \leq Q_i \leq N - \sum_{k=1}^{i-1} Q_k + n_{obj} \tag{3.16}$$

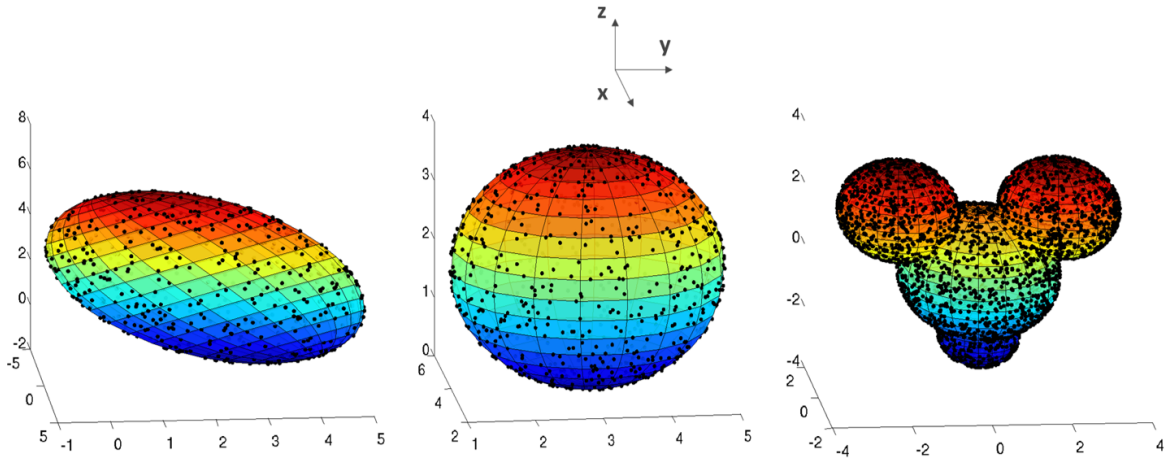

Figure 3.2: Example of a uniform random distribution of points over the surface of an ellipsoid, a sphere, and a combination of surfaces.

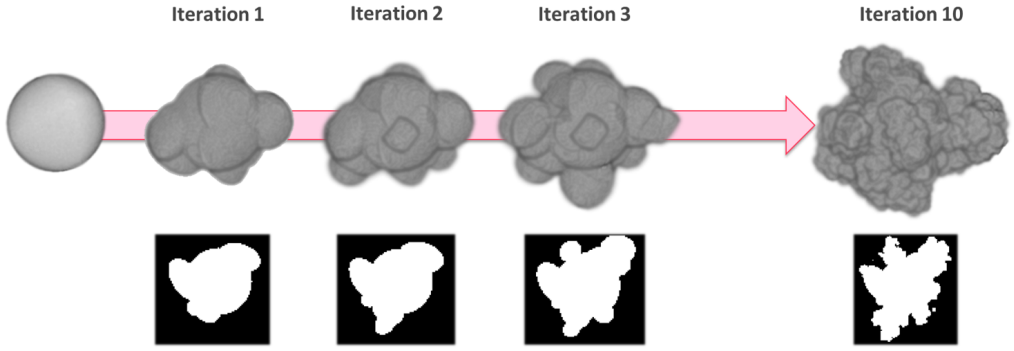

Figure 3.3: The generation of an irregular shape in 10 iterations. The three-dimensional volumes are compared to a horizontal cross-section at each iteration.

The iterative process will finish when $P_i = 0$. And consequently $N \leq \sum_{k=1}^{\infty} Q_i \leq N + n_{obj}$. We place the desired number of points N, considering an error term equal to the number of objects forming the structure at the beginning of the process. In Figure 3.2 we illustrate the random distribution of points over a sphere, an ellipsoid, and a structure generated with the combination of both type of surfaces.

To create the final irregular lesion, N_{iter} iterations of the algorithm we have just presented are performed. In Figure 3.3 we illustrate this whole process, where, for each point generated at each iteration, we place a new sphere or ellipsoid. Reducing the size of the new surfaces incorporated at each iteration and increasing the number of them, we can generate surfaces with localized deformations that increase the realistic appearance of the final lesion.

3.2.2 Margin

In the second step, we add the margin descriptor to the modeled lesions.

- Margin of lesions with sharp margins are not modified.

- To design indistinct margins, we consider that the main reason causing this description in CESM images is that iodine concentration decreases from the lesion core towards the lesion surface, while preserving the original lesion envelope generated in Section 3.2.1. However, as previously mentioned, we assign a unique material composition to each geometric primitive, which does not provide the spatial continuity of the contrast enhancement distribution we need. To overcome this, we propose a geometric discretization of each spherical element. In other words, we can fill each spherical element with smaller spherical samples to discretize our space, and, then, we can assign a different iodine concentration to each sample.

  Two popular discrete mathematical areas of study try to solve this specific problem: sphere packing and sphere covering. While the former solves the problem arranging several non-overlapped spherical elements in order to minimize the empty volume in the sampled region, the latter allows that the spheres overlap so as to maximize the volume filled by the sampled spheres. As we need a complete spherical sampling of our envelope, without any empty volume inside it, we need a sphere covering strategy. The thinnest covering of spherical elements was found by Bambah [12], although other approaches exist for higher dimensions [136]. These solutions propose a regular grid where the spherical sampling elements are placed. In our case, the definition of indistinct margins, we are interested in a concentric distribution of the sampling resolution. In other words, we need a finer resolution of the core of the structure, while we can reduce the resolution at the edges of the structure. Therefore, we have proposed a different sphere covering solution:

  1. The sampling process is illustrated in Figure 3.4 with a bidimensional example. For a sphere of radius R, we divide the space using several radii separated by angle α. Then, spheres are positioned along these radii extending from the lesion surface towards the lesion center, always tangent to the nearest radii. A concentric sphere of radius r is defined to limit the minimal size of the sampling spheres. Consequently, considering that the original spherical object is centered, the center of each sphere is defined in spherical coordinates $(\rho_k, \theta_i, \phi_j)$ as:

$$\begin{cases} \rho_k = \frac{R}{(1+\sin(\alpha))^k} & , \ k \in [1... \left\lceil \frac{\log(R)-\log(r)}{\log(1+\sin(\alpha))-\log(\sin(\alpha))} \right\rceil] \\ \theta_i = i \cdot \alpha & , \ i \in [1... \lceil \frac{2\pi}{\alpha} \rceil] \\ \phi_j = j \cdot \alpha & , \ j \in [1... \lceil \frac{\pi}{\alpha} \rceil] \end{cases} \tag{3.17}$$

     and radius r_k, common for all combinations of (i, j):

$$r_k = R \cdot \frac{\sin(\alpha)}{(1+\sin(\alpha))^{k+1}} \tag{3.18}$$

     The total number of sampling spheres is defined by the following equation:

$$N = 2 \cdot \left(\frac{\pi}{\alpha}\right)^2 \frac{\log(R) - \log(r)}{\log(1+\sin(\alpha))} \tag{3.19}$$

  2. After the sampling process, we define the iodine concentration for each element. To model gradually changing iodine enhancement, iodine concentrations assigned to each spherical primitive are computed using an inverse distance weighting approach with respect to a set of reference positions with pre-defined iodine concentrations [271]. More precisely, we can associate to N spatial positions x_i a fixed iodine concentration

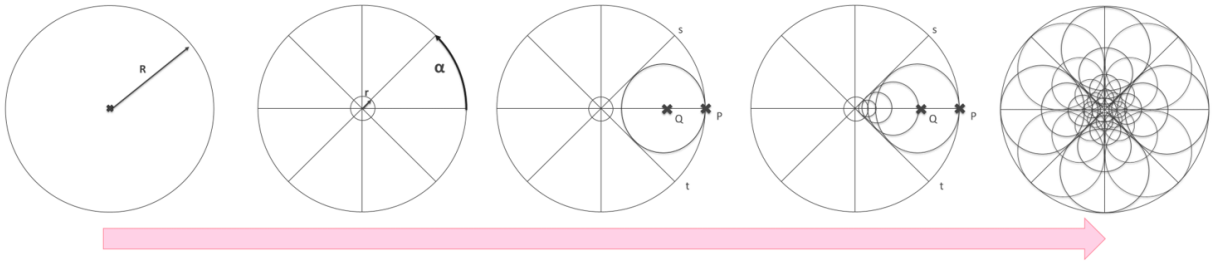

Figure 3.4: Spherical sampling.

c_i. Then, for each sphere with center position x we compute its associated iodine concentration as:

$$C(x) = \begin{cases} \frac{\sum_{i=1}^{N} w_i(x)c_i}{\sum_{i=1}^{N} w_i(x)}, & \text{if } d(x, x_i) \neq 0 \text{ for all i} \\ c_i, & \text{if } d(x, x_i) = 0 \text{ for some i} \end{cases} \tag{3.20}$$

where $w_i(x) = \frac{1}{(d(x,x_i))^p}$ is a weighting function, $d(x, x_i) = \|x - x_i\|$ is the distance between the fixed points x_i and the center x of the selected sphere, and p is a positive real number, called the power parameter, which can be defined by the user. The power parameter will define the smoothness of the iodine concentration transitions.

For indistinct lesions, the central core of the lesion is associated with a fixed iodine concentration and the space outside the lesion is set to $c_i = 0$. This way, the iodine concentration decreases smoothly from the center to the margins of the lesion. Also, as shown in Figure 3.4, our spherical sampling let some empty volume at the margins of the sampled region. To avoid rough transitions of the iodine concentration at the lesion margins, the iodine concentration of the spherical element which is sampled can be set to the iodine concentration of the surrounding space where the lesion is inserted (the space outside the lesion).

Finally, each of the elements we created is saved in decreasing size order. An example of the final distribution of contrast enhancement is illustrated in Figure 3.5.

- Spiculated margins are perceived as several linear structures perpendicular to the lesion core, which have a decreasing radius. In our case, we conceived each spicule as a a concatenation of overlapped spherical objects, growing from the surface of the initial shape created in Section 3.2.1. The overlapping of each spherical element guarantees the continuity of the whole structure. Initially, N_{spi} seed points are uniformly distributed over the lesion envelope. For each seed position $\boldsymbol{p_{(i,0)}}$, $i \in \{1...N_{spi}\}$, we grow a spicule. This is achieved in two steps:

  1. First, we create the spicule "skeleton" using a random walk algorithm. Each point $\boldsymbol{p_{(i,j)}}$, $j \in \{1...n_{length}\}$, represents the point of the random walk at step j for spicule i. This point is chosen as a uniform random position inside a section of a spherical

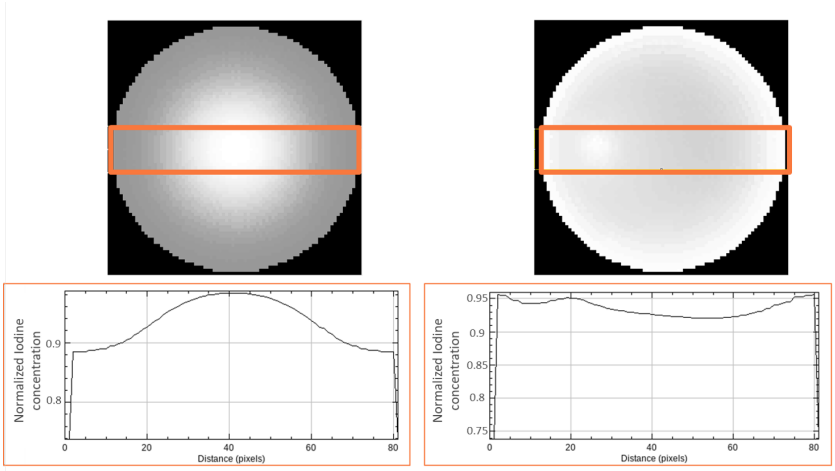

Figure 3.5: Two cross-sections of the results provided by spherical sampling. Left: a typical iodine distribution for indistinct mass-like enhancements, with a decreasing concentration towards the margins. Right: an example of a continuous heterogeneity, with a smooth distribution of the iodine concentration inside the lesion. Both profiles are computed as the vertical mean in the ROIs represented in both figures

shell $S_{(i,j)}$ defined by:

$$l_{min} \leq \rho \leq l_{max} \tag{3.21}$$

$$\arccos\left(\frac{t^z_{(i,j-1)}}{\|\vec{t}_{(i,j-1)}\|}\right) - \frac{\Omega}{2} \leq \theta \leq \arccos\left(\frac{t^z_{(i,j-1)}}{\|\vec{t}_{(i,j-1)}\|}\right) + \frac{\Omega}{2} \tag{3.22}$$

$$\arctan\left(\frac{t^y_{(i,j-1)}}{t^x_{(i,j-1)}}\right) - \frac{\Omega}{2} \leq \phi \leq \arctan\left(\frac{t^y_{(i,j-1)}}{t^x_{(i,j-1)}}\right) + \frac{\Omega}{2} \tag{3.23}$$

where (ρ, θ, ϕ) is the spherical coordinate system centered in $\boldsymbol{p_{(i,j-1)}}$, l_{min} and l_{max} are two parameters controlling the minimum and maximum step size of the random walk, Ω is a parameter controlling the angular freedom of the random walk, and $\vec{t}_{(i,j)}$ is defined by:

$$\vec{t}_{(i,j)} = \begin{cases} \vec{t}_{(i,j-1)} - \kappa(\vec{t}_{(i,j-1)} \cdot \vec{n})\vec{n} & \text{if } S_{(i,j)} \text{ intersects } \Pi_{(i,j)} \\ \frac{p_{(i,j)} - p_{(i,j-1)}}{\|p_{(i,j)} - p_{(i,j-1)}\|} & \text{otherwise} \end{cases} \tag{3.24}$$

where $\Pi_{(i,j)}$ is the plane defined by its normal vector $\vec{n}$, defined by the user, and the point $\boldsymbol{p_{(i,j-1)}}$, and κ is a scalar parameter to adjust the speed of spicules following the plane. For $j = 0$, $\vec{t}_{(i,0)}$ is chosen as the normal to the lesion surface at point $\boldsymbol{p_{(i,0)}}$. Each point $\boldsymbol{p_{(i,j)}}$ is the end point of concatenated segments characterizing the spicule "skeleton".

2. In a second step, we place spherical elemental objects with their centers aligned along the segments created for each "skeleton". The maximum and minimum radius size, the step size between the radius of two consecutive spheres as well as the sphere overlapping can be defined by the user.

Figure 3.6 illustrates both steps using a bidimensional example. All parameters described here can be combined to design different spiculated shapes, as represented in Figure 3.7.

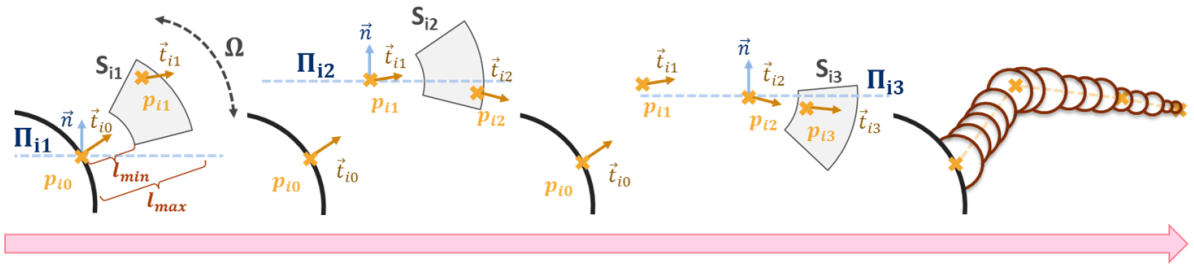

Figure 3.6: Bidimensional representation of a the random walk algorithm used to generate the spicule "skeleton", as well as the subsequent insertion of spherical elements.

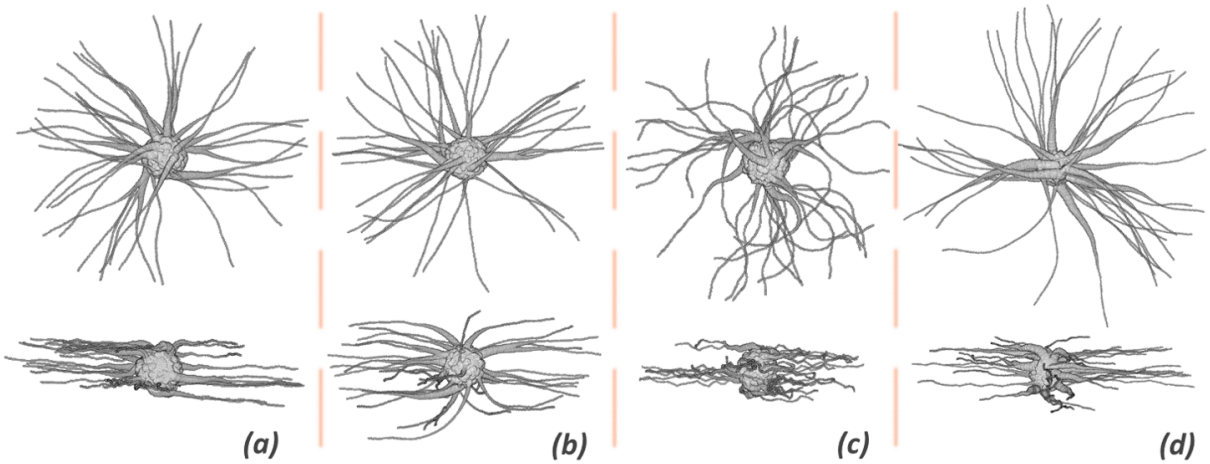

Figure 3.7: Examples of spiculated lesions generated by changing the parameters of the model. From left to right: a) lesion given as example for comparison, b) lesion generated by reducing κ, c) lesion generated increasing Ω, d) lesion generated by increasing the maximum radius of spherical elements.

3.2.3 Contrast uptake distribution

Finally, we model the distribution of contrast uptake inside the lesion. Indistinct lesions are not further modified, since they were considered in Step 2 to be characterized by a heterogeneous enhancement pattern.

- For homogeneous lesions, all the elements constituting the lesion share the same iodine concentration and, consequently, the same material will be assigned to all the surfaces previously defined.

- The heterogeneous distribution of the iodine enhancement inside the lesion can be generated using a continuous or a binary model.

  The continuous distribution can be created using the algorithm presented for indistinct lesions, as shown in Figure 3.5.

  Otherwise, we can model the heterogeneous distribution using a binary distribution. While the previously defined elements are set to a unique mixture of fibroglandular tissue and

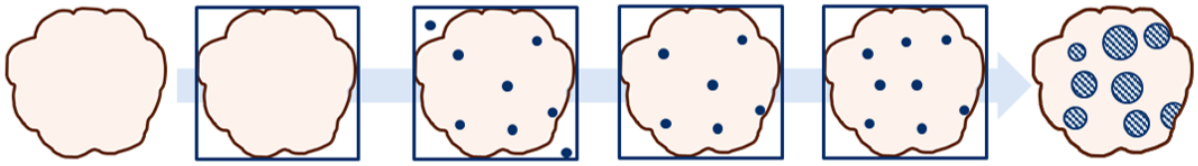

Figure 3.8: Steps to generate a binary heterogeneous lesion. In the figure, the striped disks correspond to a mixture of fibroglandular and adipose tissue, while the rest corresponds to a mixture of fibroglandular and iodine.

iodine, we create several non-enhanced spherical holes inside the structure. This approach creates a discontinuous contrast uptake distribution.

To place our spherical holes we distribute uniformly N_{hole} seed points inside the lesion. These seed points will be the center of each spherical hole element. However, as we do not have any prior information about the shape of our envelope, we need to generate the uniform distribution using a rejection-sampling technique. We compute the external bounding box of the envelope and we generate a uniform distribution of points inside this bounding box. The points outside the envelope are rejected. This process is repeated until all N_{hole} have been placed. For each seed point a spherical element with random radius r_{hole} and containing non-enhancing breast tissue (i.e. mixture of adipose and fibroglandular tissue at constant volume) is placed. An example of this process is presented in Figure 3.8.

- Rim enhancements are created by inserting a smaller non-enhancing structure inside the original lesion envelope sharing the same barycenter and with a similar shape. To do that, we need to know the magnification factor of this second structure which assures us a certain maximal rim thickness.

  An example of the rim-enhancement generation is illustrated in Figure 3.9. We consider N spherical envelopes S_i composing the original structure. These spherical envelopes are characterized by their center p_i and their radii r_i^{old}. The position of the barycenter B for the set of points p_i is given by:

$$B = \frac{1}{N}\sum_{i=1}^{N} p_i \tag{3.25}$$

  Then, to compute our magnification factor we need to find the maximum distance d_{max} among all the distances d_i from the barycenter to the opposed surface of the sphere i passing through p_i:

$$d_i = r_i^{old} + \|p_i - B\| \tag{3.26}$$

$$d_{max} = \max_i (d_i) \tag{3.27}$$

  Using this maximum distance and the desired maximum rim thickness t_{rim}, the magnification factor of the new structure Δ_M can be computed as follows:

$$\Delta_M = 1 - \frac{t_{rim}}{d_{max}} \tag{3.28}$$

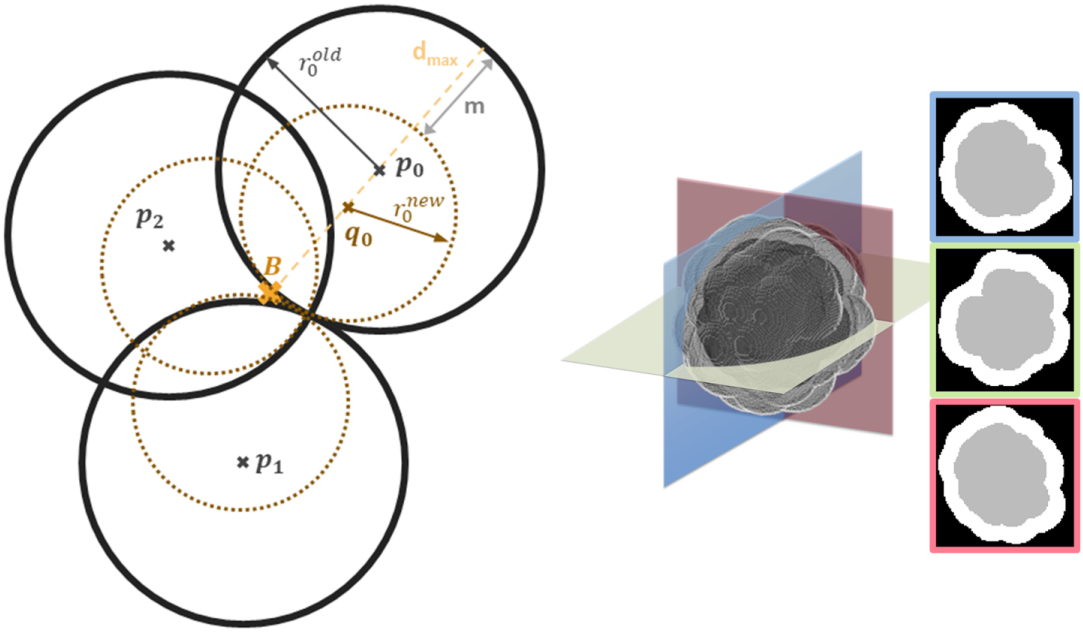

Figure 3.9: Example of the generation of a rim enhancement. Left: a bidimensional illustration of the parameters considered for the generation of the non-iodine enhancing structure. Right: a three-dimensional rim enhancement and three orthogonal cross-sections.

To complete the new smaller non-enhanced structure, we define a new set of spherical objects L_i with the following center and radius:

$$q_i = B + \Delta_M \cdot (p_i - B) \tag{3.29}$$

$$r_i^{new} = \Delta_M \cdot r_i^{old} \tag{3.30}$$

We can establish the maximum margin between the new and the original sphere as:

$$m_i = d_i - r_i^{new} - \|q_i - B\| = \frac{t_{rim} \cdot d_i}{d_{max}} \tag{3.31}$$

which guarantees our constraint of maximal rim thickness. In particular, we find that:

$$0 \leq m_i \leq t_{rim} \tag{3.32}$$

This procedure can be extended by considering also ellipsoidal objects as part of the ensemble. If we consider that S_i is an ellipsoid defined by its center p_i, its axis lengths $(a_i^{old}, b_i^{old}, c_i^{old})$ and director vectors $(\vec{d}_i^a, \vec{d}_i^b, \vec{d}_i^c)$, we redefine d_i as the distance between B and the furthest point of the intersection between S_i and the line crossing B and p_i. Similarly, the new structure L_i will be an ellipsoid with the following parameters:

$$q_i = B + \Delta_M \cdot (p_i - B) \tag{3.33}$$

$$(a_i^{new}, b_i^{new}, c_i^{new}) = \Delta_M \cdot (a_i^{old}, b_i^{old}, c_i^{old}) \tag{3.34}$$

where q_i and $(a_i^{new}, b_i^{new}, c_i^{new})$ are the center and axes lengths, respectively, of L_i.

Table 3.2: Average generation times and number of elements composing the final structure for the contrast uptakes created in Chapter 6.

Type	**Time** $[s]$	**Number of elements**
Round	0.26	60
Oval	0.46	600
Irregular	22.51	2035
Indistinct	24.81	143614
Spiculated	3.93	12615
Heterogeneous	24.52	300
Rim	0.54	200

Each lesion is described in FORBILD text file syntax (Institute of Medical Physics, Erlangen, Germany)[1]. The framework to generate the lesions was implemented in Matlab and the computation time depends on the descriptors required to simulate a particular lesion. For example, in Chapter 6 we use this framework to generate a large database of mass-like contrast uptakes employing one or several of the processes presented in this section. In Table 3.2, we present the average generation times for all these structures (using Intel® Xeon® CPU ES-2630 v2 @ 2.60GHz).

3.3 Combining contrast uptakes inside the breast texture

As presented in Section 1.2.2, several works proposed different approaches to simulate the complex anatomical structures of the breast. In this dissertation we use a simulated textured breast phantom, generated according to a previously published method by Li et al. [180]. In their work, they proposed a three-dimensional texture model using a mathematical definition defined from segmented clinical breast computed tomography (bCT) images. In this model, the medium-scale structures (i.e. adipose compartments) are represented by overlapping ellipsoids, while small-scale texture features are introduced by small Voronoi cells at the ellipsoid boundaries. Consequently, the resulting structure is a volume composed of binary voxels representing mutually exclusive fibroglandular or adipose tissue. An example of this voxelized texture is presented in Figure 3.10.

In contrast enhanced breast imaging systems, a contrast agent is introduced into the vascular system of the patient. As we have seen in Section 1.1.4, suspicious findings are not the only tissues affected by the contrast injection, but also the normal fibroglandular tissue. Due to the potential impact of breast parenchymal enhancement (BPE) on detectability and characterization of contrast uptakes, we introduced the simulation of BPE in our simulations. To simulate BPE, we replaced the material associated with voxels containing fibroglandular tissue, by a homogeneous mixture of fibroglandular tissue and iodine contrast agent at constant volume.

Once we have generated a lesion and a texture volume we combine them to generate an X-ray simulated image. As lesions are defined by analytic surfaces and textures are expressed as binary voxelized volumes, this combination cannot be made in the volume domain. Our simulation platform cannot project at the same time voxelized and analytic volumes. To overcome this problem, we propose a method to combine them in the projection domain. Considering a texture with thickness t_{tex} and composed of a homogeneous material with linear attenuation coefficient

[1] `http://www.imp.uni-erlangen.de/forbild/`

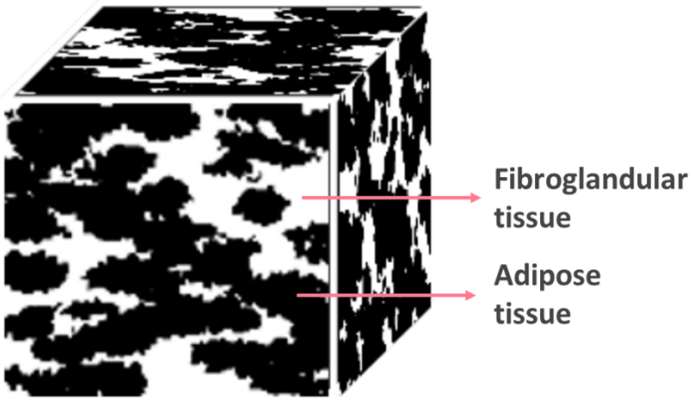

Figure 3.10: Example of the 3D stochastic solid breast texture model developed by Li et al. [180].

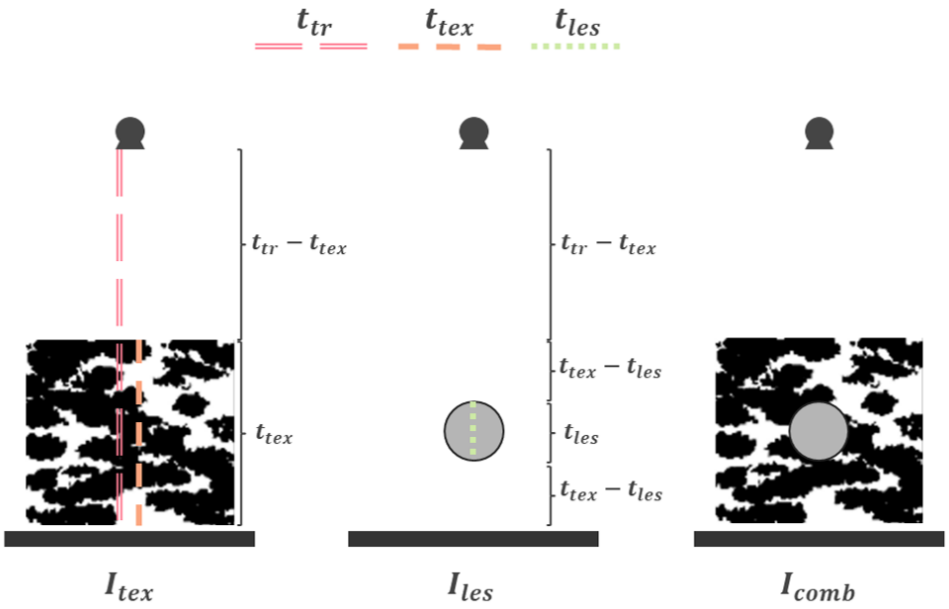

Figure 3.11: Illustration of the projections I_{text}, I_{les} and I_{comb}, and their corresponding traversed material thicknesses.

μ_{tex}, a lesion of thickness t_{les} and composed of a homogeneous material with linear attenuation coefficient μ_{les}, the total trajectory of the X-ray t_{tr}, and the linear attenuation coefficient of the air μ_{air}, we compute the projections I_{text}, I_{les} and I_{comb} respectively of the texture, the lesion, and the desired combination as:

$$I_{tex} = I_0 e^{-\mu_{air}\cdot(t_{tr}-t_{tex})-\mu_{tex}\cdot t_{tex}} \tag{3.35}$$

$$I_{les} = I_0 e^{-\mu_{air}\cdot(t_{tr}-t_{tex})-\mu_{air}\cdot(t_{tex}-t_{les})-\mu_{les}\cdot t_{les}} = I_0 e^{-\mu_{air}\cdot(t_{tr}-t_{les})-\mu_{les}\cdot t_{les}} \tag{3.36}$$

$$I_{comb} = I_0 e^{-\mu_{air}\cdot(t_{tr}-t_{tex})-\mu_{tex}\cdot(t_{tex}-t_{les})-\mu_{les}\cdot t_{les}} \tag{3.37}$$

with $t_{tr} > t_{tex} > t_{les}$. We illustrate each of these projections in Figure 3.11. With our X-ray simulation platform we are capable of generating I_{text} and I_{les}, but not the desired projection I_{comb}. Therefore, to obtain the desired combination using the projected I_{tex} and I_{les} images, we

introduce a third projection Π as follows:

$$\log(I_{comb}) = \log(I_{tex}) + \log(I_{les}) + \log(\Pi) \tag{3.38}$$

To know the content of this new projection Π, we solve Equation 3.38 and we obtain:

$$\frac{1}{\Pi} = I_0 e^{-\mu_{air}\cdot(t_{tr}-t_{les})-\mu_{tex}\cdot t_{les}} \tag{3.39}$$

From the analysis of Equations 3.39 and 3.36 we can establish that $\frac{1}{\Pi}$ corresponds to the projection of the same lesion but modified. Instead of containing the homogeneous material with linear attenuation coefficient μ_{les}, it contains a homogeneous material with linear attenuation coefficient μ_{tex}.

However, our texture is not composed of a homogeneous material with a unique linear attenuation coefficient μ_{tex} in all its voxels. To avoid this dependency, we select the texture voxels whose centers belong to the three-dimensional space that is also occupied by the generated lesion. We assign to these selected voxels the linear attenuation coefficient of pure adipose tissue μ_{adip}. This generates a modified projection of the texture volume, noted I'_{tex}. At the same time we create a lesion with exactly the same structure as the original one, but with all its elements assigned the linear attenuation coefficient μ_{adip}. We call the projection of this modified lesion I_{adip}. Considering this, we obtain the following three projections:

$$I'_{tex} = I_0 e^{-\mu_{air}\cdot(t_{tr}-t_{tex})-\mu_{tex}\cdot(t_{tex}-t_{les})-\mu_{adip}\cdot t_{les}} \tag{3.40}$$

$$I_{les} = I_0 e^{-\mu_{air}\cdot(t_{tr}-t_{tex})-\mu_{air}\cdot(t_{tex}-t_{les})-\mu_{les}\cdot t_{les}} \tag{3.41}$$

$$\frac{1}{\Pi} = I_{adip} = I_0 e^{-\mu_{adip}\cdot t_{les}-\mu_{air}\cdot(t_{tr}-t_{les})} \tag{3.42}$$

and therefore:

$$I_{comb} = e^{\log(I_{tex})+\log(I_{les})-\log(I_{adip})} \tag{3.43}$$

This procedure is illustrated in Figure 3.12a and an example of the image generated after the combination is presented in Figure 3.12b. As we can observe, only the voxels of the texture that share the same space as the lesion are modified. After computing I_{comb}, all the detection steps presented in Chapter 2 are applied.

This combination strategy has, nevertheless, some limitations. When we combine the three projections we may have two error sources: texture modification and lesion overlapping. Both errors are illustrated in Figure 3.13.

- Texture modification is caused by the alteration of voxels whose centers belong to the space occupied by the lesion. At the edges of the structure there are partial voxels that are not completely filled by the lesion volume, but their centers are placed inside the three-dimensional lesion. The material assigned to these voxels is changed to pure adipose tissue. If, at the beginning, the voxel contained fibroglandular tissue instead, we introduce an error.

- Lesion overlapping appears in the opposite scenario: a voxel partially filled by the lesion but whose center is not placed inside the three-dimensional lesion. In this case, the material assigned to the voxel is not modified. When this material is different from adipose tissue we are introducing another error source.

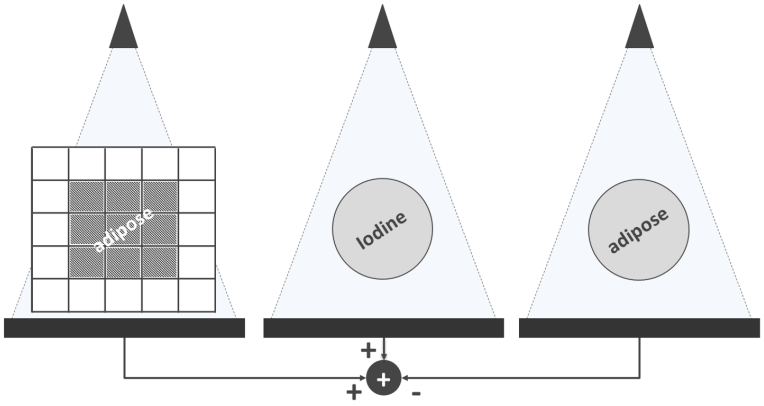

(a) The three projections proposed to combine the texture and the lesion generated in the image domain.

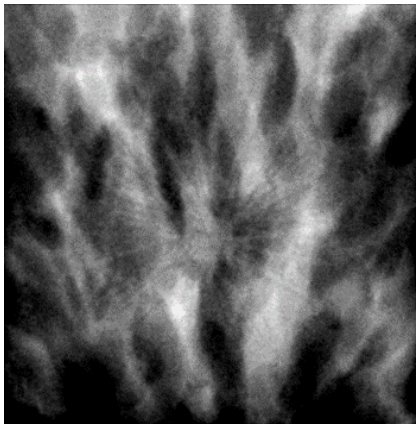

(b) Low-energy projected image of a $5cm$ voxelized texture phantom containing an analytical spiculated lesion.

Figure 3.12: Combination of several projections to insert an analytic lesion inside a voxelized background.

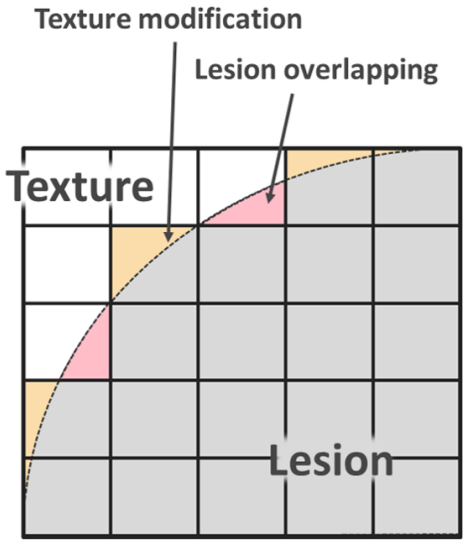

Figure 3.13: Two sources of errors when combining the texture and the lesion: texture modification and lesion overlapping.

The errors which may be included in the projection are always smaller than half the voxel size. The size of the voxels used in this study was $0.1 \times 0.1 \times 0.1mm$, similar to the dimensions of the detector pixel size ($0.1 \times 0.1mm$). However, the conical geometry used in mammographic images implies a magnification of the voxel size in the projected plane. The visual analysis of several simulated projections did not reveal any significant margin deformation caused by these errors.

3.4 Conclusion

In Section 1.2.2 of Chapter 1, we presented the different virtual surrogates described in the literature modeling the pathological findings observed in different breast modalities. We realized that there were a very limited number of works introducing any physical or virtual model of contrast-uptakes as observed in contrast-enhanced mammography. In this chapter we have presented the main challenges for the generation of virtual mass-like contrast uptakes surrogates for contrast enhanced X-ray breast imaging.

First of all, there is currently no defined lexicon available to characterize the contrast uptakes observed in X-ray clinical images. We led a literature review of the published works regarding the characteristics of contrast uptakes observed in CESM clinical images and identified the main differences with the established ACR BI-RADS® for CE-MRI. This work led us to the definition of a series of features which could be considered to characterize different contrast uptakes. This list of features helped us to generate three-dimensional models of contrast-enhancements which can be used to compare the performance of CESM and CEDBT.

Secondly, the published models to generate mass-like enhancements have some limitations. Related works presented excessively geometrical models of CESM findings [122, 175, 226] or without a complete representation of the variability of mass-like findings found in clinical images [36, 77, 158]. Our second contribution was to develop a framework capable of mixing all the possible characteristics of the previously defined lexicon. The generated lesions are composed by the aggregation of several analytical surfaces, each of them associated with the same or different linear attenuation coefficient. As we focused our work on mimicking the geometrical characteristics found in CESM findings, we only established a visual evaluation of the recombined simulated images including virtual contrast uptake surrogates. This task was performed by GE Healthcare engineers, experts in contrast enhanced X-ray imaging of the breast. Our model is entirely geometrical, without considering the biological procedures induced by tumor angiogenesis. Moreover, we have not evaluated the realism delivered by the final images, comparing them to a dataset of real findings. Despite these limitations, this strategy allows us to generate more realistic approximated images of real findings and, consequently, we can use them to conduct a study to evaluate the capability of imaging systems to provide images allowing an accurate lesion characterization. The study of models to generate non-mass-like enhancements remains for future works.

Finally, these mass-like enhancement surrogates can be inserted into a voxelized texture model which was modified to provide the characteristic BPE observed in clinical images. Few studies have included mass-like contrast uptakes surrounded by BPE [38, 77]. The difference between the voxelized definition of the texture and the analytical definition of the lesion led us to a combination of both in the projected domain. To do that we needed to modify the texture, changing the linear attenuation coefficients of some of its voxels. However, this procedure is impacted by some error sources. However, we have not found that these errors affect the margin definition in the projected domain.

All the elements we introduced in this chapter are then used in our simulation platform, to generate images reproducing the main characteristics observed in clinical images.

Chapter 4

Generation of recombined and reconstructed images

In this chapter, we present the chosen recombination algorithm for low- and high-energy acquisitions and its impact on the models of the acquisition system presented in Chapter 2. We also introduce a new reconstruction method for CEDBT adapted to the clinical task.

4.1 Recombination of low- and high-energy images

In single energy mammography, tissues are differentiated by the signal intensity observed in the projections, inducing some ambiguity when two materials with different chemical compositions or different tissue densities share a similar X-ray attenuation. This limitation interferes with the correct classification of soft tissue lesions containing a certain amount of contrast agent. Spectral imaging techniques benefit from the energy dependency of the linear attenuation coefficients to differentiate the materials composing the projected object. As proposed by Alvarez et al. [2, 3, 173], the linear attenuation coefficient $\bar{\mu}$ of an object at position r and energy E can be formulated as a linear combination of the total density ρ, the mass attenuation coefficients of M basis materials $(\mu/\rho)_m$, $m \in [1...M]$, where μ_m and ρ_m are the linear attenuation coefficient and density of a each basis material, respectively, and a function W_m representing the weight of the element m in the total mixture:

$$\bar{\mu}(r, E) = \rho(r) \cdot \sum_{m=1}^{M} (\mu/\rho)_m(E) \cdot W_m(r) \tag{4.1}$$

where (μ/ρ) is expressed in cm^2/g and ρ in g/cm^3. When a projection is computed, the volumetric concentration $C_{v,m}(r)$ of material m at position r is used instead:

$$C_{v,m}(r) = W_m(r) \cdot \rho(r) \tag{4.2}$$

which is measured in g/cm^3.

Using the volumetric concentration, we can calculate the projected surface concentration $\delta_m(i)$ of material m at the pixel element i as:

$$\delta_m(i) = \int_l C_{v,m}(r)dr \tag{4.3}$$

where l is the linear trajectory traversing the object from the X-ray source to the detector element i. The surface concentration is measured in g/cm^2.

Then, employing the surface concentration, the expression of the projection image at pixel element i is given by:

$$p(i) = \int_{E_{min}}^{E_{max}} I_0(E) \cdot \eta(E) \cdot \Gamma(E) \cdot e^{-\left(\sum_{m=1}^{M} (\mu/\rho)_m(E) \cdot \delta_m(i)\right)} dE \tag{4.4}$$

where $I_0(E)$ is the X-ray source fluency at energy E for a spectrum defined from E_{min} to E_{max}, $\eta(E)$ is the efficiency of the scintillator, and $\Gamma(E)$ is the conversion response of the detector. For a fixed object, a given geometry and a given X-ray detector, the value of $p(i)$ will only depend on the source spectrum $I_0(E)$ generated by the X-ray tube.

Therefore, the problem of spectral mammography and spectral tomosynthesis is to retrieve δ_m and W_m, as they are proportional to the quantity of each basis material composing the object. Two decomposition equation systems may be considered: in **volume domain** using Equation 4.1, or in **projection domain** using Equation 4.4. Considering N measures and an object composed of M materials, the uniqueness of the solution for each equation system and its sensitivity to noise depend on the Jacobian matrices:

$$J_{vol} = \begin{pmatrix} \partial\bar{\mu}_1/\partial W_1 & \partial\bar{\mu}_1/\partial W_2 & \dots & \partial\bar{\mu}_1/\partial W_M \\ \partial\bar{\mu}_2/\partial W_1 & \partial\bar{\mu}_2/\partial W_2 & \dots & \partial\bar{\mu}_2/\partial W_M \\ \vdots & \vdots & \ddots & \vdots \\ \partial\bar{\mu}_N/\partial W_1 & \partial\bar{\mu}_N/\partial W_2 & \dots & \partial\bar{\mu}_N/\partial W_M \end{pmatrix} \tag{4.5}$$

for a volume decomposition system, and:

$$J_{proj} = \begin{pmatrix} \partial p_1/\partial \delta_1 & \partial p_1/\partial \delta_2 & \dots & \partial p_1/\partial \delta_M \\ \partial p_2/\partial \delta_1 & \partial p_2/\partial \delta_2 & \dots & \partial p_2/\partial \delta_M \\ \vdots & \vdots & \ddots & \vdots \\ \partial p_N/\partial \delta_1 & \partial p_N/\partial \delta_2 & \dots & \partial p_N/\partial \delta_M \end{pmatrix} \tag{4.6}$$

for a projection decomposition system. The decomposition system can be solved only if its Jacobian matrix is not singular (i.e. nonzero determinant) [1, 2]. In the case of monoenergetic spectra, both decomposition equation systems can be solved by algebraic inversion of the linear system using M different X-ray beam energies. Theoretically, for polyenergetic spectra, the nonzero determinant of the Jacobian matrices is achieved using M spectra whose energies corresponding to the maximum emission of X-ray photons are different [173]. However, the accuracy of δ_m and W_m solutions and the insensitivity to measured noise generally increase if we reduce the overlap between the different input spectra [3, 149, 155].

In volume domain decomposition, M different volumes are reconstructed before recombination, one per spectral measurement. However, because of the beam hardening effect, the spectra of the X-ray beam reaching the particular position r inside the projected object from different directions may be different. Therefore, the attenuation coefficient $\bar{\mu}(r, E)$ described in Equation 4.1 will depend on the trajectory, making it difficult to achieve a correct material separation [218]. Thus, to improve the accuracy of the solution, several methods to correct the beam hardening effect have been proposed: bowtie filtration [275], post-processing correction of log-projection values $\ln(p(i))$ [119, 147], or nonlinear modified version of Equation 4.1 [9]. Even if these methods improve the accuracy of the material separation obtained in volume domain decomposition, the resulting reconstructed volumes may not be completely quantitative. Alternatively, W_m can be reconstructed after material separation in the projected domain.

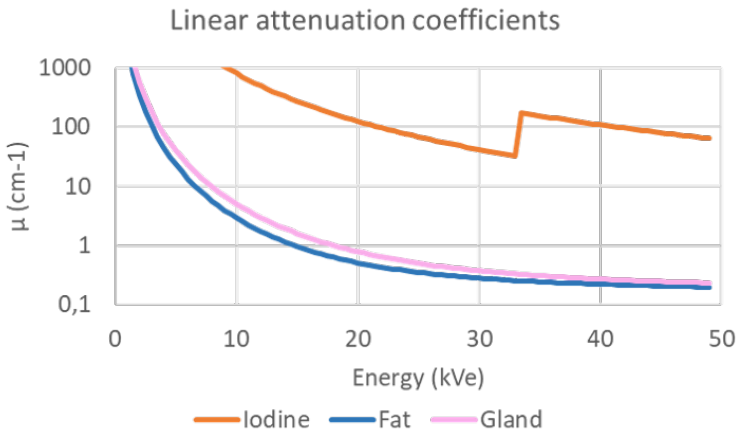

Figure 4.1: Illustration of the linear attenuation coefficient for different energies. We can observe that the two different materials composing the anatomical structure of the breast share a similar and continuous linear attenuation profile. However, this is not true for the iodine, which presents a discontinuity at 33.2 keV.

As beam hardening is already considered in Equation 4.4 (which is nonlinear), beam hardening correction will be directly addressed by the material decomposition algorithm chosen for the projected images. This can provide a better accuracy of the estimated δ_m and W_m. Without any further hypothesis, the equation system can be solved by transforming the nonlinear log-projection values $\ln(p(i))$ into a polynomial combination [174], expressing the values δ_m as a polynomial combination of the log-projection values [156, 252], using look-up tables mapping precomputed low-noise measures to different material compositions [54, 252], or adopting iterative methods [116, 303].

K-edge imaging was proposed to increase the value of the Jacobian matrix presented in Equation 4.6 and, consequently, to provide a better conditioned problem [215]. The K-edge is the binding energy of the K-shell electron of an atom of a given material. Above this energy, the attenuation coefficient of the material suffers a sudden increase. Different schemes can be considered to achieve K-edge imaging [155], but, in general terms, this technique consists in applying material decomposition to an object composed of one or several materials containing K-shell binding energy within the energy range of one of the M spectra used as input. As already introduced in Chapter 1, the contrast agent used in CESM and CEDBT is iodine. This element has a K-edge at 33.2 keV (see Figure 4.1).

Although material decomposition of M materials reducing the number of acquisitions with different spectra to $M-1$ involves an ill-conditioned problem, a priori information can be included to solve the equation system. This way we can reduce the X-ray exposure of the patient. In particular, CESM and CEDBT consider a dual-energy three-material decomposition ($M=3$) to separate the iodine from the fibroglandular and adipose tissues composing the breast. The two X-ray spectra are generally such as their energy ranges are located at each side of the iodine K-edge. They are called low- and high-energy spectra. To obtain the quantity of iodine at the projections, a volume conservation hypothesis can be added to the equation system [154]. Therefore, for these two energy beams, the three materials, and this additional constraint, we

obtain the following equation system:

$$\begin{cases} p_L(i) = \displaystyle\int_{E=E_L^{min}}^{E_L^{max}} I_{0,L}(E)\cdot\eta(E)\cdot\Gamma(E) \\ \qquad \cdot\exp\left(-\left(\frac{\mu}{\rho}\right)(E)_{gland}\cdot\delta(i)_{gland} - \left(\frac{\mu}{\rho}\right)(E)_{adip}\cdot\delta(i)_{adip} - \left(\frac{\mu}{\rho}\right)(E)_{iod}\cdot\delta(i)_{iod}\right)dE \\ p_H(i) = \displaystyle\int_{E=E_H^{min}}^{E_H^{max}} I_{0,H}(E)\cdot\eta(E)\cdot\Gamma(E) \\ \qquad \cdot\exp\left(-\left(\frac{\mu}{\rho}\right)(E)_{gland}\cdot\delta(i)_{gland} - \left(\frac{\mu}{\rho}\right)(E)_{adip}\cdot\delta(i)_{adip} - \left(\frac{\mu}{\rho}\right)(E)_{iod}\cdot\delta(i)_{iod}\right)dE \\ T_{obj}(i) = \dfrac{\delta_{iod}(i)}{\rho_{iod}} + \dfrac{\delta_{gland}(i)}{\rho_{gland}} + \dfrac{\delta_{adip}(i)}{\rho_{adip}} \end{cases} \tag{4.7}$$

where $I_{0,L}(E)$ is the input low-energy spectra defined in the energy range $[E_L^{min}, E_L^{max}]$, $I_{0,H}(E)$ is the input high-energy spectra defined in the energy range $[E_H^{min}, E_H^{max}]$, $\left(\frac{\mu}{\rho}\right)_{gland}$, $\left(\frac{\mu}{\rho}\right)_{adip}$ and $\left(\frac{\mu}{\rho}\right)_{iod}$ are, respectively, the mass attenuation coefficients for the fibroglandular and adipose tissues as well as the iodine contrast agent, and $T_{obj}(i)$ the total thickness of the object at pixel i. As the projected thickness per pixel of the object cannot be known a priori, in mammography the mechanical thickness of the compressed breast is typically used as a constant for all detector pixels $T_{obj}(i) = T$. However, some authors have proposed local estimators of this thickness [58, 203].

For monoenergetic spectra, the system can be solved directly as a linear combination of the log-projections. Thus, the final iodine thickness will be proportional to the simple log weighted subtraction of the low- and high-energy images:

$$t_{iod}(i) \propto \ln\left(p_H(i)\right) - w\cdot\ln\left(p_L(i)\right) \tag{4.8}$$

where t_{iod} is the projected iodine thickness, and w is a scalar weighting factor. The simplicity of this method has contributed to its large adoption in diverse studies [25, 28, 30, 82, 89, 141, 177, 295], including several works evaluating the characteristics and performance of CEDBT [39, 48, 107, 132, 133, 131, 134, 259, 263, 266]. However, as actual X-ray beams used in the standard mammography systems are polyenergetic, the inaccuracy of the hypothesis may imply a preservation of non-iodinated anatomical structures in the recombined iodine image. Some works suggest that anatomical texture can be further eliminated if the weight w is modified using experimental setups [40, 89, 263, 281]. Otherwise, the dual-energy three-material decomposition problem can be interpreted as a data fitting problem over the surface $f\left(\ln\left(p_H\right)\right) = \ln\left(p_L\right)$ for a given object thickness, as illustrated in Figure 4.2. Therefore, some publications proposed different polynomial combinations of the low- and high-energy images to retrieve the iodine thickness [152, 234]. For a second order approximation, the iodine thickness is expressed as:

$$t_{iod}(i) \propto \alpha_0 + \alpha_1\cdot\ln\left(p_L(i)\right) + \alpha_2\cdot\ln\left(p_H(i)\right) + \alpha_3\cdot\ln^2\left(p_L(i)\right) + \alpha_4\cdot\ln^2\left(p_H(i)\right) + \alpha_5\cdot\ln\left(p_L(i)\right)\cdot\ln\left(p_H(i)\right) \tag{4.9}$$

where the coefficients α_0 – α_5 have to be determined using some scattered known data over the dual-energy three-material decomposition surface. In particular, Puong [234] proposes an approach based on image chain simulations to retrieve several known points over the surface.

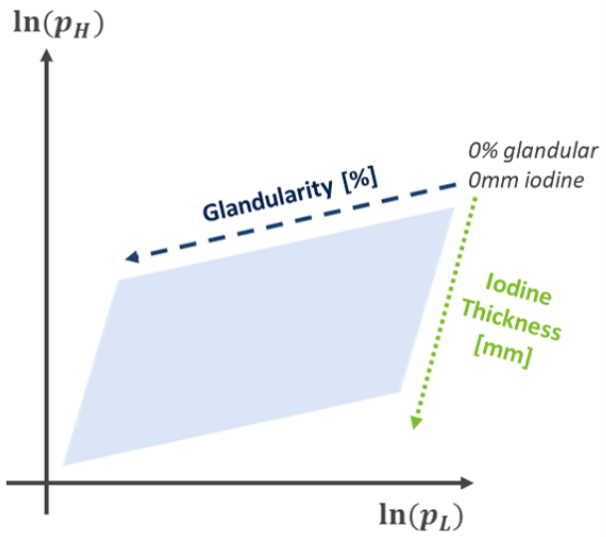

Figure 4.2: Dual-energy three-material decomposition surface. The designed area represents the space of possible $\ln(p_L(i))$ and $\ln(p_H(i))$ pairs for all different combinations of glandularity percentage and iodine thickness for one given breast thickness.

Using a virtual model of the acquisition chain, different projected signal intensities pairs are computed for diverse percentages of fibroglandular and adipose tissues as well as iodine thicknesses. The simulations are performed using numerical approximations of the chosen polyenergetic low- and high-energy spectra. The coefficients α_0 – α_5 will be then computed to fit the simulated data. The polynomial surface provides a better beam hardening correction, delivering more quantitative results and a good cancellation of the anatomical structure.

This last approach is the standard recombination algorithm used in our CESM and CEDBT experimental acquisitions and, consequently, Equation 4.9 must be considered for the propagation of each process of our model (frequency response, stochastic and memory processes) into the recombined image.

4.1.1 Recombination in simulated images

As introduced in Chapter 1, the approach proposed in this PhD only considers monoenergetic X-ray simulations. In this particular case, the system presented in Equation 4.7 can be solved analytically as a linear combination of the log-projected images. The exact amount of iodine in the projected images is given by the following equation:

$$t_{iod} = \alpha_0 + \alpha_1 \cdot \ln(p_L) + \alpha_2 \cdot \ln(p_H) \tag{4.10}$$

with the recombination coefficients defined by:

$$\begin{cases} \alpha_2 = -\dfrac{\Delta\mu_a^L}{\Delta\mu_a^H \cdot \Delta\mu_i^L - \Delta\mu_a^L \cdot \Delta\mu_i^H} \\ \alpha_1 = \dfrac{\Delta\mu_a^H}{\Delta\mu_a^H \cdot \Delta\mu_i^L - \Delta\mu_a^L \cdot \Delta\mu_i^H} \\ \alpha_0 = \dfrac{\Delta\mu_a^L \cdot \ln(I_0^H \cdot \eta^H \cdot \Gamma^H) - \Delta\mu_a^H \cdot \ln(I_0^L \cdot \eta^L \cdot \Gamma^L) + T \cdot (\mu_{gland}^H \cdot \Delta\mu_a^L - \mu_{gland}^L \cdot \Delta\mu_a^H)}{\Delta\mu_a^H \cdot \Delta\mu_i^L - \Delta\mu_a^L \cdot \Delta\mu_i^H} \end{cases} \tag{4.11}$$

where $\Delta\mu_a^E = \mu_{gland}^E - \mu_{adip}^E$ and $\Delta\mu_i^E = \mu_{gland}^E - \mu_{iod}^E$, for E equals to L or H depending on whether the value of the linear attenuation coefficient corresponds to the low or high monoenergetic spectrum. All the values presented in Equation 4.11 are known constants for a specific acquisition set-up, and they can be directly derived from the parameters defined in our simulation.

A we can observe, the recombination of mono-energetic simulated images, identified as t_{iod}^{simu}, presented in Equation 4.10 is different from the recombination of poly-energetic experimental acquisitions, identified as t_{iod}^{exp}, in Equation 4.9. Then, the propagation of stochastic, frequency and memory processes is different in simulated recombined images and experimental recombined acquisitions. To asses the clinical impact of mono-energetic spectra in our simulations, we need to analyze the propagation of each process of our model (frequency response, stochastic and memory processes) for low- and high-energy acquisitions to the final iodine recombined image and the differences between t_{iod}^{simu} and t_{iod}^{exp}.

4.1.2 Stochastic processes after material decomposition

The recombination process reduces the residual contrast between the anatomical noise caused by the projected fibroglandular and the adipose structures composing the breast and, consequently, improves the conspicuity of the lesions. However, this procedures increases the quantum noise component of the equivalent iodine thickness images [248]. Additionally, we have seen that the final iodine recombined image can be generated using different approaches of combining the low- and high-energy acquisitions. The propagation of the quantum noise from the individual acquisitions to the recombined image will then depend on this combination. In particular, we are interested in the SNR obtained in the recombined image as we know that it is directly related to the detection performance associated with imaging devices [33, 253]. While the mean value must be equal to the real iodine equivalent thickness, the variance of the stochastic process may depend on each particular recombination process.

In our case, according to the models presented in Section 2.3 of Chapter 2, a simulated monoenergetic image can be formulated as the linear combination of three additive and uncorrelated random processes: (i) a uniform random process $u \sim \mathcal{U}(0, A)$ which is related to the quantization process with linear step equals to A; (ii) a Gaussian random process $\varepsilon \sim \mathcal{N}(0, \sigma_{elec_{L,H}}^2)$ which models the electronic noise for low- and high-energy acquisitions; and (iii) a Poisson process $Y_{L,H} \sim \mathcal{P}(\lambda)$ which represents the quantum noise for the low- and high-energy acquisitions. Two empirically derived parameters dependent on the chosen X-ray energy, $G_{L,H}$ and $K_{L,H}$, were included to calibrate the mean pixel value and variance of the quantum noise model.

Considering all this, the final expression for a given low- or high-energy simulation is:

$$p_{L,H} = M \cdot \frac{G_{L,H}}{K_{L,H}} \cdot Y_{L,H}^{K} + \varepsilon + u \tag{4.12}$$

where $Y_{L,H}^{K} \sim \mathcal{P}(K_{L,H} \cdot \lambda)$, and M is the known total electronic gain. The mean value and variance of the quantization process are expressed respectively as:

$$\begin{cases} \mu_u = \frac{A}{2} \\ \sigma_u^2 = \frac{A^2}{12} \end{cases} \tag{4.13}$$

The mean value and variance of the quantum noise are expressed as:

$$\begin{cases} \mu_{q_{L,H}} = M \cdot G_{L,H} \cdot \lambda_{L,H} \\ \sigma_{q_{L,H}}^2 = M^2 \cdot \frac{G_{L,H}^2}{K_{L,H}} \cdot \lambda_{L,H} \end{cases} \tag{4.14}$$

Then, as all the random processes are decorrelated, the total mean value and variance of the model presented in Equation 4.12 is:

$$\begin{cases} \mu_{p_{L,H}} = \mu_{q_{L,H}} + \mu_u \\ \sigma_{p_{L,H}}^2 = \sigma_{q_{L,H}}^2 + \sigma_{elec_{L,H}}^2 + \sigma_u^2 \end{cases} \tag{4.15}$$

Considering Equation 4.10, the iodine recombined image is the combination of the logarithm of these random processes:

$$t_{iod}^{simu} = \alpha_0 + \alpha_1 \cdot \ln\left(M \cdot \frac{G_L}{K_L} \cdot Y_L^K + \varepsilon + u\right) + \alpha_2 \cdot \ln\left(M \cdot \frac{G_H}{K_H} \cdot Y_H^K + \varepsilon + u\right) \tag{4.16}$$

In clinical relevant set-ups and for normal operating conditions, a mammography system provides projections where $p_{L,H} \gg 1$. Under this assumption, the logarithm function can be assumed to be linear. To characterize the first and second moments of the log-projected images, we use a first order Taylor expansion at the mean value of the projection:

$$\ln\left(p_{L,H}\right) \approx \ln\left(\mu_{p_{L,H}}\right) + \frac{1}{\mu_{p_{L,H}}}\left(p_{L,H} - \mu_{p_{L,H}}\right) \tag{4.17}$$

Using this approximation, the mean and the variance of the recombined image is given by the following equations:

$$\begin{cases} \mathbb{E}\left\{\ln\left(p_{L,H}\right)\right\} \approx \mathbb{E}\left\{\ln\left(\mu_{p_{L,H}}\right) + \frac{1}{\mu_{p_{L,H}}}\left(p_{L,H} - \mu_{p_{L,H}}\right)\right\} \implies \mathbb{E}\left\{\ln\left(p_{L,H}\right)\right\} \approx \ln\left(\mu_{p_{L,H}}\right) \\ \mathbb{E}\left\{\left(\ln\left(p_{L,H}\right) - \mathbb{E}\left\{\ln\left(p_{L,H}\right)\right\}\right)^2\right\} \approx \mathbb{E}\left\{\left(\frac{1}{\mu_{p_{L,H}}}\left(p_{L,H} - \mu_{p_{L,H}}\right)\right)^2\right\} \approx \left(\frac{1}{\mu_{p_{L,H}}}\right)^2 \sigma_{p_{L,H}}^2 \end{cases} \tag{4.18}$$

The low- and high-energy projections are acquired independently, therefore, we can suppose that p_L and p_H are independent. This hypothesis lets us consider null covariance terms. Using Equation 4.16 and the approximations established in Equation 4.18, we can derive the following expressions for the mean and the variance of the iodine recombined image:

$$\begin{cases} \mathbb{E}\left\{t_{iod}^{simu}\right\} \approx \alpha_0 + \alpha_1 \cdot \ln\left(\mu_{p_L}\right) + \alpha_2 \cdot \ln\left(\mu_{p_H}\right) \\ \qquad = \alpha_0 + \alpha_1 \cdot \ln\left(\mu_{q_L} + \mu_u\right) + \alpha_2 \cdot \ln\left(\mu_{q_L} + \mu_u\right) \\ \mathbb{E}\left\{\left(t_{iod}^{simu} - \mathbb{E}\left\{t_{iod}^{simu}\right\}\right)^2\right\} \approx \left(\frac{\alpha_1}{\mu_{p_L}}\right)^2 \cdot \sigma_{p_L}^2 + \left(\frac{\alpha_2}{\mu_{p_H}}\right)^2 \cdot \sigma_{p_H}^2 \\ \qquad = \left(\frac{\alpha_1}{\mu_{q_L} + \mu_u}\right)^2 \cdot \left(\sigma_{q_L}^2 + \sigma_{elec_L}^2 + \sigma_u^2\right) + \left(\frac{\alpha_2}{\mu_{q_H} + \mu_u}\right)^2 \cdot \left(\sigma_{q_H}^2 + \sigma_{elec_H}^2 + \sigma_u^2\right) \end{cases} \tag{4.19}$$

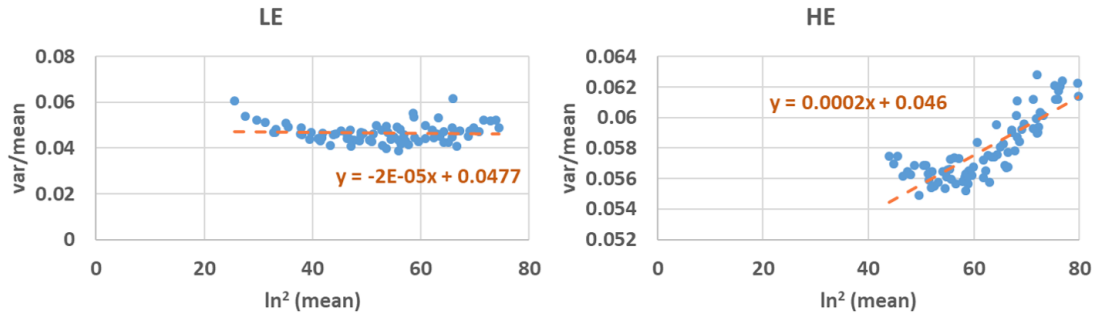

Figure 4.3: Comparison between $\frac{\sigma^2_{p_{L,H}}}{\mu_{p_{L,H}}}$ and $\ln^2\left(\mu_{p_{L,H}}\right)$ for all the experimental acquisitions made in Section 2.3.3 of Chapter 2.

As we can observe, with all the considered hypotheses (decorrelated random processes, independence of low- and high-energy acquisitions, and linear approximation of the logarithm function), the variance of the individual projections does not affect the value of the mean iodine thickness.

In the case of a polyenergetic acquisition, where the quadratic polynomial expression of Equation 4.9 is applied instead, the mean and the variance of the iodine recombined image is described by:

$$\begin{cases} \mathbb{E}\left\{t_{iod}^{exp}\right\} \approx \beta_0 + \beta_1 \cdot \ln\left(\mu_{p_L}\right) + \beta_2 \cdot \ln\left(\mu_{p_H}\right) + \beta_3 \cdot \left(\ln^2\left(\mu_{p_L}\right) + \dfrac{\sigma^2_{p_L}}{\mu_{p_L}}\right) + \beta_4 \cdot \left(\ln^2\left(\mu_{p_H}\right) + \dfrac{\sigma^2_{p_H}}{\mu_{p_H}}\right) \\ \qquad +\beta_5 \cdot \ln\left(\mu_{p_L}\right) \cdot \ln\left(\mu_{p_H}\right) \\ \mathbb{E}\left\{\left(t_{iod}^{exp} - \mathbb{E}\left\{t_{iod}^{exp}\right\}\right)^2\right\} \approx \left(\dfrac{\beta_1}{\mu_{p_L}}\right)^2 \cdot \sigma^2_{p_L} + \left(\dfrac{\beta_2}{\mu_{p_H}}\right)^2 \cdot \sigma^2_{p_H} \\ \qquad + \left(\dfrac{2 \cdot \beta_3 \cdot \ln\left(\mu_{p_L}\right)}{\mu_{p_L}}\right)^2 \cdot \sigma^2_{p_L} + \left(\dfrac{2 \cdot \beta_3 \cdot \ln\left(\mu_{p_H}\right)}{\mu_{p_H}}\right)^2 \cdot \sigma^2_{p_H} + \left(\dfrac{\beta_5}{\mu_{p_L} \cdot \mu_{p_H}}\right)^2 \cdot \sigma^2_{p_L} \cdot \sigma^2_{p_H} \\ \qquad +2 \cdot \beta_1 \cdot \beta_3 \cdot \mathrm{cov}\left(\ln\left(p_L\right), \ln^2\left(p_L\right)\right) + 2 \cdot \beta_1 \cdot \beta_5 \cdot \mathrm{cov}\left(\ln\left(p_L\right), \ln\left(p_L\right) \cdot \ln\left(p_H\right)\right) \\ \qquad +2 \cdot \beta_2 \cdot \beta_4 \cdot \mathrm{cov}\left(\ln\left(p_H\right), \ln^2\left(p_H\right)\right) + 2 \cdot \beta_2 \cdot \beta_5 \cdot \mathrm{cov}\left(\ln\left(p_H\right), \ln\left(p_L\right) \cdot \ln\left(p_H\right)\right) \\ \qquad +2 \cdot \beta_3 \cdot \beta_5 \cdot \mathrm{cov}\left(\ln^2\left(p_L\right), \ln\left(p_L\right) \cdot \ln\left(p_H\right)\right) + 2 \cdot \beta_4 \cdot \beta_5 \cdot \mathrm{cov}\left(\ln^2\left(p_H\right), \ln\left(p_L\right) \cdot \ln\left(p_H\right)\right) \end{cases} \tag{4.20}$$

where $\mathrm{cov}(a, b)$ is the covariance between the processes a and b. The complete development of the variance term can be found in [234].

Unlike the average of recombined simulated images $\mathbb{E}\left\{t_{iod}^{simu}\right\}$ found in Equation 4.19, the average of recombined experimental acquisitions $\mathbb{E}\left\{t_{iod}^{exp}\right\}$ found in Equation 4.20 seems to be influenced by the variance of low- and high-energy acquisitions. To assess this influence, we experimentally analyzed the function $\frac{\sigma^2_{p_{L,H}}}{\mu_{p_{L,H}}} = f\left(\ln^2\left(\mu_{p_{L,H}}\right)\right)$ using all the experimental acquisitions made in Section 2.3.3 of Chapter 2. The results are presented in Figure 4.3. As we observe, under "normal" conditions we have $\ln^2\left(\mu_{p_{L,H}}\right) \gg \frac{\sigma^2_{p_{L,H}}}{\mu_{p_{L,H}}}$ for both low- and high-energy spectra. In other words, the bias introduced in the mean iodine recombined value by the variance of each individual projection is minimal.

Under all the assumptions considered in Equations 4.19 and 4.20, for the same geometry, thickness constraint and projected object, both material decomposition algorithms guarantee

that:

$$\mathbb{E}\left\{t_{iod}^{simu}\right\} = \mathbb{E}\left\{t_{iod}^{exp}\right\} \tag{4.21}$$

and, therefore, for identical set-ups, we should find no difference between the average of simulated recombined images and experimental recombined acquisitions. However, the same is not true for the variance obtained at the end of each recombination approach:

$$\mathbb{E}\left\{\left(t_{iod}^{simu} - \mathbb{E}\left\{t_{iod}^{simu}\right\}\right)^2\right\} \neq \mathbb{E}\left\{\left(t_{iod}^{exp} - \mathbb{E}\left\{t_{iod}^{exp}\right\}\right)^2\right\} \tag{4.22}$$

This difference implies that the SNRs of t_{iod}^{simu} and t_{iod}^{exp} are different. That is, even if we adapted the individual low- and high-energy simulated images in Section 2.3.3 of Chapter 2 to obtain the same average signal and SNR than experimental acquisitions, the visual representation of the contrast uptakes in the simulated images may be compromised. A difference between the SNR of simulated images and experimental acquisitions may affect the detectability and characterization of contrast uptakes. To overcome this issue and provide the same SNR value for both, simulated recombined images and experimental recombined acquisitions, we propose to modify the variance of the low- and high-energy simulated images. In particular, the variance of the quantum noise of our model $\sigma_{q_{L,H}}^2$.

Before presenting this modification, we must introduce another effect to be considered in our evaluation. In the real mammography system, the equivalent iodine thickness image is normalized after recombination, so that each pixel does not represent the actual quantified projected thickness anymore but a proportional representation of it. These are the only images we have access to in real acquisition systems. The new normalized image I_{iod} is characterized by the scale factor Δ as well as by the offset δ:

$$I_{iod} = \Delta \cdot \frac{t_{iod} - \min(t_{iod})}{\max(t_{iod}) - \min(t_{iod})} + \delta \tag{4.23}$$

and, therefore:

$$\mathrm{Var}\left\{I_{iod}\right\} = S \cdot \mathrm{Var}\left\{t_{iod}\right\} \tag{4.24}$$

where $\mathrm{Var}\{a\}$ represents the variance of the process a, and $S = \left(\frac{\Delta}{\max(t_{iod}) - \min(t_{iod})}\right)^2$.

As presented in Section 2.3.3 of Chapter 2, the factor $K_{L,H}$ introduced in our simulations allows us to adjust the total SNR of the low- and high-energy acquisitions. Our goal is to include an additional term κ to modify the SNR of the low- and high-energy images and adapt the SNR of the recombined images. Given this, we will obtain $K_L^\kappa = \kappa \cdot K_L$ and $K_H^\kappa = \kappa \cdot K_H$. In particular, we want to have the following equality:

$$\mathrm{Var}\left\{I_{iod}^{exp}\right\} = \mathrm{Var}\left\{I_{iod}^{simu}\right\} \tag{4.25}$$

where $\mathrm{Var}\left\{I_{iod}^{exp}\right\}$ is the measured variance from a recombined image acquired with a real mammography system, $\mathrm{Var}\left\{I_{iod}^{simu}\right\}$ is the variance of our simulated recombined image, which needs to be adjusted. As we show in Appendix B, the value of κ can be then determined as follows:

$$\kappa = \frac{A \cdot G_L^2 \cdot \sigma_L^2 \cdot K_H + B \cdot G_H^2 \cdot \sigma_H^2 \cdot K_L}{\left(\mathrm{Var}\left\{I_{iod}^{exp}\right\}/S - F\right) \cdot K_L \cdot K_H} \tag{4.26}$$

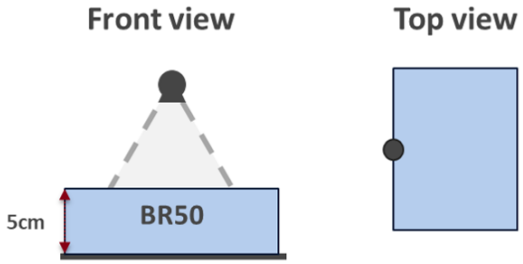

Figure 4.4: Set-up used to validate the performance of the parameter κ used to generate simulated recombined images with the same SNR as experimental recombined images.

Table 4.1: Operational point used to fit the parameter κ of our approach using a **Senographe Pristina** system. The exposure values were divided by the number of low- and high-energy expositions in the 3D mode.

	LE		**HE**	
	Real	*Simulated*	*Real*	*Simulated*
Spectrum	34kVp	23keV (monoenergetic)	49kVp	34keV (monoenergetic)
Target/Filter	Rh/Ag	Rh/Ag	Rh/Cu	Rh/Cu
Exposure	36mAs	36mAs	110mAs	110mAs
Gainmap	$2mm$ Al	$50mm$ PMMA	$2mm$ Al	$50mm$ PMMA

where

$$\begin{aligned} S &= \left(\frac{\Delta}{\max(t_{iod}) - \min(t_{iod})}\right)^2 \\ A &= \left(\frac{\alpha_1}{\mu_{q_L} + \mu_u}\right)^2 \\ B &= \left(\frac{\alpha_2}{\mu_{q_H} + \mu_u}\right)^2 \\ F &= A \cdot \left(\sigma^2_{elec_L} + \sigma^2_u\right) + B \cdot \left(\sigma^2_{elec_H} + \sigma^2_u\right) \end{aligned} \tag{4.27}$$

and $\mu_{L,H} = M \cdot \lambda_{L,H}$ and $\sigma^2_{L,H} = M^2 \cdot \lambda_{L,H}$ are the mean and variance measured values of the simulated low- and high-energy images if the parameters $G_{L,H}$ and $K^{\kappa}_{L,H}$ are not used and no other noise source is present.

To validate this approach and the efficacy of κ to adapt the SNR of simulated recombined images, we use the set-up proposed in Figure 4.4. We placed a $5cm$ plate of CIRS BR50 (50% glandular) over the detector. The validation was only performed using a Senographe Pristina system, considering 2D and 3D acquisition modes. The operational point used in simulated images and experimental acquisitions is presented in Table 4.1.

The results are presented in Figure 4.5. As we can observe, when the factor κ is included in the low- and high-energy simulations, we increase the standard deviation of both projections, increasing at the same time the standard deviation in the simulated recombined image. This helps us to preserve the SNR of experimental recombined images in our simulations. The difference of the SNRs between the simulated recombined images and experimental recombined acquisitions is smaller than 1%.

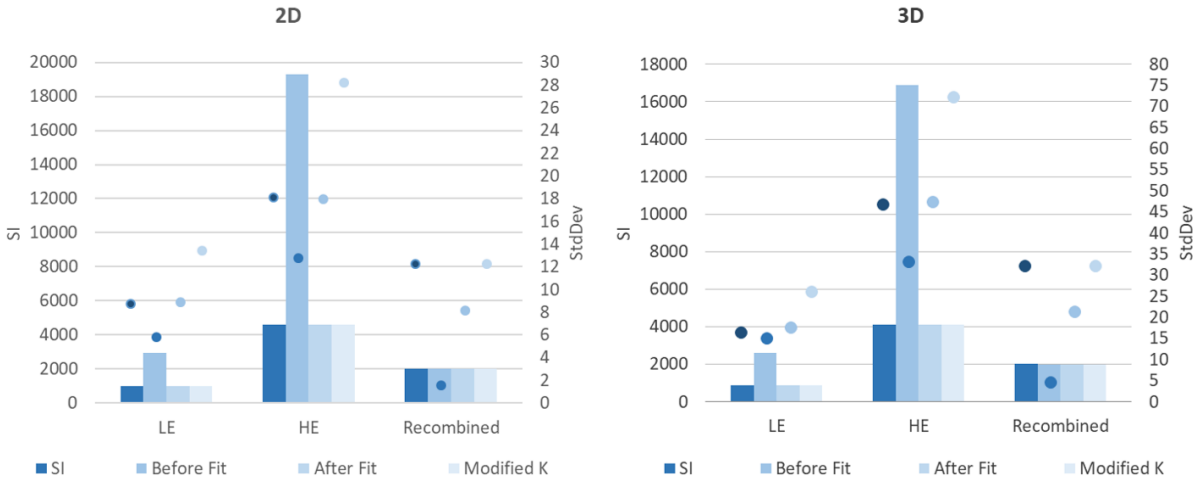

Figure 4.5: Results of the three stages to emulate the quantum noise presented in mammography and tomosynthesis acquisitions using a simulated replica of a Pristina system. From left to right: when there is no SNR correction for the low- and high-energy simulations, when the SNR is adjusted for the low- and high-energy acquisitions, and when the SNR is adapted to match the noise ratio of the recombined experimental acquisitions.

In Figure 4.6 we show several examples of the simulated images before and after the introduction of the parameter κ. As we observe, the simulated recombined images are visually nearer to the experimental ones after we applied the parameter κ, which can help us to understand the relevance of this approach.

4.1.3 Frequency response after material decomposition

The image quality of the equivalent iodine thickness image will not only be impacted by the associated stochastic processes, but also by the spatial resolution of our mammography system. The combination of the low- and high-energy images may imply the loss of some details in the recombined image. Our objective in this section is to compute a formal expression of the recombined frequency response as the combination of the low- and high-energy $MTFs$ of the mammography system. Low- and high-energy $MTFs$ were already studied in Sections 2.1 and 2.2 of Chapter 2. At the same time, we proposed an experimental approach to obtain the analytic expressions of both $MTFs$. Throughout this section we call MTF_{recomb} the frequency response in the recombined image, even if, formally, it is not the modulation transfer function of an imaging system but the frequency analysis of a post-processed image. Therefore, some typical elements found in the system $MTFs$ we already studied may not be true in our MTF_{recomb}, such as maximum response at spatial frequency 0 lp/mm and no null response over all the range of spatial frequencies.

The non-linearity introduced by the log-projections in Equation 4.10 makes it difficult to analyze the frequency response of the recombined image using the same approach as the one introduced in Sections 2.1 and 2.2 of Chapter 2. Therefore, to study the spatial resolution of dual energy systems we need to establish an extension of the theoretical background presented in those sections.

As described by Metz and Doi [206], the total frequency response of the linear composition of several parallel subsystems, each of them with a different spatial resolution, can be formulated

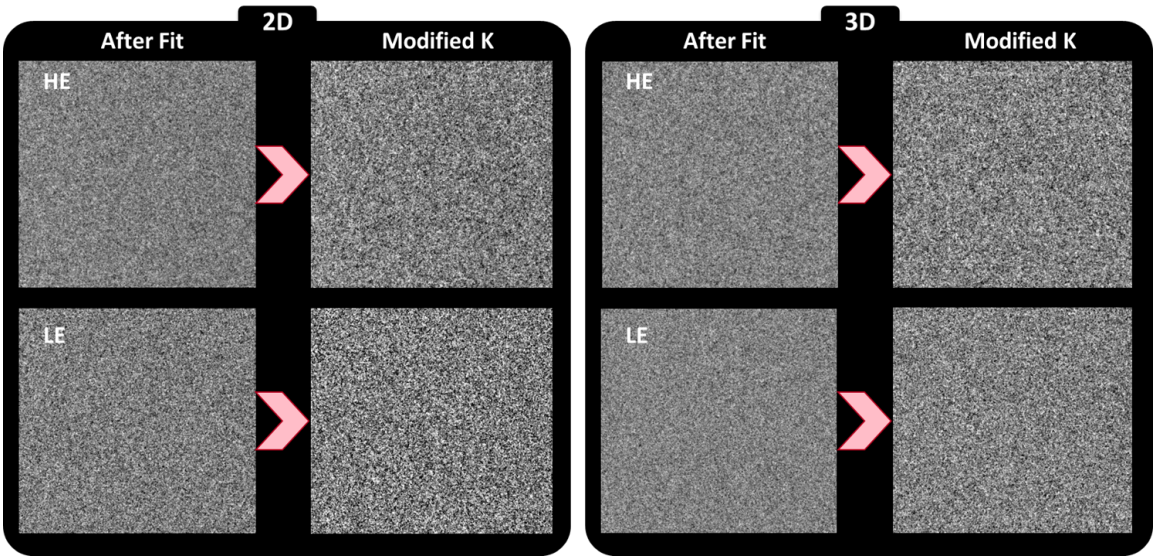

(a) Increment of noise in low- and high-energy simulations after the introduction of the new parameter κ. While the images "after fit" preserves the SNR of experimental low- and high-energy images, the images named "modified K" do not.

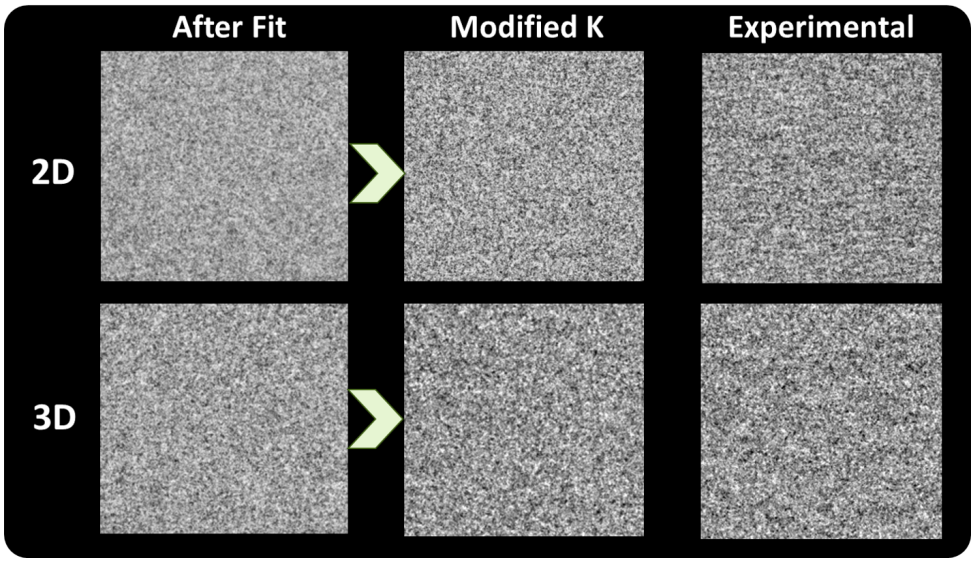

(b) Increment of noise in simulated recombined images. Experimental recombined images are also given to be compared to both simulations.

Figure 4.6: Examples of simulated low- and high-energy images and the corresponding recombined image. "After fit" group the images generated after adjusting the empirical parameters $K_{L,H}$ and $G_{L,H}$. "Modified K" group the images generated after the incorporation of the parameter κ.

as the weighted sum of each subsystem frequency response:

$$MTF_T(u,\nu) = \frac{\sum_{i=1}^{N} \Lambda_i \cdot MTF_i(u,\nu)}{\Lambda_i} \tag{4.28}$$

where N is the number of subsystems, Λ_i is the system gain for each subsystem, and considering that each subsystem frequency response is normalized $MTF_i(0,0) = 1$.

Later, this same formulation was used by Richard and Siewerdsen [249] to express the spatial resolution of recombined images in dual-energy imaging systems. In their approach, they assume that the log-weighted recombination shown in Equation 4.10 can be considered as linear when a small-signal approximation is made. If this is true, the theoretical frequency response of the dual-energy system is given by:

$$MTF_{recomb}(u,\nu) = \left| \frac{\alpha_1 \cdot k_L \cdot MTF_L(u,\nu) + \alpha_2 \cdot k_H \cdot MTF_H(u,\nu)}{\alpha_1 \cdot k_L + \alpha_2 \cdot k_H} \right| \tag{4.29}$$

where α_1 and α_2 are the recombination coefficients as shown in Equation 4.11, $MTF_L(u,\nu)$ and $MTF_H(u,\nu)$ are the frequency responses of the low- and high-energy projections as they were introduced in Sections 2.1 and 2.2 of Chapter 2, and k_L and k_H are the gains determined by the signal in the low- and high-energy log-projections as follows:

$$\begin{cases} k_L = \ln\left(p_L^{obj}\right) - \ln\left(p_L^{back}\right) \\ k_H = \ln\left(p_H^{obj}\right) - \ln\left(p_H^{back}\right) \end{cases} \tag{4.30}$$

where $p_{L,H}^{obj}$ is the value of the projected signal when the object of interest is present, and $p_{L,H}^{back}$ is the value of the projected signal when there is no object of interest, for the low- and high-energy acquisitions. We also define the relative gain parameter k_{rel} and the relative weighting factor ω as:

$$\begin{cases} k_{rel} = k_L / k_H \\ \omega = \alpha_1 / \alpha_2 \end{cases} \tag{4.31}$$

Therefore, Equation 4.29 can be rewritten as:

$$MTF_{recomb}(u,\nu) = \left| \frac{\omega \cdot k_{rel} \cdot MTF_L(u,\nu) + MTF_H(u,\nu)}{\omega \cdot k_{rel} + 1} \right| \tag{4.32}$$

This equation establishes two main dependencies. The first of them, given by ω, expresses that the total frequency response after material decomposition depends of the material basis on which we recombined the low- and high-energy images. Secondly, and more interesting, the dependency on the parameter k_{rel} reveals that the frequency response of the dual-energy system stands on the specific object of interest to be analyzed, as different objects with different compositions will have different relative gains.

To validate the theoretical expression of MTF_{recomb} presented in Equation 4.32, we have simulated the entire acquisition process for two recombined projections using two different materials, aluminum (Al) and PMMA, as examples of two common materials used in dual-energy imaging. We computed the theoretical frequency response of the dual-energy system MTF_{recomb} as the combination of the known low- and high-energy system $MTFs$ using the parameters k_L and k_H specific for each test object. Then, we compared this theoretical frequency response to the MTF measured directly on the recombined image.

The validation was performed using two different test objects for each simulation, a $1mm$ aluminum sheet and a $2mm$ PMMA plate. They were positioned as illustrated in Figure 4.7. The simulations replicated the acquisition process of a Senographe Pristina system removing all stochastic variability (simulations without considering any noise source). The simulations were performed using the operational point presented in Table 4.2. The same software tool presented in Section 2.2 of Chapter 2 was used to measure the MTF in the recombined image.

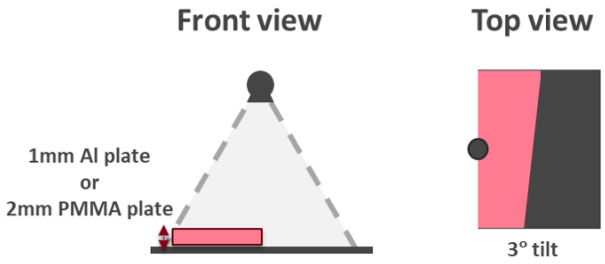

Figure 4.7: Set-up used to validate the theoretical MTF_{recomb} presented in Equation 4.32.

Table 4.2: Operational point used for the generation of low- and high-energy projections to analyze the frequency response of the recombined images. The images were only acquired in 2D mode. To avoid geometrical problems in our simulations, the considered gainmap was only a simulated projection of the air traversed by the X-rays.

	Simulated	
	LE	**HE**
Spectrum	23keV (monoenergetic)	34keV (monoenergetic)
Target/Filter	Rh/Ag	Rh/Cu
Exposure	36mAs	110mAs
Gainmap	air (no phantom)	air (no phantom)

To estimate the theoretical MTF_{recomb} according to Equation 4.32, we used the analytic MTF_L and MTF_H computed in Section 2.2 of Chapter 2. In particular, the theoretical $MTFs$ of the scintillator glare for the low- and high-energy acquisitions were computed from the continuous expression $H_T^{L,H}(u,\nu,t)$ introduced in Section 2.2 for $t=0$, and it was multiplied by the detector frequency response H_{det} presented in Section 2.1.1:

$$MTF_{L,H}(u,\nu) = H_T^{L,H}(u,\nu,0) \cdot H_{det}(u,\nu) \tag{4.33}$$

The value of ω was computed for iodine recombination using Equation 4.31, and the values of k_L and k_H were computed from each of the low- and high-energy log-projections on each side of the test object edge as established in Equation 4.30.

The simulated recombined images are presented in Figure 4.8, while the comparison between the theoretical and measured MTF_{recomb} for both test objects is presented in Figure 4.9. As introduced at the beginning of this section, these recombined $MTFs$ do not follow the typical properties of system $MTFs$. For example, the recombined image of the aluminum plate presents an under-over-shooting artifact at the plate edge, as it can be observed in Figure 4.8. This artifact causes that the maximum frequency response is at 2 lp/mm instead of 0 lp/mm as it is the case in system $MTFs$. We can observe that the theoretical and measured MTF_{recomb} present similar characteristics, however, the low contrast of the recombined image introduces a considerable amount of noise into the measured $MTFs$, increasing the error between both curves ($MSE = 0.02$ for aluminum and $MSE = 0.001$ for PMMA). Additionally, the small difference observed can also be caused by the hypothesis assumed in Equation 4.32. As predicted in Equation 4.32, the curves are completely different for different materials composing the object of interest and, consequently, different values of k_{rel} (Equation 4.31).

In the comparison of the clinical task, between CESM and CEDBT, the object of interest will be composed by a mixture of glandular tissue and a certain concentration of iodine uptake.

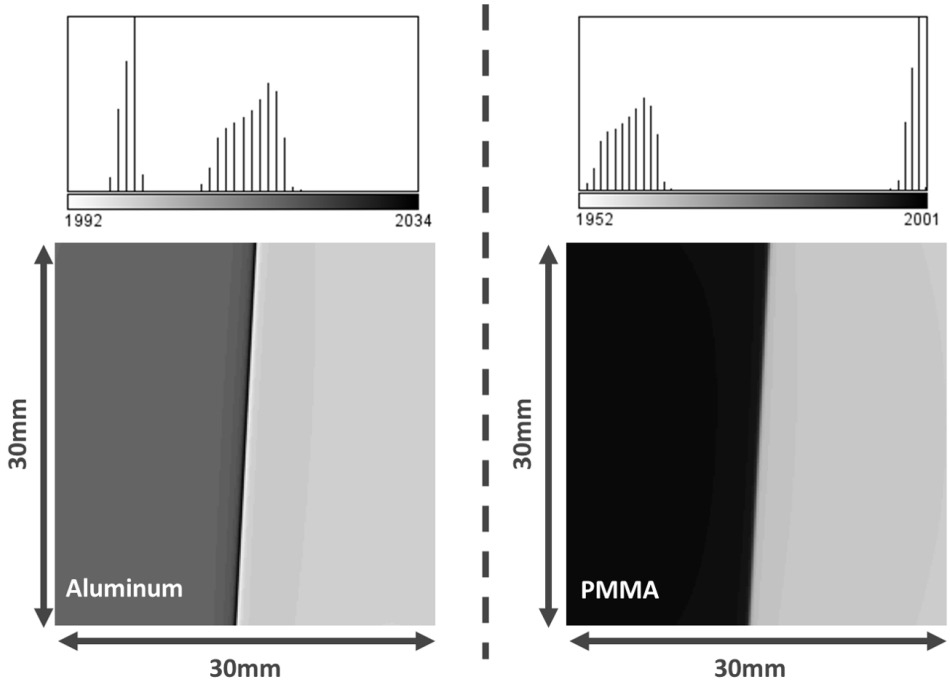

Figure 4.8: ROIs $100 \times 100mm$ of the simulated edges and their respective histograms for the complete simulation. Left: the recombined image obtained after the simulation of an $1mm$ aluminum edge. Right: the recombined image after the simulation of a $2mm$ PMMA edge. Both images were generated without considering any noise source.

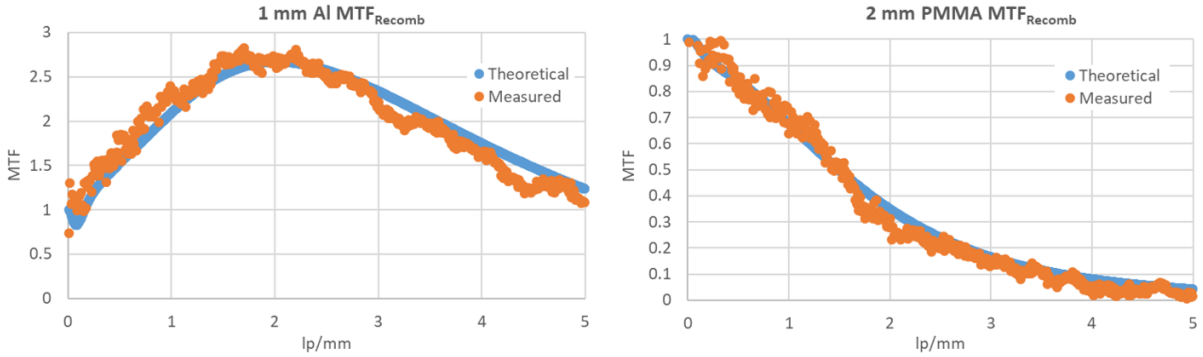

Figure 4.9: Comparison between theoretical and measured frequency responses for dual-energy images. Left: MTF_{recomb} for a $1mm$ aluminum sheet ($k_{rel} = 2.78$, $\omega = -0.38$). Right: MTF_{recomb} for a $2mm$ PMMA plate ($k_{rel} = 1.63$, $\omega = -0.38$).

Otherwise, the background will be constituted by fibroglandular or adipose tissue. The frequency response will then rely upon these combinations of materials. We investigated the dual-energy frequency response for six different combinations of these materials: three mixtures of iodine concentrations ($0.5mg/cm^3$, $1mg/cm^3$ and $2mg/cm^3$) mixed with pure gladular tissue as objects of interest, and two different backgrounds made of pure fibroglandular and pure adipose tissue. Considering the linear attenuation coefficients of each material, we can compute the relative

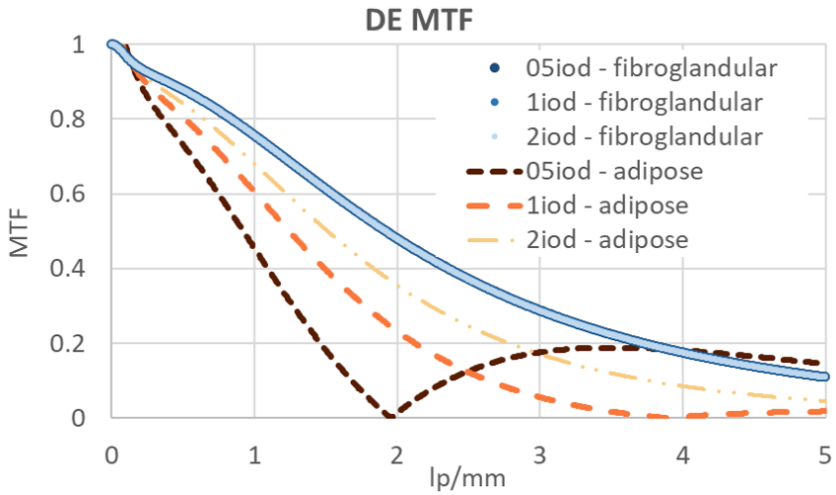

Figure 4.10: MTF_{recomb} for different combinations of objects of interest and backgrounds with $\omega = -0.38$. In dots the superposed three mixtures of iodine concentration and pure glandular tissue over a pure fibroglandular background: $0.5mg/cm^3$ ($k_{rel} = 0.52$), $1mg/cm^3$ ($k_{rel} = 0.52$) and $2mg/cm^3$ ($k_{rel} = 0.52$); and in discontinuous lines the three mixtures over a pure adipose background: $0.5mg/cm^3$ ($k_{rel} = 2.23$), $1mg/cm^3$ ($k_{rel} = 1.95$) and $2mg/cm^3$ ($k_{rel} = 1.60$).

weighting factor as:

$$k_{rel} = \frac{\ln\left(p_L^{obj}\right) - \ln\left(p_L^{back}\right)}{\ln\left(p_H^{obj}\right) - \ln\left(p_H^{back}\right)} = \frac{\ln\left(I_{0,L} \cdot \exp(-\mu_L^{obj} \cdot t)\right) - \ln\left(I_{0,L} \cdot \exp(-\mu_L^{back} \cdot t)\right)}{\ln\left(I_{0,H} \cdot \exp(-\mu_H^{obj} \cdot t)\right) - \ln\left(I_{0,H} \cdot \exp(-\mu_H^{back} \cdot t)\right)} = \frac{\mu_L^{obj} - \mu_L^{back}}{\mu_H^{obj} - \mu_H^{back}} \tag{4.34}$$

where $\mu_{L,H}^{obj}$ is the linear attenuation coefficient of the object of interest and $\mu_{L,H}^{back}$ is the linear attenuation coefficient of the background, for low- and high-energy spectra (respectively L and H).

The results are presented in Figure 4.10. As we can observe, if the background is composed of fibroglandular tissue, the frequency response of the dual energy system will not be impacted by variations of the iodine concentration in the mixture of the object of interest. This is explained by the similar values of k_{rel} shared by the three materials ($0.5mg/cm^3$ with $k_{rel} = 0.52$, $1mg/cm^3$ with $k_{rel} = 0.52$ and $2mg/cm^3$ with $k_{rel} = 0.52$). However, this is no longer true when the background is composed of pure adipose tissue. In this case, the frequency response is modified depending on the level of iodine mixed with the glandular tissue of the object of interest, and even canceling some frequencies. This effect may imply a reduced detectability for some low contrasted iodine structures. This is explained by the different values of k_{rel} obtained for the three materials ($0.5mg/cm^3$ with $k_{rel} = 2.23$, $1mg/cm^3$ with $k_{rel} = 1.95$ and $2mg/cm^3$ with $k_{rel} = 1.60$).

In our discussion, we have not further investigated the implications of the material dependency in the dual-energy frequency response, and we will consider it hereinafter as a concomitant consequence of the material decomposition process commonly shared by CESM and CEDBT.

4.1.4 Memory processes after material decomposition

Another process that may significantly impact a dual-energy system is the variation of the intensity in each pair of low- and high-energy projections over time as a result of the detector lag. As described in Section 2.4 of Chapter 2, this is particularly important in the CEDBT acquisition sequence, when the different angular projections are subsequently acquired and the time between two successive paired acquisitions is very short. In this case, a residual signal from one acquisition may be propagated to consecutive projections. This signal offset added to the projected pairs has not yet been considered in the material decomposition algorithm and, therefore, it introduces a quantification error of the projected equivalent iodine thickness. The error magnitude may differ depending on the recombination approach. Therefore, in this section, we analyze how Equation 4.10, used in monoenergetic simulations to obtain t_{iod}^{simu}, and Equation 4.9, used in polyenergetic experimental acquisitions to obtain t_{iod}^{exp}, influence the anatomical texture cancellation.

We differentiate the *n-th* low- and high-energy projections without lag ($p_L[n]$ and $p_H[n]$) from the *n-th* projections with lag ($P_L[n]$ and $P_H[n]$), estimated as:

$$\begin{cases} P_L[n] = p_L[n] + \sum_{k=1}^{n-1} \left(h_L[2(n-k)] \cdot p_L[k] + h_H[2(n-k)-1] \cdot p_H[k] \right) = p_L[n] + \delta_L[n] \\ P_H[n] = p_H[n] + \sum_{k=1}^{n-1} \left(h_H[2(n-k)] \cdot p_H[k] + h_H[2(n-k)+1] \cdot p_L[k] \right) = p_H[n] + \delta_H[n] \end{cases} \tag{4.35}$$

where $h_{L,H}[n]$ is the *n-th* lag coefficient for low- and high-energy acquisitions (L and H respectively) computed in Section 2.4 of Chapter 2, and $\delta_{L,H}[n]$ is the offset introduced in *n-th* low- and high-energy acquisitions as consequence of the lag effect. The log-projections can be approximated as follows:

$$\begin{cases} \ln\left(P_L[n]\right) = \ln\left(p_L[n] + \delta_L[n]\right) = \ln\left(p_L[n]\right) + \ln\left(1 + \dfrac{\delta_L[n]}{p_L[n]}\right) \approx I_L[n] + \Delta_L[n] \\ \ln\left(P_H[n]\right) = \ln\left(p_H[n] + \delta_H[n]\right) = \ln\left(p_H[n]\right) + \ln\left(1 + \dfrac{\delta_H[n]}{p_H[n]}\right) \approx I_H[n] + \Delta_H[n] \end{cases} \tag{4.36}$$

where $\Delta_{L,H}[n] = \delta_{L,H}[n]/p_{L,H}[n] \ll 1$ for low- and high-energy acquisitions, and $I_{L,H}[n] = \ln\left(p_{L,H}[n]\right)$ represents the log-projected low -and high-energy images.

From now on, we include the following assumptions:

- We do not consider in our model the effect that beam-hardening may have.

- After the adjustment of the average signal and SNR of simulated images performed in Section 2.3.3 of Chapter 2 we consider that the average intensities for low- and high-energy projections for simulated $I_{L,H}^{simu}[n]$ images and experimental $I_{L,H}^{exp}[n]$ acquisitions are the same:

$$I_{L,H}[n] = I_{L,H}^{simu}[n] = I_{L,H}^{exp}[n] \tag{4.37}$$

- The lag coefficients computed in Section 2.4 of Chapter 2 are perfectly estimated and therefore the offset introduced in *n-th* low- and high-energy acquisitions is the same for simulated $\Delta_{L,H}[n]^{simu}$ images and experimental $\Delta_{L,H}[n]^{exp}$ acquisitions:

$$\Delta_{L,H}[n] = \Delta_{L,H}[n]^{simu} = \Delta_{L,H}[n]^{exp} \tag{4.38}$$

Considering all these hypothesis, the effect of lag for monoenergetic simulations can be derived by combining Equations 4.10, 4.37 and 4.38:

$$\begin{aligned} T_{iod}^{simu}[n] &= \alpha_0^{simu} + \alpha_1^{simu} \cdot (I_L[n] + \Delta_L[n]) + \alpha_2^{simu} \cdot (I_H[n] + \Delta_H[n]) \\ &= t_{iod}^{simu}[n] + \alpha_1^{simu} \cdot \Delta_L[n] + \alpha_2^{mono} \cdot \Delta_H[n] \end{aligned} \tag{4.39}$$

where $T_{iod}^{simu}[n]$ is the equivalent iodine thickness for the *n-th* pair of low- and high-monoenergetic simulated images with lag, $t_{iod}^{simu}[n]$ the equivalent iodine thickness if there is no lag present in the simulated acquisition process, and α_i^{simu} with $i \in \{0, 1, 2\}$ are the recombination coefficients for monoenergetic acquisitions computed with Equation 4.11.

Similarly, if we consider the lag process for the recombination of polyenergetic experimental images (Equation 4.9), we obtain:

$$\begin{aligned} T_{iod}^{exp}[n] &= \alpha_0^{exp} + \alpha_1^{exp} \cdot (I_L[n] + \Delta_L[n]) + \alpha_2^{exp} \cdot (I_H[n] + \Delta_H[n]) + \alpha_3^{exp} \cdot (I_L[n] + \Delta_L[n])^2 \\ &\quad + \alpha_4^{exp} \cdot (I_H[n] + \Delta_H[n])^2 + \alpha_5^{exp} \cdot (I_L[n] + \Delta_L[n]) \cdot (I_H[n] + \Delta_H[n]) \\ &= t_{iod}^{exp}[n] + \alpha_1^{exp} \cdot \Delta_L[n] + \alpha_2^{exp} \cdot \Delta_H[n] + \alpha_3^{exp} \cdot \left(2I_L[n] \cdot \Delta_L[n] + \Delta_L^2[n]\right) \\ &\quad + \alpha_4^{exp} \cdot \left(2I_H[n] \cdot \Delta_H[n] + \Delta_H^2[n]\right) \\ &\quad + \alpha_5^{exp} \cdot (I_L[n] \cdot \Delta_L[n] + I_H[n] \cdot \Delta_H[n] + \Delta_L[n] \cdot \Delta_H[n]) \end{aligned} \tag{4.40}$$

where $T_{iod}^{exp}[n]$ is the equivalent iodine thickness for the *n-th* pair of low- and high-polyenergetic acquisitions with lag, $t_{iod}^{exp}[n]$ the equivalent iodine thickness if there is no lag present in the acquisition process, and α_i^{exp} with $i \in \{0, 1, 2, 3, 4, 5\}$ are the recombination coefficients for polyenergetic acquisitions computed with the method proposed by Puong [234].

Assuming that the image recombination process described by Equations 4.10 and 4.9 provides the same average iodine equivalent thickness image, i.e. $t_{iod}^{simu} = t_{iod}^{exp}$, the signal difference between our simulations and the real acquisitions caused by the lag effect can be expressed as:

$$\begin{aligned} T_{iod}^{exp}[n] - T_{iod}^{simu}[n] &= \Delta_L[n] \cdot \left(\alpha_1^{exp} + \alpha_3^{exp} \cdot (\Delta_L[n] + 2I_L[n]) + \alpha_5^{exp} \cdot I_H[n] - \alpha_1^{simu}\right) \\ &\quad + \Delta_H[n] \cdot \left(\alpha_2^{exp} + \alpha_4^{exp} \cdot (\Delta_H[n] + 2I_H[n]) + \alpha_5^{exp} \cdot I_L[n] - \alpha_2^{simu}\right) \\ &\quad + \alpha_5^{exp} \cdot \Delta_L[n] \cdot \Delta_H[n] \end{aligned} \tag{4.41}$$

This difference is not specific to the quadratic image recombination (Equation 4.9). A similar result may be found if the approach chosen for image recombination in CEDBT is the log-weighted subtraction of low- and high-energy images (Equation 4.10), as it is the case in several studies where the performance of CEDBT was evaluated [107, 131, 134, 266].

In Equation 4.41, we demonstrated that subsequent recombined images from simulated images and experimental acquisitions may have a different average signal intensity. We need to evaluate the magnitude of this difference. To do that, we computed the analytic low- and high-energy signal intensities, $p_L[n]$ and $p_H[n]$ respectively, for different materials and one unique trajectory (one unique sample point), assuming that the average signal for simulated (monoenergetic) images and experimental (polyenergetic) acquisitions is the same. Then, we used Equations 4.39 and 4.40 to compute $T_{iod}^{simu}[n]$ and $T_{iod}^{exp}[n]$. In other words, in this validation, both $T_{iod}^{simu}[n]$ and $T_{iod}^{exp}[n]$ were simulated for a single sample point.

In particular, we computed the sample intensities $p_L[0]$ and $p_H[0]$ using Equation 4.4 and considering the characteristic parameters $\eta(E)$ and $\Gamma(E)$ of a Senographe Pristina detector. $I_0(E)$ was computed according to the operational point given in Table 4.3. The polyenergetic spectra

Table 4.3: Operational point used for the generation of low- and high-energy intensities $p_L[0]$ and $p_H[0]$ to analyze the impact of lag in the recombined images. We considered only the 3D mode so the mAs values were divided by the number of projections of the acquisitions sequence (9 projections). No gainmap was considered because we limited our study to generate a unique sample intensity value.

	Simulated (one sample point)	
	LE	**HE**
Spectrum	34kVp (SpeXim)	49kVp (SpeXim)
Target/Filter	Rh/Ag	Rh/Cu
Exposure	36mAs	110mAs
Gainmap	No gainmap	No gainmap

were simulated using the "Spectrum Simulator" SpeXim previously developed and validated at GE Healthcare for mammography spectra [209]. We considered a static CEDBT acquisition sequence for a Senographe Pristina system where $p_{L,H}[i] = p_{L,H}[j]\ \forall(i,j) \in \{1...9\}$. Three different materials with $5cm$ thickness were used: pure glandular tissue (CIRS BR100), 50% mixture of glandular and adipose tissue (CIRS BR50), and pure adipose tissue (CIRS BR0). $P_L[n]$ and $P_H[n]$ were computed according to Equation 4.35 using the lag coefficients obtained in Section 2.4 of Chapter 2. Coefficients α_i^{simu} with $i \in \{0,1,2\}$ were computed using Equation 4.11 and coefficients α_i^{exp} with $i \in \{0,1,2,3,4,5\}$ were retrieved using the method proposed by Puong [234]. Then, we computed $T_{iod}^{simu}[n]$ and $T_{iod}^{exp}[n]$ using the coefficients α_i^{simu} and α_i^{exp}, respectively. The images were normalized using Equation 4.23, mapping the equivalent iodine thickness of the glandular and adipose mixture to a reference intensity value representing no iodine presence in the image (in all our experiences this value was set to 2000 counts). Additionally, we compared the simulated $T_{iod}^{simu}[n]$ and $T_{iod}^{exp}[n]$ signals with the real intensity values of a recombined image given by a Senographe Pristina mammography system. The average intensity of a 200×200 pixels ROI over a $5cm$ plate of pure adipose equivalent tissue (CIRS BR0) for the first 6 recombined pairs was considered.

The results are illustrated in Figure 4.11. As we can observe, from the second recombined frame, the texture cancellation ceases to be perfect, and the recombined intensities for CIRS BR0 and BR100 are no longer the same as the no-iodine reference. This is a direct cause of the lag effect. In particular, we find a negative iodine thickness in CIRS BR0 plates and a positive iodine thickness in CIRS BR100 plates. The small differences between the acquired curve (in continuous green) and the simulated curve using the polyenergetic recombination coefficients α_i^{exp} (in discontinuous dark yellow) can be attributed to tube instabilities during acquisition. Therefore, in a Senographe Pristina, the magnitude of the difference between monoenergetic (continuous blue) and polyenergetic (discontinuous yellow) in subsequent recombined images is lower than 2 counts, which represents a surface contrast uptake equal to 0.05 mg/cm^2.

4.1.5 Validation of simulated recombined pairs

For the validation of the simulated images after recombination, we propose three set-ups, illustrated in Figure 4.12, using different available test objects containing iodine inserts:

- The RK-CIRS test object is composed of a semi-circular $10mm$ thick plate with two symmetrical halves (two equal quadrants). Each half has an equivalent attenuation to 0% and 50% glandular densities (CIRS BR0 and BR50), respectively. Each half includes 4

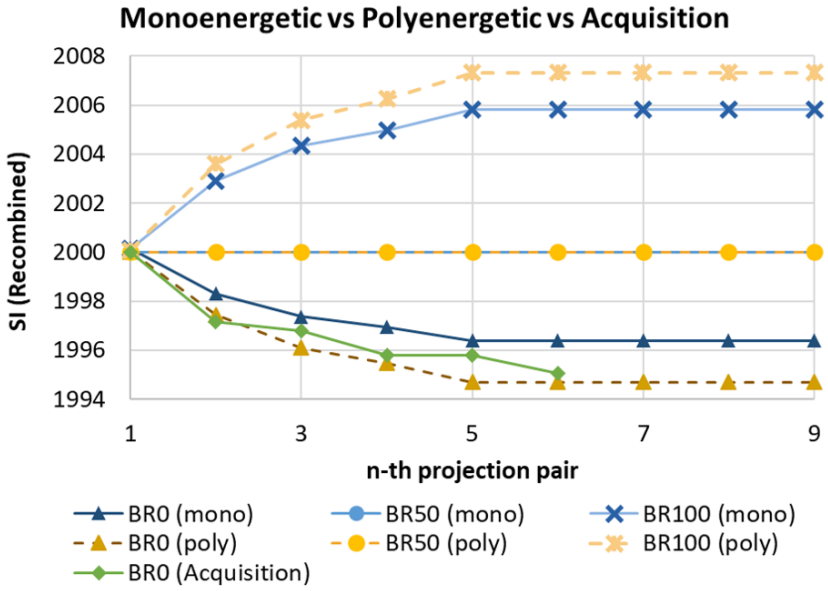

Figure 4.11: Intensity profiles of recombined signals from monoenergetic (in continuous blue) and polyenergetic (in discontinuous yellow) simulated samples for $5cm$ CIRS BR0, BR50 and BR100 plates. The average intensity profile (in continuous green) of a recombined signal from a real acquisition of a $5cm$ CIRS BR0 plate is also given for comparison.

cylindrical inserts with iodine volumetric concentrations equal to 0.25, 0.5, 1 and $2mg/cm^3$. The cylinder dimensions are $10mm$ in length and $10mm$ in diameter.

- The Sunny15 test object is composed of a rectangular $10mm$ thick plate with equivalent attenuation to 0% glandular density and two symmetric halves. Each half contains 6 different cylindrical inserts with iodine volumetric concentrations equal to 0.1, 0.2, 0.5, 1, 2 and $4mg/cm^3$. The cylinder dimensions are $10mm$ in length and $10mm$ in diameter.

- The SunnyMorpho test object is composed of a rectangular $20mm$ thick plate made of PMMA. It includes 4 spherical inserts with 2 different iodine volumetric concentrations (1 and $2mg/cm^3$) and 2 different radii (2.5 and $5mm$).

Each phantom was placed at the middle of a pile of CIRS BR50 plates to complete a total height of $50mm$ for each set-up. Each of these test objects was also digitally replicated using the analytic definitions provided by the FORBILD syntax[1].

The validation was performed for two mammography systems: Senographe Pristina, and Senographe DS. The operational points for each system were fixed as shown in Tables 4.4 and 4.5. To generate equivalent simulated images, these set-ups were adapted in the X-ray simulation platform following the methods developed in Chapter 2. Due to a limited access to the Senographe DS system, the validation of the recombined images was only performed using the Sunny15 test object for this mammography unit.

To complete the validation, two types of sequences were acquired and simulated: a CESM sequence (one low- and high-energy projections) using only the Pristina system and its simulated

[1] `http://www.imp.uni-erlangen.de/forbild/`

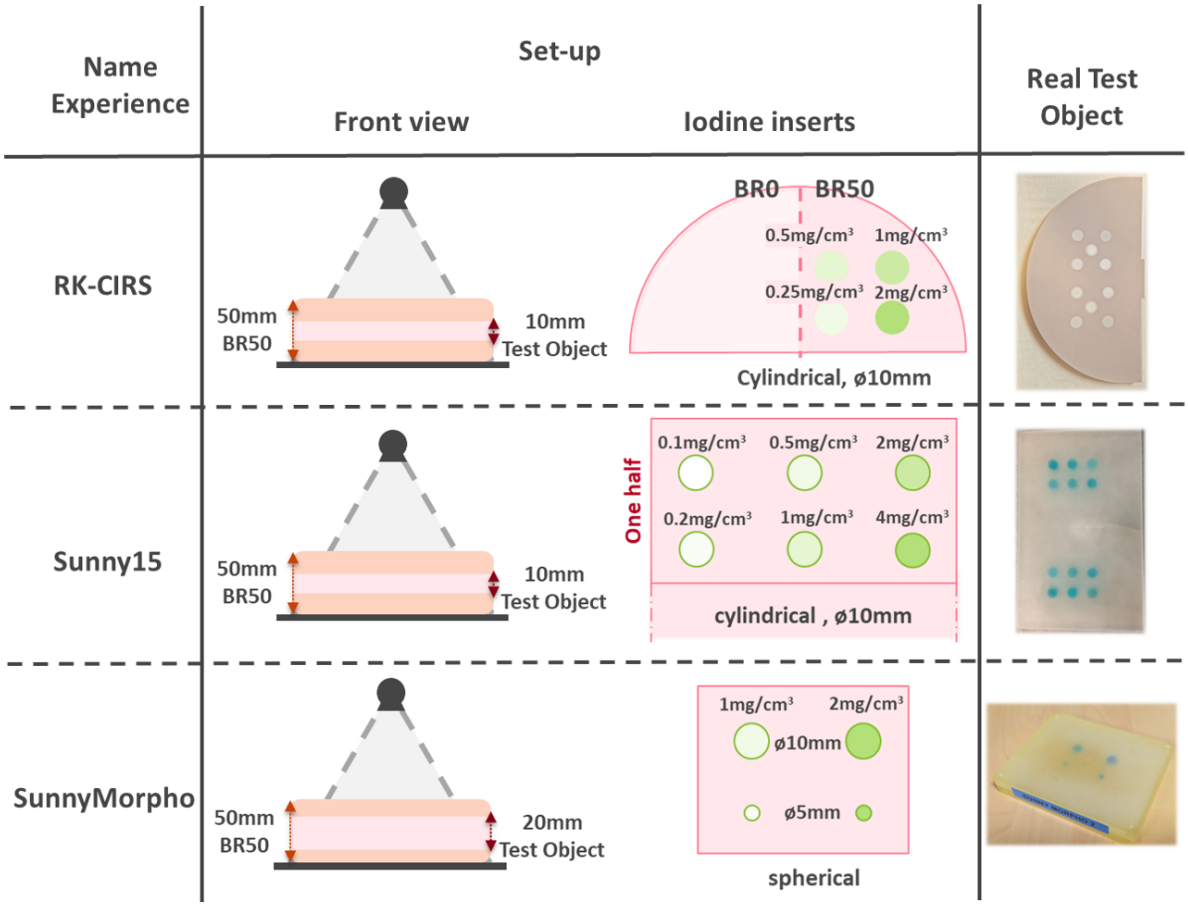

Figure 4.12: Set-up and real test objects used for the validation of the recombined images obtained with the simulation platform.

Table 4.4: Operational point used for the validation of the recombined pairs for the **Pristina** system. The exposure values were divided by the number of low- and high-energy expositions.

	LE		**HE**	
	Real	*Simulated*	*Real*	*Simulated*
Spectrum	34kVp	23keV (monoenergetic)	49kVp	34keV (monoenergetic)
Target/Filter	Rh/Ag	Rh/Ag	Rh/Cu	Rh/Cu
Exposure	36mAs	36mAs	110mAs	110mAs
Gainmap	2mm Al	50mm PMMA	2mm Al	50mm PMMA

replica; and a static CEDBT sequence (several low- and high-energy projections at the angular position of the X-ray tube) using the Pristina and DS systems and their simulated replicas.

For each test object, each type of acquisition sequence and each mammography system, the validation was performed by measuring the average and standard deviation of a ROI per iodine insert and four ROIs around each insert. Then, the contrast between the signal over the iodine inserts and the background surrounding them was computed. The comparison between the iodine contrasts and the background standard deviation in acquired and simulated images, as well as an example of the chosen ROIs, is presented in Figure 4.13.

Table 4.5: Operational point used for the validation of the recombined pairs for the **DS** system. The exposure values were divided by the number of low- and high-energy expositions.

	LE		**HE**	
	Real	*Simulated*	*Real*	*Simulated*
Spectrum	28kVp	20keV (monoenergetic)	49kVp	39keV (monoenergetic)
Target/Filter	Mo/Mo	Mo/Mo	Rh/Cu	Rh/Cu
Exposure	110mAs	110mAs	320mAs	320mAs
Gainmap	25mm PMMA	50mm PMMA	25mm PMMA	50mm PMMA

We observe that, for all the measures made in the recombined images of the real acquisitions, identical iodine inserts do not share the exact same recombined signal contrast. The bias introduced by the variability of the materials composing the different test objects, plus the presence of impurities, may lead to variations of the equivalent linear attenuation coefficients of the object. However, the lack of information about the purity of the materials avoid to mirror the same bias in simulated objects, where we model pure ideal materials. Among the test objects used to validate the recombined images from the Pristina system, we found that our simulations offer a better correlation with the RK-CIRS test object. In this test object we found the following contrast difference between both recombined images: 2.96 ($0.25mg/cm^3$), 0.49 ($0.5mg/cm^3$), 0.66 ($1mg/cm^3$) and 1.05 ($2mg/cm^3$) in CESM images, and 5.58 ($0.25mg/cm^3$), 0.71 ($0.5mg/cm^3$), 2.13 ($1mg/cm^3$) and 4.15 ($2mg/cm^3$) in CEDBT images. These differences are smaller than the differences obtained between the different test objects used in this validation and, consequently, are considered as tolerable errors which may not imply severe bias between the real acquisitions system and our simulation platform.

4.2 Image reconstruction

In Digital Breast Tomosynthesis (DBT), after the acquisition sequence, the projections are submitted to a reconstruction algorithm, providing of cross-sectional images of the breast. The main difference with respect to Computed Tomography (CT) is the limited angular range considered during the acquisition sequence. This limit, added to the finite number of projections with a higher angular gap between them, leads to an ill-conditioned inverse problem where the number of unknowns is much larger than the number of available data. Consequently, there is no unique solution to the problem. Regularization constraints are integrated in the two classical classes of methods, analytical and iterative ones. A review of several reconstruction algorithms used in DBT can be found in [137, 246].

4.2.1 Reconstruction in digital breast tomosynthesis (DBT)

The analytical approximation most commonly used in DBT image reconstruction is the **Filtered Brackprojection (FBP)**. The underlying model of the image acquisition chain is based on the Radon transform $\mathcal{R}\{\cdot\}$, that maps an object distribution to a set of line integrals [239]. In particular, for the CT parallel geometry illustrated in Figure 4.14a, we can associate the object attenuation distribution $\bar{\mu}(\boldsymbol{r})$ and the line integrals $g_\theta(s)$ using the Radon transform:

$$g_\theta(s) = \mathcal{R}_\theta\{\bar{\mu}\}(s) = \int_{-\infty}^{+\infty} \bar{\mu}(s \cdot \boldsymbol{u} + t \cdot \boldsymbol{n}) dt \tag{4.42}$$

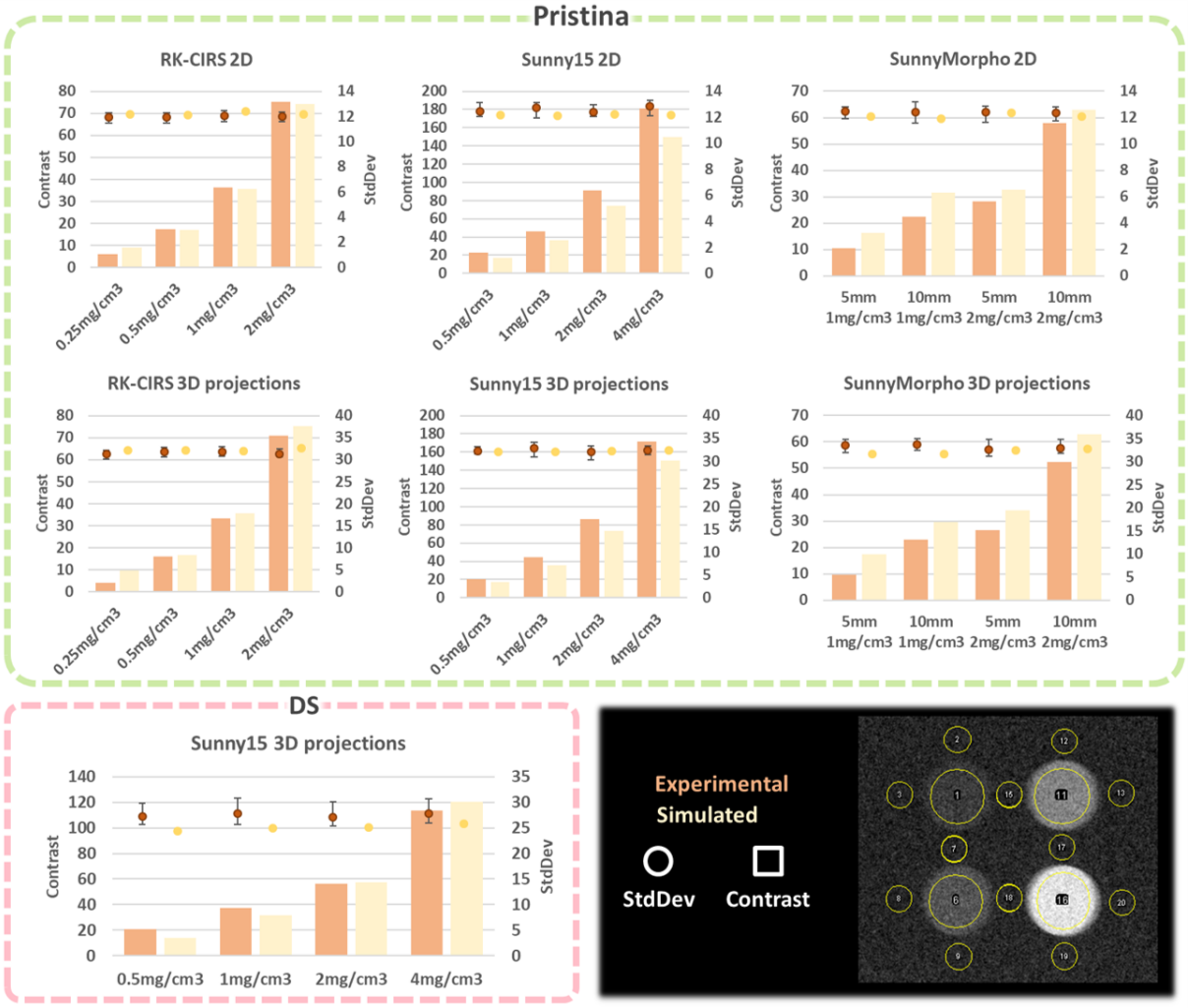

Figure 4.13: Comparison between recombined pairs of low- and high-energy images acquired in real mammography systems and recombined pairs generated with the X-ray simulation platform. The rectangular bars represent the measured mean signals. Similarly, the round markers represent the measured standard deviations (error bars for minimum and maximum standard deviation found between 5 different acquisitions). We compared three different set-ups (RK-CIRS, Sunny15 and SunnyMorpho), two modalities (2D and 3D) and two systems (Senographe Pristina and Senographe DS). An example of the selected ROIs is also presented.

where $\boldsymbol{u} = (\cos(\theta), \sin(\theta)) \in \mathbb{R}^2$ is a unit vector defining the angle of the projection, $\boldsymbol{n} = (\sin(\theta), -\cos(\theta)) \in \mathbb{R}^2$ is a unit vector perpendicular to $\boldsymbol{u}$, and $s = \boldsymbol{r}^\intercal \cdot \boldsymbol{u}$ is the distance of the line from the origin, where $\boldsymbol{r} = (x, z) \in \mathbb{R}^2$ is the domain of the object distribution.

The central slice theorem [13] establishes that the 1D Fourier transform of a projection, characterized by $\theta = \theta'$, corresponds to a line of the 2D Fourier transform of the object distribution $\mathcal{F}_{2D}\{\bar{\mu}\}(\boldsymbol{\omega}) = \bar{M}(\boldsymbol{\omega})$, where $\boldsymbol{\omega} = (\omega_x, \omega_z) \in \mathbb{R}^2$:

$$\bar{M}(\omega \cdot \cos(\theta'), \omega \cdot \sin(\theta')) = \mathcal{F}_{1D}\{g_{\theta'}(s)\}(\omega) \tag{4.43}$$

Therefore, using the 2D inverse Fourier transform in polar coordinates (ω, θ), it can be shown [148] that the inverse Radon transform is given by:

$$\bar{\mu}(\boldsymbol{r}) = \int_{\theta=0}^{\pi} \mathcal{F}_{2D}^{-1}\{|\omega| \mathcal{F}_{1D}\{g_\theta(s)\}(\omega \cdot \cos(\theta), \omega \cdot \sin(\theta))\}\Big|_{s=\boldsymbol{r}^\intercal \cdot \boldsymbol{u}} d\theta \tag{4.44}$$

where $\mathcal{F}_{1D}\{\cdot\}$ is the 1D Fourier transform and $\mathcal{F}_{2D}^{-1}\{\cdot\}$ is the 2D the inverse Fourier transform. Therefore, the object attenuation distribution can be computed by filtering the projections with a "ramp" filter $H_{FBP}(\omega) = |\omega|$, then, backprojecting over the volume domain and finally adding to the other backprojeted projections defined by θ.

The importance of the "ramp" filter is shown in Figure 4.14b. If simple backprojection (SBP) is applied (without filtering), the sampling density decreases when we move away from the center of the object, causing that the point spread function is not an ideal point-like distribution but a function of $1/\|r\|$. This effect is alleviated by the "ramp" filter, homogenizing the sampling density over the volume domain. However, if the acquired data are noisy, this filter increases the high frequency noise which may reduce the image quality. To reduce this effect, we can assume that the useful signal is band limited. Because of this, FBP can be regularized by filtering with a supplementary filter, usually called apodization function in the spectral domain. Therefore, the final filter applied to projections will be:

$$H_T(\omega) = |\omega| \cdot H_{apod}(\omega) \tag{4.45}$$

where $H_{apod}(\omega)$ can be chosen from a large selection of functions [311].

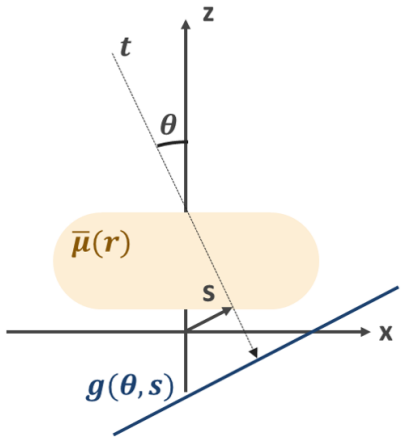

(a) Parallel projection geometry and traditional Radon transform. The object $\bar{\mu}(r)$ is projected onto the plane defined by θ and s giving as result $g(\theta, s)$.

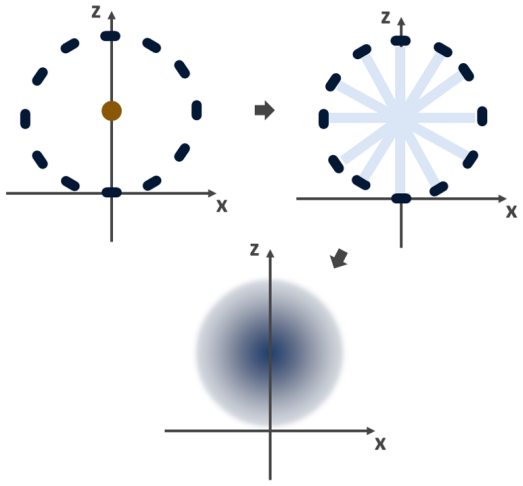

(b) Density of the sampled distribution as a result of simple backprojection. We can observe that the object is blurred all over the volume domain.

Figure 4.14: Projection and backprojection in CT parallel beam geometry.

However, the DBT acquisition sequence does not respect the continuous angular sampling assumed in Equation 4.44. Instead, as we already introduced, in DBT we acquire a limited number of angular projections at discrete positions of the source. Therefore, DBT suffers from data incompleteness. The central slice theorem helps us to understand this. On the one hand,

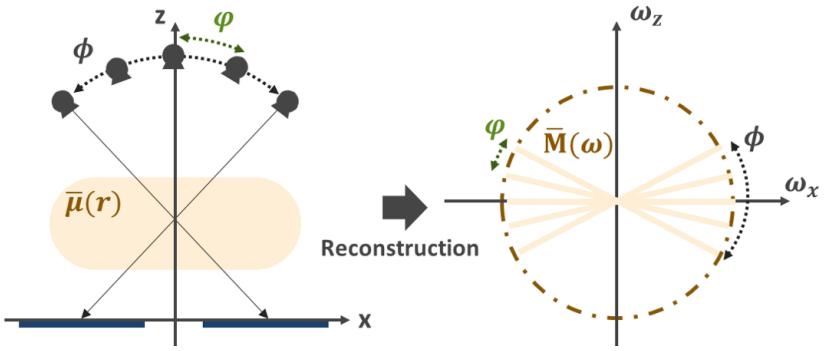

Figure 4.15: Duality between spatial sampling and the correspondent information in the Fourier domain for tomosynthesis acquisitions. As we can observe, a limited angular range implies that a large amount of data in the frequency domain is missing.

due to a limited angular range ϕ, the projections acquired in DBT only sample a partial section of the object frequency spectrum. Thus, the smaller the angular range, the smaller the sampled Fourier region of the object. On the other hand, as in CT, the discrete angular sampling along the angular range defined by ϕ precludes to retrieve the spectral information between two consecutive angular steps separated by φ. Both issues are illustrated in Figure 4.15. Consequently, Equation 4.44 is discretized as follows:

$$\bar{\mu}(\boldsymbol{r}) = \sum_{i=0}^{\phi/\varphi} \mathcal{F}_{2D}^{-1}\{|\omega|\mathcal{F}_{1D}\{g_{\theta_i}(s)\}(\omega \cdot \cos(\theta_i), \omega \cdot \sin(\theta_i))\}\Big|_{s=\boldsymbol{r}^\intercal \cdot \boldsymbol{u}} \tag{4.46}$$

where $\theta_i = i \cdot \varphi - \frac{\phi}{2}$.

This data incompleteness induces several artifacts in the reconstructed object, in particular, streak artifacts related to localized objects, signal overshoots in the scan direction over high contrasted objects, and replication artifacts at the edges of long and highly contrasted objects.

Another class of methods relies on the formulation of the reconstruction as a minimization problem under regularity assumption:

$$\bar{\mu}'(r) = \arg\min_{\bar{\mu}}\{D(f(\bar{\mu}(r)), \mathbb{G}) + \lambda \cdot R(\bar{\mu}(r))\} \tag{4.47}$$

where $\bar{\mu}'(r)$ is the final reconstructed object, $D(x_1, x_2)$ is the data fidelity function measuring the dissimilarity between x_1 and x_2, $f(x)$ is a function modeling the projection process, $\mathbb{G}$ represents the stack of all available projections $g_\theta(s)$, λ is a constant controlling the smoothness applied to the final reconstructed object, and $R(\cdot)$ is a penalization function measuring the roughness of the solution. Due to the large dimensionality of the problem it cannot be solved analytically. Instead, various **iterative image reconstruction (IIR)** methods have been proposed studying different projection models, as well as diverse regularization functions and optimization methods to minimize the problem [267, 310]. Despite the heterogeneity of these solutions, two groups can be differentiated: algebraic reconstruction techniques and statistical reconstruction methods.

In *algebraic reconstruction*, the problem is discretized and formulated as a system of linear equations with $f(x) = Ax$, where A is the projection matrix that can be estimated as the intersection length between the path of each X-ray and element of the object distribution. The most common algorithm of this group is the Simultaneous Algebraic Reconstruction Technique (SART) [4]. In *statistical reconstruction*, the unknown object distribution is considered as a

random variable and $f(x)$ follows a specific probability distribution. The advantage of this method is that it can consider the underlying physical processes of the image acquisition process and, therefore, the noises and inhomogeneities that the acquired data may contain.

The regularity assumption is introduced to mitigate the ill-posed nature of the tomosynthesis reconstruction due to the missing data. The goal of regularization is to find a reconstructed volume that is the most similar to the true projections and which meets prior knowledge on the solution, such as geometric or stochastic features. Several regularization functions have been investigated in tomography reconstruction, including quadratic [251], nonquadratic [106] functions, and total variation (TV) [169] methods.

The nature of CEDBT images is slightly different from that of DBT images, with higher contrasted objects and less high frequency information due to anatomical texture cancellation. This motivates new optimized approaches, based on the same theoretical framework as exposed here, more adapted to these characteristics. In the following sections we explore the FBP, iterative and statistical reconstruction methods introduced for CEDBT, as well as a new FBP approach optimized for the CEDBT clinical task.

4.2.2 Reconstruction in CEDBT

The idea behind CEDBT is to obtain a volume where the gray level of each voxel represents a local iodine volumetric concentration. Consequently, the main difference between DBT and CEDBT is the recombination stage of the low- and high-energy data. As introduced in Section 4.1, the order of the reconstruction and recombination steps is not trivial and may influence the final image quality. Each of the potential worflows has its own benefits and drawbacks [266].

First, each pair of low- and high-energy projections can be considered as two independent DBT acquisitions, reconstructed as two independent volumes and then recombined in the volume domain. This order of operations assumes that acquisition sequences are completely independent and, thus, the acquisition geometry can be different for low- and high-energy projections without any impact on the final recombined volume. However, according to what we have presented in Section 4.1, due to the beam-hardening effect the estimated attenuation volumes $\bar{\mu}_L(r)$ and $\bar{\mu}_H(r)$ deviate from the real material attenuation values at position r. This difference between the estimated and the true volumes may introduce several artifacts in the recombined volumes. This workflow has been implemented in several references [48, 107, 131, 134, 185, 200].

In a second class of approaches, the recombined images can be computed before the reconstruction step. If the recombination process considers the beam-hardening effect, the equivalent iodine thickness is free from any error related to this physical phenomenon, avoiding misrepresentations in the reconstructed iodine volume. Yet, a defect in the system geometry may produce misregistered low- an high-energy pairs and, therefore, artifacts in the recombined projections. This workflow has been also considered by a large amount of CEDBT studies [39, 49, 53, 139, 124, 132, 133, 171, 235, 259]. In our work, we considered the low- and high-energy pairs perfectly registered. Consequently, we apply the reconstruction algorithm to the equivalent iodine thickness projections, recombined using Equation 4.9.

When reconstruction follows recombination, we can distinguish the main differences between DBT and CEDBT reconstruction. In DBT, the line integral presented in Equation 4.42 is described by Equations 4.1 and 4.4 as follows:

$$g_\theta(s) = \sum_{m=1}^{M} \left(\frac{\mu}{\rho}\right)_m (E) \cdot \delta_m(\theta, s) \approx -\ln\left(\frac{p(\theta, s)}{I_0 \cdot \eta \cdot \Gamma}\right) \tag{4.48}$$

so, in the acquired images, all the heterogeneous materials composing an object, such as glandular and adipose tissues, are projected over the same surface. The goal of reconstruction, in this case, is to estimate an object distribution proportional to $\sum_{m=1}^{M}(\mu/\rho)_m(E)\cdot C_{v,m}(r)$.

In CEDBT, the goal of the reconstruction is different. We only work with one of the materials present in the object. The available data is proportional to $\frac{\delta_{iodine}}{\rho_{iodine}}$, the equivalent projected iodine thickness, and we search to obtain an object distribution proportional to $\frac{C_{v,iodine}}{\rho_{iodine}}$, the local volumetric concentration of iodine. Having only one material increases the sparsity of the reconstructed volume.

The z-resolution of iodine contrast is consequence of the data incompleteness of tomosynthesis acquisition. For example, assuming the schema illustrated in Figure 4.16, where we have a single contrast uptake of height h inside an object of height H, the minimal thickness Δz which can be correctly reconstructed will depend on the angular range ϕ of the acquisition sequence and the diameter of the contrast uptake of interest L. This dependence is equal to:

$$\Delta z = \frac{L}{\tan(\phi/2)} \tag{4.49}$$

Therefore, if the maximal spatial resolution is Δz, the reconstructed slices will not be longer proportional to the local volumetric concentration, but to $\int_{\Delta z}\frac{C_{v,iodine}}{\rho_{iodine}}dz$ instead. Then, if the height h is smaller than the spatial resolution Δz, the minimal iodine concentration which can be reconstructed is:

$$\int_h \frac{C_{v,iodine}}{\rho_{iodine}}dz = \frac{\delta_{iodine}^{object}}{\rho_{iodine}^{object}} \tag{4.50}$$

where $\frac{\delta_{iodine}^{object}}{\rho_{iodine}^{object}}$ is the total iodine thickness of the object of interest. This means that we will not be able to measure the local iodine concentration but the total iodine contained in the whole object, loosing the detailed information about the local enhancement distribution. This is an obvious disadvantage, as we loose the information about the distribution of the contrast enhancement, the margins and the shape, the three characteristics needed to assess the malignancy of a lesion.

In the early CEDBT feasibility study carried on by Chen et al. [49], pre-contrast and post-contrast injection tomosynthesis images were reconstructed using a traditional FBP algorithm. Subtracted images were then computed in the volume domain. Although this preliminary evaluation of CEDBT performance suffers from several artifacts induced by the misregistration of pre- and post-contrast volumes due to the lengthy acquisition time and the resultant patient motion, the usefulness of a simple FBP reconstruction method prior to recombination was established. More recently, FBP was also used before recombination. Hu et al. [131] proposed a cascaded linear system model to evaluate the theoretical performance of CESM and CEDBT and how different physical factors, such as X-ray spectra, subtraction technique, and the signal from iodine contrast, may affect the final image quality. Huang et al. [134] reconstructed volumes from low- and high-energy projections of real human patients using FBP, and then recombined both volumes using a log weighted subtraction. In their work they evaluated the clinical performance of their CEDBT workflow against CESM. Their results indicate an improved characterization of margins in CEDBT with a slightly inferior contrast enhancement level in in-plane slices.

After the preliminary results of Chen et al. [49], Puong et al. [235] introduced a new dual-energy CEDBT solution where recombined low- and high-energy pairs were reconstructed using a SART iterative reconstruction algorithm. The proposed acquisition sequence and technology attempt to reduce the acquisition time and, therefore, potential artifacts due to breast motion during acquisition. This was confirmed later by Carton et al. [39]. Puong et al. established the

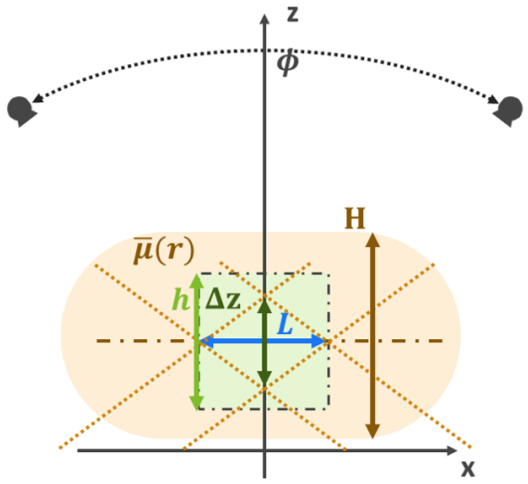

Figure 4.16: The limited depth-resolution Δz of the reconstructed iodine volumetric concentration which can be reconstructed due the limited angular range ϕ of the acquisition sequence. Considering that the total height of the contrast uptake is h, when $\Delta z \geq h$ CEDBT do not represents an advantage, as it is not capable of measuring the local iodine concentration but the total iodide contained in the whole object. This is the same information we obtain in CESM.

equivalence between the optimization of the low- and high-energy acquisition techniques on the recombined volume and the optimization of these techniques on the iodine equivalent thickness images. Additionally, they analyzed the impact of limited angular range and scattered radiation on iodine quantification. The SART algorithm used by Puong et al. was further improved by Iordache et al. [139], introducing a regularization term as in Equation 4.47 to reduce the noise present in the reconstructed images, improving the detection of contrast uptakes without altering their sharpness and morphology.

Hill et al. [124] evaluated the lesion contrast and SDNR when using FBP or SART for different contrast uptake patterns. In their study they found a similar quality of results in reconstructed volumes with both algorithms. In particular, accuracy of the equivalent iodine concentration was the same, obtaining only a lower SDNR with FBP in the biggest considered lesions (larger than 4 mm in diameter). This can be explained by the significant noise level present in high frequencies when standard FBP is applied, while it may be improved with an apodization function.

The third most used reconstruction algorithm for CEDBT is the Ordered Subsets Transmission Reconstruction (OSTR). This method was developed by Hudson et al. [135], and it was first introduced for CEDBT reconstruction by Lu et al. [186]. The reconstruction algorithm is applied on the low- and high-energy acquisitions before recombination. In this statistical reconstruction algorithm, it is assumed that the available data follows a Poisson distribution:

$$y^i_{LE,HE} \sim \mathcal{P}\left(b^i_{LE,HE} \cdot e^{-\left[A\mu_{LE,HE}\right]^i} + s^i_{LE,HE}\right) \tag{4.51}$$

were $i = 1...N$ for N measured X-rays, $y_{LE,HE}$ represents the low- and high-energy X-ray transmission, $b_{LE,HE}$ is the object-free X-ray transmission constant, A is the projection matrix defining the line integrals of the object voxels, $\mu_{LE,HE}$ represents the low- and high-energy linear attenuation coefficients of the object distribution to be estimated, $s_{LE,HE}$ is a constant representing the low- and high-energy scattered signal. Considering these elements and ignoring

constant terms, the following log-likelihood function of the object distribution can be derived:

$$\ln\left(\mathcal{L}\left(\mu_{LE,HE}|y_{LE,HE}\right)\right) = \sum_{i=1}^{N}\Big(y^i_{LE,HE}\cdot\ln\Big(b^i_{LE,HE}\cdot e^{-\left[A\mu_{LE,HE}\right]^i}+s^i_{LE,HE}\Big) - \left(b_{LE,HE}\cdot e^{-A\mu_{LE,HE}}+s_{LE,HE}\right)\Big) \tag{4.52}$$

Then, an Ordered Subset (OS) algorithm can be applied to solve Equation 4.47, where:

$$D(f(\bar{\mu}(r)),\mathbb{G}) = \ln\left(\mathcal{L}\left(\mu_{LE,HE}|y_{LE,HE}\right)\right) \tag{4.53}$$

Scaduto et al. [266] presented a comparison of the results obtained with FBP and OSTR evaluating several reconstruction schemes. They found that OSTR provides a higher SDNR than FBP for contrast uptakes with high iodine concentration (i.e. $2mg/cm3$), while the results for lower iodine concentrations were similar. The decreased SDNR in FBP reconstruction was associated with the low contrast in reconstructed slices due to the ramp filter used in FBP and, thus, the loss of low-frequency signal.

4.2.3 Optimizing FBP for CEDBT clinical task

As introduced in Section 4.2.2, traditional FBP reconstruction has two main problems when applied in CEDBT and compared to other reconstruction methods: high-frequency noise and low contrast.

The ramp filter used in FBP emphasizes the high-frequency noise present in the acquired data. Many types of apodization windows have been studied in signal processing. This windows are used to reduce the magnitude of a given signal near the Nyquist frequency (half the sampling frequency), and therefore to remove the high-frequency noise that does no provide any useful information. Using a proper apodization function we can modify the ramp filter, as introduced in Equation 4.45, and denoise the reconstructed volume.

Otherwise, the ramp filter is used in CT, accordingly to Equation 4.44, to homogenize the non-uniform Fourier sampling. However, when spatial sampling is incomplete, as it is the case for DBT and CEDBT, this filter causes a general loss of information over the low-frequencies of the MTF, attenuating the contrast of the low-frequency structures and causing a "flatness" effect [204]. This is is specially important in CEDBT when FBP is used after recombining the low- and high-energy projections, when the resulting images generally contain very sparse data, with high-contrasted and large structures. Zhou et al. [315] proposed a modification of the ramp filter to preserve some of the low-frequency signal present in the DBT projections:

$$H_{Zhao}(\omega) = \begin{cases}\omega_c & if \quad |\omega| < \omega_c \\ \omega & if \quad |\omega| \geq \omega_c\end{cases} \tag{4.54}$$

where ω_c is a constant representing the transition frequency, and ω_s is the sampling frequency. In Figure 4.17 we illustrate the configuration of this modified ramp filter. To our knowledge, this modification of the ramp filter and its impact on the reconstructed volume has never been studied for the reconstruction of CEDBT volumes.

The combination of different apodization windows and ω_c values will have different impacts on the quality of the final reconstructed volume. Moreover, the detectability of contrast uptakes and volume resolution may drastically change when we include these elements in the reconstruction algorithm. We evaluated the effects of different combinations of apodization windows

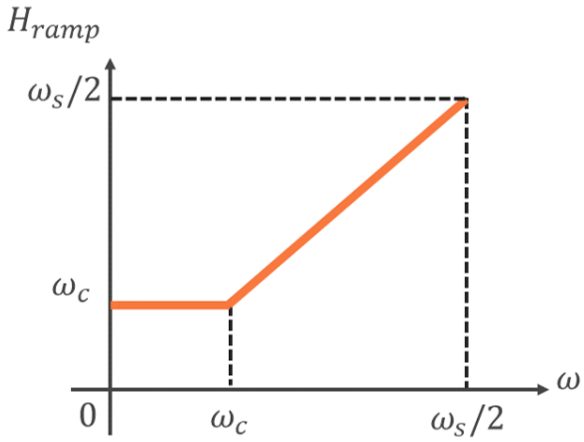

Figure 4.17: Ramp filter following the modifications proposed by Zhou et al [315].

and ω_c values using the simulated X-ray chain presented in Section 2 and the set-ups illustrated in Figure 4.18. We used two values of ω_c: 0.5 lp/mm (called "Ramp 1") and 1 lp/mm (called "Ramp 2"); combined with four different apodization windows: Shepp-Logan, Cosinus, Hamming, and Hann, which are formulated as:

$$\begin{aligned} H_{Shepp}(\omega) &= \text{sinc}\left(\frac{\omega}{\omega_s}\right) \\ H_{Cosinus}(\omega) &= \cos\left(\pi\frac{\omega}{\omega_s}\right) \\ H_{Hamming}(\omega) &\approx 0.54 + 0.46\cos\left(\pi\frac{\omega}{2\omega_s} + \pi\right) \\ H_{Hanning}(\omega) &= 0.5 + 0.5\cos\left(\pi\frac{\omega}{2\omega_s} + \pi\right) \end{aligned} \tag{4.55}$$

where $\text{sinc}(x) = \frac{sin(\pi x)}{\pi x}$.

These functions are presented in Figure 4.19a. Similarly, in Figure 4.19b, we present the final filter $H_T(\omega)$ (modified ramp and apodization) to be applied on projected data before reconstruction. In our case $\omega_s = 10$ lp/mm due to the pixel size in our detector.

To evaluate detectability, we measured the SDNR in the reconstructed in-focus slice of a $50mm$ thick plate composed of 50% glandular and 50% adipose equivalent tissue (BR50) with four combinations of cylindrical inserts: two different diameters ($5mm$ and $10mm$) and two iodine concentrations ($1mg/cm^3$ and $2mg/cm^3$).

We showed in Section 4.1.3 that the resolution of recombined images depends on the material of interest. Here, in order to assess the resolution obtained in the reconstructed volumes using the different proposed filters, we only compute the spatial resolution of low- and high-energy reconstructed volumes. In particular, resolution was measured using the same set-up as the one proposed by Zhao et al. [312]. In this case, a $2mm$ tungsten edge, slightly tilted (3°), was inserted at $25mm$ height of a plate with the same thickness and composition as the one previously mentioned. The MTF was measured in the in-focus slice using the methodology described in Section 2.1.2 of Chapter 2.

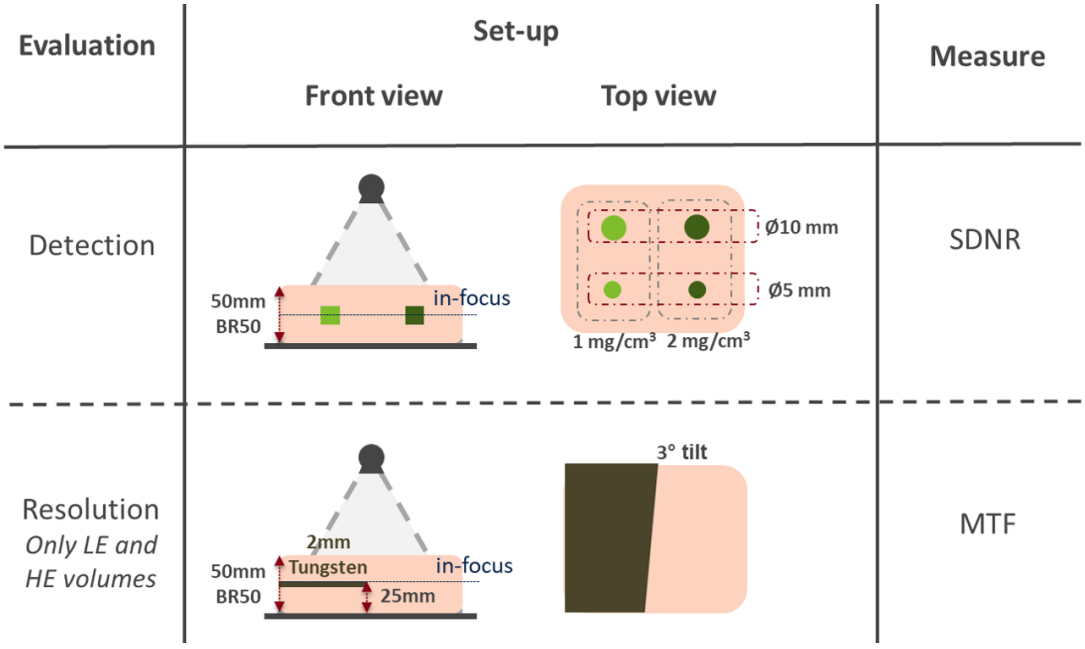

Figure 4.18: Set-up for quality measures of the applied reconstruction methods.

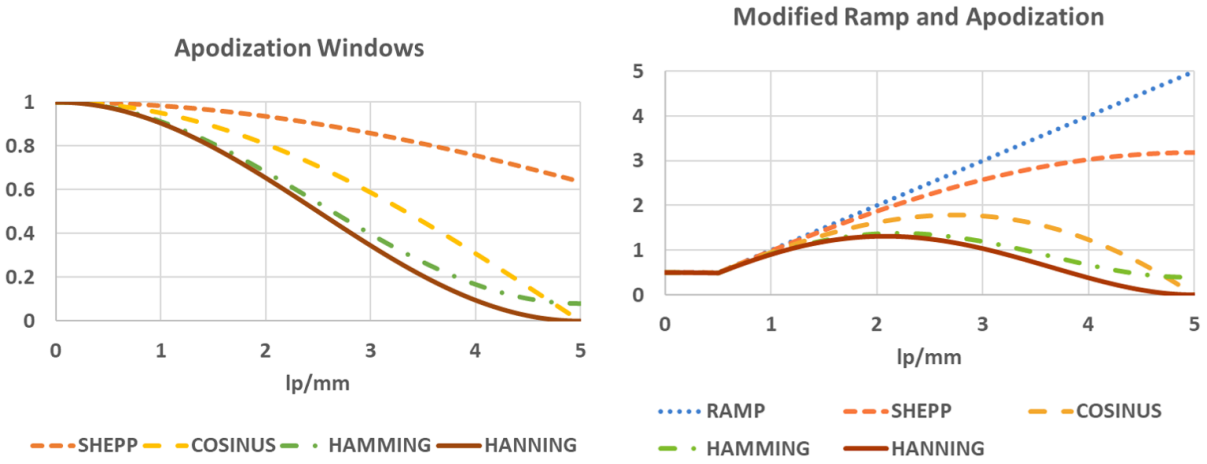

(a) Set of apodization windows evaluated for CEDBT reconstruction.

(b) Magnitude of the Ramp 1 combined with the different apodization windows..

Figure 4.19: Filtering for optimized FBP in CEDBT reconstruction.

Additionally, the MTF and SDNR of each proposed reconstruction method was also compared with a simulated CESM image, and two other established reconstruction methods: SBP and an adaptive iterative reconstruction algorithm (ASIR) developed by GE Healthcare. Simulations were performed using the Pristina geometry and acquisition sequences described in Section 1.3.1. Low- and high-energy acquisitions were generated using the parameters presented in Table 4.6.

The results are presented in Figures 4.20 and 4.21. First, we can observe that with ASIR we obtain a very low SDNR in reconstructed volumes. This result was expected, as ASIR is optimized to increase the contrast of microcalcifications in DBT reconstructed slices. Therefore,

Table 4.6: Operational point used for the generation of CEDBT projection pairs to assess different FBP approaches. The exposure values were divided by the number of low- and high-energy expositions.

	Simulated	
	LE	**HE**
Spectrum	23keV (monoenergetic)	34keV (monoenergetic)
Target/Filter	Rh/Ag	Rh/Cu
Exposure	36mAs	110mAs
Gainmap	50mm PMMA	50mm PMMA

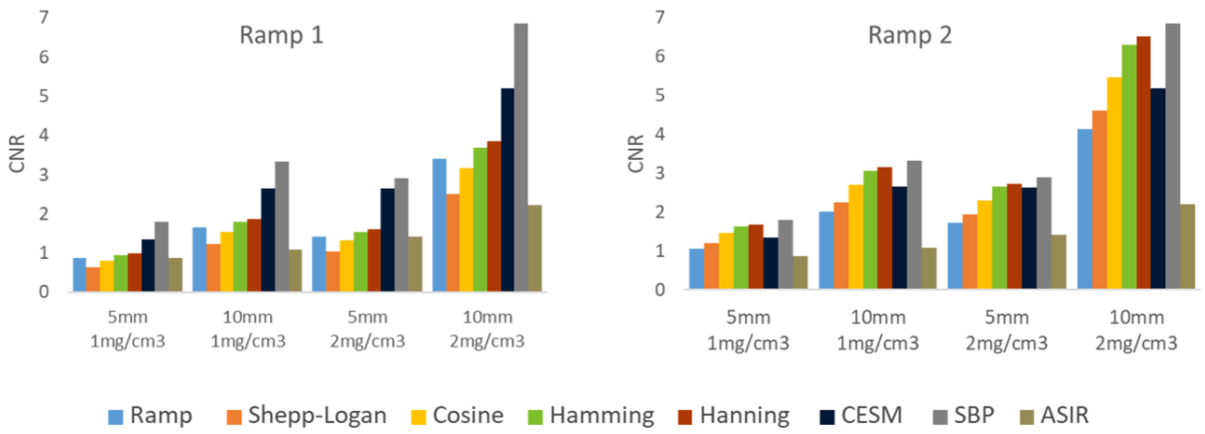

Figure 4.20: SDNR obtained for four contrast uptakes of different size and iodine concentration, and different combinations of modified ramp filter and apodization windows. Additionally, for comparison, the SDNRs in CESM projections, SBP and ASIR reconstructed volumes are also included.

in CEDBT, reconstructed noise is enhanced and the SDNR is reduced when we consider large contrast uptake signals.

The proposed modified ramp filters are better adapted to the purpose of CEDBT, enhancing large high contrasted patterns and preserving fine structures such as spicules. However, as observed in our results, the Ramp 1 filter continues to offer a lower SDNR in reconstructed slices than in CESM images. Indeed, as illustrated in Figure 4.21, the total MTF in the central reconstructed slice diminishes the lower frequencies (between 0 and $0.5 lp/mm$, meaning objects bigger than $1mm$ of diameter), while enhancing the middle frequencies (between 0.5 and $2.5 lp/mm$, objects between 0.2 and $1mm$ of diameter). Although certain fine elements, such us spicules or heterogeneities, may lie in the middle frequency band, background noise will also be enhanced, while the intensity of the main contrast uptakes will be reduced.

Otherwise, although the proposed Ramp 2 filter without apodization offers similar performance in terms of SDNR to the Ramp 1 filter, when apodization is applied, the SDNR increases, obtaining even better SDNR results than in CESM. In Tables 4.7 and 4.8 we show the absolute difference between the SDNR in CESM and the rest of reconstruction methods. This increased SDNR can also be explained through the resulting MTFs. In the case of the Ramp 2 filter, the low-frequencies are not attenuated while the high frequencies are reduced when we apply an apodization window, reducing the total noise in the image.

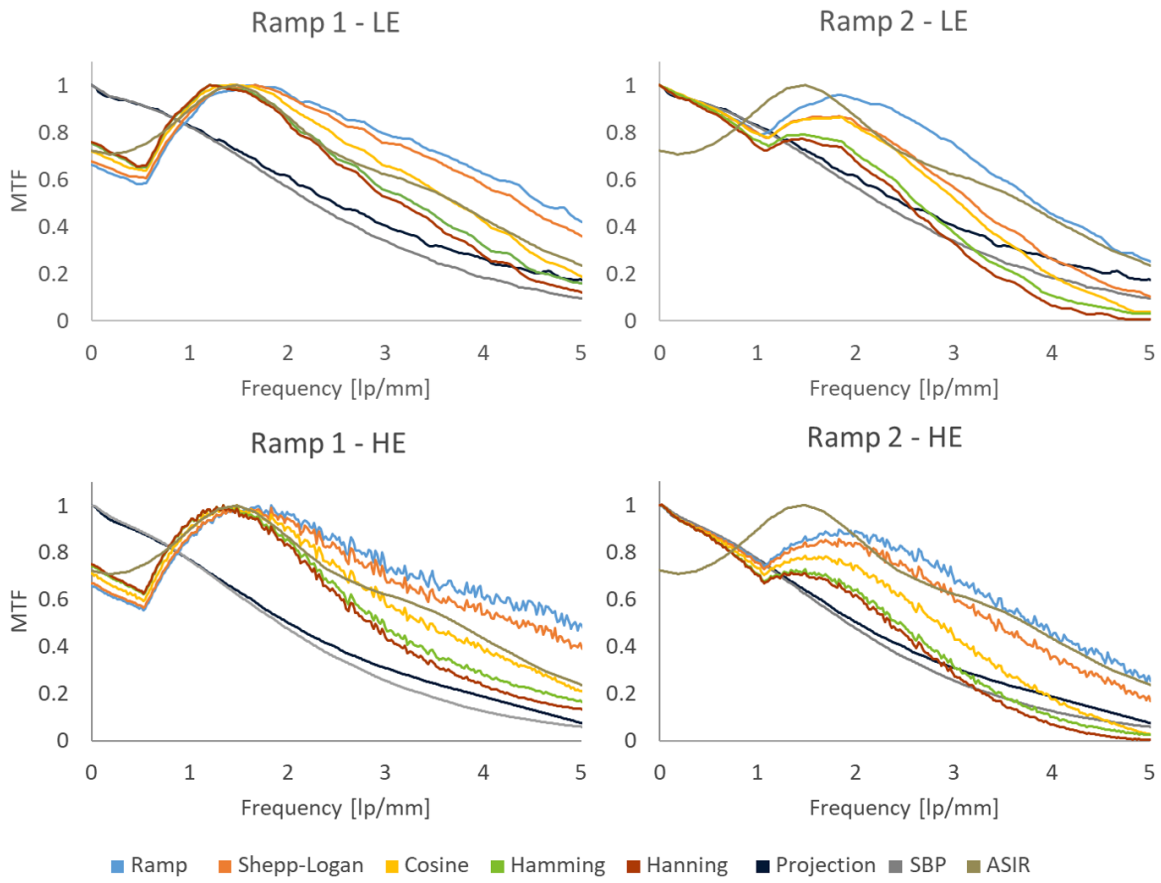

Figure 4.21: MTFs measured in the in-focus slice for low- and high-energy FBP reconstructed volumes using different combinations of modified ramp filters and apodization windows. Additionally, for comparison, the MTFs in low- and high-energy projections, SBP and ASIR reconstructed volumes are also included.

Table 4.7: Difference between the SDNR in CESM images and CEDBT reconstructed in focus slices for all the reconstruction methods studied in this section using the modified ramp filter Ramp 1, SBP and ASIR.

	Ramp	**Shepp**	**Cosine**	**Hamming**	**Hanning**	**SBP**	**ASIR**
$5mm\ 1mg/cm^3$	-0.46	-0.70	-0.53	-0.39	-0.35	0.46	-0.46
$10mm\ 1mg/cm^3$	-1.00	-1.44	-1.11	-0.86	-0.79	0.68	-1.57
$5mm\ 2\ mg/cm^3$	-1.22	-1.60	-1.32	-1.12	-1.04	0.26	-1.23
$10mm\ 2mg/cm^3$	-1.80	-2.70	-2.03	-1.51	-1.35	1.66	-2.98

To visualize how these results may affect the quality of real clinical data, we simulated cases with lesions and reconstructed them with the proposed reconstruction methods. Using the same acquisition parameters as before, we simulated the projections of a textured volume containing a spiculated lesion as seen in Chapter 3. The iodine concentration of the lesion was fixed to $0.8mg/cm^3$, and it was inserted in a textured 3D breast phantom, with 27% volumetric glandular density. Background contrast uptake can decrease the overall quality of the reconstructed slices due to out-of-plane artifacts as presented in Section 4.2. Consequently, the attenuation

Table 4.8: Difference between the SDNR in CESM images and CEDBT reconstructed in focus slices for all the reconstruction methods studied in this section using the modified ramp filter Ramp 2, SBP and ASIR.

	Ramp	**Shepp**	**Cosine**	**Hamming**	**Hanning**	**SBP**	**ASIR**
$5mm\ 1mg/cm^3$	-0.27	-0.15	0.12	0.29	0.34	0.46	-0.46
$10mm\ 1mg/cm^3$	-0.64	-0.40	0.04	0.41	0.50	0.68	-1.57
$5mm\ 2mg/cm^3$	-0.91	-0.70	-0.35	0.00	0.09	0.26	-1.23
$10mm\ 2mg/cm^3$	-1.07	-0.59	0.28	1.12	1.33	1.66	-2.98

coefficients corresponding to homogeneous mixtures of fibroglandular tissue and $0.1mg/cm3$ iodine were assigned to the fibroglandular tissue background in order to be more realistic. The results of these simulations are illustrated in Figure 4.22. We can observe that these images well illustrate our conclusions. While the lesions presented in images reconstructed with the Ramp 1 filter and ASIR can be hardly appreciated, the Ramp 2 filter increases the contrast and also reduces the background noise when combined with the apodization windows.

The results indicate that the best trade-off between preservation of large contrast uptakes and fine details while reducing the background noise is the Ramp 2 filter combined with a Hamming or Hann apodization window. For the results presented in Chapters 5 and 6, we used Ramp 2 combined with the Hamming window.

4.3 Conclusion

In Chapter 2 we presented an improved X-ray simulation platform to provide realistic low- and high-energy pairs of images accordingly with the characteristics required by CESM and CEDBT. However, we showed in Section 1.3.3 of Chapter 1 that, after retrieving the low- and high-energy pairs collected during the acquisition sequence, the images are recombined (CESM) and reconstructed (CEDBT) to obtain a representation of the iodine contrast content inside the breast. If we want to perform a study comparing the performance of CESM and CEDBT, we need to provide recombined images reproducing the same characteristics observed in experimental recombined images. Additionally, one of the goals of this work was to improve the reconstruction algorithm to obtain CEDBT slices with higher quality.

In this chapter we have presented the physical phenomena and mathematical principles involved in the recombination and reconstruction of breast X-ray images. These methods are applied to the simulated low- and high-energy projections to obtain the images used in CESM and CEDBT. The characteristics of these final images are extremely important, as they will influence the evaluation between both modalities, the main goal of this work.

First, we have shown that choosing one of the recombination expressions proposed in the literature is not trivial. The choice of log-weighted subtraction or polynomial fitting will have an impact on the final noise, resolution and offset of memory processes. In our case, we were limited by the nature of our mono-energetic simulations and a linear log-weighted expression was used for the recombination process applied to simulations. As we were interested in providing iodine equivalent images with the same lesion detectability, we have modified the SNR of the projections provided by the simulation platform. However, we did not adapted the resolution or the offset due to memory processes. Further investigation involving polyenergetic simulations

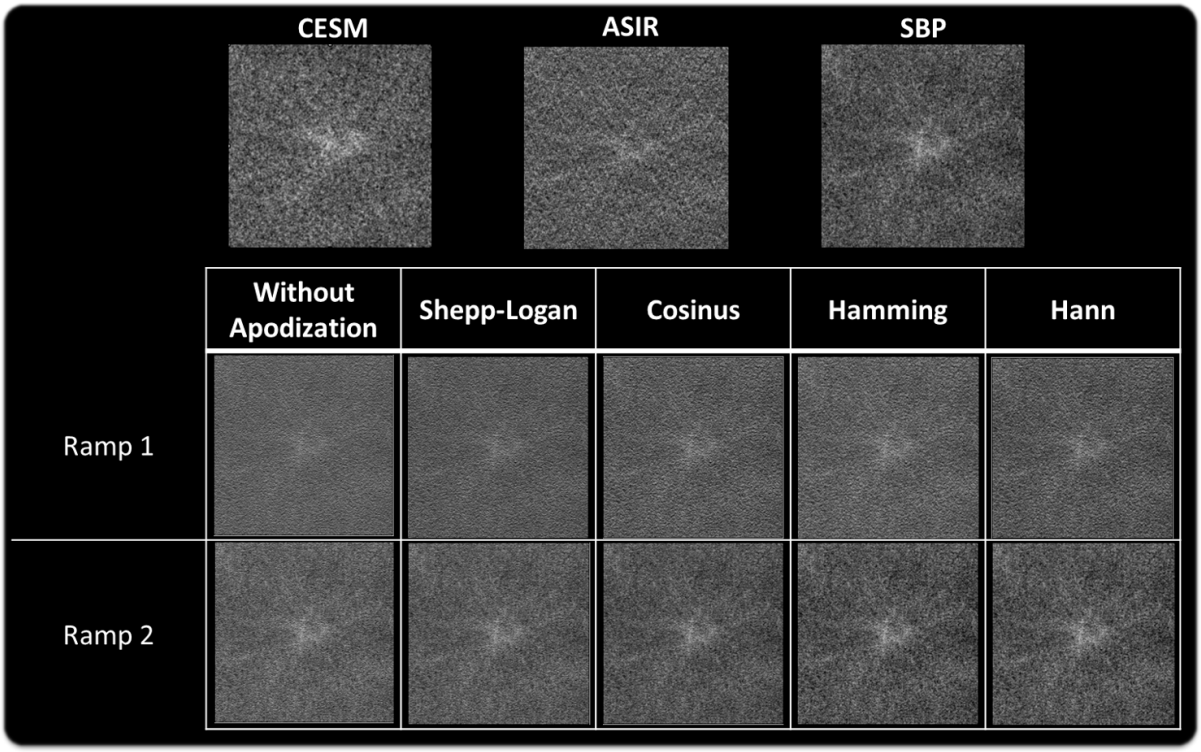

(a) Set of CESM image and CEDBT in-focus slices with different reconstruction methods for a spiculated enhancement.

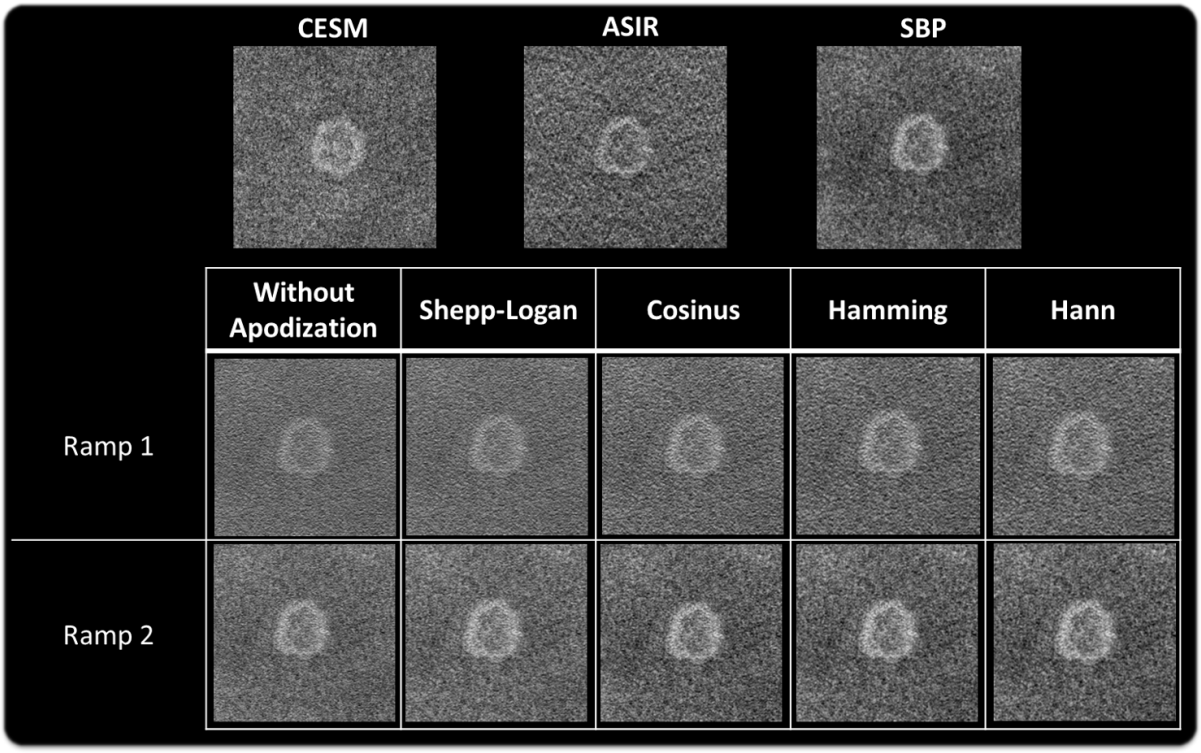

(b) Set of CESM image and CEDBT in-focus slices with different reconstruction methods for a rim enhancement.

Figure 4.22: Visual comparison between the reconstruction methods presented in Section 4.2.3.

is needed to verify that the characteristics of the polynomial fitting applied to real images are shared also by the simulated images.

In addition, this chapter contains the analysis of the frequency response as well as the impact of the memory processes on the final recombined mammography image. To our knowledge, both analysis have never been studied.

Next, we provided an overview of the available methods and limitations for CEDBT reconstruction. We found that there is not an established order to perform the recombination and reconstruction steps. The published CEDBT studies use both workflows interchangeably. To avoid the dependency between the beam-hardening effect and the reconstruction algorithm, we have recombined the low- and high-energy pairs before reconstructing the volume. Other solutions to avoid the problem of beam-hardening in reconstructed volumes could be considered. For example, in CT reconstruction, several iterative approaches have been proposed [162, 292].

Regarding the reconstruction algorithms, the comparison between FBP reconstruction and its alternatives (e.g. SART, OSTR...) showed that FBP leads to increased noise in high-frequencies and hardly visible contrast uptakes due to a low contrasted image. Instead of looking for completely new reconstruction approaches, we have considered the modification of the FBP filter to overcome both limitations. Because the information present in CEDBT images consists of contrast uptakes which are larger than the structures observed in DBT, the structures we need to reconstruct belong to the low-frequency band of the spatial spectrum which is almost rejected by the ramp filter. Motivated by the possible scope for improvement of the FBP implementation in CEDBT reconstruction, we optimized the shape of the ramp filter applied to the projections to consider this hypothesis. We also considered different regularization filters to reduce the high-frequency noise which does not provide any clinical information.

Therefore, the contribution of this work to CEDBT reconstruction was twofold: the study of several filter modifications enhancing the low-frequency components of the recombined image against high-frequency noise, and the comparison of their respective performance in simulated images. We observed that our proposed filter provides an increased contrast-to-noise ratio of contrast uptakes compared to ASIR, a commercial standard iterative reconstruction method for DBT. At the same time, our method also preserves the fine structures belonging to breast masses which must be visible in CEDBT images.

This preliminary work will help us to evaluate the clinical performance of CESM and CEDBT having a same detectability level. In future work, we may investigate how the quality of the image could be further improved using our FBP implementation as an initial volume of an iterative reconstruction. Moreover, a regularization term which considers the sparsity of the final volume could also be included.

Chapter 5

CEDBT system design improvements

From the first preliminary results evaluating the performance of CEDBT published in 2007 [49] to the last work assessing the benefits of this technique in 2018 [134], the design of mammography systems has been improved. The system design does not only include the aggregation of technological upgrades but also the adoption of advanced and more sophisticated acquisition designs. In the case of CEDBT, this compendium of improvements has a positive impact on the quality of the projections and, consequently, on the recombined and reconstructed images.

Ten years ago, Carton et al. [41] evaluated the image quality of recombined projections before reconstruction for a Senographe DS-based CEDBT prototype. In particular, they determined that the main factors limiting the image quality in CEDBT were the lag and the X-ray scatter. To improve the image quality, they modified the acquisition sequence and included a new anti-scatter grid. These modifications were considered in the development of the recently commercialized Senographe Pristina system. However, to our knowledge, the image quality improvement of CEDBT reconstructed images provided by a Senographe Pristina system has never been quantified. The characteristics of the CEDBT prototype based on the Senographe DS, as well as those of the CEDBT prototype based on the Senographe Pristina, were presented in Section 1.3.1 of Chapter 1. Additionally, in Chapter 2, we provided a model to simulate the acquisitions realized by a mammography system, and we described how it was adapted to simulate both systems.

The first physical process considered by Carton et al. [41] was the lag effect. The memory behavior of the Senographe DS and Pristina detector over time and the associated lag effect has a negligible impact on CESM recombined images. However, the fast cadence and concatenation of low- and high-energy projections in CEDBT acquisition sequences, along with the low signal intensities of this modality, may impact the cancellation of anatomical texture in the recombined images. In Senographe Pristina a new lag-reduction acquisition sequence was introduced. This new sequence allows the system to read out the detector several times between consecutive X-ray exposures. The first read-out is recorded and used as the acquired image, while the others are just applied to reduce the number of trapped charges before the next exposition.

Secondly, the X-ray scatter field is a source of cupping artifacts and reduced resolution of contrast uptakes. The Senographe DS includes an anti-scatter grid for Full-Field Digital Mammography (FFDM) and CESM modalities. This anti-scatter grid is made of radio-opaque septas perpendicular to the chest-wall and oriented towards the X-ray source (Figure 5.1a). This

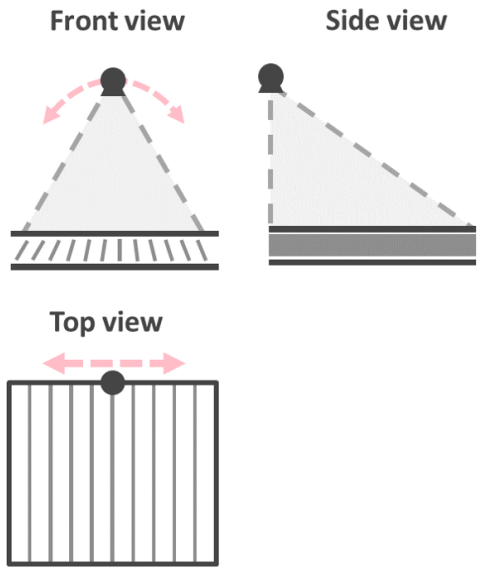

(a) Position of grid septas in the anti-scatter grid of a Senographe DS sytem. This anti-scatter grid is used only in FFDM and CESM modalities. Due to the high X-ray primary beam cutoff in DBT and CEDBT prototype, the anti-scatter grid was removed in the prototypes for these modalities.

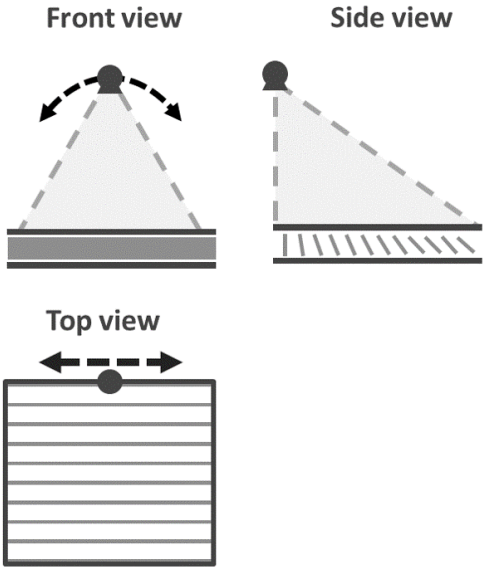

(b) Position of grid septas in the anti-scatter grid of a Senographe Pristina sytem. This anti-scatter grid is used in all modes, and has been optimized for both low- and high-energy image acquisitions.

Figure 5.1: Anti-scatter grid geometry in the two different mammography systems.

geometry offers a low primary beam cutoff when the X-ray source stays static and at the focal point of the radio-opaque septas during the acquisition sequence. However, in Digital Breast Tomosynthesis (DBT) and CEDBT, when the tube rotates during the acquisition sequence, the primary X-ray beam suffers a significant cutoff. Therefore, in the Senographe DS-based CEDBT prototype no anti-scatter grid was attached to the detector of the system, increasing the impact of scatter on the acquired low- and high-energy pairs of projections. In the Senographe Pristina, the orientation of the anti-scatter grid was changed. In this system, the radio-opaque septas are positioned parallel to the chest-wall and oriented towards the X-ray source (Figure 5.1b). In this case, even if the X-ray source rotates during the acquisition sequence, the primary beam cutoff continues to be low. Also, the septas of this new anti-scatter grid have been designed to provide a better scatter rejection in high-energy acquisitions, which contributes to have a better image quality in CESM and CEDBT modalities.

The goal of this chapter is to provide a comparison of the image quality in reconstructed CEDBT images between both systems, Senographe DS and Senographe Pristina, using simulated images. In particular, we assess the capacity of each system to provide quantitative results, allowing for a correct analysis of the observed contrast uptakes in reconstructed slices. To this end, we analyze the ability of the recombination algorithm to cancel the texture from the normal breast tissue, allowing for a better detectability of contrast uptakes inserted in different breast compositions (cf. Section 5.1). Then, we analyze the magnitude of the residual anatomical texture when breast parenchyma holds different amounts of contrast uptake and the capacity to quantify different background enhancements (cf. Section 5.2). We also evaluate the performance of each system in distinguishing a contrast uptake due to a lesion which is surrounded by natural

background enhancement (cf. Section 5.3). Finally, we analyze the magnitude of cupping artifacts due to the scatter field and compare it to the signal intensity due to contrast uptakes (cf. Section 5.4).

5.1 Texture cancellation

The main goal of contrast enhanced X-ray breast imaging is to obtain images where the anatomical information has been removed, presenting only information about the contrast uptake distribution. In this context, texture cancellation is the ability of the contrast enhanced X-ray technique to represent glandular and adipose tissues with similar homogenized intensities, while contrast uptakes can be distinguished with different intensities depending on the concentration of the contrast agent. There are several elements which can be related to the effectiveness of the texture cancellation in recombined images, such as the choice of the recombination algorithm (intrinsic factor) or potential breast motion between acquisitions (extrinsic factor). In this chapter we only focus on the improvement due to the system design differences between Senographe DS and Senographe Pristina in terms of lag and scatter rejection.

To assess the texture cancellation performance, we employ the Texture Cancellation index (TC), which measures the prevalence of a specific iodine concentration over two different breast tissues with distinct glandularities:

$$TC(Gland_A, Gland_B, C_{iodine}) = \frac{|SI(Gland_A) - SI(Gland_B)|}{|SI(Gland_A) - SI(C_{iodine})|} \tag{5.1}$$

where $Gland_A$ and $Gland_B$ are two ROIs with different glandularities, C_{iodine} is a ROI with a specific iodine concentration, and $SI(\cdot)$ means the signal intensity average in a given ROI. Ideally, TC should be as low as possible for all values of iodine concentration C_{iodine}. Two systems can be compared based on the lowest value of C_{iodine} for which $TC < 1$. This means, the lowest iodine concentration provided by the imaging system having a higher contrast than the signal intensity difference between glandularities A and B of the background.

The set-up used to measure the TC index for reconstructed volumes of Senographe DS and Prisitina simulated acquisitions is illustrated in Figure 5.2. The test object is composed of two homogeneous plates with a height of $50mm$, each of them including symmetric iodine inserts. These iodine inserts are cylindrical, with $10mm$ height and $5mm$ radius. Six different iodine concentrations are considered: 0.1, 0.2, 0.5, 1, 2 and $4mg/cm^3$. Two combinations of homogeneous plates are used: an equivalent $50mm$ 100% glandular tissue plate (BR100) placed aside an equivalent $50mm$ 50% glandular tissue plate (BR50), and an equivalent $50mm$ 0% glandular tissue plate (BR0) placed aside an equivalent $50mm$ 50% glandular tissue plate (BR50).

The automatic exposure settings for this set-up were reproduced in our simulation platform (Tables 5.1 and 5.2). The low- and high-energy projected pairs were recombined using Equation 4.10, and reconstructed using the modified FBP method described in Section 4.2.3. The TC index was measured in the in-focus slice situated at $25mm$ from the object support.

In Figure 5.3 the reader may appreciate the appearance of the reconstructed in-focus slices simulated in this study for both Senographe DS and Senographe Pristina systems. The results are illustrated in Figure 5.4. As we can observe, the texture cancellation in a Senographe Pristina reconstructed slice notably outperforms the results obtained with the Senographe DS acquisitions for all the range of iodine concentrations considered in this study. While the

Table 5.1: Operational point used for the validation of the recombined pairs for the **Senographe Pristina** system.

	LE		**HE**	
	Real	*Simulated*	*Real*	*Simulated*
Spectrum	34kVp	23keV (monoenergetic)	49kVp	34keV (monoenergetic)
Target/Filter	Rh/Ag	Rh/Ag	Rh/Cu	Rh/Cu
Exposure	36mAs	36mAs	110mAs	110mAs
Gainmap	2mm Al	50mm PMMA	2mm Al	50mm PMMA

Table 5.2: Operational point used for the validation of the recombined pairs for the **DS** system.

	LE		**HE**	
	Real	*Simulated*	*Real*	*Simulated*
Spectrum	28kVp	20keV (monoenergetic)	49kVp	39keV (monoenergetic)
Target/Filter	Mo/Mo	Mo/Mo	Rh/Cu	Rh/Cu
Exposure	110mAs	110mAs	320mAs	320mAs
Gainmap	25mm PMMA	50mm PMMA	25mm PMMA	50mm PMMA

TC index is lower than the acceptable threshold for all concentrations in Senographe Pristina ($TC_{Pristina}(Gland_A, Gland_B, C_{iodine}) < 1$, for $C_{iodine} \geq 0.1 mg/cm^3$), the Senographe DS only fulfills this requirement when a iodine concentration equal to $4 mg/cm^3$ is compared to the contrast between 0% and 50% glandular tissues.

The main reason of this divergence between the results obtained for the two mammography systems may be related to the increased lag found in the Senographe DS platform. This was investigated by generating simulated replicas of the same experimental set-up but removing the lag component from the Senographe DS X-ray simulations. In Figure 5.5, we show how the TC index is considerably improved when the acquisitions do not show any lag offset. However, the lag is not the only component impacting texture cancellation. In our results, we can also observe that even if the lag is no present in Senographe DS acquisitions, we still obtain a slightly worse TC value result than the TC index measured in Senographe Pristina images where the lag was included. This may be directly related to the higher X-ray scatter contribution in the Senographe DS acquisitions, which reduces the contrast of the contrast uptakes in the recombined images.

5.2 Parenchyma enhancement

Breast Parenchyma Enhancement (BPE) is due to the presence of contrast uptake in normal fibroglandular tissue. This biological response to the contrast agent injection results in the enhancement of the background in the recombined images. However, even if BPE is uncorrelated to the presence of a lesion, its analysis can be important [265]. Therefore, the recombined images obtained with a mammography system must be capable of distinguishing different iodine concentrations distributed over the background.

The anatomical texture observed in mammography images has been traditionally modeled in several works [32, 47, 115] by a power-law expression depending on the spatial frequency:

$$WS(\nu) \approx \frac{\alpha}{(c\nu)^{\beta}} \tag{5.2}$$

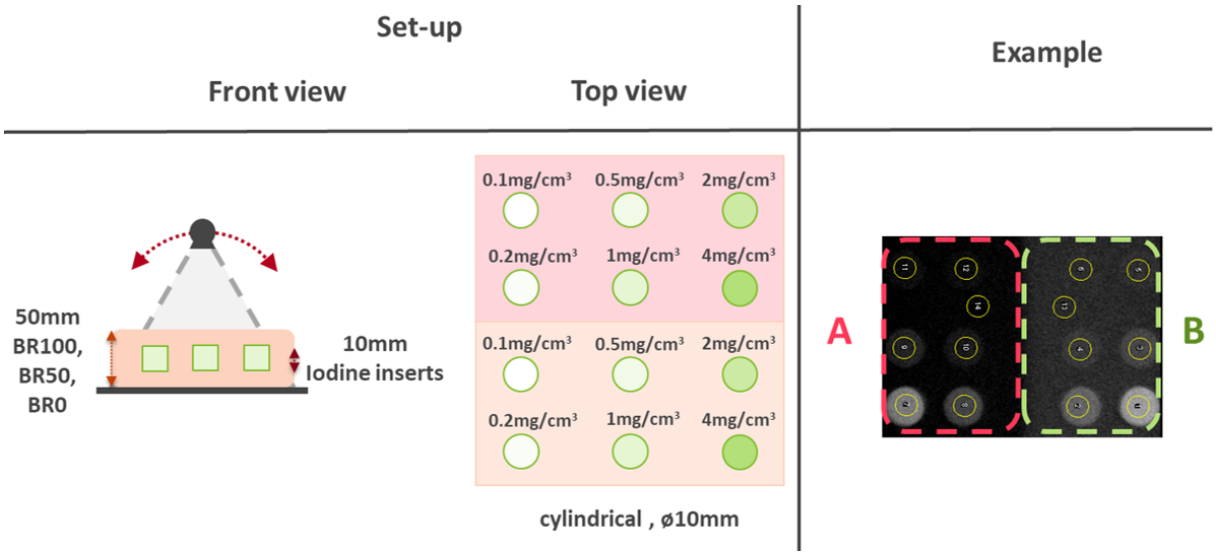

Figure 5.2: Set-up used to measure the Texture Cancellation index (TC) of different mammography systems. An example of a simulated image and the different ROIs considered for each measurement are also illustrated.

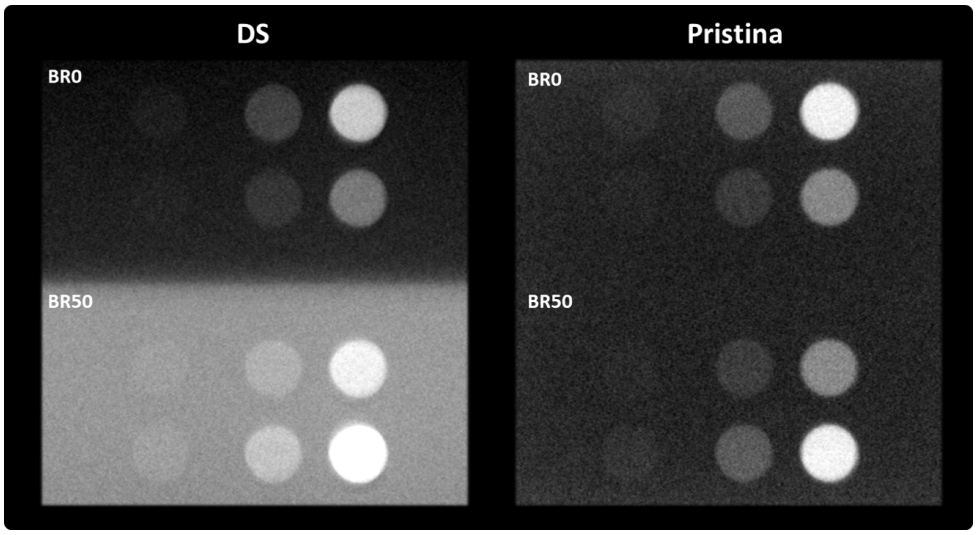

Figure 5.3: In-focus slices used for texture cancellation evaluation in Senographe DS and Senographe Pristina systems.

where $WS(\nu)$ is the noise power spectrum, or Wiener spectrum, of the mammography image over the spatial frequencies ν, α is a constant dependency on the texture noise magnitude, c is a constant assumed to be equal to 1 and dimension $(lp/mm)^{-1}$ so the denominator is dimensionless, and β is the exponent of the power-law expression. The magnitude of this last parameter describes the anatomical breast structure and the lesion detectability in mammography images [248].

Some works have used the magnitude of the exponent β to evaluate the texture cancellation performance in CESM images, instead of the TC index presented in the previous section. However, they are not equivalent measures. While the TC index measures the performance of the

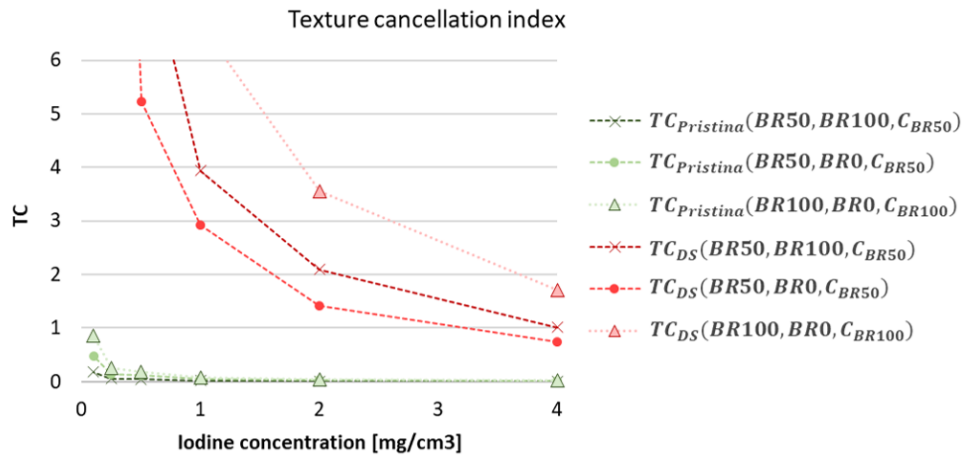

Figure 5.4: Texture cancellation (TC) index in Senographe DS and Senographe Pristina systems for three different glandularity combinations.

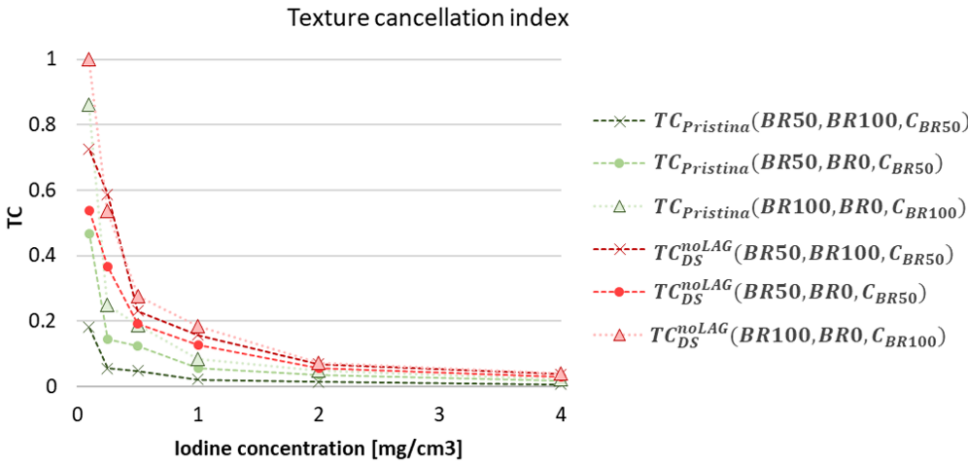

Figure 5.5: Texture cancellation for an in-focus slice obtained using the complete model of the Senographe Pristina acquisition system and a reduced version of the Senographe DS model where the lag was not included.

recombination algorithm using phantoms with a non-iodinated background, the β parameter is usually computed in real cases where the anatomical background does contain iodine, in the form of BPE. Therefore, the β parameter does not only inform us about the performance of the recombination algorithm, but also about the level of iodine absorbed by the breast parenchyma. Hence the importance of computing both, the TC index and the β parameter.

Jong et al. [146] investigated the performance of subtracted mammographies after the injection of a contrast agent to detect and characterize lesions, gathering 22 patients. Dromain et al. [79] studied the ability of contrast-enhanced single energy mammography to depict angiogenesis, using a cohort of 20 patients. In both studies, several acquisitions were made at different times after the first projection to evaluate the contrast kinetics. The analysis of the anatomical texture in the resulting images for both studies was published later by Hill et al. [120]. Regarding the images coming from the study by Jong et al., they found a value of β in the $[3.03 - 3.17]$ range when the contrast agent was not present, depending on the acquisition time. In subtracted

Table 5.3: Averaged β values documented in contrast-enhanced mammography. (*) β computed in single-energy contrast-enhanced images

	$\overline{\beta_{LE}}$	$\overline{\beta_{HE}}$	$\overline{\beta_{DE}}$
Jong et al. [146](*)	3.06		1.62
Dromain et al. [79](*)	3.04		1.61
Melissa et al. [123] (*)	3.1		1.5
Melissa et al. [121]	3.2	3.11	1.22
Carton et al. [38]	3.21	3.13	1.25

images, the parameter β oscillates inside the range of $[1.4 - 1.84]$, showing that anatomical noise is substantially reduced. For the images acquired in the study by Dromain et al., the β value of the single energy images is comprised in the $[2.98 - 3.19]$ range, and the recombined images are characterized by a β value in $[1.18 - 3.91]$. However, due to the nature of these clinical studies, no information about the contrast agent concentration in the breast parenchyma was given. Hill et al. [123] also developed a mathematical breast phantom reproducing the visual anatomical complexity of pre-contrast, post-contrast, and subtracted mammography images. To obtain a BPE consistent with the average uptake observed in the study performed by Jong et al., the breast parenchyma iodine concentration considered in their simulations was $0.125 mg/cm^3$. The measured β of their pre-contrast simulated images were included in the range $[2.4 - 3.1]$, while the average β observed in simulated images was 2.1 ± 0.2. To match their clinical data, Melissa et al. included a small rigid motion between the low- and high-energy acquisitions, obtaining finally an average value of β equal to 1.4 ± 0.2. Later, Hill et al. [121] extended their study to the analysis of clinical recombined images, this time using dual-energy CESM acquisitions. Using a clinical set composed of 98 different patients, they computed the texture noise from the recombined images, as well as the one of the low- and high-energy acquisitions. They obtained the following average magnitudes: $\beta_{LE} = 3.2$, $\beta_{HE} = 3.11$ and $\beta_{DE} = 1.22$. More recently, Carton et al. [38] evaluated the detectability of breast masses over a non-uniform background using simulated images. In their study they generated simulated low- and high-energy pairs of images of a numerical anthropomorphic breast phantom. Their model included a breast parenchyma iodine concentration range between 0.2 and $0.5 mg/cm^3$. Additionally, a rigid motion between low- and high-energy projections was considered. They found the following average β values: $\beta_{LE} = 3.47$, $\beta_{HE} = 3.30$ and $\beta_{DE} = 1.13$.

All the published results are summarized in Table 5.3. The value of β is clearly inferior on dual-energy images, which can be identified with a better texture cancellation. The value of β found in the works of Hill et al. and Carton et al. will be the reference of our simulations. To our knowledge there is no study evaluating the parameter β in reconstructed CEDBT slices.

In this section we want to evaluate how the increment of iodine contrast uptake distributed among the parenchyma tissue is visually represented in CEDBT slices for different mammography systems. To do that, we compute the β parameter of reconstructed CEDBT slices using the same procedure as the one described by Hill et al. [121] for CESM projections. Additionally, at the end of this section, we also use the β parameter to assess the different visual representation of the BPE which may be appreciated between CESM projections and CEDBT slices for the same background iodine contrast uptake.

According to Equation 5.2, to compute the value of the parameter β for a particular image, we need to measure its noise power spectrum, or Wiener spectrum (WS). The WS of a mammogram, defined in the spectral domain, represents all the information concerning the different

noise sources composing the statistics of the image. Principally, in its most generalized form, the total WS_T of a mammography image is composed of three independent noise sources:

$$WS_T(\nu_x,\nu_y) = WS_Q(\nu_x,\nu_y) + WS_{elec}(\nu_x,\nu_y) + WS_{An}(\nu_x,\nu_y)\cdot MTF^2(\nu_x,\nu_y) \tag{5.3}$$

where WS_Q is the component due to quantum noise, WS_{elec} is the electronic noise added to the acquisition, WS_{An} is the anatomical noise contribution for a specific projected object blurred by the system frequency response represented by the MTF, and ν_x and ν_y are the horizontal and vertical spatial frequencies. We are interested in the evaluation of WS_T in a limited range of frequencies where it is dominated by the anatomical noise. WS_T can be estimated from the average measure of the squared magnitudes of M ROIs, named I, placed over the whole image, as follows:

$$WS_T(\nu_x,\nu_y) = \frac{1}{M}\sum_{i=1}^{M}\left(\frac{p_x\cdot p_y}{N_x\cdot N_y}\left|\mathcal{F}\left\{W(x,y)\left(I(x,y)-\overline{I}\right)\right\}\right|^2\right) \tag{5.4}$$

where p_x and p_y are the dimensions of the detector pixels, N_x and N_y are the number of vertical and horizontal pixels of each ROI, $\mathcal{F}$ is the bidimensional Fourier Transform, and $\overline{I}$ is the average intensity of the ROI. Additionally, a Tukey apodization window $W(x,y)$ is applied to reduce spectral leakage. This bidimensional window is separable so it can be generated using oriented unidimensional expressions, i.e. $W(x,y) = w(x)w(y)'$, defined as:

$$w(x) = \begin{cases} \frac{1}{2}\left[1+\cos\left(\frac{2\pi}{r}\left(\frac{x-1}{N_x-1}-\frac{r}{2}\right)\right)\right] & ,if \quad 0 < \frac{x-1}{N_x-1} < \frac{r}{2} \\ 1 & ,if \quad \frac{r}{2} \le \frac{x-1}{N_x-1} < 1-\frac{r}{2} \\ \frac{1}{2}\left[1+\cos\left(\frac{2\pi}{r}\left(\frac{x-1}{N_x-1}-1+\frac{r}{2}\right)\right)\right] & ,if \quad 1-\frac{r}{2} < \frac{x-1}{N_x-1} \le 1 \end{cases} \tag{5.5}$$

where $r \in [0,1]$. In our case, $r = 0.5$. The subtraction in Equation 5.4 of the average intensity inside the ROI, $\overline{I(x,y)}$, will remove the information laying over $(\nu_u = 0, \nu_v = 0)$. This means that there is no continuous component in the final spectrum ($WS_T(0,0) = 0$). Moreover, the use of the apodization window may decrease the magnitude of the total spectrum at low frequencies. All this must be considered to determine the frequency range where the anatomical noise will be measured.

The averaged $WS_T(\nu_u,\nu_v)$, due to its isotropic shape, can be converted to polar coordinates, i.e. $WS_T(\rho,\theta)$. Following this, the bidimensional noise spectrum can be averaged over the radial angle θ to obtain a unidimensional expression $WS_T(\rho)$ which can be fitted to the power law presented in Equation 5.2. The values of α and β can then be computed as the least square solution of the data over the chosen frequency range, $[\rho_l,\rho_u]$, considering the following log-transformed form:

$$\log_{10}\left(WS_T\left(\rho_{[l,u]}\right)\right) = \log_{10}(\alpha) - \beta\cdot\log_{10}\left(\rho_{[l,u]}\right) \tag{5.6}$$

In this study we will adopt the same frequency bounds as used by Hill et al. [121], consequently: $\rho_l = 0.17mm^{-1}$ and $\rho_u = 0.3mm^{-1}$.

The set-up used to compute the value of β for both mammography systems and different levels of BPE is presented in Figure 5.6. Our test object is a modification of the DRAP texture model described in Section 3.3. To a $50\times50\times25mm^3$ voxelized prism we added two additional layers, one under and one over the prism, of equivalent pure adipose tissue of $12.5mm$ height each, obtaining a total 27% volumetric glandular density. In total, we generated 40 random voxelized volumes with different fibroglandular distributions. The voxels representing the breast glandular

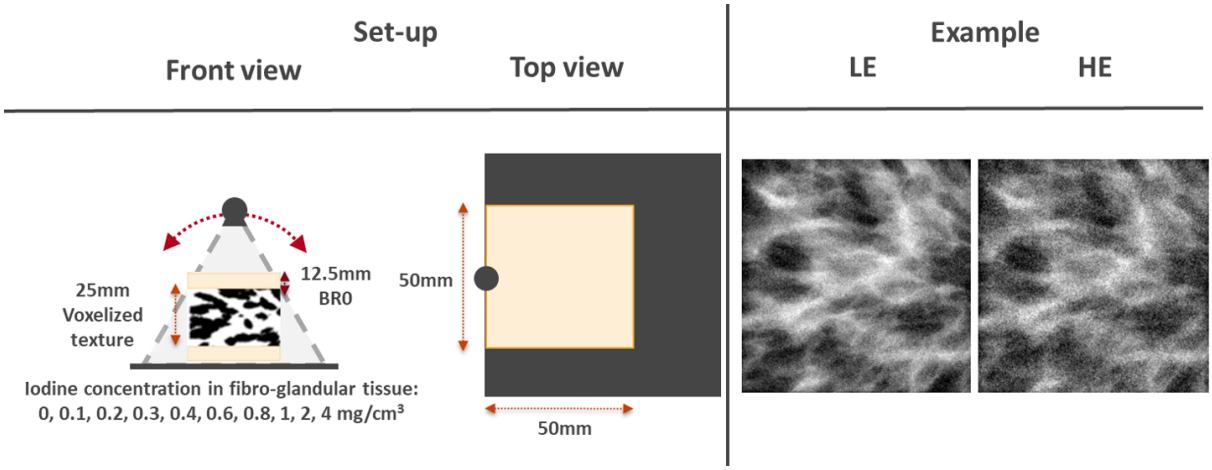

Figure 5.6: Set-up considered to measure the β parameter for different BPE levels related to a large range of iodine concentrations allocated in the fibroglandular tissue. A pair of Senographe Pristina low- and high-energy simulated projections is given as example.

architecture were assigned to attenuation coefficients corresponding to various homogeneous mixtures of fibroglandular tissue and iodine concentrations (0, 0.1, 0.2, 0.3, 0.4, 0.6, 0.8, 1, 2, $4mg/cm^3$).

The simulation platform was adapted using the same operational point as described in Section 5.1 to replicate the characteristics of the Senographe DS and Senographe Pristina mammography systems (Tables 5.1 and 5.2). The low- and high-energy projected pairs were recombined using Equation 4.10, and reconstructed using the modified FBP method described in Section 4.2.3. Some examples of the reconstructed slices for these two systems are presented in Figure 5.7. To study the different BPE representation between CESM projections and CEDBT slices we only used the characteristics of the Senographe Pristina mammography system.

The value of β for each mammography system and iodine concentration was estimated using the reconstructed slice located at $25mm$ from the object support. For each of the 40 reconstructed volumes, the Wiener spectrum was estimated using the average of 4 squared overlapped patches with size 256×256 pixels. The overlapping ratio was set to 50%. To test the statistical difference between the represented BPE levels for each mammography system, we used a Wilcoxon paired test [299] for each couple of iodine concentrations.

The estimated Wiener spectra for all the simulated images (40 in focus CEDBT slices per system and iodine concentration) are illustrated in Figure 5.8. As the reader may appreciate, the magnitudes of the Wiener spectra estimated from Senographe Pristina slices are uniformly distributed, with a narrow overlapping between two consecutive iodine concentrations of the background contrast uptake. This is not the case for the simulated Senographe DS CEDBT slices. The Wiener spectra estimated from this system are overlapped. This can be interpreted as an increased complexity to differentiate cases with different background contrast uptake.

This observation is also verified by the average β and α fitted values presented in Figure 5.9. We show that the average β estimated from Senographe Pristina slices in the iodine concentration range between 0 and $0.8mg/cm^3$ is uniformly distributed, with a wide separation between the values for two consecutive iodine concentrations. At the same time we show that the value of β is almost independent of the iodine concentration when evaluated in the Senographe DS.

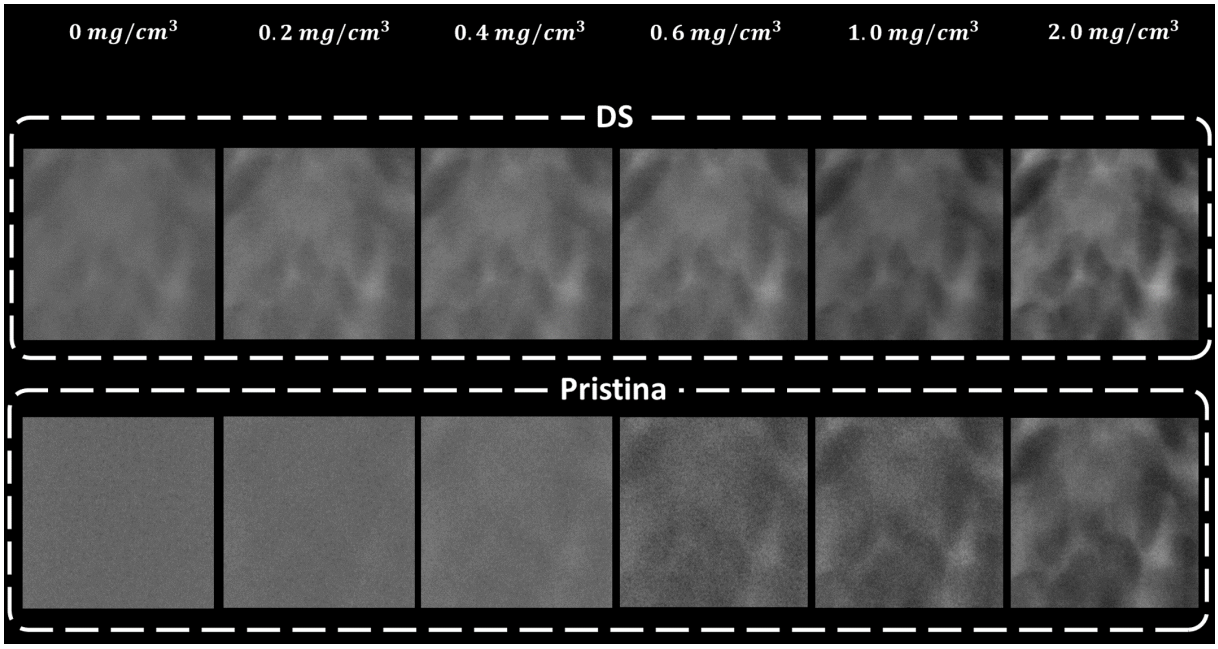

Figure 5.7: Examples of reconstructed slices for different mixtures of fibroglandular tissue and BPE iodine concentrations.

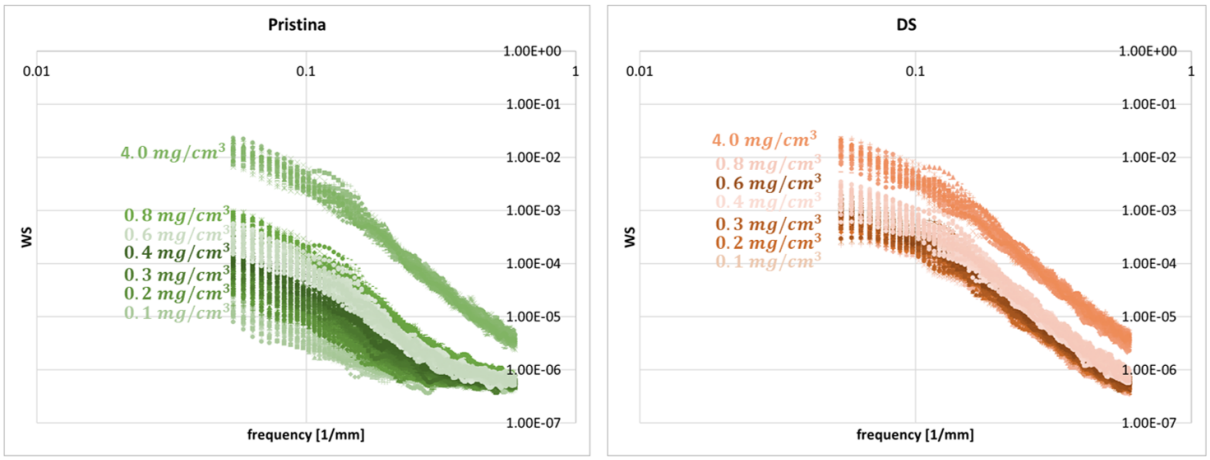

Figure 5.8: Wiener spectra estimated for both mammography systems. The color shade indicates all the points obtained from the 40 slices used to estimate each noise spectrum.

The statistical analysis corroborates this result. As we show in Table 5.4, there is no significant statistical difference (Wilcoxon $p\text{-}value > 0.05$) between the values of β obtained for different background iodine concentrations in the Senographe DS slices. By contrast, in Senographe Pristina slices we find that in the range from 0 to $0.6 mg/cm^3$ the values of β are significantly different (Wilcoxon $p\text{-}value < 0.01$), however, from $0.8 mg/cm^3$ the value reaches an asymptotic value. This is an expected result, as the anatomical information in recombined images with high background iodine concentrations should be identical their respective single energy images.

The results of the comparison between the β values in CESM and CEDBT for a Senographe Pristina system are illustrated in Figure 5.10. As we can observe, the β curve for CESM is

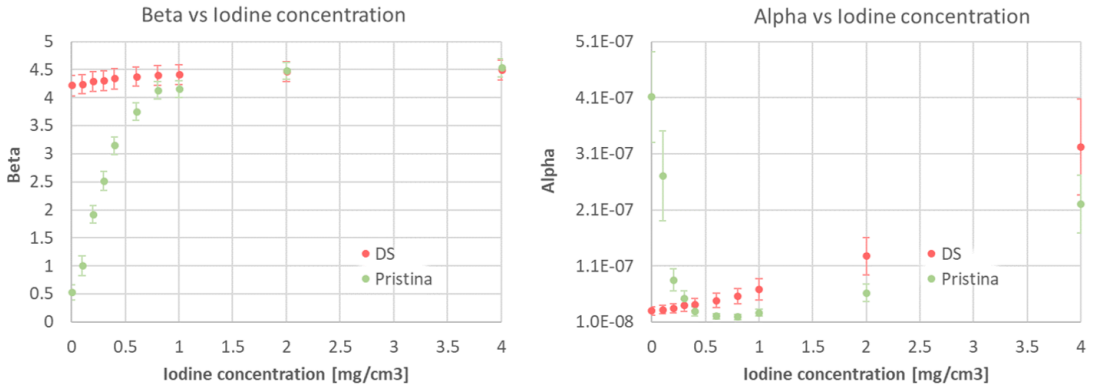

Figure 5.9: Average of fitted β and α values for Senographe DS and Senographe Pristina mammography systems. The error bars represent the 95% confidence interval.

Table 5.4: Distribution of p-values for Senographe DS (left) and Senographe Pristina (right) of the Wilcoxon test between the values of β obtained for different iodine concentrations $[mg/cm^3]$ in the fibroglandular tissue. The color code is the following: green means that $p\text{-}value < 0.05$, orange represents that $0.01 < p\text{-}value < 0.05$, and red is assigned when $p\text{-}value > 0.05$.

p-value	0.1	0.2	0.3	0.4	0.6	0.8	1	2	4
0									
0.1	-								
0.2	-	-							
0.3	-	-	-						
0.4	-	-	-	-					
0.6	-	-	-	-	-				
0.8	-	-	-	-	-	-			
1	-	-	-	-	-	-	-		
2	-	-	-	-	-	-	-	-	

p-value	0.1	0.2	0.3	0.4	0.6	0.8	1	2	4
0									
0.1	-								
0.2	-	-							
0.3	-	-	-						
0.4	-	-	-	-					
0.6	-	-	-	-	-				
0.8	-	-	-	-	-	-			
1	-	-	-	-	-	-	-		
2	-	-	-	-	-	-	-	-	

systematically below the curve for CEDBT. The average and maximal distances between the values of β are equal to 0.48 and 0.73 (for $0.2mg/cm^3$), respectively. This may be caused by the projection of the fibroglandular architecture in CESM, decreasing the variability of the image structures related to the background contrast uptake.

The asymptotic value for the two curves is also different: $\beta_{CESM} = 3.96$ and $\beta_{CEDBT} = 4.54$. These asymptotic values of β should be the same as those found in low-energy projections and DBT reconstructed slices, respectively. This means that, to validate our β estimation method and the results obtained, we can compare our asymptotic results to the β values found in their respective single energy images. Mainprize et al. [199] evaluated the magnitude of β for the same textured test object we used in our simulations. In their work, they compared the value of β in mammography and tomosynthesis images, for simulated and experimentally acquired images of a virtual and physical replica. They found that the simulated images of the virtual phantom share similar values to the measures performed in the images of the physical phantom: $\beta_{mammo} = 3.72$ and $\beta_{DBT} = 4.55$ in simulated images compared to $\beta_{mammo} = 3.76$ and $\beta_{DBT} = 4.33$ in experimentally acquired images. As we can observe, these values are comparable to the asymptotic values we found in our CESM and CEDBT β curves.

Otherwise, the values of β for CESM recombined images found in the literature correspond to the estimated measures between 0.1 and $0.2mg/cm^3$ in our simulated CESM images. This

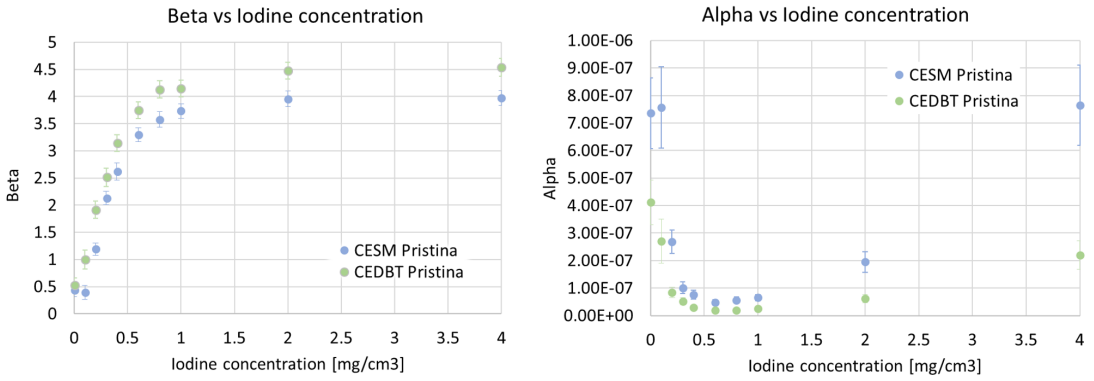

Figure 5.10: Average of fitted β and α values for CESM and CEDBT in a Senographe Pristina mammography system. The error bars represent the 95% confidence interval.

corresponds to the iodine concentration levels considered in clinical studies. Based on these results, to reproduce the standard contrast uptake in normal fibroglandular tissue in the evaluation study presented in Section 6, we use a iodine concentration equal to $0.125 mg/cm^3$.

Consequently, we can conclude that Senographe Pristina diminishes the β value against Senographe DS in CEDBT. In addition, the capability of imaging BPE improves with Senographe Pristina. This is a relevant result because, due to the lower value of β found in Senographe Pristina CEDBT slices for a wide range of background iodine concentrations, we can expect a better detectability of the contrast uptakes.

5.3 Detectability of contrast uptakes

As we have presented in the previous section, the detectability of contrast uptakes is associated with the performance of texture cancellation. However, there are also other factors that impact the depiction of lesions in contrast-enhanced X-ray, such as the background noise and the intensity of the enhanced lesion. A traditional measure to assess detectability is the SDNR. This measure has already been used to evaluate the CEDBT detectability performance in several works [133, 266] and has been proved to be correlated to human detection performance [153]. It is defined as follows:

$$SDNR = \frac{\mu_{lesion} - \mu_{BK}}{\sigma_{BK}} \tag{5.7}$$

where μ_{lesion} is the average signal of the recombined image over the contrast uptake, μ_{BK} is the average signal of the recombined image over the background surrounding the contrast uptake, and σ_{BK} is the standard deviation of the signal over the background. Consequently, this measure helps us to understand whether the variability of the signal intensity due to the presence of a iodine uptake can be differentiated from the signal fluctuations of the background.

In this section we want to assess the detection performance offered by the Senographe DS and the Senographe Pristina in CEDBT slices. This means, the performance differentiating the contrast uptake due to a lesion from the textured contrast uptake of the background surrounding the lesion background, for several combinations of different iodine concentrations in the lesion and background texture patterns.

The set-up used in this section to compare the improvement in CEDBT detectability is illustrated in Figure 5.11. A spherical lesion surrogate of $0.8cm$ in diameter and different mixtures

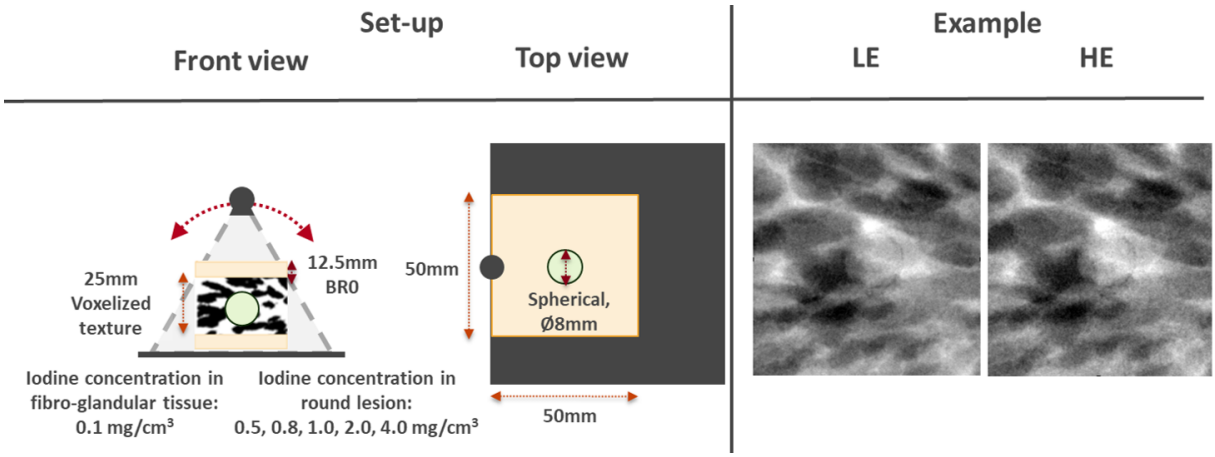

Figure 5.11: Set-up designed to measure the SDNR of contrast uptakes in spherical lesions with different iodine concentration levels. The spherical lesion surrogate is included in the middle of a voxelized texture, with fibroglandular architecture composed by a homogeneous mixture of glandular tissue and $0.1 mg/cm^3$ iodine concentration. A pair of Senographe Pristina low- and high-energy simulated projections is given as an example.

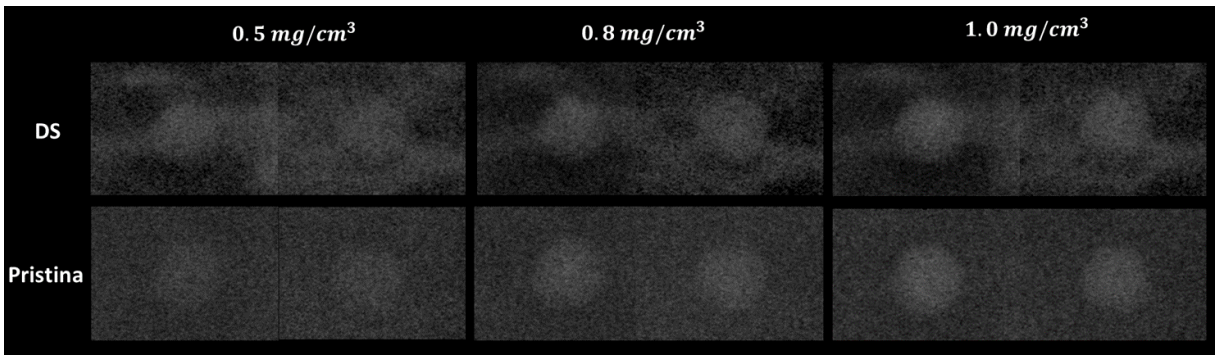

Figure 5.12: Examples of reconstructed slices for spherical contrast uptakes with different iodine concentrations.

of glandular and iodine concentrations (0.5, 0.8, 1.0, 2.0 and $4.0 mg/cm^3$) is placed in the middle of a voxelized prism. This voxelized prism is a modification of the DRAP texture model described in Section 3.3. We added two additional layers to a $50 \times 50 \times 25 mm^3$ voxelized prism, one under and one over the prism, of equivalent pure adipose tissue of $12.5 mm$ height each, obtaining a total 27% volumetric glandular density. The fibroglandular voxels are modified to represent the attenuation of an homogeneous mixture of glandular tissue and $0.1 mg/cm^3$ iodine concentration. We generated 40 volumes per iodine concentration and mammography system.

Simulations were adapted following the operational points described in Section 5.1 for Senographe DS and Senographe Pristina mammography systems (Tables 5.1 and 5.2). Additionally, we used Equation 4.10 to obtain the recombined projections, and the reconstruction method presented in Section 4.2.3 to compute the CEDBT slices. The SDNR was measured in the in-focus slice at $25 mm$ from the object support. In Figure 5.12, we show some examples of the in-focus slices generated for both imagery systems.

To estimate the SDNR we segmented a $5 mm$ in diameter round ROI centered at the lesion, as well as a square $20 \times 20 mm$ ROI also centered at the lesion where the signal belonging to the

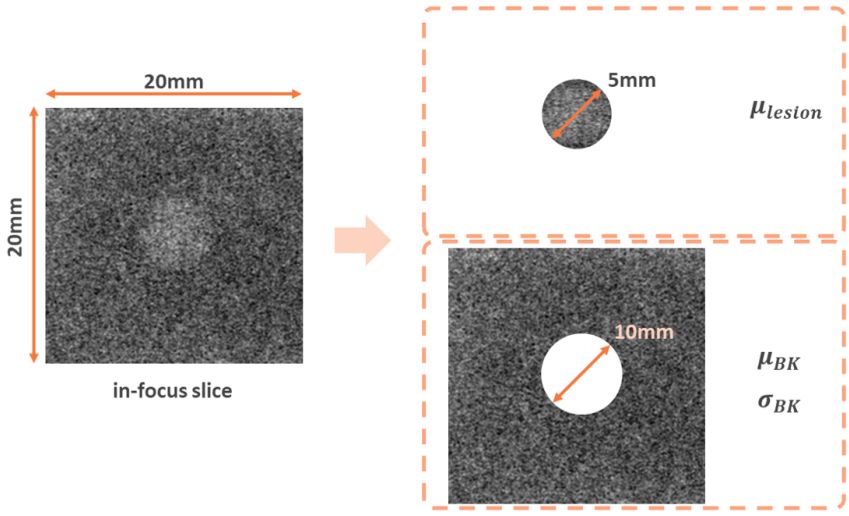

Figure 5.13: Representation of the segmented ROIs used in the estimation of the SDNR for each CEDBT slice included in our detectability comparison.

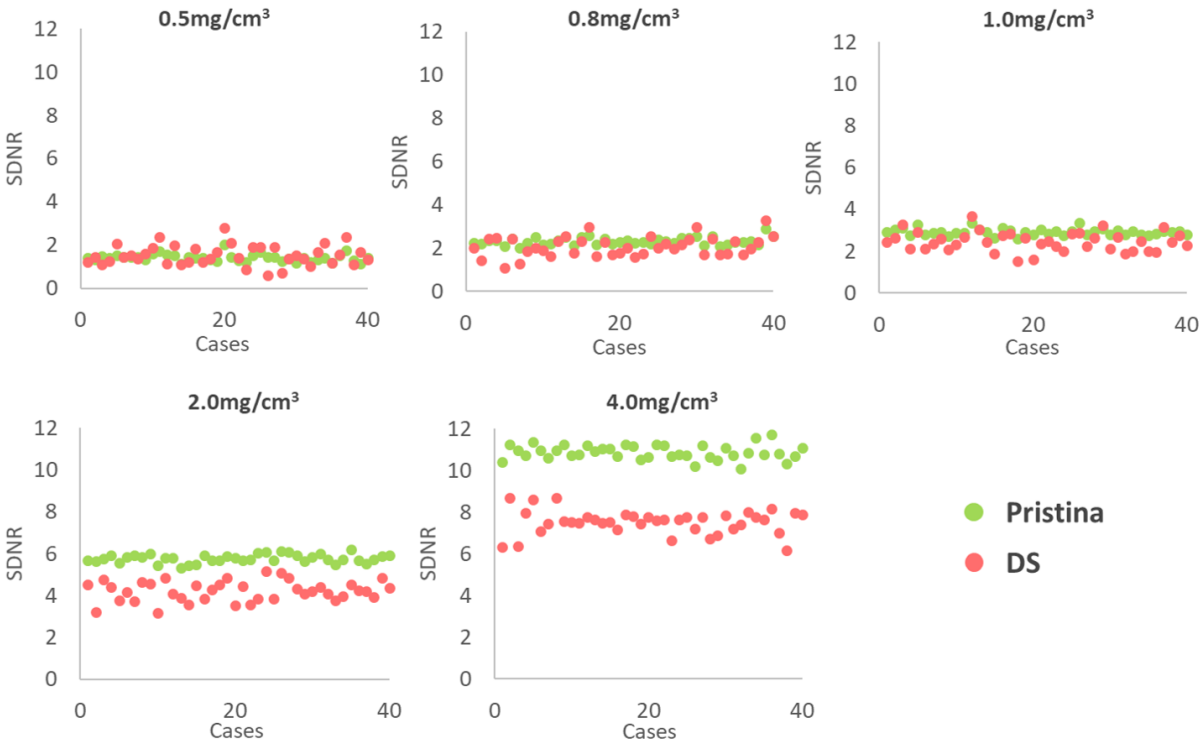

Figure 5.14: Results of the detectability analysis in CEDBT in-focus slices performed for both mammography systems. We show the SDNR estimated for each generated case: 40 different textured backgrounds and five different lesion iodine concentrations.

lesion was removed out (Figure 5.13). The average SDNR and 95% confidence interval for each series of 40 images were computed. Additionally, a Wilcoxon significant test to compare the statistical difference of SDNR in both mammography systems was calculated. The results are presented in Figure 5.14 and Table 5.5.

Table 5.5: Detectability differences between both mammography systems. For each iodine concentration we show the average SDNR and 95% confidence interval obtained for the 40 cases simulated. Additionally, we also include the *p-value* of the Wilcoxon test to assess the significance of the difference between the estimated SNDR.

	$0.5mg/cm^3$	$0.8mg/cm^3$	$1mg/cm^3$	$2mg/cm^3$	$4mg/cm^3$
Senographe DS	1.53 ± 0.15	2.07 ± 0.15	2.46 ± 0.15	4.22 ± 0.15	7.53 ± 0.18
Senographe Pristina	1.43 ± 0.05	2.32 ± 0.06	2.92 ± 0.05	5.77 ± 0.06	10.88 ± 0.11
p-value	0.08	0.0002	0	0	0

The *p-value* of the Wilcoxon significant test reveals that the SDNR of CEDBT images from Senographe Pristina is higher than the one found in Senographe DS images for iodine concentrations higher than $0.8mg/cm^3$ (*p-value* < 0.05), while, for the iodine concentration $0.5mg/cm^3$, both systems share a similar SDNR (*p-value* $= 0.08$) and, therefore, an equivalent detectability. In addition to this, we can observe in Figure 5.14 that the difference between both averaged SDNRs is increasingly proportional to the iodine concentration of the lesion. Considering that the background is always the same (i.e. the BPE level is not modified among our simulated volumes in this set-up), this means that the increased iodine concentration is better represented in the reconstructed Senographe Pristina slices, as it could already be observed in Section 4.1.5. Also, in Table 5.5, we show that the confidence interval of the SDNDR estimated in CESBT slices of the Senographe DS is higher than in the Senographe Pristina. This may be due to the higher value of β found in reconstructed CEDBT slices for the Senographe DS, which increases the variability of the average signal intensity and standard deviation of the background contrast uptake.

Therefore, we found a higher detection performance in the reconstructed CEDBT slices for the Senographe Pristina system. This is consistent with the lower value of β found in Section 5.2 and the better texture cancellation found in Section 5.1 for Senographe Pristina CEDBT images.

5.4 Cupping artifact in recombined images

The recombination process presented in Chapter 4 is constrained by a series of hypotheses, such as a constant thickness over all the whole surface of the projected object or an acquisition model that ignores the non-stationary contribution of the scattered X-ray field (while we know for example, that the magnitude of the scatter is different at the edges of an object for example). These limitations are materialized in recombined images through several types of undesired artifacts (see Section 1.1.4 of Chapter 1 for more information about these artifacts). Among them, cupping artifacts in the recombined images (also known as rim or breast-in-breast artifacts) appear as an undesired contrast enhanced region parallel to the breast edge (Figure 5.15), which could be mistakenly interpreted as a real contrast uptake. Already present in recombined projections, it is propagated to the different slices, so it is a common problem for CESM and CEDBT images. The reduction of this type of artifact is an important task, because it could affect the detection and evaluation of contrast uptakes.

Cupping artifacts originate from the X-ray scattered field in low- and high-energy acquisitions [41]. Therefore, a dedicated anti-scatter grid rejecting scatter radiation from high energy photons should alleviate the impact of this type of artifacts. As we have described in the introduction of this chapter, the CEDBT prototype based on the Senographe DS system did not

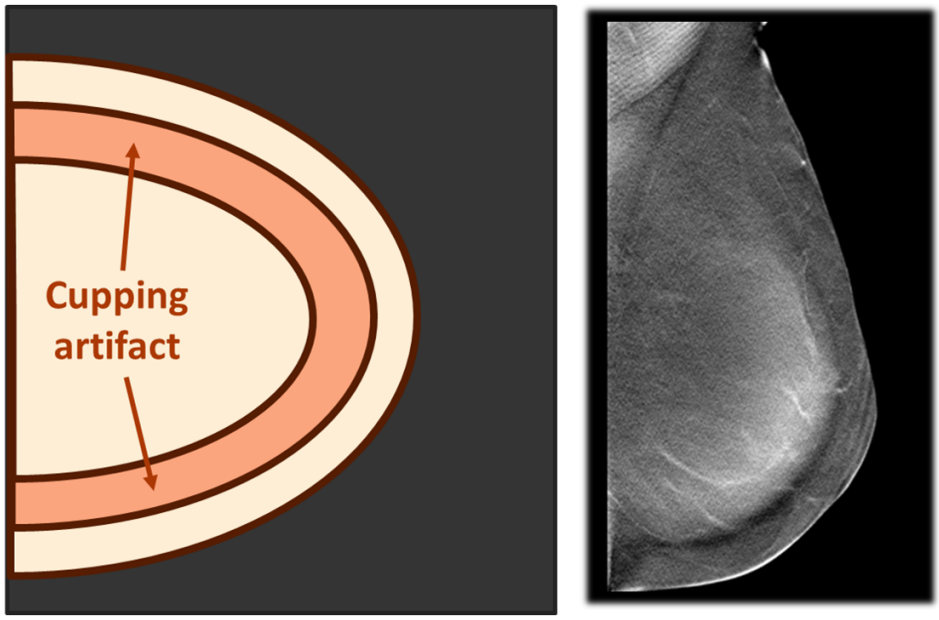

Figure 5.15: Illustration of the region where we may find the cupping artifact after the recombination of the low- and high-energy acquisitions of a breast-shaped object, and a clinical example acquired from a mammography system without anti-scatter grid.

include an anti-scatter grid. This requirement was addressed later, in Senographe Pristina, which includes an anti-scatter grid optimized for both low- and high-energy image acquisitions and for both FFDM and DBT modalities.

In this section we want to assess the impact that cupping artifacts have on the detection of contrast uptakes. To do that, we simulated low- and high-energy projected images of an anthropomorphic phantom with and without different iodine inserts considering the characteristics of a Senographe Pristina with and without anti-scatter grid. Then, we recombined them to evaluate the magnitude of the cupping artifacts and the absolute contrast of the iodine inserts in both cases.

The correct evaluation of cupping artifacts in simulated images depends on the quality of the simulation (similarity to experimental cases) of non-stationary X-ray scatter fields in low- and high-energy, particularly at the edge of objects. In Section 2.2 of Chapter 2, we presented a new simulation approach to model the X-ray scatter in low- and high-energy images for a Senographe Pristina with and without anti-scatter grid. Our method presented a limitation for high-energy simulations without anti-scatter grid and objects thicker that $25mm$, which must be considered.

If we want to evaluate the magnitude of the cupping artifacts using simulated acquisitions of an anthropomorphic phantom we need a digital surrogate of the physical anthropomorphic test objects used in the evaluation of the image quality of mammography systems. In particular, we were interestedion simulating the shape of the CIRS 011A test object. This test object, that imitates the shape of a $45mm$-thick compressed breast, has been previously used to measure the magnitude of the scatter in a mammography system [72]. To compute the digital mesh surface of this object, in order to include it in our simulation framework, we followed the steps illustrated in Figure 5.16. First, we performed a complete computed tomography (CT) acquisition of the test

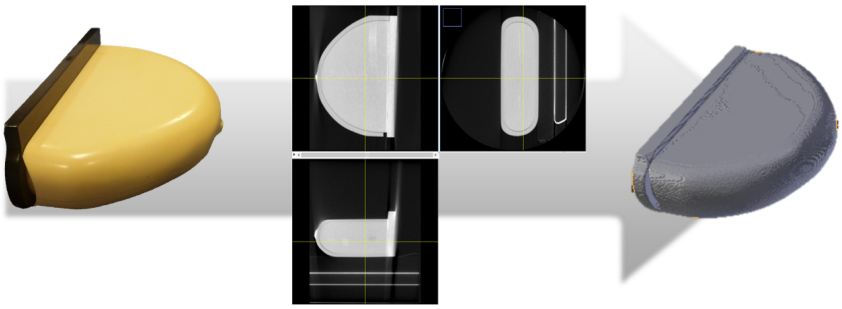

Figure 5.16: Illustration of the conversion from the physical CIRS 011A test object to a digital mesh replica of its envelope, using a computed tomography acquisition.

object using an Innova™ system (General Electric). Then, the volume and the corresponding mesh surface was computed using CT data and the ITK-SNAP software [308]. This meshed surface can be used in the X-ray simulation platform presented in Chapter 2 and combined with the lesion surrogates presented in Chapter 3.

Some differences between the physical test object and its virtual surrogate need to be considered. According to the technical sheet of the CIRS 011A test object, the model simulates a 50% glandular/50% adipose equivalent tissue, with a removable $0.5cm$ adipose tissue-equivalent layer. This removable layer was not included in its virtual surrogate, where we considered a homogeneous distribution of 50% glandular/50% adipose equivalent tissue (CIRS BR50). Also, our surrogate does not include the inserts present inside the physical phantom. Finally, while the surface of the physical test object is continuous, the sampling precision of the thickness in our virtual surrogate is $0.5mm$, which causes some minimal discontinuities in the final image.

5.4.1 Evaluation of the cupping artifact magnitude and range

As illustrated in Figure 5.15, the cupping artifact may appear in the recombined image with a positive contrast in a region belonging to adipose or glandular tissue parallel to the breast edge. Our objective is to evaluate the magnitude of the average signal found in this region of the recombined image for simulations with and without anti-scatter grid, and compare it to the signal intensity found in the non-enhanced tissue. To do that, we measure the signal intensity of $N+1$ radial profiles p_m of the recombined image $I(x,y)$ for a given angle $\theta_m = -\frac{\pi}{2} + \frac{m\pi}{N}$ with $m \in \{0...N\}$ and a distance d from the center of the projected object c_0 (Figure 5.17):

$$p_m(I, c_0, d, \theta_m) = I(c_0 + d \cdot \sin(\theta_m), c_0 + d \cdot \cos(\theta_m)) \tag{5.8}$$

To avoid noisy measures, the $N+1$ radial profiles can be averaged over different ranges of θ to obtain average profiles $SI(I, c_0, d)$. To do this, we follow the schema illustrated in Figure 5.17. We compute one averaged angular profile SI_T considering the complete range of θ equal to $[-\frac{\pi}{2}, \frac{\pi}{2}]$, and S averaged profiles SI_s, where $s \in \{0...S-1\}$ is the number of the averaged sectors, for θ ranges equal to $[-\frac{\pi}{2} + \frac{\pi s}{S}, -\frac{\pi}{2} + \frac{\pi(s+1))}{S}]$:

$$SI_T(I, c_0, d) = \frac{1}{N} \sum_{i=1}^{N} p_i(I, c_0, d, \theta_i) \tag{5.9}$$

$$SI_s(I, c_0, d) = \frac{S}{N} \sum_{i=s\cdot(N+1)/S}^{(s+1)\cdot(N+1)/S-1} p_i(I, c_0, d, \theta_i) \tag{5.10}$$

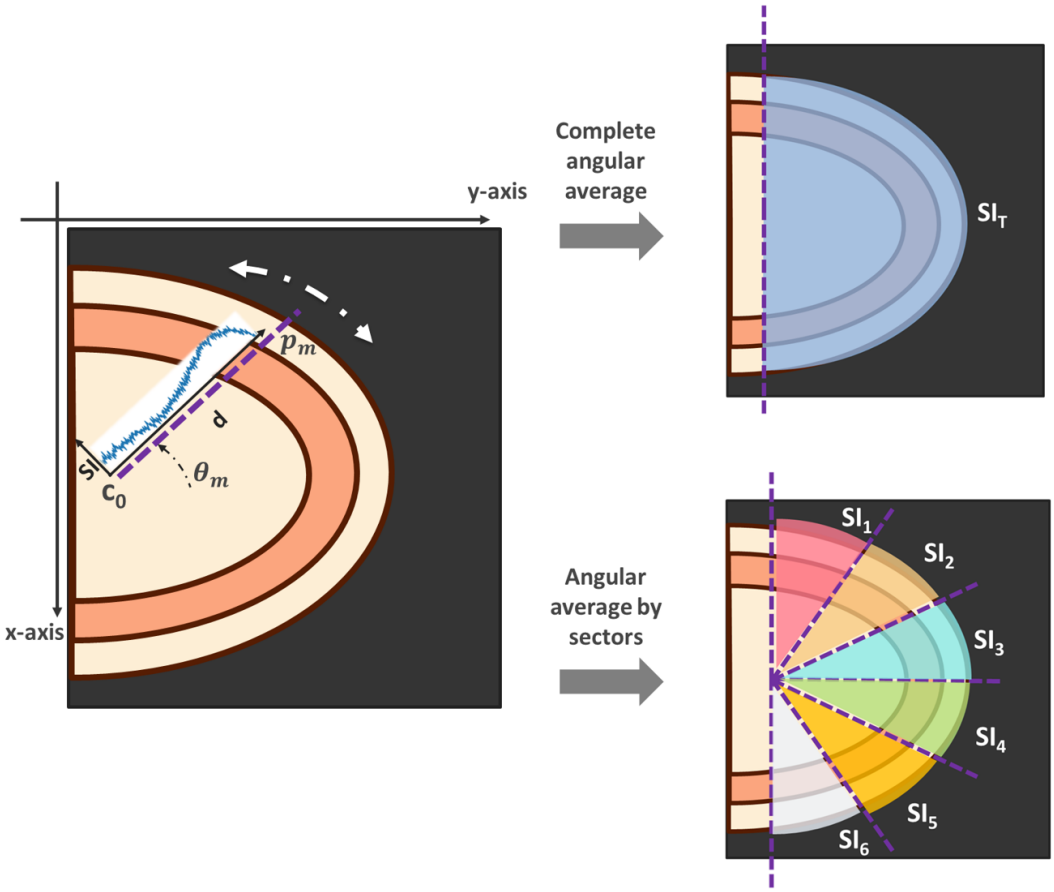

Figure 5.17: Schema illustrating the radial profiles acquired along the anthropomorphic phantom. From c_0 to the object test edge, we measure the signal intensity of the recombined image I for several angles θ_m, following the axis d. All these profiles can be averaged to estimate the total contribution of the cupping artifact (SI_T), or averaged over several regions to estimate the contribution of the cupping artifact in a given direction (SI_s).

Then, the impact of the cupping artifact can be evaluated from each averaged profile using two different measures, the range R and the magnitude M. While the range R measures the width of the artifact, the magnitude measures its intensity (Figure 5.18). These measures are defined as:

$$R = d_{peak} - d_{center} \tag{5.11}$$

$$M = SI(I, c_0, d_{peak}) - SI(I, c_0, d_{center}) \tag{5.12}$$

where $SI(I, c_0, d)$ is an averaged profile, either SI_T or SI_s, $d_{peak} = \arg\max_d(SI(I, c_0, d))$ is the position along the averaged profile where it reaches its maximum value, and d_{center} is the position along the averaged profile where it is flat onwards.

To obtain both measures, we used the set-up illustrated in Figure 5.19. The flat edge of the CIRS 011A virtual envelope was positioned at the chest-wall side of a 200×200 mm detector and centered along the x-axis. We set the equivalent linear attenuation coefficient of the envelope content to a homogeneous mixture of 50% fibroglandular and 50% adipose tissue (CIRS BR50). The center c_0 was placed at the center of the x-axis and separated $15mm$ from the chest-wall.

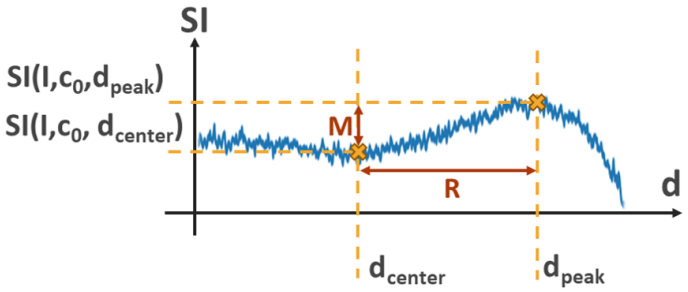

Figure 5.18: An example of a radial profile. The magnitude of the cupping artifact M can be estimated as the difference of signal intensity at the maximum of the artifact ($SI(I, c_0, d_{peak})$) and the signal intensity at the edge of the artifact ($SI(I, c_0, d_{center})$). The range of the artifact R can be estimated using the positions where both signal intensities were measured.

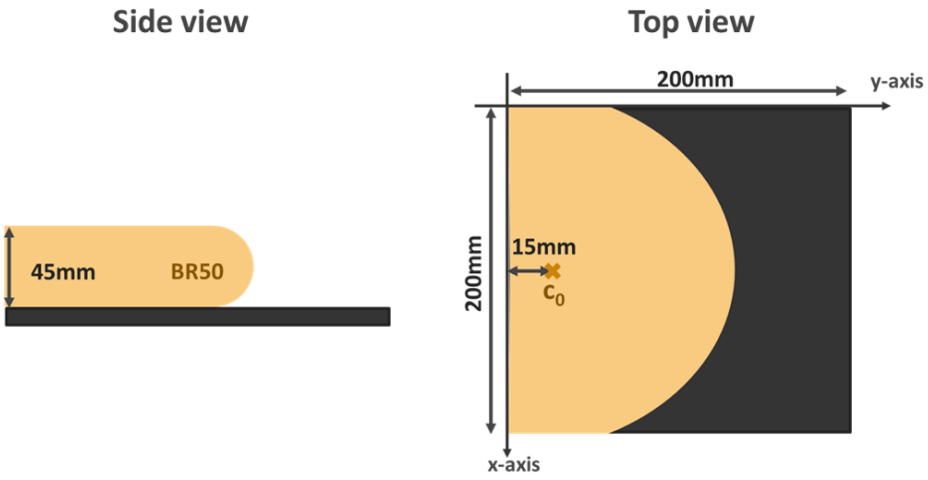

Figure 5.19: Placement of the virtual surrogate of the anthropomorphic test object over the detector and position of the center c_0 used to estimate the radial profiles.

The number of profiles chosen was $N = 200$, divided in $S = 6$ sectors. Two types of low- and high-energy images were simulated: with and without anti-scatter grid, according to the models presented in Section 2.2 of Chapter 2. The rest of the processes was adapted following the characteristics of a Senographe Pristina. The operational point used in these simulations is given in Table 5.6. The recombined images were post-processed using an algorithm that retrieves the average signal intensity at the border of the object, where the thickness is not constant.

The resulting images are illustrated in Figure 5.20. As we expected, the simulated image which considers the anti-scatter grid is more uniform than the one which does not consider the anti-scatter grid, where we can better appreciate the breast-in-breast artifact. The "stain-like" regions which are observed in the recombined images, causing signal intensity discontinuities, appear as the result of the sampling precision of the thickness in our virtual surrogate. We measured the signal intensity difference due to this discontinuity using the average signal intensity measured in the ROIs presented in Figure 5.21. Therefore, the signal intensity difference due to the sampling precision is equal to 2.8 counts in the recombined image using simulations with anti-scatter grid, and equal to 4.1 counts in the recombined image using simulations without

Table 5.6: Operational point used for the simulation of the low- and high-energy acquisitions of the anthropomorphic test object.

	Simulated	
	LE	**HE**
Spectrum	23keV (monoenergetic)	34keV (monoenergetic)
Target/Filter	Rh/Ag	Rh/Cu
Exposure	36mAs	110mAs
Gainmap	50mm PMMA	50mm PMMA

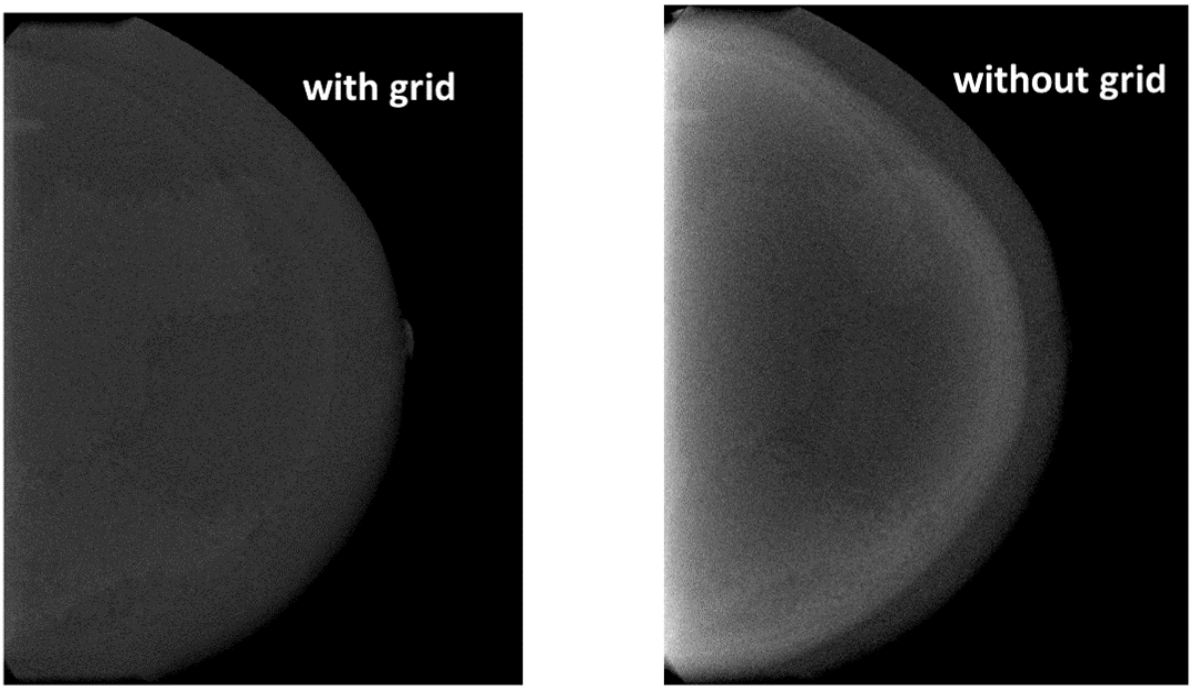

(a) Recombined image of the virtual anthropomorphic test object considering the anti-scatter grid.

(b) Recombined image of the virtual anthropomorphic test object without considering the anti-scatter grid.

Figure 5.20: Recombined images of the low- and high-energy simulations of the virtual anthropomorphic test object.

anti-scatter grid. These signal intensity differences represent less than an equivalent superficial iodine concentration of $0.25 mg/cm^2$, as described in the results illustrated in Figure 4.13 of Chapter 4.

The measured averaged angular profiles SI_T and SI_s for recombined images using simulations with and without anti-scatter grid are illustrated in Figure 5.22. Additionally, in Table 5.7 we present the value of M and R for each profile. We did not find any cupping artifact in sector 6 in the simulations performed considering the anti-scatter grid and, consequently, the value N/A was used instead.

Regarding the magnitude M of the cupping artifact, we can observe a noticeable difference between the recombined image which considers the presence of an anti-scatter grid and the one which does not. The average magnitude M in the recombined image which considers the grid

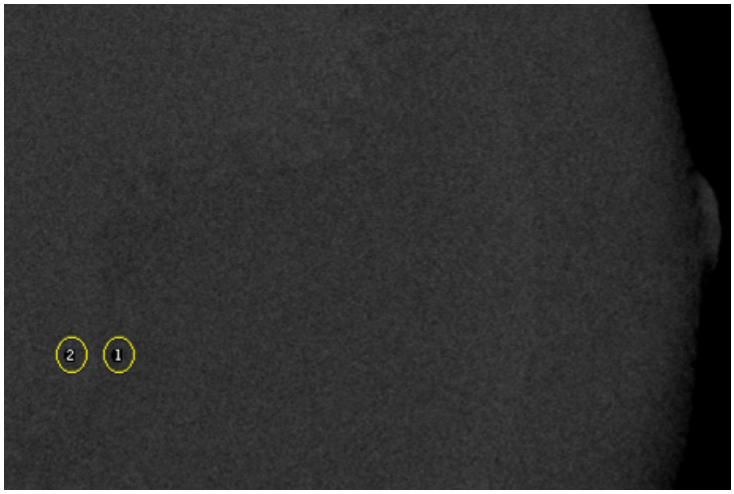

Figure 5.21: ROIs used to estimate the influence of the thickness sampling precision. The same ROI placement was used for the recombined images with and without anti-scatter grid.

is equal to 2.69 counts, smaller than the error produced by our sampling thickness precision of $0.5mm$, and, therefore, it is barely distinguishable (Figure 5.20a). This is not the case for the recombined image that does not consider any anti-scatter grid. In this image we observe a noticeable cupping artifact appearing parallel to the edge of the object, having an average magnitude M of 27.98, more than ten times the magnitude in simulations with grid. This magnitude represents a $0.8mg/cm^2$ equivalent superficial iodine uptake concentration. The ranges R of the cupping artifact are also higher in recombined images that do not consider any grid, which is translated by a higher region where this artifact has an influence.

Considering these results, it can be concluded from our simulations that the image quality of Senographe Pristina recombined images is significantly better compared to the image quality of the images provided by Senographe DS, which is consistent with the results found in recombined images using physical systems [41].

5.4.2 Contrast uptakes in the presence of cupping artifact

The cupping artifact could be mistakenly interpreted as a real contrast-uptake (or even by the natural BPE present inside the breast). Moreover, if there is any real contrast-uptake present in the image, its visibility may depend on its position (i.e. near the cupping artifact or over the flat background of the recombined image). Our goal in this section is to evaluate the contrast values of different contrast-uptakes distributed along an anthropomorphic phantom, and compare them to the magnitude of the cupping artifact in simulated images when considering or not the anti-scatter grid.

To do that, we used the virtual surrogate of the CIRS 011A anthropomorphic phantom introduced in Section 5.4.1 and include several virtual iodine inserts in it. The simulations with and without anti-scatter grid were performed according to the set-up illustrated in Figure 5.23 and the operational point presented in Table 5.6. Inside the anthropomorphic surrogate, we included four spherical objects of $4mm$ radius each and composed of a homogeneous mixture of glandular tissue and iodine (concentration equal to $1mg/cm^3$). The object identified as 1 was placed between the region of the cupping artifact and the breast edge, the object 2 was placed over the region of the cupping artifact, the object 3 was placed in a region of the recombined

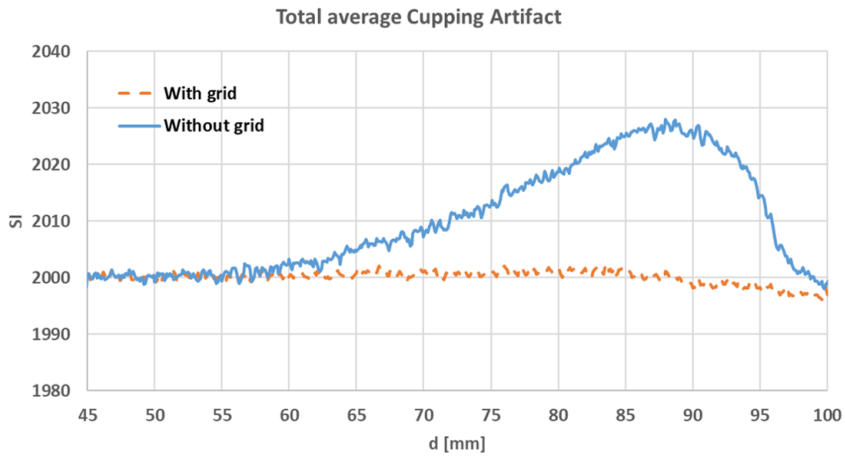

(a) Averaged SI_T profile measured in simulations with and without grid.

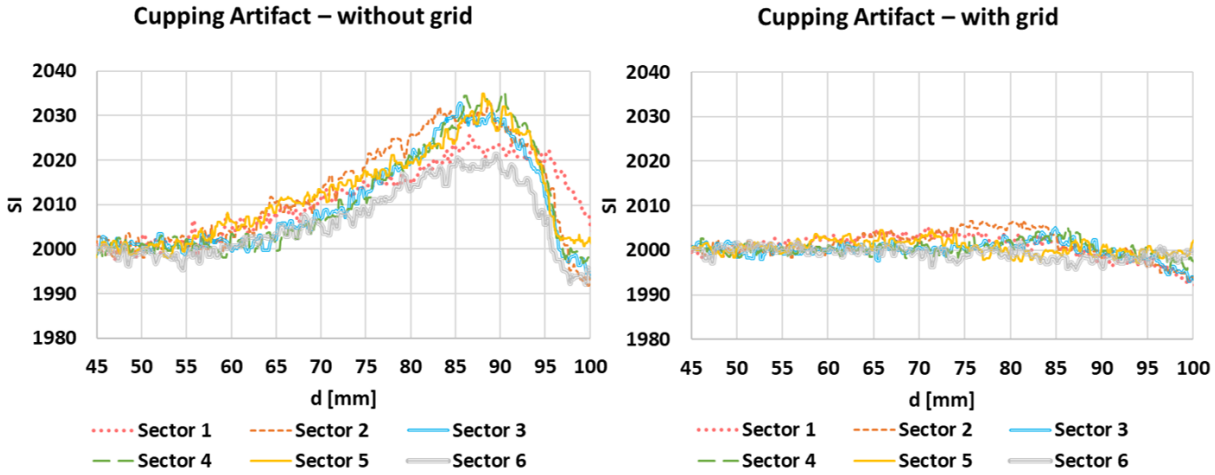

(b) Averaged SI_s profiles for each sector s measured in simulations with and without grid.

Figure 5.22: Averaged SI profiles for simulated images with and without anti-scatter grid.

Table 5.7: Results of the magnitude M and ratio R estimated over the recombined images with and without considering the anti-scatter grid.

		Sector 1	Sector 2	Sector 3	Sector 4	Sector 5	Sector 6	Total
M	**With grid**	4.82	6.50	5.08	5.34	4.66	N/A	2.69
	Without grid	25.49	32.74	32.76	35.21	34.91	21.35	27.98
R	**With grid**	17.70	14.00	17.80	18.80	14.80	N/A	17.00
[mm]	**Without grid**	36.50	34.30	33.50	38.10	32.20	24.60	31.40

image with uniform background and, finally, the object 4 was placed near the region of influence of the cupping artifact observed in images without grid in Section 5.4.1.

To measure the absolute contrast between the iodine inserts and the background we used the images already simulated in Section 5.4.1, where there was no iodine insert. Following the schema in Figure 5.24a, we subtracted the recombined images without iodine inserts to the recombined images with iodine inserts. The result is an image with the only presence of the signal intensity difference due to the iodine inserts. In other words, in this image we can compute

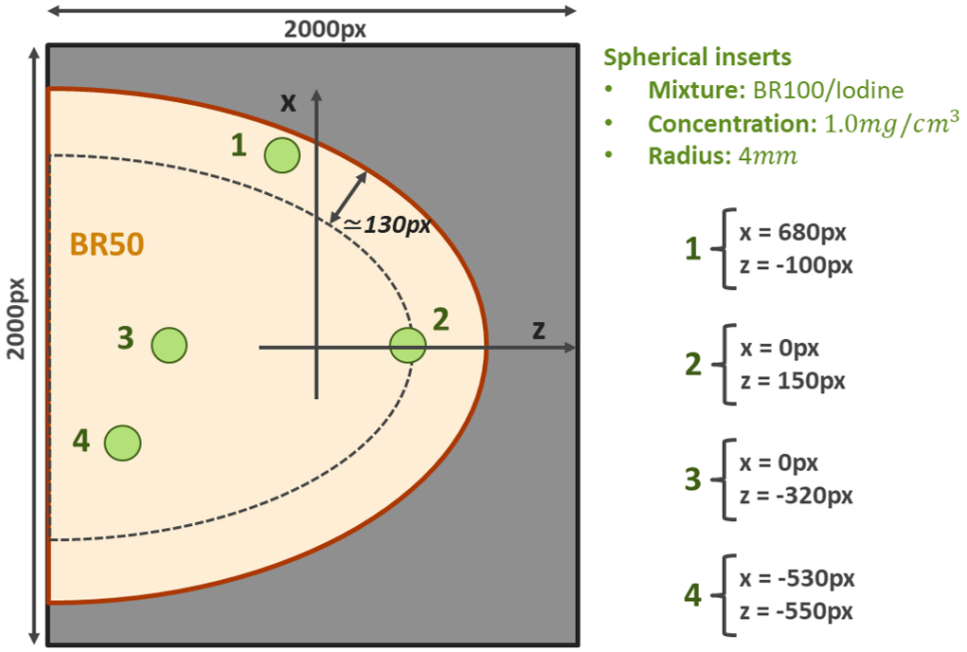

Figure 5.23: Placement of the iodine inserts in the anthropomorphic test object. The dotted line represents the region of influence of the cupping artifact present in the recombined image.

the absolute contrast measuring the average signal intensity in the ROIs corresponding to the iodine inserts (Figure 5.24b).

The values of the absolute contrast for each iodine insert are presented in Table 5.8. We observe that the absolute contrast of all iodine inserts is higher in the recombined image derived from acquisitions performed with an anti-scatter grid. Except for the insert near the object edge, all inserts in the recombined images considering the anti-scatter grid share similar contrast values. This is not the case when we consider images acquired with no grid, for which the contrast of the iodine inserts over the region of influence of the cupping artifact is higher than in the region with uniform background. Therefore, due to the lack of an anti-scatter grid, we cannot provide an accurate quantification of the iodine concentration based on a measure of the average signal intensity. Finally, the absolute contrast found in recombined images without anti-scatter grid is smaller than the magnitude of the cupping artifact computed in Section 5.4.1.

5.4.3 Discussion

We presented a quantitative comparison of the cupping artifact in recombined images with and without considering the anti-scatter grid in a Senographe Pristina system. Our approach was based on simulations of the acquisition process, using to this effect a virtual version of a physical anthropomorphic test object and virtual iodine inserts. The advantage of our simulated approach is that we can create an anthropomorphic phantom with different iodine inserts placed at the desired positions, while there are no commercial physical anthropomorphic phantom allowing this configuration.

Although our results show a considerable improvement when an anti-scatter grid is considered, our simulations are constrained by some limitations. First, as discussed in Chapter 2, some physical phenomena were not included in our simulations, such as the heel effect. This may

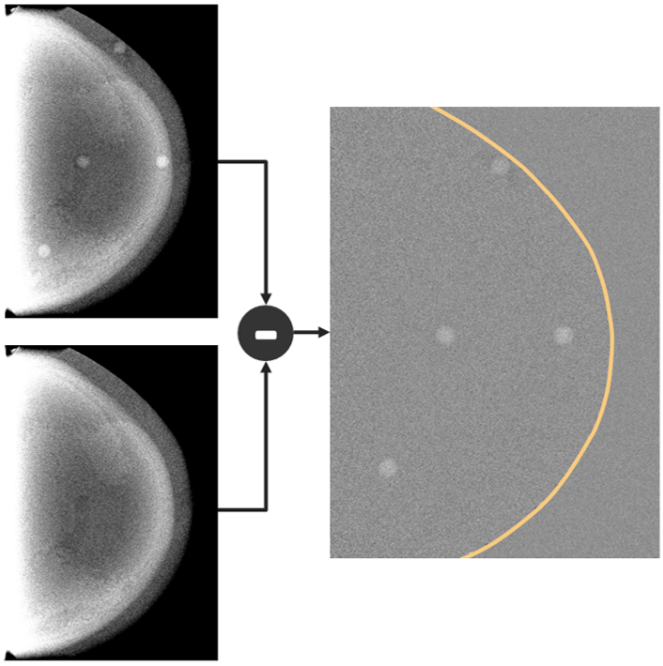

(a) The subtraction of the recombined image with iodine inserts and the same image without them leads us to an almost uniform image where we only find the signal difference introduced by the iodine inserts.

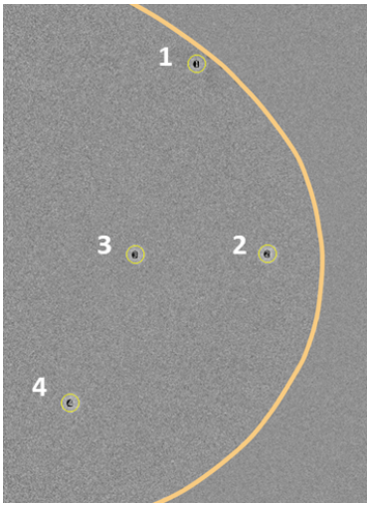

(b) The ROIs used to estimate the absolute contrast of each iodine insert.

Figure 5.24: Schema of the images used to estimate the absolute contrast of the iodine inserts included in the anthropomorphic test object.

Table 5.8: Values of the absolute contrast for each iodine insert.

	ROI 1	**ROI 2**	**ROI 3**	**ROI 4**
With grid	14.52	22.45	23.32	23.77
Without grid	10.63	19.21	15.08	18.07

reduce the realism of the low- and high-energy simulated images and, therefore, it may affect the representation of the cupping artifact in the recombined images. Moreover, we showed in Section 2.2.4 of Chapter 2 that our scatter model for high energy images without anti-scatter grid underestimates the scatter field generated in a real mammography system. This limitation may reduce the magnitude of the cupping artifact evaluated in this section for recombined images without anti-scatter grid. Therefore, it is expected that in experimental acquisitions the differences between recombined images with and without anti-scatter grid found in this section will be even greater.

Moreover, in this chapter we only compared projected recombined images. We did not evaluate the impact of the cupping artifact in reconstructed slices. However, it is expected that the replication of the artifact through the reconstructed slices leads to similar results.

Despite these limitations, the comparison showed that the magnitude and region of influence of the cupping artifact is notably higher when the anti-scatter grid has been removed. At the same time, when there is no anti-scatter grid, the absolute contrast of contrast uptakes is smaller and does not remain stable, which means that the quantification of a contrast uptake

would depend on its position. These results must be compared to experimental acquisitions in future works.

5.5 Conclusion

The design of mammography systems has been improved since the first preliminary results evaluating the performance of CEDBT. To our knowledge there was no published work comparing the image quality improvement due to current system designs. In this chapter, we compared the image quality of Senographe DS-based and Senographe Pristina-based CEDBT prototypes using the simulation platform introduced in Chapter 2. Our approach was focused on the impact of the lag effect and scattering processes on recombined and reconstructed slices. The acquisition sequence of Senographe Pristina is optimized to reduce the lag introduced in subsequent acquisitions and this imaging system incorporates an anti-scatter grid to reduce the contribution of the X-ray scatter field, while Senographe DS suffers from an elevated signal increment through subsequent low- and high-energy acquisitions due to the lag effect and the lack of anti-scatter grid in CEDBT mode. Therefore, the acquired images with Senographe DS include a significantly higher X-ray scatter contribution compared to Senographe Pristina.

We demonstrated the noticeable image quality improvement provided by Senographe Pristina in terms of non enhanced texture cancellation, detectability of contrast uptakes, quantification of breast parechyma enhancement and reduction of artifacts which may be mistakenly considered as actual iodine contrast uptakes.

Analyzing the results more closely, all these outcomes show that the almost lag-free acquisition sequence introduced in Senographe Pristina allows for better texture cancellation than in Senographe DS recombined images, as well as a better representation of the BPE and an increased detectability of contrast uptakes. This decrease of the texture cancellation performance is caused by the signal pollution introduced by the lag effect. With each subsequent acquisition, the average signal of low- and high-energy acquisitions increases, avoiding the perfect recombination of such pairs of images. However, we also showed that even in perfect lag conditions (no signal increment in subsequent acquisitions) the texture cancellation in Senographe DS acquisitions continued to be inferior to the cancellation provided by Senographe Pristina recombined images. This is related to the higher X-ray scatter contribution present in Senographe DS acquisitions which does not use any anti-scatter grid.

The lack of an anti-scatter grid in Senographe DS also causes more apparition of cupping artifacts in the recombined image which may be mistakenly interpreted as contrast uptakes. We showed that these artifacts are almost absent in recombined images when considering an anti-scatter grid which reduces the scatter field in low- and high-energy acquisitions. Additionally, the scatter field does not only influence the cupping artifact, but also the absolute contrast value of contrast uptakes which can change depending on the position of the contrast uptake along the breast. The integration of an anti-scatter grid allowsus to provide more quantitative results as well as an increased specificity of contrast uptakes as no fake contrast uptake is introduced in the form of cupping artifacts.

Nevertheless, the results presented in this chapter were computed using a simulated approach. All the physical phenomena included in our simulation chain were validated in Chapter 2, however some phenomena, such as the heel effect and a realistic focal spot, were not included. Moreover, our thickness-dependent scatter model was limited by high-energy acquisitions with

no anti-scatter grid. Therefore, all the results presented in this chapter must be compared to real experimental acquisitions to be fully validated.

Chapter 6

A comparison of CEDBT and CESM potential clinical performance

As discussed in Chapter 1, virtual clinical trials (VCT) can be considered as an alternative to traditional clinical trials, especially when potential new system designs are considered. The validity of such virtual clinical studies depends on how realistic the simulated surrogates reproduce the features of a real system. We provided a complete simulation platform which reproduces with fidelity the frequency, statitical and memory characteristics of single-energy images (cf. Chapter 2), as well as those of dual-energy recombined images (cf. Chapter 4). Additionally, we introduced a new model of contrast uptakes to be used in the context of contrast enhanced X-ray breast imaging (cf. Chapter 3). Leveraging these different contributions, we can generate synthetic CEDBT and CESM images mirroring real clinical cases.

In this chapter, we present a virtual clinical evaluation of CEDBT and CESM performance. We aim at comparing the detectability and characterization performance of CEDBT and CESM for mass-like enhancements.

To this end, in Section 6.1, we describe the components used in our virtual clinical trial and the clinical protocol implemented to assess the clinical performance enabled by the X-ray imaging systems, while in Section 6.2, we present the results of the study.

6.1 Human reader study

In a traditional clinical trial we can distinguish three main elements: the patient cohort, which can cover a certain range of pathologies; the imaging technique to be evaluated; and the reader, who performs the evaluation of the acquired images. The goal of a VCT (virtual clinical trial) is to replace some or all of these elements by simulated components. In this work, we focused our efforts on the virtualization of the patient cohort, by simulating different mass-like contrast uptakes, and the X-ray chain. Although the reader response to dual energy X-ray images has been studied by some research teams [38, 132, 250], the only clinical task which was evaluated by these models is detection. In our study, we aim to evaluate the detectability and the characterization performance of mass-like enhancements in CESM and CEDBT images. The image analysis was not replaced by any virtual component and we kept a traditional human reading of the generated images.

6.1.1 Definition of the dataset

The simulated patient cohort was generated using the methods developed in Chapter 3. Considering the pathology surrogates, we simulated seven breast mass types. These three-dimensional models cover the entire mass-like enhancement descriptors presented in Table 3.1. Table 6.1 shows the morphological lesion characteristics, dimensions and parameters used in this study. We did not focus our study on the impact of the lesion size on the characterization. Consequently, the average diameter of all surrogates was fixed to $\mathbf{8mm}$. The size was chosen based on the study performed by Dromain in 2015 [77]. This size allows us to include lesions that are not easily differentiated from the anatomical background and, therefore, best compare the detection performance between CESM and CEDBT.

We performed a preliminary study to verify the meaningfulness of define the different levels of iodine concentration to be used in our simulated lesions. This is important because we will use four types of confidence levels: not confident at all, not confident, confident and very confident, to assess the characterization performance for each reader. To improve the pertinence of our results we need the answers distributed among these four confidence levels. Therefore, in this preliminary study, we asked a reader to give his confidence level on the characterization of 88 CESM images of different lesion types. Three iodine concentrations were considered: **0.3, 0.5 and 0.8$\boldsymbol{mg/cm^3}$**. The results are presented in Figure 6.1. As we can observe, these iodine concentrations help us to retrieve a homogeneous range of confidence answers. For low iodine concentrations ($0.3mg/cm^3$) we have a majority of low confidence levels, while, intermediate and higher iodine concentrations (0.5 and $0.8mg/cm^3$) are associated with intermediate and high confidence levels.

In projected images, the accurate detection of a contrast uptake depends on the superficial iodine concentration, which is the integrated volumetric iodine concentration along the X-ray path. Because in our study we have contrast uptakes with heterogeneous and rim enhancement distributions, where the volumetric concentration is not uniformly distributed inside the contrast uptake, their superficial iodine concentration may be different from the rest of the contrast uptakes. It is important that all contrast uptakes represented in our database share the same superficial iodine concentration and, therefore, the same detectability. A different detection performance, associated with a different superficial iodine concentration, does not provide any information about the impact that the type of shape, margin or enhancement distribution may have on the detection of the contrast uptake. Moreover, it may also affect the characterization task, introducing a bias in our study. To avoid this bias, we modified the volumetric concentration of contrast uptakes with rim and heterogeneous enhancement distributions. The correction is made using the average diameter fixed for the surrogates of our database (d =8mm), the effective diameter d_{eff} which considers only the enhanced tissue of rim and heterogeneous enhancement distributions and the standard volumetric iodine concentrations defined in our database (C_{std} =0.3, 0.5 and $0.8mg/cm^3$). Then, the corrected volumetric concentration C_{corr} is estimated as follows:

$$C_{corr} = C_{std} \cdot \frac{d}{d_{eff}} \tag{6.1}$$

Rim patterns are described in clinical images using a wide range of enhancement thicknesses, from a very thin layer only covering the lesion margins, to a thick wall just leaving without enhancement a small central region of the lesion [293]. In this study, we used the same dimensions as Dromain [77] and we fixed the thickness of rim enhancements to $1.31mm$. Because the central core of these patterns does not take any enhancement, the volumetric iodine concentration of the rim must be corrected to offer the same superficial iodine concentration and, therefore, the

Table 6.1: Parameters used to generate the dataset of lesion surrogates for each of the seven types of masses present in the study. According to the notations used in Section 3 each of the parameters is associated with the shape, margins or enhancement of the lesion. For the shape: r is the radius of the first sphere created, a, b and c are the half axis lengths if the first element is an ellipsoid, N_{iter} is the number of iterations adding spherical elements to the previous surface, N is the number of spheres generated per iteration, and r_{iter} are the minimum and maximum radii of the spheres generated per iteration. For the margins: α and r are the paremeters defining the spherical sampling, p is power parameter which defines the softness of the weighting function, n_{length} is the number of segments creating a spicule, l_{min} and l_{max} are the minimum and maximum length of each segment, respectively, Ω is the angular freedom of the spicules, κ is the parameter defining the speed to approach the plane were the spicules are contained, N_{spi} is the number of spicules, and ϕ_o and ϕ_e are the diameters of the spicule at the beginning and at the end, respectively. For the enhancement: N_{hole} is the number of spherical holes created inside the lesion, r_{hole} are the minimum and maximum radius of the spherical holes, and t is the thickness of the rim enhancement.

Morphological descriptors			**Parameters used for surrogate generation**		
Shape	*Margin*	*Enhancement*	*Shape*	*Margin*	*Enhancement*
Round	Sharp	Homogeneous	$r = 2.5mm$ $N_{iter} = 1$ $N = 60$ $r_{iter} = [1.6, 2]mm$		
		Heterogeneous			$N_{hole} = 237$ $r_{hole} = [0.45, 0.6]mm$
		Rim			$t = 1.31$
	Indistinct	Heterogeneous	$r = 5mm$	$\alpha = 2.5^{\circ}$ $r = 0.4mm$ $p = 2$	
Oval	Sharp	Homogeneous	$a = 2.5mm$ $b = 4.5mm$ $c = 2.5mm$ $N_{iter} = 1$ $N = 600$ $r_{iter} = [0.2, 0.6]mm$		
Irregular	Sharp	Homogeneous	$a = 1mm$ $b = 1mm$ $c = 3mm$ $N_{iter} = 5$ $N = 5, 5, 10, 15, 2000$ $r_{iter} = [0.7, 1.2]$, $[0.7, 1.2]mm$, $[0.7, 1.2]mm$, $[0.7, 1.2]mm$, $[0.3, 0.3]mm$		
	Spiculated	Homogeneous	$r = 2.5mm$ $N_{iter} = 1$ $N = 180$ $r_{iter} = [0.3, 0.5]mm$	$n_{length} = 25$ $l_{min} = 0.4mm$ $l_{max} = 0.9mm$ $\Omega = 20^{\circ}$ $\kappa = 2$ $N_{spi} = 40$ $\phi_o = 1.6mm$ $\phi_e = 0.2mm$	

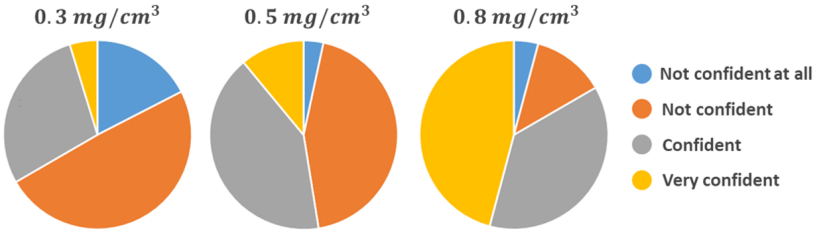

Figure 6.1: Percentage of confidence levels answered by one reader when the reader was asked to characterize 88 CESM simulated images of lesions with different iodine concentrations.

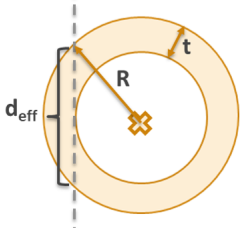

Figure 6.2: Maximum projected thickness in rim enhancements.

same detectability than the rest of contrast uptakes. As shown in Figure 6.2, the maximum thickness d_{eff} projected on a mass-like enhancement of radius R and rim thickness t can be computed with the following relation:

$$d_{eff} = 2\sqrt{R^2 - (R-t)^2} \tag{6.2}$$

Therefore, for the concentrations and sizes chosen in our study, the volumetric iodine concentrations of the rim enhancements after correction are C_{corr} = **0.4, 0.7 and 1.1mg/cm^3**. To validate these modified volumetric iodine concentrations, we compared the SDNR measured in recombined images of contrast uptakes with homogeneous and rim enhancements. As we can observe in Figure 6.3, the corrected volumetric iodine concentrations for contrast uptakes with rim enhancement distribution deliver a similar SDNR to the volumetric iodine concentrations chosen in our study for contrast uptakes with homogeneous enhancements. This allows us to avoid any type of detectability bias. In addition, Figure 6.4 allows for a visual comparison of CESM images between contrast uptakes with homogeneous and rim enhancements for different volumetric iodine concentrations.

The iodine concentrations of heterogeneous lesions were also modified to avoid a detectability disparity among all the elements of the database. In our database, the diameter size of each hole (adipose compartments as described in Chapter 3) is chosen uniformly between 0.45 and 0.6mm. Before computing the concentration correction factor, we need to compute the average projected effective thickness for these models. To this end, we have simulated ten different heterogeneous lesions with the characteristics previously described. The effective diameter of the contrast uptake, leaving out the adipose "holes", was equal to d_{eff} =4.81±0.01mm. This remaining diameter leads to the following corrected volumetric iodine concentrations C_{corr} = **0.5, 0.8 an 1.3mg/cm^3**. To validate these modified volumetric iodine concentrations, we compared the SDNR measured in recombined images of contrast uptakes with homogeneous and heterogeneous enhancements. As we can observe in Figure 6.5, the average SDNR measured in homogeneous contrast uptakes is inside the range of the SDNR obtained for the modified volumetric iodine concentrations in heterogeneous contrast uptakes. Additionally, in Figure 6.6 we present a

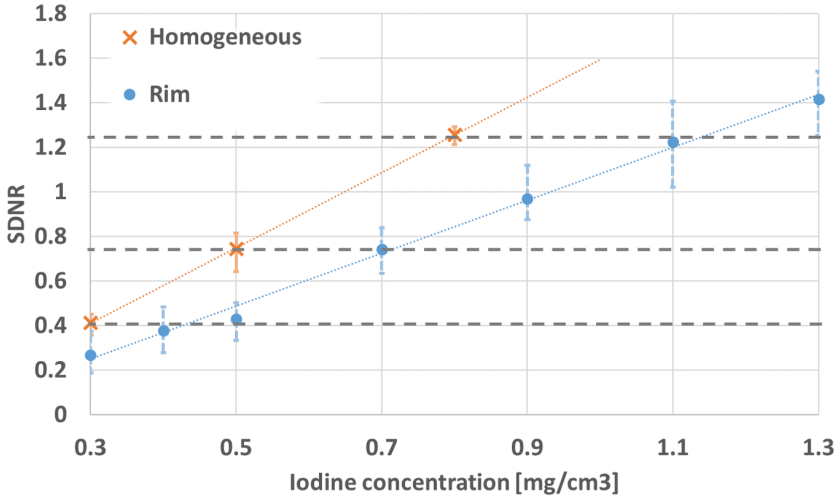

Figure 6.3: Comparison between the SDNR measured in masses with homogeneous and rim enhancements. The error bars illustrate the minimum and maximum values of SDNR (number of images: 7).

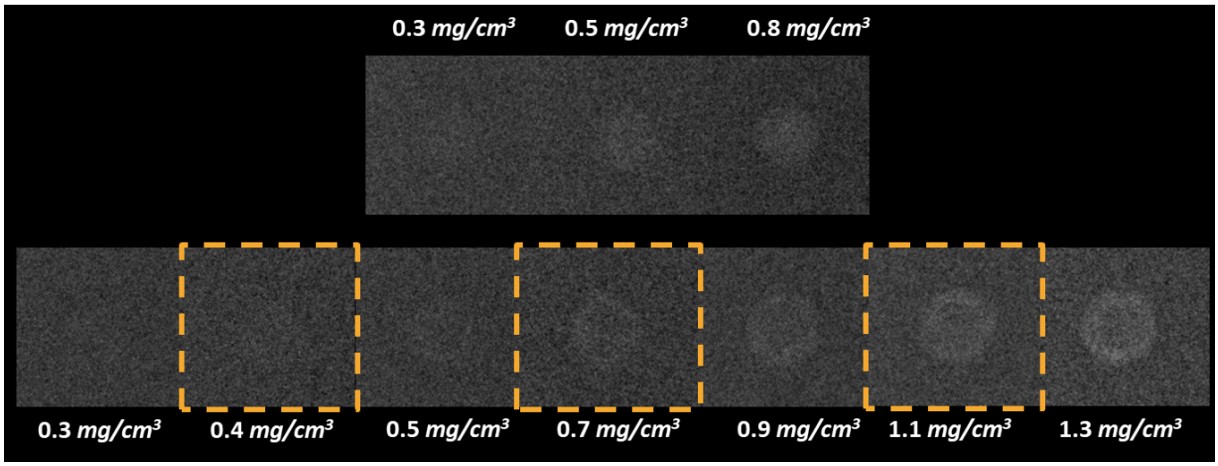

Figure 6.4: Visual comparison between the chosen iodine concentrations for 8 mm in diameter homogeneous spherical contrast uptakes (top) and rim enhancements (bottom).

visual comparison of CESM images between homogeneous and heterogeneous contrast uptakes for different iodine concentrations.

The diameter of spicules was fixed based on the literature review presented in Table 6.2. Originating from the mass core surface with a maximum diameter size equal to $1.6mm$, the spicules have a progressively decreasing width till the diameter size is equal to $0.2mm$. Assuming that the spiculated structure is distorted when compression is applied, the generated spicules were forced to follow the detector plane. The angular freedom Ω was set to 20°.

In oval contrast uptakes, the direction of the main axes were set randomly for each of the generated lesions.

Some examples of the masses generated for the study are illustrated in Figure 6.7.

All the generated masses were inserted in the center of a textured 3D breast phantom (cf. Chapter 3), with 27% volumetric glandular density. The dimensions of this phantom were fixed

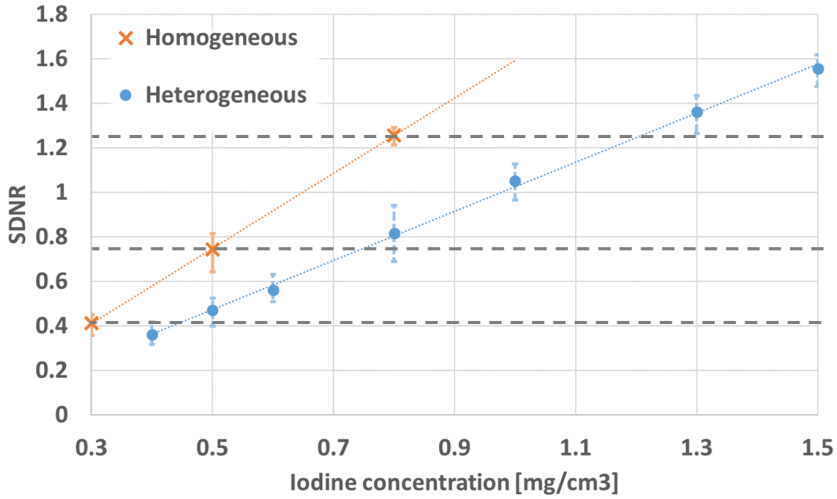

Figure 6.5: Comparison between the SDNR measured in masses with homogeneous and heterogeneous enhancements. The vertical error bars illustrate the minimum and maximum values of SDNR (number of images: 7).

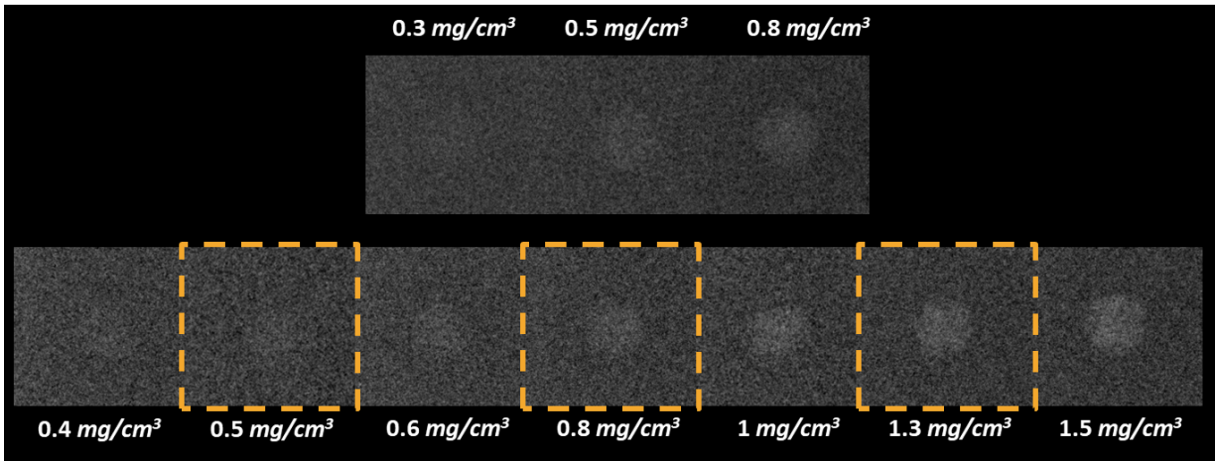

Figure 6.6: Visual comparison between the chosen iodine concentrations for homogeneous spherical objects and heterogeneous enhancements ($8mm$ diameter).

to $50\times50\times50mm$. To model the Breast Parenchyma Enhancement (BPE) observed in clinical images, attenuation coefficients corresponding to homogeneous mixtures of fibroglandular tissue and $0.1mg/cm^3$ iodine were assigned to the fibroglandular tissue background (cf. Chapter 5).

Table 6.2: Measures of spicule widths found in different publications.

Publication	Measured width
Sampat et al. [261]	Two readers: 0.278 and $0.221mm$
Zwiggelaar et al. [317]	One reader: 0.05 to $1mm$
Muralidhar et al. [214]	Two readers: $0.968\pm0.615mm$ and $0.641\pm0.393mm$
Jasionowska et al. [142]	One reader: $0.45mm$

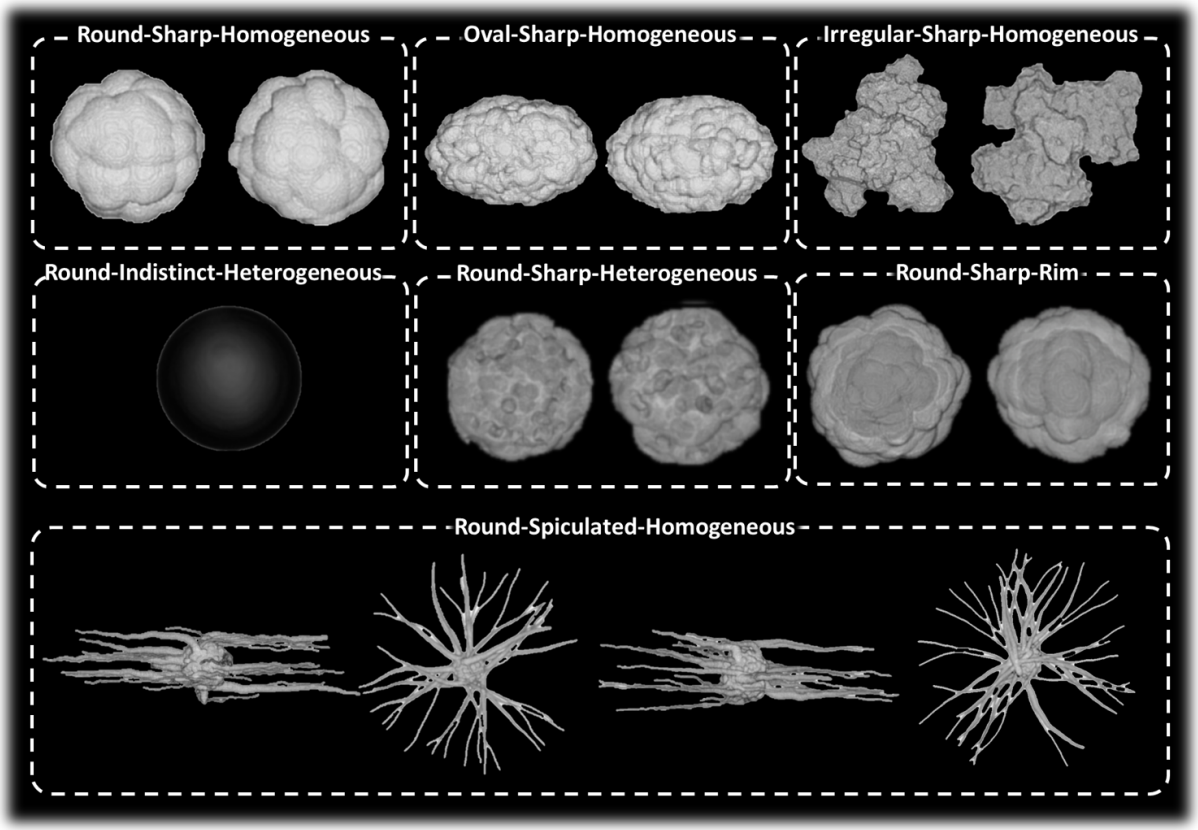

Figure 6.7: Examples of the three-dimensional models created as lesions surrogates.

In total, to evaluate characterization and detectability of contrast uptakes, 105 CESM and 105 CEDBT images with lesion (5 images per iodine concentration, 3 levels of iodine concentration and 7 types of lesion) and 40 CESM and 40 CEDBT images without lesion were generated.

6.1.2 Acquisition system parameters

CatSim X-ray simulation platform was used to simulate the images included in our virtual clinical trial (cf. Chapters 2 and 4). The nominal geometry of a Senographe Pristina was modeled. Mono-energetic spectra (22keV for LE, and 34keV for HE images) were considered. The total LE and HE quantum flux for the 9 CEDBT projections was the same as for the LE and HE CESM images. More precisely, the flux was tuned to match the signal-to-noise ratio (SNR) of real CESM images of a $5cm$ thick uniform breast equivalent section acquired with the automatic exposure mode. Electronic noise, lag and scatter were also modeled and included in our simulations.

Iodine-enhancement images were then produced by recombining the LE and HE images. The reconstruction method proposed in Chapter 4 was used to compute the CEDBT slices from the set of recombined projections. In total, 50 slices per volume were generated, with $1mm$ separation between them.

6.1.3 Image evaluation

Five GE Healthcare engineers, experts in mammography imaging, participated in the human observer study. Before performing the actual study, all readers participated in a training session, where several examples of images with all mass-lesion types and iodine concentrations as those in the actual study were presented. This training was performed with all the readers together, allowing them to discuss about the features presented in the example images and find an agreement over the definition of the characteristics shown by the lesions. Additionally, all readers were submitted to a quiz where the correct answer was given after their interpretations. After training, each reader reviewed 57 trials in total, which were not included in the study to avoid any bias.

Reading sessions were conducted in a darkened room on a 5-Megapixel monitor. For each trial, a randomly selected iodine-recombined CESM image or a full stack of iodine-recombined CEDBT slices was presented (examples in Figure 6.8). Images were presented at 100% resolution. Contrast, brightness and zoom levels were fixed. Between two trials a uniform gray image was displayed, to reduce bias between consecutive trials. The reader was asked to answer the following questionnaire for each trial:

Questionnaire 2.

Q1: Is there a lesion? (Yes / No)

Q2: What is the shape of the mass? (Round / Oval / Irregular)

Q3: How can you describe its margins? (Circumscribed / Indistinct/ Spiculated)

Q4: How can you describe the distribution of its contrast enhancement? (Homogeneous / Heterogeneous / Rim)

For each question: What is your confidence level? Not confident at all / Not confident / Confident / Very confident.

If Q1 was answered with "No", the rest of the questions were not answered. The readers had no time limitation to answer the questionnaire.

6.1.4 Data analysis

ROC analysis (cf. Annex A) was already used in several research works to demonstrate the statistical superiority of system upgrades [44, 110], to compare different imaging techniques [188, 240], or to assess the difference between several workflows [168, 194]. In our study, the software platform iMRMC proposed by the FDA [104] was used to compute detectability and characterization ROC curves, as well as their areas under the curve (AUC). Average ROC curves which consider the response of all the readers are calculated using the method proposed by Chen et al. [50]. The average AUCs and their corresponding standard deviations are computed using the one-shot estimator introduced by Gallas [103]. The statistical significance of the difference in the AUCs for CESM and CEDBT was estimated with the Dorfman-Berbaum-Metz (DBM) [126] method for multi-reader ROC analysis at 0.05 significance level. Fleiss' kappa coefficient [99] was derived to measure the agreement between reader responses. These results were associated to the kappa magnitude interpretations given by Fleiss [100].

The lesions included in our database combine different characteristics in a single surrogate. This may induce a bias in the data analysis. For example, all heterogenous lesions are round

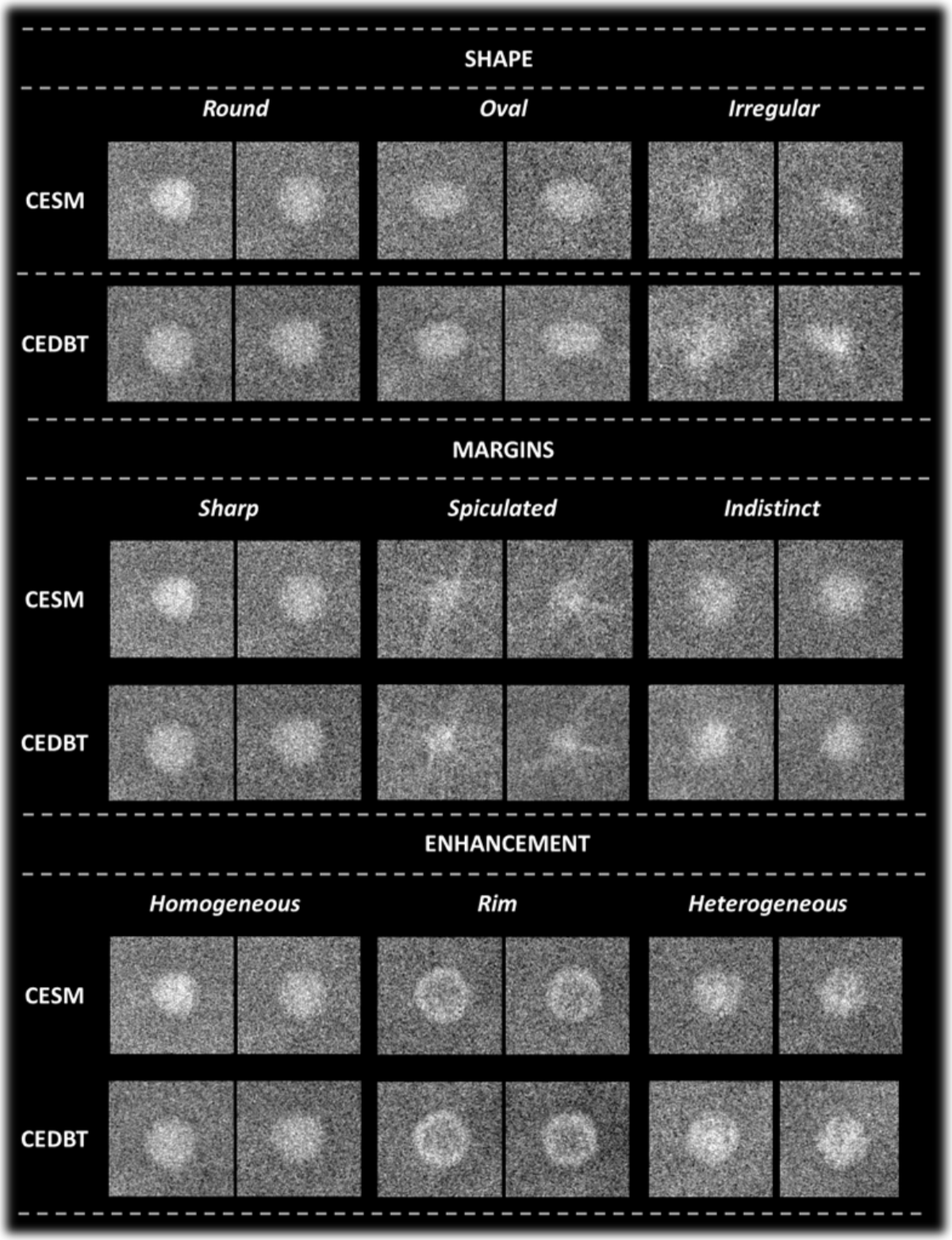

Figure 6.8: Examples of CESM and in-focus CEDBT slices generated for the study.

Table 6.3: Lesions grouped into categories to avoid learning bias.

Analysis of	***Generated lesions***		
Shape	round- sharp- homogeneous	oval- sharp- homogeneous	irregular- sharp- homogeneous
Margins	round- sharp- homogeneous	round- spiculated- homogeneous	round- indistinct- homogeneous
Enhancement	round- sharp- homogeneous	round- sharp- heterogeneous	round- sharp- rim

and sharp, while all oval lesions are homogeneous. A reader can learn this pattern and always answer homogeneous for oval images. To avoid this, we grouped the lesions as in Table 6.3 for our analysis. This means that, for example, to analyze the irregular shape of a lesion, we will only use the answers to Q2 given to round-sharp-homogeneous, oval-sharp-homogenous, and irregular-sharp-homogeneous. In other words, to analyze one of the global characteristics of the lexicon (shape, margins and enhancement), we only compare it to lesions which share the other two characteristics. This aggregation reduces the number of images evaluated per modality for each characteristic to **45 cases** (15 images containing the feature to evaluate, and 30 which contain other feature).

In addition, we have also classified the lesions in two classes, malignant and benign, based on their features. Lesions which are: irregular, spiculated, indistinct, heterogeneous, or rim, are labeled as **malignant**, while the other lesions are labeled as **benign**. This aggregation increases the number of images evaluated per modality, CESM and CEDBT, and class, malignant and benign, to **135 cases**.

6.2 Results

After the image evaluation, we retrieved a total of 1450 questionnaires answering the items presented in the Questionnaire 2. The answers were pre-processed to adapt them to the format accepted by the iMRMC software tool [104]. A numbered ranking was assigned to each confidence level used by the readers. This way, the ranking 1 was assigned to the answer "Not confident at all", ranking 2 to the answer "Not confident", ranking 3 to the answer "Confident" and ranking 4 to the answer "Very confident". Additionally, when the answer was incorrect (i.e. the reader detected a contrast uptake while it was a case without contrast uptake or the reader described the contrast uptake using a particular characteristic that was not present in the ground truth), the confidence level answered by the reader was ignored and a fifth ranking 0 was used instead. These rankings were used to create the ROC curves for each reader and the average ROC curve, as described in Annex A.

The answers to Q1 were used to evaluate the detection performance of CESM and CEDBT. As this question was answered for all the cases, a total of 1450 answers were considered (725 CESM cases and 725 CEDBT cases). The results and analysis of this evaluation is presented in Section 6.2.1. Using the rankings mentioned above, we computed the detectability ROC curves and their respective AUC values for each modality. For a more complete analysis we detailed

the percentage of missed contrast uptakes per category (False Negatives) and the number of non-existing contrast uptakes rated by each reader.

The answers to Q2, Q3 and Q4 for the contrast uptakes accurately detected were used to evaluate the characterization performance of CESM and CEDBT. The results and analysis of this evaluation is presented in Section 6.2.2. To compute the ROC curves and their corresponding AUC values for the characterization of shape, margins and enhancement, only the rankings given to the images corresponding to the groups presented in Table 6.3 were considered. The total number of answers retrieved to evaluate each characteristic is given in Table 6.4.

Table 6.4: Total number of answers obtained for the evaluation of the characterization of contrast uptakes in CESM and CEDBT, considering all five readers.

	CESM	***CEDBT***	**Total**
Shape	193	199	392
Margins	195	209	404
Enhancement	215	213	428

To complete our characterization analysis, we studied the agreement between the answers given by the readers. This allows for a better understanding of the characterization performance found for CEDBT and CESM. Considering this, the answers to Q2, Q3 and Q4 given by each reader, without considering the ratings assigned, were also used to compute the agreement between the five readers for the characterization task. As described in Section 6.1.4, we used the Fleiss' kappa coefficient to measure this agreement. In addition, we evaluated the distribution of the ratings assigned to the answers to Q2, Q3 and Q4 for each reader and iodine concentration of the contrast uptakes.

6.2.1 Detectability

As illustrated in Figure 6.9, the ROC and AUC analysis for the detectability study shows that, pooled over all readers and types of mass-like contrast uptakes, the detection of contrast uptakes was similar in CESM and CEDBT cases. In particular, although the CEDBT ROC curve is always above the CESM ROC curve, the DBM (Dorfman-Berbaum-Metz) test did not show any statistical difference between both AUCs ($p\text{-}value = 0.52$).

A more extensive analysis of non-detected contrast uptakes is presented in Figure 6.10. As we can observe, the proportion of missed contrast uptakes was almost concentrated on low contrasted contrast uptakes, while all contrast uptakes with the highest iodine concentration were detected for both modalities. We noticed a higher rate of irregular and spiculated contrast uptakes which were missed. This behavior could be explained by their shape, which is easily mixed with the enhanced background.

In Table 6.5, we show the difference between the percentages of missed contrast uptakes in CESM and CEDBT. We found an improved detection of oval, irregular and spiculated contrast uptakes in CEDBT. In particular, half of the missed spiculated contrast uptakes in CESM are detected in CEDBT slices. This may be explained by the CEDBT distribution of the contrast uptake three-dimensional information into multiple planes which makes the distinction between background and lesion easier. We also found less non-detected contrast uptakes in CEDBT slices for round, sharp and homogeneous characteristics. CESM offered a perfect detection for rim enhancements while in CEDBT there was a single case which was missed. Also, we found a higher rate of non-detected heterogeneous contrast uptakes in CEDBT. This may be also due to

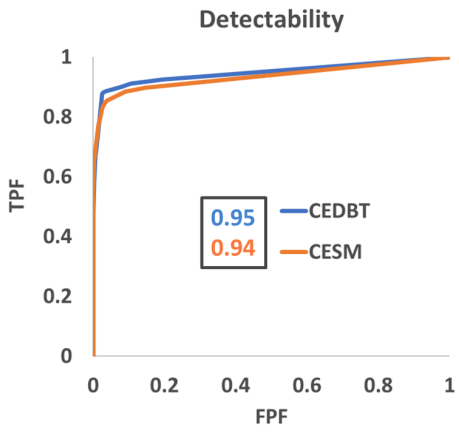

Figure 6.9: Detectability ROC curves and respective AUC values based on the answers of five readers over the ensemble of simulated images for CEDBT and CESM.

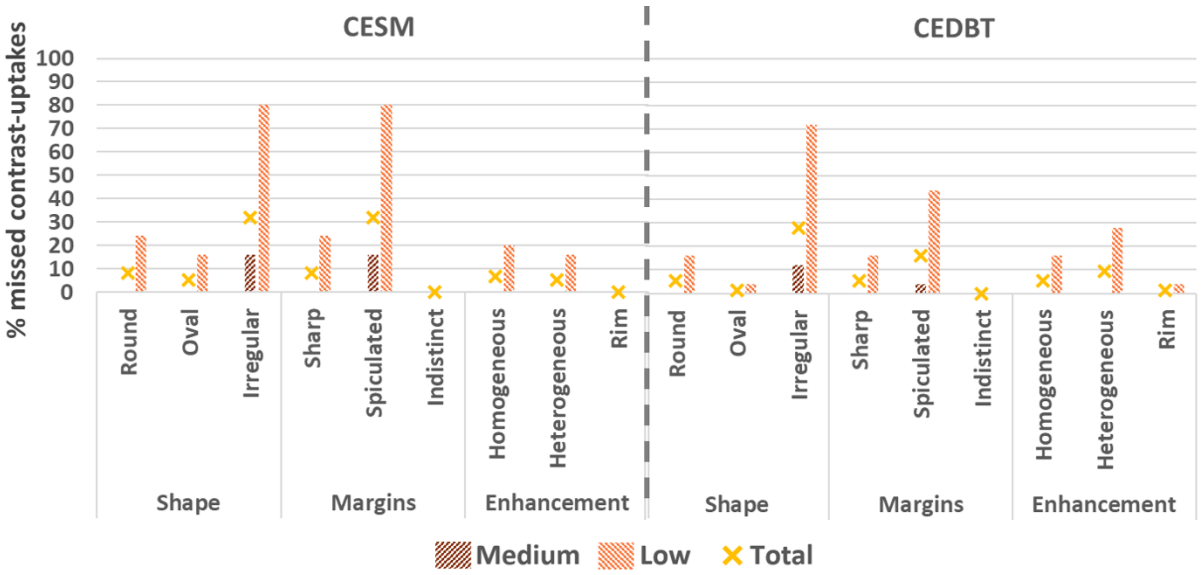

Figure 6.10: Percentage of non detected contrast uptakes classified by characteristic and iodine concentration. All contrast uptake with high iodine concentration where detected and, consequently, they were not included in this figure.

the distribution of information of CEDBT into multiple planes, as the partial information of a heterogeneous contrast uptake distribution (against the projected information in CESM) could be easier mistaken by normal parenchymal enhancement.

Both modalities, CESM and CEDBT, offer a perfect detection of indistinct contrast uptakes. The origin of this is uncertain but it may be caused by the soft transition of the margins of the generated contrast uptake. As presented in Section 3.3 of Chapter 3, when we want to include a contrast uptake surrogate inside the textured phantom, all the information of the voxels, where the contrast uptake is placed, is removed. In indistinct models, the final surrogate is bigger than the contrast uptake. In other words, the iodine concentration is centralized at the core of the model, and the margins lose progressively the iodine concentration. This creates an isolation

Table 6.5: Difference between the total percentage of missed contrast uptakes in CESM and CEDBT.

Modality	Shape			Margins			Enhancement		
	Round	Oval	Irregular	Sharp	Spiculated	Indistinct	Homogeneous	Heterogeneous	Rim
CESM	8.00%	5.33%	32.00%	8.00%	32.00%	0.00%	6.67%	5.33%	0.00%
CEDBT	5.33%	1.33%	28.00%	5.33%	16.00%	0.00%	5.33%	9.33%	1.33%
Difference (CEDBT-CESM)	2.67%	4.00%	4.00%	2.67%	16.00%	0.00%	1.33%	-4.00%	-1.33%

Table 6.6: Number of missed contrast uptakes per reader and per characteristic for CESM cases.

	Low					*Medium*					Missed by at least
	R1	R2	R3	R4	R5	R1	R2	R3	R4	R5	one reader
Round	1	1	2	1	1	0	0	0	0	0	2
Oval	1	1	1	1	0	0	0	0	0	0	1
Irregular	5	4	4	2	5	2	1	0	1	0	7
Sharp	1	1	2	1	1	0	0	0	0	0	2
Spiculated	4	5	4	4	3	2	2	0	0	0	8
Indistinct	0	0	0	0	0	0	0	0	0	0	0
Homogeneous	1	1	2	1	0	0	0	0	0	0	2
Heterogeneous	0	1	1	0	2	0	0	0	0	0	3
Rim	0	0	0	0	0	0	0	0	0	0	0

problem: there is no texture surrounding the surrogate. This effect may introduce a bias in the analysis of indistinct contrast uptakes which must be considered.

The number of missed contrast uptakes per reader and per characteristic is given in Tables 6.6 and 6.7 for CESM and CEDBT cases, respectively. In these tables we also present the number of missed contrast uptakes by at least one of the readers. In general, all readers missed less contrast uptakes when they read the CEDBT slices. However, a slight increment of missed heterogeneous contrast uptakes for three readers and low iodine concentrations was identified. A detailed analysis showed that this increment is concentrated on cases which were already missed by at least one reader in CESM images and, therefore, corresponds to contrast uptakes very difficult to identify.

Table 6.7: Number of missed contrast uptakes per reader and per characteristic for CEDBT cases.

	Low					*Medium*					Missed by at least
	R1	R2	R3	R4	R5	R1	R2	R3	R4	R5	one reader
Round	1	1	1	1	0	0	0	0	0	0	1
Oval	0	1	0	0	0	0	0	0	0	0	1
Irregular	4	3	4	3	4	1	1	1	1	0	6
Sharp	1	1	1	1	0	0	0	0	0	0	1
Spiculated	3	2	3	2	1	0	0	1	0	0	4
Indistinct	0	0	0	0	0	0	0	0	0	0	0
Homogeneous	1	1	1	1	0	0	0	0	0	0	1
Heterogeneous	1	2	1	2	1	0	0	0	0	0	3
Rim	0	0	0	1	0	0	0	0	0	0	1

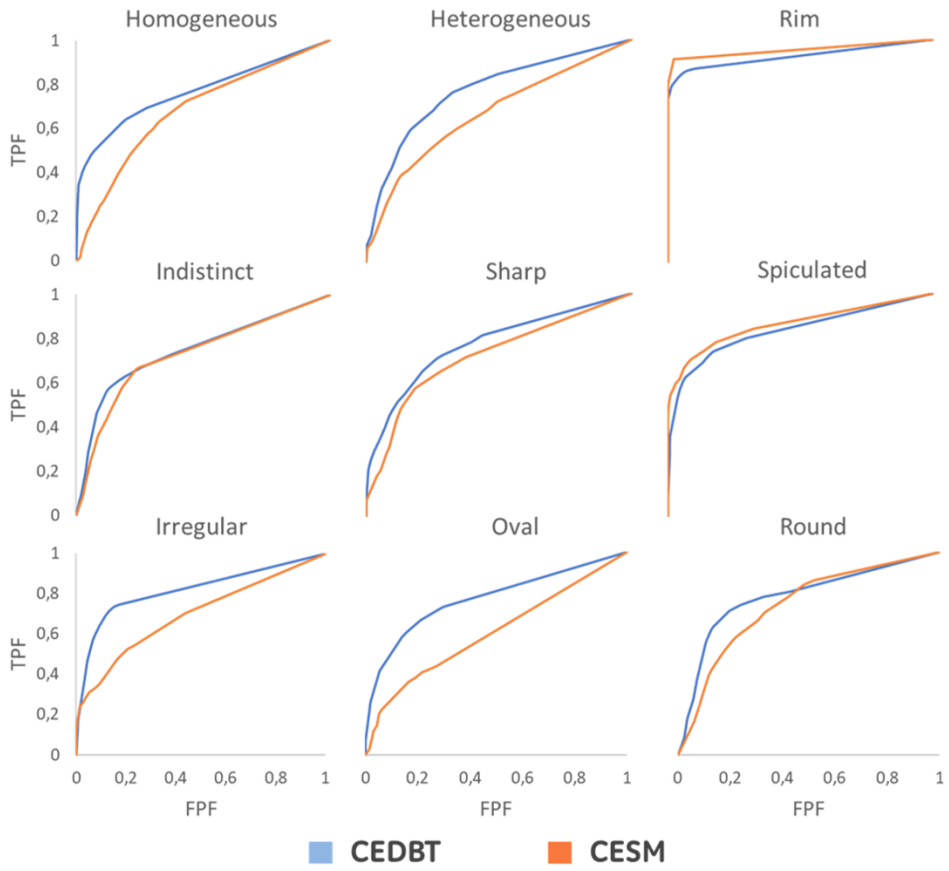

Figure 6.11: Characterization ROC curves of the five readers, for CEDBT and CESM. From top to bottom: contrast enhancement distribution, margin, and shape descriptors.

6.2.2 Characterization

The ROC curves obtained for the characterization study are illustrated in Figure 6.11. We observe that CEDBT outperforms CESM for the characterization of shapes (irregular, oval and round) as well as homogeneous and heterogeneous contrast uptake distributions. Otherwise, we found a less substantial difference between the ROC curves for the characterization of margins (indistinct, sharp and spiculated) and rim enhancements. In Table 6.8, we show the AUC values corresponding to each ROC curve as well as the results of the DBM test for each characteristic. A significant difference was found for oval masses ($p\text{-}value < 0.01$ using the DBM test).

The significant statistical difference found in oval contrast uptakes may be due to three-dimensional information provided by CEDBT in its multiple slices. Oval shapes parallel to the X-ray trajectory were interpreted as round in CESM projections, while readers achieved to observe the elongation of the contrast uptake across the several slices provided in CEDBT cases.

A more exhaustive analysis of the retrieved data showed that one reader, compared to the other four readers, underperformed in the characterization of spiculated masses for CEDBT. The reader AUC values for the characterization of spiculated contrast uptakes in CEDBT and CESM cases were equal to 0.65 and 0.86 compared to the total pooled AUC values 0.84 and 0.86, respectively. Without considering this reader, the spiculated AUC value for CEDBT increases to 0.88. However, the AUC values for CEDBT and CESM are still non significantly different.

Table 6.8: Analysis of AUC obtained for different characteristics. Results computed using the one-shot estimator of the AUC [103]. Statistical differences between AUCs were computed using the DBM method [126]. Significant differences are indicated in green (p-*value* < 0.05).

		AUC (one-shot)		*p-value*
		CESM	*CEDBT*	**(BDM)**
Shape	*Round*	0.73±0.06	0.78±0.04	0.40
	Oval	0.60±0.06	0.77±0.04	0.002
	Irregular	0.69±0.06	0.82±0.07	0.07
Margins	*Sharp*	0.72±0.05	0.77±0.09	0.40
	Spiculated	0.86±0.05	0.84±0.08	0.26
	Indistinct	0.73±0.03	0.75±0.03	0.96
Enhancement	*Homogeneous*	0.68±0.06	0.77±0.06	0.19
	Heterogeneous	0.67±0.06	0.77±0.07	0.18
	Rim	0.95±0.03	0.92±0.03	0.33

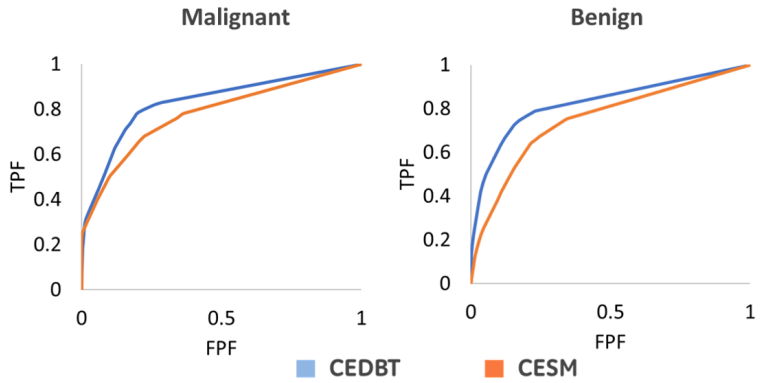

Figure 6.12: Characterization ROC curves for malign and benign labels.

The lack of a significant statistical difference for the rest of characteristics, despite the differences observed between the ROC curves, may be caused by the reduced number of cases included in the database for each characteristic. As described in Section 6.1.4, we also consider two groups of contrast uptakes with a higher number of cases for each group: malign versus benign lesion characteristics. In Figure 6.12 we illustrate the ROC curves for both groups and modalities. We can observe that CEDBT outperforms CESM for both groups. The results of the DBM test are presented in Table 6.9. In this case, we obtain statistically significant AUC values between CEDBT and CESM for both groups (p-*value* < 0.01). Therefore, we can conclude that CEDBT offers a better characterization of malignant and benign contrast uptakes than CESM.

Table 6.9: Analysis of AUC obtained for malignancy characterization. Results computed using the one-shot estimator of the AUC [103]. Statistical differences between AUCs were computed using the DBM method [126]. Significant differences are indicated in green (p-*value* < 0.05).

	AUC (one-shot)		*p-value*
	CESM	*CEDBT*	**(BDM)**
Malign	0.78±0.03	0.83±0.03	0.009
Benign	0.75±0.03	0.83±0.02	0.003

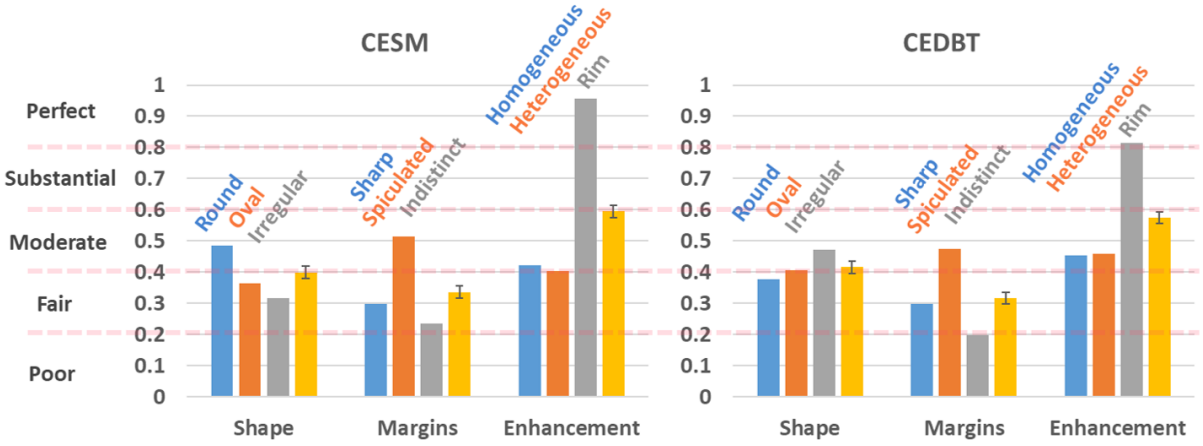

Figure 6.13: Agreement between the five readers Fleiss' kappa for all the range of lesion characteristics evaluated in the study. In yellow we present the global magnitudes for shape, margins, and enhancement answers.

Table 6.10: Fleiss' kappa coefficient for each descriptor and modality, and its respective confidence interval ($p\text{-}value = 0.05$).

	Shape	**Margin**	**Enhancement**
CESM	0.40 [0.38-0.42]	0.34 [0.32-0.35]	0.59 [0.58-0.61]
CEDBT	0.42 [0.40-0.43]	0.32 [0.30-0.33]	0.57 [0.56-0.59]

The inter-reader agreement pooled over all five readers was similar for CESM and CEDBT, for all the three contrast uptake descriptors considered: shape, margins and enhancement. The highest response consensus was found for enhancement pattern and the lowest one for margin type (Figure 6.13 and Table 6.10). Arranging these results to the interpretation scale given by Fleiss [100] (poor [0-0.2], fair [0.2-0.4], moderate [0.4-0.6], substantial [0.6-0.8] and perfect [0.8-1]), the agreement for shape and enhancement descriptors is "Moderate", while the agreement for the answers related to the margins is only "Fair". The agreement indicates the efficiency of our training session. While the similar agreements between CESM and CEDBT may indicate that each individual reader learned how each characteristic is represented in each modality, the low agreement for the evaluation of margins may be due to the lack of a common understanding of each characteristic. The training sessions must be adapted to these results for future studies.

The distribution of the confidence levels given by the five readers to the different iodine concentrations is illustrated in Figure 6.14. The goal of the iodine concentrations chosen in our study was to homogenize the confidence answers among the cases presented to the readers. In particular, we searched to obtain confidence answers 1 and 2 for low iodine concentrations, 2 and 3 for medium iodine concentrations, and 3 and 4 for high iodine concentrations. All the readers used the full range of confidence levels. While four readers increased their confidence with the iodine concentration of the evaluated contrast uptakes as we expected, reader 3 showed less confidence in his/her responses. This is the same reader who underperformed in the characterization of spiculated masses.

Figure 6.14: Confidence levels for each iodine concentration (High=$0.8mg/cm^3$, Medium=$0.5mg/cm^3$, Low=$0.3mg/cm^3$). Confidence level 0 is attributed to missed lesions. The size of the disks is proportional to the percentage of answers given by the reader for a specific iodine concentration and a specific confidence level.

6.3 Conclusion

Previous works showed that CESM and CEDBT can be used to improve breast lesion detection at the same time they provide an accurate diagnosis of cancerous growths. However, the incremented clinical value of CEDBT compared to CESM was not well understood, and the definition of the CEDBT clinical benefits is the objective of ongoing studies.

In this section, we attempted to answer the following question: what are the clinical advantages of CEDBT over CESM? To do that, we proposed a virtual clinical study to compare the performance of CESM and CEDBT. In particular, we were interested in evaluating the detectability and characterization of lesions with different iodine concentrations and morphologies. To do that, we simulated 105 CEDBT and 105 CESM cases containing lesion surrogates which represent a complete collection of the main characteristics observed in clinical cases. Our database was completed with 40 CEDBT and 40 CESM cases without any lesion. Five human readers were asked to evaluate each case following a common questionnaire for all cases.

We showed that CESM and CEDBT share a similar detectability for the complete range of different mass-like contrast uptakes which can be found in clinical situations. However, CEDBT seems to be a more suitable modality to detect spiculated lesions which may be missed in CESM exams. The spicules can be traced across different CEDBT planes during review navigation over slices (Figure 6.15), which may explain how a reader can differentiate them from the background and, therefore, detect and characterize the mass. At the same time, CEDBT slices helped to increase the detection of oval and irregular lesions for similar reasons.

The perfect detection of lesions with rim enhancements and indistinct margins, compared to the rest of the database, may be due to a study bias that needs to be further studied for future studies.

Regarding the characterization of contrast uptakes, the shape and enhancement distribution patterns of breast masses was found better for CEDBT reconstructed slices than for CESM images. This can be explained by the fact that CEDBT distributes the 3D information into multiple planes, allowing the reader to follow the structures over the different slices and decorrelate the information coming from the contrast uptake of interest and the natural enhancement of the anatomical background. The characterization of lesion margins was found similar for CESM

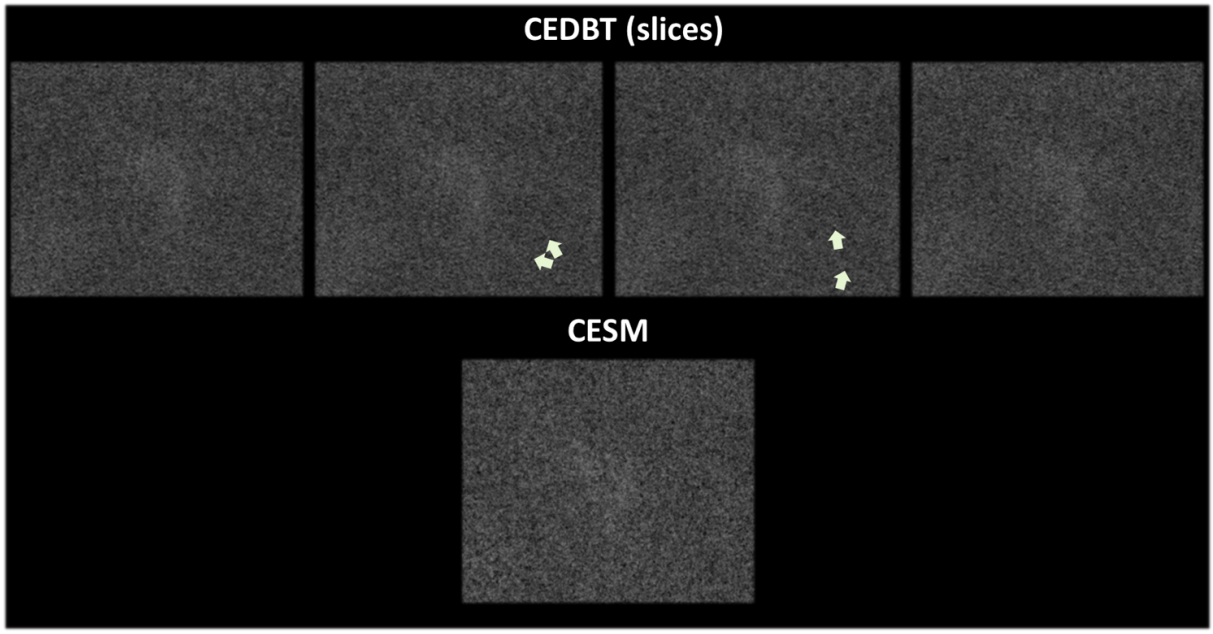

Figure 6.15: During navigation of CEDBT slices, the readers were capable to recognize spiculated structures which were difficult to observe in CESM images. The recognition of these structures helped to detect the mass-like enhancement.

and CEDBT. We presume that this can be attributed to the presence of off-focal artifacts in the reconstructed slices.

The statistical analysis showed that, despite that some CEDBT ROC curves seem to outperform the results obtained with CESM images, the only lesions showing a significant characterization difference were oval masses ($p\text{-}value < 0.01$). This could be due to the reduced sample size for each characteristic included in our database (the characterization performance of each descriptor is made using only 45 trials). To increase the sample size, we grouped the cases into two classes, malignant and benign, depending on the attributes of the contrast uptakes they contain. This allow us to have a sample size of 135 trials to evaluate the characterization performance of each class. In this case, we observed that CEDBT is significantly better than CESM to depict malignant and benign attributes. Although we improved the statistical significance, when lesions are divided in two groups, the particular benefits of CEDBT are more difficult to interpret. In other words, we increased the significance of our results at the expense of a specifity loss. We cannot point to the major characteristics that are being more discernible in CEDBT. Therefore, a better dimensionality of the study could be necessary to find a more important difference between both modalities. In this context, the split-plot study designs discussed by Obuchowski et al. in [223] could help improving the statistical power of our study.

Other elements must be also consider for future studies. Even if we increased the realism in our simulation platform, some phenomena were not included, such as heel effect, focal spot size and shape, and patient's movement. The impact of these effects remains for further investigation. Also, we used a reconstruction FBP filter to match the CNR between CESM and CEDBT images. However, the recombination of LE and HE images delivers an MTF of the DE recombined image where some frequencies are attenuated [249]. Future work will include reconstruction techniques able to reduce this effect. Finally, the detectability and characterization tasks were performed using a simulation framework. As a future work, the clinical results anticipated thanks to the

proposed simulation platform should be compared to true clinical evaluations when a commercial CEDBT imaging system will be available.

Conclusion and perspectives

Contrast enhanced X-ray imaging of the breast emerges as a solution for certain tasks where full field digital mammography (FFDM) underperforms, such as screening of women with dense breasts or diagnosis and staging of breast lesions [18]. Currently, among all contrast enhanced breast imaging techniques, contrast-enhanced magnetic resonance imaging (CE-MRI) is the clinical gold standard. However, CE-MRI has several disadvantages: high cost, low accessibility, poor patient experience and long acquisition time. This is why X-ray based techniques provide an additional value and demonstrate to be an actual alternative to CE-MRI [90]. Two methods are considered: contrast-enhanced spectral mammography (CESM) and contrast-enhanced digital breast tomosynthesis (CEDBT). Although both of them have demonstrated a positive advantage when compared to FFDM, the differences between them were not clearly established [53]. The main purpose of this work was to study whether CEDBT provides an additional clinical value due to its three-dimensional information compared to CESM, based on realistic simulation of imaging systems and breasts containing both normal tissues and lesions.

Main results and contributions

To overcome the lack of availability of a commercial CEDBT system and, therefore, true clinical cases, we have examined in Chapter 1 the published works on virtual clinical trials (VCT). This approach has been already used extensively as a pre-clinical alternative to evaluate the performance of a new breast imaging technique [8, 86, 111]. We observed that, while there is a very large list of publications proposing solutions to simulate the X-ray chain [5, 66, 87, 248], as well as models of breast lesions [15, 83, 122] and anatomy [22, 37, 180], they are not completely adapted to the needs of our study. In particular, X-ray simulation platforms may be time consuming, missing some of the processes which may impact the evaluation of CESM and CEDBT cases (such as lag), or only offering limited models of certain processes based on unrealistic hypotheses (such as stationary scatter). Similarly, we did not found any model for virtual contrast uptake surrogates which can reproduce the complete set of characteristics found in clinical CESM images. Finally, while there are several models of the breast anatomy, there are only few simulated studies of the remaining anatomical texture observed in contrast enhanced breast imaging.

Contributions to the simulation of X-ray images

Our first contribution was to improve an already existing analytic mammography simulation platform [209] by adding the physical processes which are key to the evaluation of CESM and CEDBT cases (see Chapter 2). We did not modify the projection of the primary field using a ray-tracing algorithm and the definition of the geometry of the acquisition system. In a second step, the primary simulated image is degraded to match the characteristics of a real acquisition. We

modeled this degradation as three types of processes: those modifying the frequency response, those contributing to the output statistics, and those considering the memory of the system (i.e. previous acquisitions). Each of the models was adapted for CESM and CEDBT using empirical data to simulate two different mammography commercial systems: Senographe DS and Senographe Pristina.

The use of a polyenergetic spectrum to generate the simulated images increases the computation complexity, therefore an equivalent monochromatic spectrum was used in all our simulations. This is a limitation of our simulations. On the one hand, beam hardening is an effect which may impact the quality of CEDBT images and which is completely correlated to polyenergetic nature of the spectra. On the other hand, as presented in Chapter 4, the recombination of low- and high-energy pairs is also affected by the polychromaticity of the spectra. Further studies must then evaluate the impact on image quality, and more importantly on clinical outcomes, of monoenergetic compared to polyenergetic simulations.

To characterize the frequency response of the X-ray acquisition chain, we assumed that it behaves as a Linear Time-Invariant (LTI) system. Two sources modifying the frequency response were considered. First, we included the low-pass frequency response of the limited-size detector elements. Our implementation offers an almost identical Modulation Transfer Function (MTF) of the detector compared to the theoretical curve ($MSE < 0.0001$).

In our model, we considered a square pixel shape. This is only an approximation of real systems, where the pixel surface is truncated by the electronics. Although a square pixel shape is considered a fair approximation for detectors in mammography systems, our model can be easily adapted in future works to less conventional pixel shapes.

The frequency response of an X-ray system, characterized by its MTF, is also affected by the scattered field and the optical glare. As the magnitude of the scattered field depends, among other factors, on the length of the X-ray path traversing an object, it is a non-stationary process. Several authors have proposed different analytic solutions to deliver X-ray projections that consider the thickness traversed by the X-rays. However, they were limited by the large number of simulations or acquisitions required to fit their models. In this work, we developed an analytic model based on a small number of empirical measures and an easily repeatable set-up, reducing the time needed to fit the model. This new method allows us to simulate the effect of the thickness dependent scattered field and the optical glare for systems with and without anti-scatter grid, improving significantly the realism of the results when using a stationary additive scatter model.

Our model was considered isotropic, while this hypothesis is false, especially for systems with an anti-scatter grid. To include the natural anisotropy of the scatter field, we could use our method to fit the vertical and horizontal MTFs for several thicknesses. Then, a bidimensional kernel could be generated interpolating both MTFs. Also, our scatter kernels only depend on the object thickness, while there are other effects contributing to the scatter field, such as the object composition, airgap of the X-rays after traversing the object, and angle of acquisition. These elements may impact the characterization of different structures in the final image and, therefore, they must be considered in the future to improve the model.

Three sources of noise were considered. First, the quantization step at the end of the detection process was modeled by reproducing the same quantization process used in the real acquisition systems. Secondly, all acquisitions are contaminated by the random processes internal to the circuitry of the detector. We mixed all these heterogeneous noise sources in what is commonly known as electronic noise. To model this random signal, we included in our simu-

lations an Additive White Gaussian Noise (AWGN). This signal was adapted using empirical measures. We showed that the difference between the distribution given by our model and the distribution of the electronic noise of real acquisitions is smaller than the difference between the electronic noise distribution of two different acquisitions performed on the same system. Finally, we also included in our simulations the random effect of the quantum noise. Two complementary solutions are presented in currently published works: Signal-to-Noise Ratio (SNR) fitting or Noise Power Spectrum (NPS) fitting. In this work we developed a SNR fitting solution. Our model, based on a modified Poisson random sampling, uses empirical measures to adapt the SNR and signal intensity of the simulated images. This model leads to an error inferior to 1% between SNR and signal intensity of simulated and acquired images. This percentage is smaller than the average mean and SNR difference found between different real images acquired with the same set-up.

However, our noise models present some limitations. To begin with, we consider the sampling quantum process as a single statistic gain stage with a deterministic gain parameter, while, in real systems, the final stochastic distribution of the optical photons arriving at the detector depends on the efficiency of the scintillator (which is non-uniform and characterized by a random conversion gain known as Swank noise [284]). Other physical phenomena such as the random generation of K fluorescent X-rays [63] was neither considered. In the same way, scatter is also composed of several stages in real acquisitions systems, which are interleaved with random processes [274]. Our unique scattering stage is placed before integrating the quantum noise in simulated images. This causes the Normalized Noise Power Spectrum (NNPS) of our simulation to be different from the experimental NNPS and, therefore, we obtain a different noise texture. The characterization of certain patterns in the final image may be influenced by the noise texture, so the improvement of the noise realism must be studied in future works. Although additive noise models have been presented in the literature to adapt the real NNPS [193], these models only consider uniform objects, which is not adapted for our heterogeneous phantoms (anatomical background plus breast lesions). One solution to provide a more realistic noise texture may be to implement the scattering and noise stages using several interleaved stages, approximating the real physical processes in a most faithful way and, therefore, delivering a noise color closer to the one appearing in experimentally acquired images.

The third and final type of process we included in the simulation chain models the memory of the detector during the CEDBT acquisition sequence. This effect is usually called lag and introduces another error term into the final projections that we must consider. Although this effect was already modeled in Computed Tomography (CT) images, to our knowledge there was no work introducing a lag model for CEDBT. We defined the lag process as a Finite-duration Impulse Response (FIR) LTI system, where the impulse response represents the memory term for each subsequent projection. The terms of the impulse response where estimated using empirical measures of the evolution of the signal intensity during an acquisition sequence. This model introduces an error between the signal intensity of simulated and experimentally acquired CEDBT sequences smaller than 0.32% when modeling Senographe Pristina and smaller than 2% when modeling Senographe DS. Despite the error introduced in Senographe Pristina simulations, the signal intensity of the simulated sequences remains within the variability of the measures performed on a physical Senographe Pristina system. This is not the case for simulated Senographe DS CEDBT sequences, where we found slight underestimations and overestimations of the experimental measures.

These results show the limitations of our model. We identified several further lines of investigation. First, the estimation of our lag coefficients do not consider the complete variability

of experimental set-ups. Secondly, we considered a FIR system, meaning that the output of previous frames does not impact the output of the current frame. This may not be the case in experimental acquisitions where the saturation of detectors increases during the acquisition sequence. Finally, our lag model do not consider all the contributors to the memory process, such as the scintillator afterglow or the charge transfer effect. These other sources of the lag effect may cause additional interactions over time.

Despite some limitations that will be discussed in the "Perspectives" section, the developed models included in the X-ray simulation platform allowed us to simulate low- and high-energy image pairs according to the characteristics of physical CESM and CEDBT systems, improving the realism of the simulations and being capable of generating images which can be used to compare the clinical performance of CESM and CEDBT, the main goal of this work.

Contributions to the simulation of pathological breasts

In contrast to CE-MRI, there is no standard descriptors defining the characteristics of CESM suspicious findings. In this work we presented a review of the current characteristics found in several clinical CESM studies, and summarized the currently used CESM descriptors accordingly. Due to the complexity of non-mass-like enhancements and motivated by the work of Dromain [77], we focused our efforts into the generation of mass-like enhancements. Published works generating mass-like enhancements surrogates used excessively geometrical models of CESM findings [122, 175, 226] or did not consider a complete representation of the variability of mass-like findings found in clinical images [36, 77, 158]. In particular, each mass-like enhancement is classified in different categories. For each category, we developed a lesion model allowing for the generation of mass surrogates. The novelty of our work is that the lesions are created using any combination of the descriptors and, therefore, it allowed us to build a larger and more diverse database than in other published works.

As we focused our work on mimicking the geometrical characteristics found in CESM findings, we only established a visual evaluation of the recombined simulated images including virtual contrast uptake surrogates. This task was performed by GE Healthcare engineers, experts in contrast enhanced X-ray imaging of the breast.

Furthermore, several authors suggested that breast parenchyma enhancement (BPE) must also be considered in the diagnosis of CESM clinical cases [11, 265, 287]. We included this effect in our simulations, modifying the breast anatomy model already developed by Li et al. [180]. The breast model and the lesion surrogates were combined to offer projected images of contrast uptakes embedded in an heterogeneous background.

Our model for pathological breast phantoms is, nevertheless, limited by several points. The descriptors used for CESM images have not yet been validated in a comprehensive Lexicon adopted by the radiology community. Moreover, we have not evaluated the realism delivered by the final images, comparing them to a dataset of real findings, which it will be the focus of future studies. The use of a validated Lexicon is needed so we can increase the clinical similarity of the characteristics included in the lesion surrogates. Also, in our simulations, the combination of the texture background and the virtual lesions introduces a very thin adipose layer surrounding all the created masses. As this may not be true, new combination methods must be studied to discard this assumption.

Contributions to recombination and reconstruction

To provide recombined images with the same characteristics as experimental recombined images, we compared the impact of log-weighted subtraction and polynomial combination of low-

and high-energy pairs. Our study was focused on three main axes: stochastic processes, frequency response, and memory processes. Three main contributions must be highlighted. First, we adjusted the noise present in simulated low- and high-energy images to provide simulated recombined images which share the same noise statistics as experimental recombined images. Secondly, we have proved that the frequency response of the recombined image depends not only on the retrieved material of interest, but also on the particular materials being projected.

We limited our study to identify the elements impacting the frequency response and quantify their effect for log-weighted subtraction algorithms. Further investigations must be performed to obtain the frequency response given by polynomial recombination algorithm.

Finally, we proved that the impact of the memory processes is different depending on the recombination algorithm, resulting in a different average signal intensity in subsequent recombined images. To our knowledge, our evaluation of the frequency response in recombined images for dual-energy X-ray breast systems and the assessment of the lag impact depending on the recombination algorithm were totally original.

The review of different CEDBT reconstruction approaches considered in the literature showed the limitations of the current algorithms. We contributed to the reconstruction of CEDBT volumes by proposing a modified version of the Filtered Backprojection (FBP) algorithm. Compared to traditional FBP, our method increases the contrast in the regions with contrast uptakes while reducing the high-frequency noise. Moreover, we compared it to ASIR, an iterative reconstruction algorithm used in DBT, obtaining an improvement in terms of SDNR and, therefore, in detectability of contrast uptakes. We provided examples showing the visual improvement resulting from our method.

However, according to the main research direction of our work, we limited our study to the reconstruction of simulated images. Further studies must also consider clinical images when available to validate the performance of our reconstruction approach.

Results from the analysis of CEDBT technical improvement

The preservation of the contrast uptake features is associated with the technical limitations of the X-ray system used for the acquisition of the low- and high-energy pairs. Therefore, the performance of CEDBT may improve thanks to technology evolution. To our knowledge there were no studies comparing the quality of CEDBT reconstructed volumes for two systems with distinctive technological characteristics. In Chapter 5, we exposed the main uncertainty sources originating from technological limitations which contribute to a poor quantification of contrast uptakes. In particular, we evaluated the performance of two commercially available systems (a Senographe DS and a Senographe Pristina) based on simulations. First, we proved that moderate lag and scatter effects can drastically reduce the cancellation of the background texture in recombined images. While the Texture Cancellation (TC) index was smaller than 1 for iodine concentrations higher than $0.1 mg/cm^3$ using a Senographe Pristina system, the Senographe DS system only offers a TC smaller than 1 for iodine concentrations higher than $4 mg/cm^3$. This means that, for the same texture cancellation performance, Senographe Pristina allows detecting contrast uptakes with lower iodine concentrations. Secondly, we analyzed the performance of the BPE representation in reconstructed slices using the β parameter, which measures the residual anatomical texture which remains after the recombination of the low- and high-energy acquired images. We found that the distribution of β estimated for different background uptake concentrations in Senographe Pristina is sparse. This is translated by a better visual representation of the BPE, with a statistically different β distribution for different background uptake

concentrations ($p\text{-}value < 0.001$ of Wilcoxon test). However, this is no longer true when the images are acquired using the Senographe DS system ($p\text{-}value > 0.2$ of Wilcoxon test). Thirdly, we evaluated the detectability of contrast uptakes in both systems measuring the SDNR for spherical elements with different iodine content embedded in a heterogeneous background. We proved that the estimated SDNR using a Senographe Pristina system is statistically superior to the SDNR when using a Senographe DS system for concentrations larger than $0.8 mg/cm^3$ ($p\text{-}value < 0.001$ of Wilcoxon test). Finally, we analyzed how the incorporation of an anti-scatter grid specifically designed for high-energy spectra (as it is the case with the Senographe Pristina), influences the presence of artifacts in the recombined images. We showed that cupping artifacts are almost removed when such anti-scatter grid is used. In particular, the magnitude M (difference of the signal intensity over the artifact and the background) of the artifact decreases from $M = 27.98$ when there is no grid, to $M = 2.69$, when the grid is considered. We also found that the presence of an elevated X-ray scattered field in the image modifies the absolute contrast of different iodine inserts depending on their position inside the object. This last result indicates the challenge to quantify the iodine content in a recombined image due to the X-ray scattered field.

Results from the evaluation of CESM and CEDBT clinical performance

The main goal of our work was to assess the clinical added value of CEDBT over CESM. Our last contribution was to perform a virtual clinical trial (VCT) evaluating the detectability and characterization performance of CESM and CEDBT. To this end, we simulated 105 CESM and 105 CEDBT cases including diverse lesions covering the whole spectrum of features defined by the set of descriptors we used. We also generated 40 CESM and 40 CEDBT additional cases without lesion. The full stack of simulated images was evaluated by five GE Healthcare engineers, experts in mammography imaging. The analysis of their answers using state-of-the-art tools [99, 104] allowed us to estimate the detectability and characterization Receiver Operating Characteristic (ROC) curves, as well as their respective Areas Under the Curve (AUC). We found that with our implementations the overall detectability was similar for CESM and CEDBT ($AUC_{CESM} = 0.94$ and $AUC_{CEDBT} = 0.95$ with $p\text{-}value = 0.52$). However we noticed that spiculated lesions with lower iodine concentrations were better detected in CEDBT. Therefore, CEDBT enables a better differentiation of contrast uptakes with the background. Thanks to the availability of several planes, the reader gets to disassociate the information belonging to the core of a contrast uptake and the natural enhancement of the anatomical background. The study on the characterization led to higher AUC values in CEDBT than in CESM for the evaluation of shape and enhancement distribution patterns. Similarly to detection, the fact that CEDBT distributes the 3D information into multiple planes helps the reader to follow each structure, obtain more structural information about the contrast uptake and, therefore, improve the characterization of the shape and the distribution of the contrast uptake inside the finding. The characterization of lesion margins was found similar for CESM and CEDBT. We presume that this can be attributed to the presence of off-focal artifacts in the reconstructed slices.

However, we only found a meaningful statistical difference in the case of oval masses ($p\text{-}value = 0.002$). To improve the number of cases per category and increase the significance of our results, we grouped all the cases into two groups: malignant and benign. Gathering our cases we found a superiority of CEDBT compared to CESM for both groups ($p\text{-}value = 0.009$ in the malignant group and $p\text{-}value = 0.003$ in the benign group). Therefore, we have shown that CEDBT improves also the overall characterization of mass-like enhancements providing a better categorization of their features.

In this study we did not evaluate non-mass-like enhancements, due to the complexity to simulate such structures. We expect that the detectability and characterization superiority of CEDBT compared to CESM is also achieved for non-mass-like enhancements, and their evaluation will be the focus of future studies.

To sum up, our contributions provided the necessary computational tools to perform a pertinent VCT study evaluating the performance of CESM and CEDBT. We improved the realism of an X-ray simulation chain incorporating several processes not considered in the current literature and created a totally original simulation platform to create contrast uptake surrogates which consider the CESM clinical information. We performed a new analytic analysis on the impact of the recombination algorithm to the different processes present in the X-ray chain. We improved the current performance of FBP reconstruction, increasing the detectability of contrast uptakes in CEDBT. We performed an unprecedented thorough analysis of the technical advancement of CEDBT. Finally, our evaluation concluded that CEDBT shows a certain added clinical value compared to CESM, with an enhanced detection of spiculated masses and a better characterization of both malignant and benign findings.

Perspectives

Several directions are still open to further improvement and investigation.

The current state of the simulation platform allows us to simulate low- and high-energy acquisitions with similar characteristics to the real acquisitions. However, there are several physical phenomena which were not included in the simulation platform, such as the heel effect, focal spot size and shape, and patient's movement. These effects could also have an impact on the evaluation of CESM and CEDBT and they will be one of the objectives of future research. Furthermore, there is an additional noise source which was not considered: the structure noise. Associated with detector response over time and different individual pixel response, this noise is complex to measure and, therefore, to simulate. In addition, it can be mostly removed using a simple gainmap correction. However, there are published work measuring its impact on the total NNPS [212], which could be used to include this effect in the simulation chain.

Besides the traditional approaches to simulate the physical processes behind the X-ray image formation, some elements could be improved using deep learning methods. This way, if we want to model another system, we could augment the realism of simulations using deep learning approaches instead of performing additional measurements or calibrations. We would need a set of images generated by the real system and the current simulation tool. Then, we could train a neural network to learn the mapping between the simulated images and the ground truth, which are the acquired images. When this mapping is learned, we would need to introduce a simulated image into the network to obtain a more realistic output. For example, quantum noise distribution could be learned from experimental acquisitions with different set-ups. To our knowledge, this has never been studied. In all works we found in the literature on similar topics, the inverse problem was addressed: how to suppress noise in images using deep learning approaches, instead of including a realistic one in noiseless images. Two approaches may be considered. First, the use of Generative Adversarial Networks (GANs) with an unpaired database. The possible limitations of this approach is the known training instability and the loss of structure features that need to be preserved. Secondly, we could use a U-Net architecture with paired data. The problem of this solution is to find an exactly equivalent phantom distribution to obtain identical features in simulated and acquired images. One solution is to use fake

paired data. This means that we can obtain "ideal" simulated noiseless images averaging several images acquired at higher dose in the exactly same position as the phantom. However, neural networks are known to be deterministic. Once trained, they will always give the same output for a given input. Noise is stochastic, we can measure its statistics but we cannot predict its impact pixel-wise. This cleavage between neural networks and noise characteristics makes it impossible to address the problem in the spatial domain with paired models. Therefore, frequency domain training including a small random signal may be necessary.

As we showed in our discussion, the incremental simulation realism leveraged in this work can be used to perform more relevant contrast enhanced mammography studies. Similarly, all the elements incorporated in the image simulation chain will also help to reproduce with higher fidelity other modalities or systems, such as dual-energy X-ray absorptiometry (DXA). At the same time, the simulation framework developed in this work can be also used to test new configurations and guide future technical developments.

Regarding the reconstruction algorithms, future research must focus on exploiting the characteristic sparsity of CEDBT volumes. Although our modified FBP uses a regularization filter to reduce high-frequency noise, iterative reconstruction solutions may be adequate to introduce a regularization term, considering that the reconstructed volume only contains very localized contrast uptakes. We could also consider reconstruction approaches based on learned data using deep learning architectures. In this case, our simulation platform could be really helpful, generating a large dataset of simulated images where we know exactly the ground truth.

The VCT evaluation we performed has several limitations which must be considered in future studies. In the very first place, our study suffers from a limited number of cases. This constraint was caused by the reading time needed for each human observer. Two solutions may be considered: model observers and split-plot study designs. Model observers are mathematical tools which model the response of a human observer to a particular induced signal [16] and a given test. These models have been already used to evaluate the mass lesion detection performance in recombined images [38]. However, we have not found any work related to contrast uptake characterization of CESM or CEDBT images. New models could be used to automatize the detection and characterization task and use a larger dataset of simulated images. Otherwise, we could choose to continue using a human observer study, but modifying the structure of the evaluation. The split-plot study design divides the number of total cases in several benches which are read independently by different groups of readers [223]. This architecture allows increasing the number of cases evaluated and the number of readers, which helps improving the statistical power of the study. Also, even if we have trained all readers together before the examination of the cases, we only found a moderate agreement between their answers for shape and enhancement characteristics, and a fair agreement for the answers related to the definition of the margins. More emphasis must be placed on the training phase for future studies in order to improve the agreement between readers and the statistical power of the whole study. Finally, the results we presented must be compared to true clinical evaluations when a commercial system allowing CESM and CEDBT acquisitions will be available.

Publications

- R. Sánchez De La Rosa, A-K. Carton, P. Milioni de Carvalho, Z. Li, S. Muller, and Isabelle Bloch. "Preliminary study of CEDBT and CESM performances using simulated analytical contrast uptakes." In 2018 IEEE 15th International Symposium on Biomedical Imaging (ISBI 2018), pp. 792-795. IEEE, 2018.
- R. Sánchez De La Rosa, A-K. Carton, P. Milioni de Carvalho, Isabelle Bloch, and S. Muller. "Analysis of Cedbt and CESM Performance Using a Realistic X-Ray Simulation Platform." In 2019 IEEE 16th International Symposium on Biomedical Imaging (ISBI 2019), pp. 1070-1073. IEEE, 2019.
- R. Sánchez De La Rosa, A-K. Carton, P. Milioni de Carvalho, Isabelle Bloch, and S. Muller. "Fast estimation of a continuous non-stationary scatter kernel in mammography systems" Submitted to Medical Physics

Apendix

Appendix A

MRMC Studies

When we need to assess the performance of a new diagnostic imaging modality, several issues arise. One of them is the evaluation of the clinical improvement offered by the new modality against other diagnostic tools or modalities. To perform such an evaluation we need to consider several factors degrading the image reading, such as the the human variation, the difference between cases and the difference between modalities. To do that we need a statistical model that defines the distribution of the response to a certain type of modality. Once the model is established, we can evaluate whether two responses are statistically different.

A.1 Evaluation of diagnostic systems

The main and most widely used tool to describe the accuracy of a diagnostic test is the Receiver Operating Characteristic (ROC) curve. The ROC curve associates a sensitivity or true positive fraction (TPF), the probability that an actual positive is identified as such, to a false positive fraction ($FPF = 1 - specificity$), the specificity being the probability that an actual negative is identified as such. More precisely, the TPF is defined as the ratio between the number of true positives and the number of abnormal cases, while the FPF is defined as ration between the number of false positives and the number of normal cases.

The ROC curve is created by progressively modifying the decision threshold over the parameter that defines if a case is finally classified as positive or negative. The Area Under the Curve (AUC) is used as the gold metric to evaluate the overall diagnostic accuracy. Depending on the hypothesis made on the data considered, to build the ROC curve we will develop two different approaches: parametric, when we consider that the data follows a certain distribution, or non-parametric, when we do not make any assumption on the distribution of the data.

A.1.1 Parametric approach

In the parametric approach [286], we consider that there is a probability distribution behind the answers given by a particular reader (also known as rater). We call this distribution the reader stimulus. Then, a reader is stimulated differently when we present an image belonging to the population of cases containing the disease D, or when we present an image that does not belong to the population of cases not containing the disease, $\bar{D}$. We can consider the hypothesis that

both stimulus (called S_1 and S_2, respectively) follow a Normal distribution:

$$Y_{S_1} \sim N\left(\mu_{S_1}, \sigma^2_{S_1}\right) \tag{A.1}$$

$$Y_{S_2} \sim N\left(\mu_{S_2}, \sigma^2_{S_2}\right) \tag{A.2}$$

where Y_{S_1} is the normal distribution of the stimulus to the cases containing the disease with mean and variance equal to μ_{S_1} and $\sigma^2_{S_1}$ respectively, and Y_{S_2} is the normal distribution of the stimulus to the cases without the disease with mean and variance equal to μ_{S_2} and $\sigma^2_{S_2}$ respectively.

This hypothesis leads us to the bi-normal estimator of the ROC curve and the AUC [95]. Using these two Normal distributions, we can establish a sliding threshold t which defines a continuous ROC curve, defined analytically as:

$$ROC(t) = \phi\left(a + b\phi^{-1}(t)\right) \tag{A.3}$$

where ϕ is a standard normal cumulative distribution function, $a = \frac{\mu_{S_1} - \mu_{S_2}}{\sigma_{S_1}}$, $b = \frac{\sigma_{S_2}}{\sigma S_1}$. Similarly, we can compute the AUC at a certain threshold level t using the same parameters a and b:

$$AUC(t) = \phi\left(\frac{a}{\sqrt{1+b^2}}\right) \tag{A.4}$$

The computation of the parametric ROC and AUC is illustrated in Figure A.1.

To compute the parameters a and b we can use the theoretical framework defined by Dorfman et al. [73]. We consider as before that the reader stimulus to the image follows a Normal distribution, which we do not known a priori and whose parameters have to be estimated. The reader will rate the case using different confidence ratings R_j, and, therefore, dividing the stimulus with the thresholds between two ratings Z_k (Figure A.2). Knowing this, we can establish the following probabilities for the ratings:

$$P\left(R_j \mid S_2\right) = \phi\left(Z_{k=j}\right) - \phi\left(Z_{k=j-1}\right) \tag{A.5}$$

$$P\left(R_j \mid S_1\right) = \phi\left(bZ_{k=j} - a\right) - \phi\left(bZ_{k=j-1} - a\right) \tag{A.6}$$

where $P\left(R_j \mid S_2\right)$ is the probability of rating a case without disease with the confidence R_j and $P\left(R_j \mid S_1\right)$ is the probability of rating a case with disease with the confidence R_j. The thresholds can be estimated using the first equation for a given stimulus S_i as follows:

$$Z_k = \left(\sum_{j=1}^{k} \frac{r_{ij}}{n_i}\right)^{-1} \tag{A.7}$$

where r_{ij} is the number of R_j to stimulus S_i, and n_i is the number of cases considered for the stimulus S_i. Then, the parameters a_i and b_i can be estimated using the following equations:

$$b_i Z_k - a_i = \left(\sum_{j=1}^{k} \frac{r_{ij}}{n_i}\right)^{-1} \tag{A.8}$$

$$b_i Z_{k+1} - a_i = \left(\sum_{j=1}^{k+1} \frac{r_{ij}}{n_i}\right)^{-1} \tag{A.9}$$

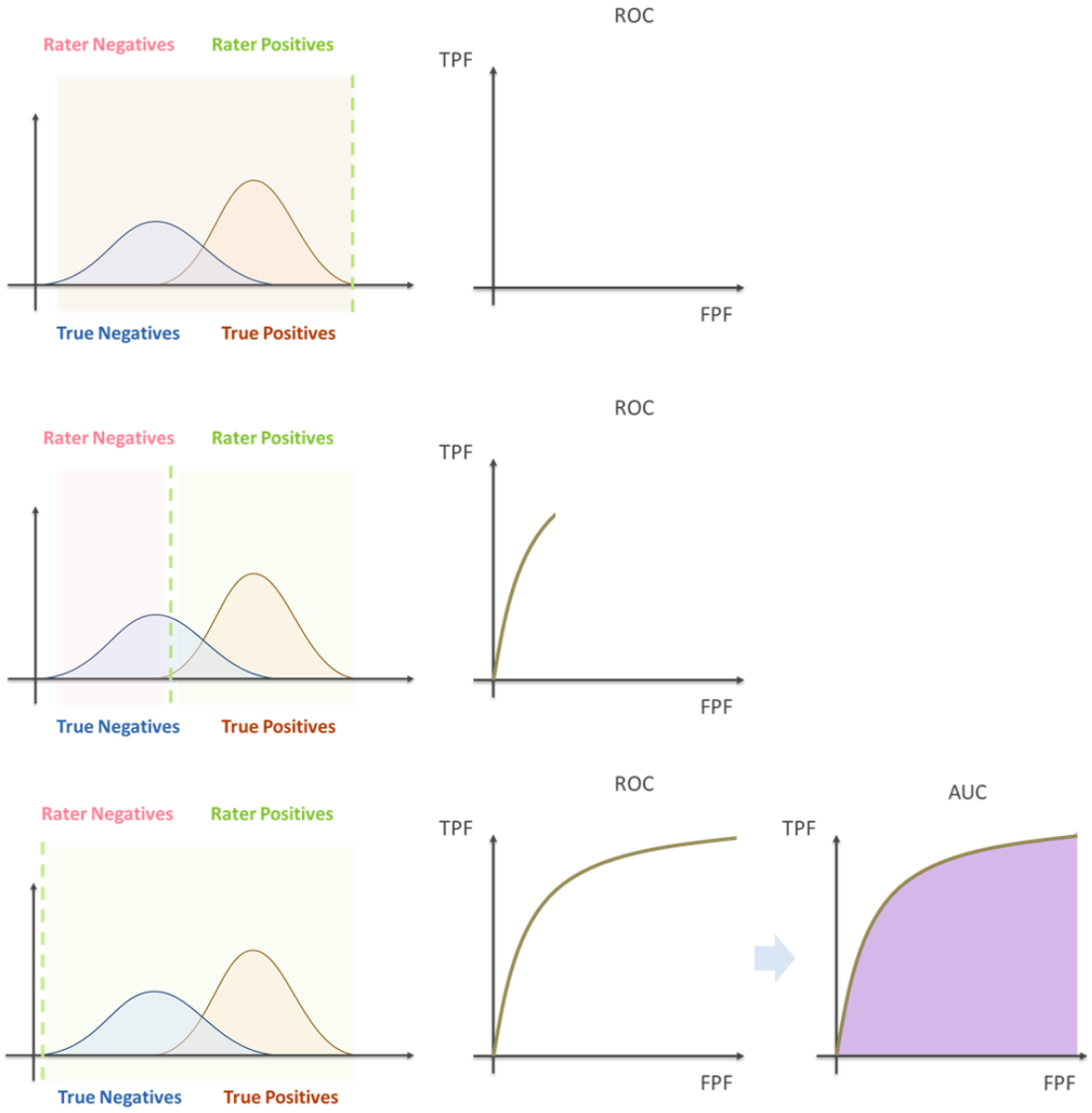

Figure A.1: Building the ROC curve and computing the associated AUC. We have two distributions corresponding to the stimulus that True Negatives (TN, without the disease) and True Positives (TP, with the disease) cases cause to a particular reader. If we apply a sliding threshold that implies a binary decision, considering that everything higher than the threshold is classified as Positive and everything below is classified as Negative, we can obtain a continuous fraction of True Positives (TPF, diseased cases that are correctly classified) and False Positives (FPF, non diseased cases that are wrongly classified). This continuous values are used to build the ROC curve.

where a_i and b_i is the value of the parameters a and b for stimulus S_i.

Although Hanley [112] presented several arguments in favor of this bi-normal estimator, it has been criticized by other authors [96, 118]. Several alternative models of the stimulus have

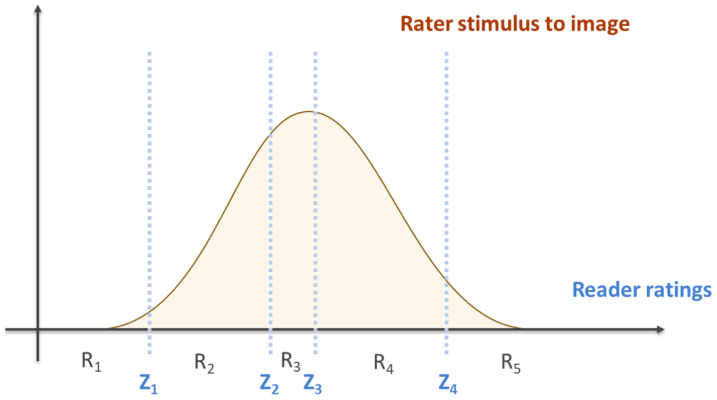

Figure A.2: Considering that the stimulus of the reader exposed to a new case follows a Gaussian distribution, the reader will assign different ratings depending on the confidence he has that the case belongs to a specific category.

been also considered such as bi-gamma, bi-beta, bi-lognormal distributions, and others [75, 202, 316].

A.1.2 Non-parametric approach

In a human evaluation study, a reader observes each of the images in the database. For each case, he gives a rate considering how confident he is that the case belongs to the diseased population. Consider the example given in Table A.1. We have a total of $N_D = 30$ cases belonging to the diseased population, and $N_{\bar{D}} = 19$ cases belonging to the normal population. For each image in our example, the reader gave a confidence level i from $i = 1...5$. For each confidence level we have $x_D[i]$ images in population D and $x_{\bar{D}}[i]$ images in population $\bar{D}$. The goal of non-parametric approaches is to obtain the ROC curve and AUC from these data without using any hypothesis. First, the non-parametric ROC curve can be computed using a trapezoidal approach. This method applies the ROC curve definition over the observed data. It computes a finite number of discrete samples of the ROC curve and, then, joins them with linear segments (Figure A.3). In particular, the TPF of each discrete sample of the ROC curve for a threshold on the confidence level $t \in [0... \max(i)]$ is defined as:

$$TPF[t] = \begin{cases} \frac{1}{N} \sum_{i=1}^{t} x_D[i] & , \; if \; t > 0 \\ 0 & , \; if \; t = 0 \end{cases} \tag{A.10}$$

and the FPF of each discrete sample of the ROC curve for a threshold level t is defined as:

$$FPF[t] = \begin{cases} \frac{1}{N} \sum_{i=1}^{t} x_{\bar{D}}[i] & , \; if \; t > 0 \\ 0 & , \; if \; t = 0 \end{cases} \tag{A.11}$$

The ROC function is then: $ROC(FPF[t]) = TPF[t]$.

The AUC can be estimated directly from the trapezoidal ROC. However, this procedure does not provide any statistical information. To do that, we can use the non-parametric Wilcoxon statistic test [114]. This test is used to verify whether a quantitative variable such as the number of cases x in population D tends to be greater than in $\bar{D}$, without assuming how x is distributed in both populations. The null hypothesis considered in this statistical test is that we cannot

Table A.1: Example of the ratings given by a reader in a diagnostic study.

	Ratings				
	$i=1$	$i=2$	$i=3$	$i=4$	$i=5$
Number of abnormal cases rated i in population D ($x_D[i]$)	3	8	12	5	2
Number of normal cases rated i in population $\bar{D}$ ($x_{\bar{D}}[i]$)	10	6	2	1	0

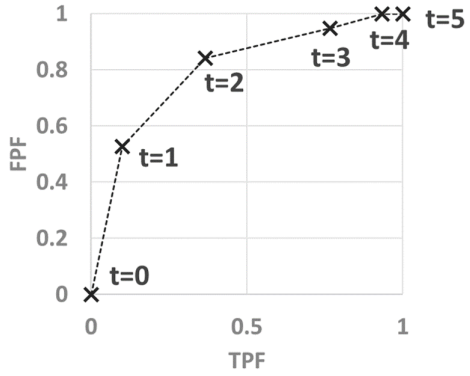

Figure A.3: Example of ROC curve computed using the trapezoidal method and the data given in Table A.1. The corresponding AUC to this curve can be computed using the Wilcoxon estimator W or adding the areas under each trapezoid. In both cases we obtain $AUC = 0.79$.

determine the population based only on x. In other words, that the value of x_D is just as likely to be smaller than the value of x_{barD}, as well as the opposite:

$$H_0 : Prob\,(x_D > x_{\bar{D}}) = 0.5 \tag{A.12}$$

Therefore, to test the validity of this hypothesis, the Wilcoxon test compares all the samples between both populations according to the step function:

$$S(x_D[i], x_{\bar{D}}[j]) = \begin{cases} 1 & , \; if \; x_D > x_{\bar{D}} \\ 0.5 & , \; if \; x_D = x_{\bar{D}} \\ 0 & , \; if \; x_D < x_{\bar{D}} \end{cases} \tag{A.13}$$

Then we average all the comparisons made with this rule and obtain:

$$W = \frac{1}{N_D N_{\bar{D}}} \sum_{i=1}^{N_D} \sum_{j=1}^{N_{\bar{D}}} S(x_D[i], x_{\bar{D}}[j]) \tag{A.14}$$

It can be demonstrated that W is equal to the area under the trapezoidal ROC [114]. From this statistical test we can obtain also the standard deviation caused by the cases in each population:

$$\sigma(W) = \sqrt{\frac{W(1-W) + (N_D - 1)(Q_1 - W^2) + (N_{\bar{D}} - 1)(Q_2 - W^2)}{N_D N_{\bar{D}}}} \tag{A.15}$$

where $Q_1 = \frac{W}{2-W}$ and $Q_2 = \frac{2W^2}{1+W}$.

However, this statistic suffers from several issues. On the one hand, the value of $\sigma(W)^2$ is a biased estimator of the variance. On the other hand, it does not consider multiple readers.

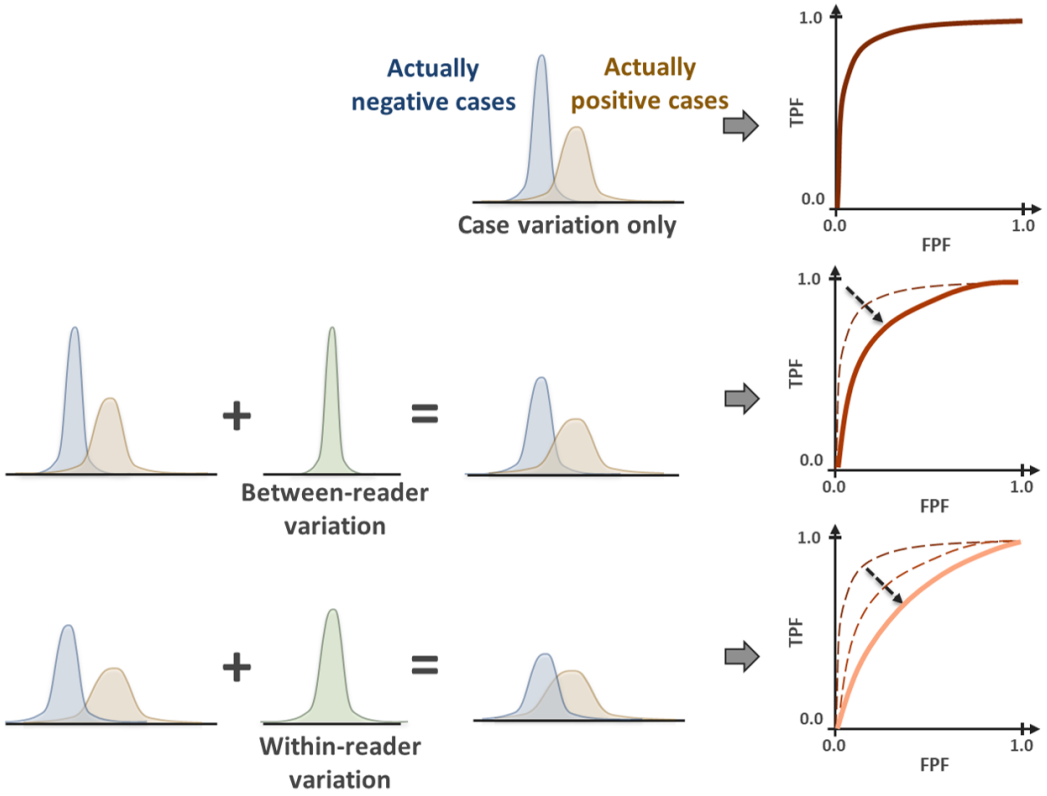

Figure A.4: When several readers evaluate the same dataset, we need to consider the new variability elements introduced in the study, that lower the ROC curve and decrease the AUC.

A.2 Multiple Readers Multiple Cases (MRMC)

When multiple readers evaluate the same populations of cases, we need to consider not only the deviation caused by the cases in each population, but also the between-reader and within-reader deviations. As defined by Metz et al. [207]:

$$\begin{pmatrix}\text{Decision-variable outcome for a particular case, reader and reading occasion}\end{pmatrix} = \begin{pmatrix}\underline{\text{mean}} \text{ for the truth-state of the case}\end{pmatrix} + \begin{pmatrix}\underline{\text{case variation}} \text{ for the particular case in the truth-state}\end{pmatrix} + \begin{pmatrix}\underline{\text{between-reader variation}} \text{ for the truth-state case and reader}\end{pmatrix} + \begin{pmatrix}\underline{\text{within-reader variation}} \text{ for the truth-state case, reader, and reading occasion}\end{pmatrix} \tag{A.16}$$

All these error sources broaden the distributions of negative and positive cases, lower the ROC curve, decrease the AUC, and therefore reduce the accuracy of the diagnostic, as illustrated in Figure A.4. The goal of MRMC theory is to consider all these deviations when computing the estimate of the AUC, the ROC curve and the statistical significance between two AUCs from different medical treatments or imaging techniques applied on the same population.

A.2.1 Estimation of AUC: single-shot

In MRMC studies the AUC of a case set is modeled as:

$$A_{jk} = \mu + r_j + c_k + (rc)_{jk} + Z_{jk} \tag{A.17}$$

where A_{jk} is the AUC for the j^{th} reader given the k^{th} case set, μ is the averaged AUC over all readers and case sets, r_j is the random reader effect, c_k is the random case effect, $(rc)_{jk}$ is the possible reader case interaction effect and Z_{jk} is the internal noise considered in the model.

Several proposals can be found to estimate the value of the AUC following the model shown before, such as bootstrap, jackknife or non-iterative methods (DeLong decomposition, McNeil correlation, Obuchowski correction for clustered data...) [70, 105, 113, 222]. In our PhD we focused on the One-shot estimator developed by Gallas [103]. This estimator is unbiased and performs similar to the widely-established jackknife estimator with a higher efficiency for small number of cases.

Using the One-shot estimator, the mean AUC is computed as the average of the Wilcoxon AUC among R readers:

$$\mu = \frac{1}{R}\sum_{r=1}^{R}\frac{1}{N_D N_{\bar{D}}}\sum_{i=1}^{N_D}\sum_{j=1}^{N_{\bar{D}}} S_r(x_D[i], x_{\bar{D}}[j]) \tag{A.18}$$

where $S_r(\cdot,\cdot)$ is the step function already defined for the Wilcoxon test for reader r.

The variance of the estimator considering all the deviation described by Metz can be also computed:

$$\sigma^2(W) = \frac{1}{R}\left(c_1M_1 + c_2M_2 + c_3M_3 + c_4M_4\right) + \frac{R-1}{R}\left(c_1M_5 + c_2M_6 + c_3M_7 + c_4M_8\right) - M_8 \tag{A.19}$$

where $c_1 = \frac{1}{N_D N_{\bar{D}}}$, $c_2 = \frac{N_D-1}{N_D N_{\bar{D}}}$, $c_3 = \frac{N_{\bar{D}}-1}{N_D N_{\bar{D}}}$, $c_4 = \frac{(N_D-1)(N_{\bar{D}}-1)}{N_D N_{\bar{D}}}$, and the terms $M_1...M_8$ are associated with the different deviation elements. Thus, we have a unique case deviation term:

$$M_1 = \sum_{r=1}^{R}\sum_{i=1}^{N_D}\sum_{j=1}^{N_{\bar{D}}}\frac{S_r^2(x_D[i], x_{\bar{D}}[j])}{R N_D N_{\bar{D}}} \tag{A.20}$$

three within-reader deviation terms:

$$M_2 = \sum_{r=1}^{R}\sum_{i=1}^{N_D}\sum_{j=1}^{N_{\bar{D}}}\sum_{m\neq i}^{N_D}\frac{S_r(x_D[i], x_{\bar{D}}[j])S_r(x_D[m], x_{\bar{D}}[j])}{R N_D N_{\bar{D}}\left(N_D-1\right)} \tag{A.21}$$

$$M_3 = \sum_{r=1}^{R}\sum_{i=1}^{N_D}\sum_{j=1}^{N_{\bar{D}}}\sum_{m\neq j}^{N_{\bar{D}}}\frac{S_r(x_D[i], x_{\bar{D}}[j])S_r(x_D[i], x_{\bar{D}}[m])}{R N_D N_{\bar{D}}\left(N_{\bar{D}}-1\right)} \tag{A.22}$$

$$M_4 = \sum_{r=1}^{R}\sum_{i=1}^{N_D}\sum_{j=1}^{N_{\bar{D}}}\sum_{m\neq i}^{N_D}\sum_{k\neq j}^{N_{\bar{D}}}\frac{S_r(x_D[i], x_{\bar{D}}[j])S_r(x_D[m], x_{\bar{D}}[k])}{R N_D N_{\bar{D}}\left(N_D-1\right)\left(N_{\bar{D}}-1\right)} \tag{A.23}$$

three between-reader deviation terms:

$$M_5 = \sum_{r=1}^{R}\sum_{i=1}^{N_D}\sum_{j=1}^{N_{\bar{D}}}\sum_{s\neq r}^{R}\frac{S_r(x_D[i], x_{\bar{D}}[j])S_s(x_D[i], x_{\bar{D}}[j])}{R N_D N_{\bar{D}}\left(R-1\right)} \tag{A.24}$$

$$M_6 = \sum_{r=1}^{R}\sum_{i=1}^{N_D}\sum_{j=1}^{N_{\bar{D}}}\sum_{m\neq i}^{N_D}\sum_{s\neq r}^{R}\frac{S_r(x_D[i], x_{\bar{D}}[j])S_s(x_D[m], x_{\bar{D}}[j])}{R N_D N_{\bar{D}}\left(N_D-1\right)\left(R-1\right)} \tag{A.25}$$

$$M_7 = \sum_{r=1}^{R}\sum_{i=1}^{N_D}\sum_{j=1}^{N_{\bar{D}}}\sum_{m\neq j}^{N_{\bar{D}}}\sum_{s\neq r}^{R}\frac{S_r(x_D[i], x_{\bar{D}}[j])S_s(x_D[i], x_{\bar{D}}[m])}{R N_D N_{\bar{D}}\left(N_{\bar{D}}-1\right)\left(R-1\right)} \tag{A.26}$$

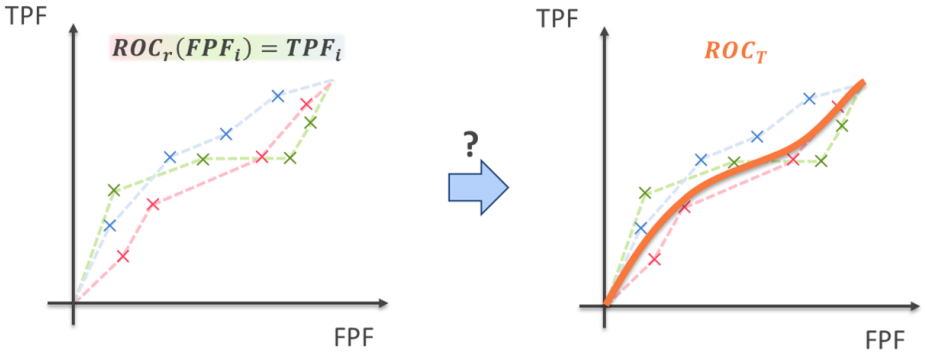

Figure A.5: When several readers evaluate a dataset, we need to provide the total ROC curve of the study. However, the transformation from several ROC curves to a unique total curve is not trivial.

and one reader-case deviation term:

$$M_8 = \sum_{r=1}^{R}\sum_{i=1}^{N_D}\sum_{j=1}^{N_{\bar{D}}}\sum_{m\neq i}^{N_D}\sum_{k\neq j}^{N_{\bar{D}}}\sum_{s\neq r}^{R}\frac{S_r(x_D[i],x_{\bar{D}}[j])S_s(x_D[m],x_{\bar{D}}[k])}{RN_DN_{\bar{D}}\left(N_D-1\right)\left(N_{\bar{D}}-1\right)\left(R-1\right)} \tag{A.27}$$

This estimator considers that all the evaluated images are independent and identically distributed (IID), as well as all the readers and the ratings when conditioned on the generating reader and image.

A.2.2 Building an average ROC

The One-shot estimator provides a value for the total AUC of a study with several readers, however we do not have yet an expression for the total ROC curve. The transformation of the individual ROC curves to a total ROC curve is not straightforward (Figure A.5), and there are several ways we can average the cloud of points retrieved for the individual readers [43, 97, 205, 285], which may not preserve the AUC (the area under the averaged ROC curved and the AUC computed through statistical methods may not be the same).

Chen et al. [50] proposed a simple way to average all the ROC curves obtained for each reader, preserving at the same time the AUC. To use this method we consider that our ROC curve for each reader is continuous (in the non-parametric case the ROC curve is piece-wise linear). Then, we transform each of the ROC curves to the (u, v) space for a given angle θ with the following polar conversion:

$$\begin{cases} u_r = FPF_r\cos(\theta) + TPF_r\sin(\theta) \\ v_r = -FPF_r\sin(\theta) + TPF_r\cos(\theta) \end{cases} \tag{A.28}$$

where (FPF_r, TPF_r) are the continuous values of the ROC curve for each reader r, and (u_r, v_r) the transformed values for each reader.

Once we have transformed our ROC curves we can average v_r for each u, obtaining a single pair (u, v). Finally, we go back to the original domain to retrieve the total ROC curve using:

$$\begin{cases} FPF = u\cos(\theta) - v\sin(\theta) \\ TPF = u\sin(\theta) + v\cos(\theta) \end{cases} \tag{A.29}$$

Although this method can be used for different values of θ, in this PhD we opted by a diagonal averaging using $\theta = \pi/4\ rad$. As this averaging method preserves the AUC for any value of θ, this angle parameter does not produce a noticeable difference in real-world applications.

A.2.3 Hypothesis test: DBM

We have presented a theoretical framework to evaluate the collected data from a study, as in Table A.1, for several readers. But, what happens if we want to evaluate different medical treatments or image techniques applied to the dataset? We could say that the treatment with higher AUC is better than the one with a smaller value. However, we have presented that the AUC follows a specific statistic, with a defined mean and variance. Therefore:

$$AUC_{t_1} \sim \left(\mu_1, \sigma_1^2\right) \tag{A.30}$$

$$AUC_{t_2} \sim \left(\mu_2, \sigma_2^2\right) \tag{A.31}$$

where t_1 and t_2 refer to the two different treatments or image techniques applied to the dataset.

To answer our question we try to demonstrate the following null hypothesis:

$$H_0 :\ AUC_{t_1} - AUC_{t_2} = 0 \tag{A.32}$$

This hypothesis could be tested using the same non-parametric Wilcoxon statistics as used before [279], however several methods have demonstrated to outperform this method and they are the current standard (for more information see the comparison made by Obuchowski et al. in [224]). The first widely used method is the Dorfman-Berbaum-Metz (DBM) method [74], that we have used in this PhD.

The goal of the DBM hypothesis test is to model $A = AUC_{t_1} - AUC_{t_2}$ and check whether it corresponds to a Gaussian with zero mean. The model of this subtraction is similar to the model presented in Equation A.17, but adding the term considering the variation of the AUC due to the random treatment effect:

$$A_{ijk} = \mu + r_j + c_k + (rc)_{jk} + \boldsymbol{\tau_i} + \boldsymbol{(\tau r)_{ij}} + \boldsymbol{(\tau c)_{ij}} + \boldsymbol{(\tau rc)_{ijk}} + Z_{jk} \tag{A.33}$$

where where A_{ijk} is the AUC for the i^{th} treatment and the j^{th} reader given the k^{th} case set, and τ refers the different treatments or image techniques applied to the dataset. Similarly, the variance is composed of several components:

$$\sigma^2(A) = \sigma_r^2 + \sigma_c^2 + \sigma_{\tau r}^2 + \sigma_{\tau c}^2 + \sigma_{rc}^2 + \sigma_{\tau rc}^2 + \sigma_Z^2 \tag{A.34}$$

To test the null-hypothesis the DBM method uses an ANOVA F statistic based on AUC pseudo-values. These AUC pseudo-values are estimated using the jackknife method [291]. The ANOVA test checks the probability in the cumulative F distribution defined as:

$$F = \frac{\text{Variance between treatments}}{\text{Variance within treatments}} \tag{A.35}$$

Under the null-hypothesis of no difference between the two methods, F has an approximate F_{df_1,df_2} distribution, where df_1 is the degree of freedom due to the number of treatments and df_2 is the Satterthwaite [262] degree of freedom. Considering this, the value of F is estimated as:

$$F = \frac{\text{MS}(\tau)}{\text{MS}(\tau \cdot r) + \text{MS}(\tau \cdot c) - \text{MS}(\tau \cdot r \cdot c)} \tag{A.36}$$

where MSτ, MS$(\tau \cdot r)$, MS$(\tau \cdot c)$ and MS$(\tau \cdot r \cdot c)$ represent the mean square values corresponding to the effects produced by the treatment, treatment×reader, treatment×case and treatment×reader×case variations, respectively. The degrees of freedom are estimated as follows:

$$df_1 = t - 1 \tag{A.37}$$

$$df_2 = \frac{[\mathrm{MS}(\tau \cdot r) + \mathrm{MS}(\tau \cdot c) - \mathrm{MS}(\tau \cdot r \cdot c)]^2}{\frac{\mathrm{MS}^2(\tau \cdot r)}{(t-1)(r-1)} + \frac{\mathrm{MS}^2(\tau \cdot c)}{(t-1)(c-1)} + \frac{\mathrm{MS}^2(\tau \cdot r \cdot c)}{(t-1)(r-1)(c-1)}} \tag{A.38}$$

where t is the number of different treatments considered in the study.

We have presented the classical DBM estimators of F, df_1 and df_2, used in this PhD. However, Hillis et al. [126] have proposed another definition of F and df_2 to reduce the bias of these estimators. Hillis et al. [127] also proved that the DBM and the other most used hypothesis test used in MRMC studies, called Obuchowski-Rockette (OR) method, share the same characteristics under certain assumptions. Finally, most of the hypothesis tests used in the literature use a variation of the ANOVA F test presented here, based on different calculations of the variances.

A.2.4 Increasing analysis performance with split-plot study design

In all the methods presented until now we have considered that all readers evaluate all the images in the dataset. This is called a **factorial** study design. One disadvantage of this study design is that, for a large dataset, the reading time per reader is very high. For example, in the study presented in this PhD, to evaluate 290 cases each reader spent, in average, 5 hours. Therefore, even if the available dataset can be increased (in our case, generating more simulated images), the available time of our readers is a strong constraint. A solution to this problem is to organize our study using a **split-plot** study design. In this design we divide our cases and readers into smaller blocks (see Figure A.6), where each reader only evaluates a batch of cases of the dataset. There are several methods to evaluate the AUC in this type of study design: modified OR model, marginal-mean ANOVA, three-sample U-statistic... Obuchowski et al. [223] evaluated the performance of three different statistical methods for this type of study design (OR, marginal-mean ANOVA and an extension of the three-sample U-statistics), obtaining similar results.

When a study is designed using a split-plot pattern, we can increase the efficiency of the study. This is caused by an increased number of cases evaluated and available readers to evaluate the dataset. However, we must not split the cases into too small-sized block, because we would obtain fewer empirical points sampling the ROC space. It is usually recommended to use at least 20 diseased and 20 non-diseased cases per block [223].

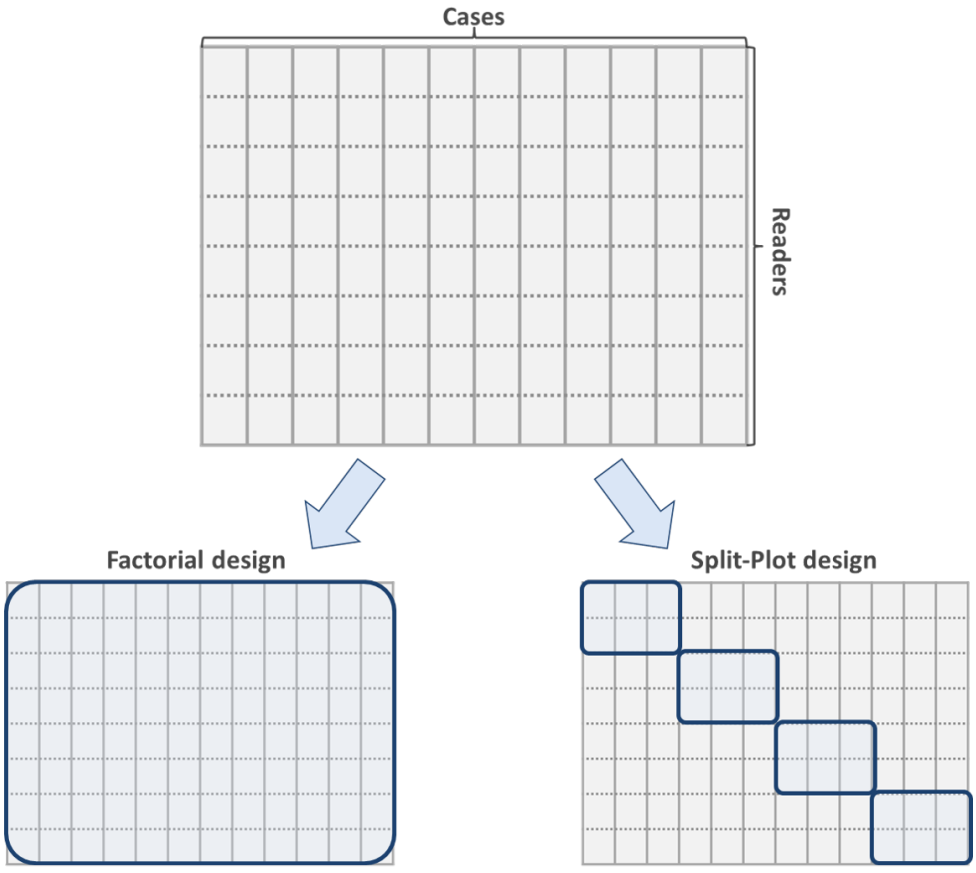

Figure A.6: The evaluation of a specific study with a fixed number of cases and readers can be performed using different designs. In the factorial design all readers evaluate all cases, while in the split-plot design the elements of the study (cases-readers) are divided in several blocks.

Appendix B

Adjusting stochastic processes after material decomposition

In Section 2.3.3 of Chapter 2 we introduced the factor $K_{L,H}$ for low- (L) and high-energy (H) simulated images. This factor, estimated through empirical measures, allows us to provide simulated images with the same SNR as low- and high-energy experimental acquisitions. However, in Section 4.1.2 of Chapter 4, we proved that this is not enough to match the SNR of the final simulated recombined images. Instead, we included a new term κ that multiplies the factor $K_{L,H}$ to obtain $K^{\kappa}_{L,H} = \kappa \cdot K_{L,H}$, modifying the variance of the final image and, therefore, the SNR without changing the average intensity of the recombined image. In this appendix we detail the steps of the calculation of κ .

To obtain the final recombined image we require three stages:

- We acquire the low- and high-energy images $p_{L,H}$. The variance of the simulated image at this step, given in Equation 4.15, is:

$$\sigma^2_{p_{L,H}} = \sigma^2_{q_{L,H}} + \sigma^2_{elec_{L,H}} + \sigma^2_u \tag{B.1}$$

  where $\sigma^2_{q_{L,H}}$ is the variance of the low- and high-energy quantum noise processes, $\sigma^2_{elec_{L,H}}$ is the known variance of the low- and high-energy electronic noise processes, and σ^2_u is the known variance of the low- and high-energy quantization noise processes. In particular, the variance of the quantum noise is estimated in Equation 4.14 as:

$$\sigma^2_{q_{L,H}} = M^2 \cdot \frac{G^2_{L,H}}{K_{L,H}} \cdot \lambda_{L,H} \tag{B.2}$$

  where M is the known total electronic gain, $G_{L,H}$ is an empirically derived parameter adjusting the mean pixel value of the quantum noise process (and, therefore, is a constant in this equation), and $K_{L,H}$ is an empirically derived parameter which can be modified to adjust the variance of the quantum noise model.

- After the acquisition of both images, we combine them to obtain the equivalent iodine thickness t^{simu}_{iod}. The variance of this new image, estimated in Equation 4.19, is:

$$\mathrm{Var}\left\{t^{simu}_{iod}\right\} \approx \left(\frac{\alpha_1}{\mu_{q_L} + \mu_u}\right)^2 \cdot \left(\sigma^2_{q_L} + \sigma^2_{elec_L} + \sigma^2_u\right) + \left(\frac{\alpha_2}{\mu_{q_H} + \mu_u}\right)^2 \cdot \left(\sigma^2_{q_H} + \sigma^2_{elec_H} + \sigma^2_u\right) \tag{B.3}$$

where α_1 and α_2 are the recombination coefficients introduced in Equation 4.11, $\mu_{q_{L,H}} = M \cdot G_{L,H} \cdot \lambda_{L,H}$ is the known average of the low- and high-energy quantum noise processes (Equation 4.14) and μ_u is the known average of the low- and high-energy quantization noise processes (Equation 4.13).

- The last step is to normalize the equivalent iodine thickness as it is performed in real acquisitions systems. This is achieved using Equation 4.23. The final variance of the recombined image is:

$$\mathrm{Var}\left\{I_{iod}^{simu}\right\} = \left(\frac{\Delta}{\max(t_{iod}) - \min(t_{iod})}\right)^2 \cdot \mathrm{Var}\left\{t_{iod}^{simu}\right\} \tag{B.4}$$

where Δ, $\min(t_{iod})$ and $\max(t_{iod})$ are all known constant characteristic scale factors.

The term κ is introduced to have the following equality:

$$\mathrm{Var}\left\{I_{iod}^{exp}\right\} = \mathrm{Var}\left\{I_{iod}^{simu}\right\} \tag{B.5}$$

where $\mathrm{Var}\left\{I_{iod}^{exp}\right\}$ is the variance of experimental recombined images after normalization which can be measured directly on acquired images using a real mammography system, and $\mathrm{Var}\left\{I_{iod}^{simu}\right\}$ is the variance of simulated recombined images after normalization which needs to be adjusted. Since in the expression of $\mathrm{Var}\left\{I_{iod}^{simu}\right\}$ all but the parameter $K_{L,H}$ are well known constants, our goal is to modify this parameter in low- and high-energy simulations to provide the equality given in Equation B.5.

In this context, κ is an additional parameter multiplying both K_L and K_H parameters so we introduce the same modification in low- and high-energy simulations ($K_{L,H}^{\kappa} = \kappa \cdot K_{L,H}$). That said, we need to solve the following equation:

$$\begin{aligned}\mathrm{Var}\left\{I_{iod}^{exp}\right\} = \left(\frac{\Delta}{\max(t_{iod}) - \min(t_{iod})}\right)^2 \cdot \Bigg(\left(\frac{\alpha_1}{G_L \cdot \mu_L + \mu_u}\right)^2 \cdot \left(\frac{G_L^2 \cdot \sigma_L^2}{K_L^{\kappa}} + \sigma_{elec_L}^2 + \sigma_u^2\right) \\ + \left(\frac{\alpha_2}{G_H \cdot \mu_H + \mu_u}\right)^2 \cdot \left(\frac{G_H^2 \cdot \sigma_H^2}{K_H^{\kappa}} + \sigma_{elec_H}^2 + \sigma_u^2\right)\Bigg)\end{aligned} \tag{B.6}$$

where $\mu_{L,H} = M \cdot \lambda_{L,H}$ and $\sigma_{L,H}^2 = M^2 \cdot \lambda_{L,H}$ are the mean and variance measured values of the simulated low- and high-energy images if the parameters $G_{L,H}$ and $K_{L,H}^{\kappa}$ are not used and no other noise source is present. For ease of reading we introduce the following variables:

$$\begin{aligned} S &= \left(\frac{\Delta}{\max(t_{iod}) - \min(t_{iod})}\right)^2 \\ A &= \left(\frac{\alpha_1}{G_L \cdot \mu_L + \mu_u}\right)^2 \\ B &= \left(\frac{\alpha_2}{G_H \cdot \mu_H + \mu_u}\right)^2 \\ F &= A \cdot \left(\sigma_{elec_L}^2 + \sigma_u^2\right) + B \cdot \left(\sigma_{elec_H}^2 + \sigma_u^2\right) \end{aligned} \tag{B.7}$$

Then, Equation B.6 can be expressed as:

$$\begin{aligned}\mathrm{Var}\left\{I_{iod}^{exp}\right\} &= S \cdot \left(A \cdot \frac{G_L^2 \cdot \sigma_L^2}{\kappa \cdot K_L} + B \cdot \frac{G_H^2 \cdot \sigma_H^2}{\kappa \cdot K_H} + F\right) \\ &= S \cdot \left(\frac{A \cdot G_L^2 \cdot \sigma_L^2 \cdot K_H + B \cdot G_H^2 \cdot \sigma_H^2 \cdot K_L}{\kappa \cdot K_L \cdot K_H} + F\right)\end{aligned} \tag{B.8}$$

and, therefore, κ can be computed as:

$$\kappa = \frac{A \cdot G_L^2 \cdot \sigma_L^2 \cdot K_H + B \cdot G_H^2 \cdot \sigma_H^2 \cdot K_L}{\left(\mathrm{Var}\left\{I_{iod}^{exp}\right\}/S - F\right) \cdot K_L \cdot K_H} \tag{B.9}$$

where all values are known constants or measures on the experimental and simulated images.

Bibliography

[1] R. E. Alvarez. "Dimensionality and noise in energy selective x-ray imaging". In: *Medical Physics* 40.11 (2013), pp. 1–13.

[2] R. E. Alvarez and A. Macovski. "Energy-selective reconstructions in X-ray computerized tomography." In: *Physics in Medicine and Biology* 21.5 (1976), pp. 733–744.

[3] R. E. Alvarez, J. A. Seibert, and S. K. Thompson. "Comparison of dual energy detector system performance". In: *Medical Physics* 31.3 (2004), pp. 556–565.

[4] A. H. Andersen and A. C. Kak. "Simultaneous algebraic reconstruction technique (SART): a superior implementation of the ART algorithm". In: *Ultrasonic Imaging* 6.1 (1984), pp. 81–94.

[5] A. Badal and A. Badano. "Accelerating Monte Carlo simulations of photon transport in a voxelized geometry using a massively parallel graphics processing unit". In: *Medical Physics* 36.11 (2009), pp. 4878–4880.

[6] A. Badal et al. "penMesh - Monte Carlo radiation transport simulation in a triangle mesh geometry." In: *IEEE Transactions on Medical Imaging* 28.12 (2009), pp. 1894–1901.

[7] A. Badano et al. "Anisotropic imaging performance in breast tomosynthesis". In: *Medical Physics* 34.11 (2007), p. 4076.

[8] A. Badano et al. "Evaluation of Digital Breast Tomosynthesis as Replacement of Full-Field Digital Mammography Using an In Silico Imaging Trial". In: *JAMA Network Open* 1.7 (2018), e185474.

[9] M. Baer et al. "Image-based dual energy CT using optimized precorrection functions: A practical new approach to material decomposition in the image domain". In: *Medical Physics* 36.8 (2009), p. 3818.

[10] P. R. Bakic et al. "Mammogram synthesis using a 3D simulation. I. Breast tissue model and image acquisition simulation." In: *Medical Physics* 29.9 (2002), pp. 2131–9.

[11] P. A. Baltzer et al. "False-positive findings at contrast-enhanced breast MRI: A BI-RADS descriptor study". In: *American Journal of Roentgenology* 194.6 (2010), pp. 1658–1663.

[12] R. P. Bambah. "On lattice coverings by spheres". In: *National Institute of Science of India*. Vol. 20. 1. 1954, pp. 25–52.

[13] H. H. Barrett and W Swindell. "Radiological imaging: the theory of image formation, detection, and processing". In: *Detection and Processing* 2 (1996).

[14] M. Båth et al. "Method of simulating dose reduction for digital radiographic systems". In: *Radiation Protection Dosimetry* 114.1-3 (2005), pp. 253–259.

[15] M. Berks et al. “Modelling structural deformations in mammographic tissue using the dual-tree complex wavelet”. In: *International Workshop on Digital Mammography*. 2010, pp. 145–152.

[16] J. Beutel, H. L. Kundel, and R. L. Van Metter. *Handbook of medical imaging*. Vol. 1. SPIE, 2000.

[17] C. Bhimani et al. “Contrast-enhanced Spectral Mammography: Modality-specific artifacts and other factors which may interfere with image quality”. In: *Academic Radiology* 24.1 (2017), pp. 89–94.

[18] C. Bhimani et al. “Contrast-enhanced Spectral Mammography: Technique, Indications, and Clinical Applications”. In: *Academic Radiology* 24.1 (2017), pp. 84–88.

[19] U. Bick et al. “Evaluation of contrast-enhanced digital mammography”. In: *European Journal of Radiology* 78.1 (2009), pp. 112–121.

[20] K Bliznakova, Z Kolitsi, and N Pallikarakis. “Dual-energy mammography: simulation studies”. In: *Physics in Medicine and Biology* 51.18 (2006), pp. 4497–4515.

[21] K Bliznakova et al. “A three-dimensional breast software phantom for mammography simulation”. In: *Physics in Medicine and Biology* 48.22 (2003), pp. 3699–3719.

[22] K Bliznakova et al. “Evaluation of an improved algorithm for producing realistic 3D breast software phantoms: Application for mammography”. In: *Medical Physics* 37.11 (2010), pp. 5604–5617.

[23] K. S. Blum et al. “Use of low-energy contrast-enhanced spectral mammography (CESM) as diagnostic mammography-proof of concept”. In: *Radiography* 21.4 (2015), pp. 352–358.

[24] F. O. Bochud, C. K. Abbey, and M. P. Eckstein. “Statistical texture synthesis of mammographic images with clustered lumpybackgrounds”. In: *Optics Express* 4.1 (1998), pp. 33–43.

[25] J. M. Boone. “Color mammography. Image generation and receiver operating characteristic evaluation.” In: *Investigative Radiology* 26.6 (1991), pp. 521–527.

[26] J. M. Boone, B. A. Arnold, and J. A. Seibert. “Characterization of the point spread function and modulation transfer function of scattered radiation using a digital imaging system”. In: *Medical Physics* 13.2 (1986), pp. 254–256.

[27] J. M. Boone and V. N. Cooper. “Scatter/primary in mammography: Monte Carlo validation”. In: *Medical Physics* 27.8 (2000), pp. 1818–1831.

[28] J. M. Boone, G. S. Shaber, and M. Tecotzky. “Dual-energy mammography: A detector analysis”. In: *Medical Physics* 17.4 (1990), pp. 665–675.

[29] J. M. Boone et al. “Scatter/primary in mammography: Comprehensive results”. In: *Medical Physics* 27.10 (2000), pp. 2408–2416.

[30] D. S. Brettle and A. R. Cowen. “Dual-energy digital mammography utilizing stimulated phosphor computed radiography”. In: *Physics in Medicine and Biology* 39.11 (1994), pp. 1989–2004.

[31] E. Buhr, S. Günther-Kohfahl, and U. Neitzel. “Accuracy of a simple method for deriving the presampled modulation transfer function of a digital radiographic system from an edge image”. In: *Medical Physics* 30.9 (2003), pp. 2323–2331.

[32] A. E. Burgess. "Mammographic structure: data preparation and spatial statistics analysis". In: *SPIE Conference on Image Sciennce Proceedings* 3661.February (1999), pp. 642–653.

[33] A. E. Burgess. "Visual perception studies and observer models in medical imaging". In: *Seminars in Nuclear Medicine* 41.6 (2011), pp. 419–436.

[34] A. E. Burgess et al. "Human observer detection experiments with mammograms and power-law noise". In: *Medical Physics* 419.2001 (2014), pp. 419–437.

[35] E. S. Burnside et al. "The ACR BI-RADS experience: learning from history". In: *Journal of the American College of Radiology* 6.12 (2009), pp. 851–860.

[36] M. Caballo, R. Mann, and I. Sechopoulos. "Patient-based 4D digital breast phantom for perfusion contrast-enhanced breast CT imaging". In: *Medical Physics* 45.10 (2018), pp. 4448–4460.

[37] A.-K. Carton et al. "A virtual human breast phantom using surface meshes and geometric internal structures". In: *International Workshop on Digital Mammography* (2014), pp. 356–363.

[38] A.-K. Carton et al. "Assessment of mass detection performance in contrast enhanced digital mammography". In: *Medical Imaging 2015: Image Perception, Observer Performance, and Technology Assessment*. Vol. 9416. 2015, p. 941608.

[39] A.-K. Carton et al. "Dual-energy contrast-enhanced digital breast tomosynthesis - A feasibility study". In: *British Journal of Radiology* 83.988 (2010), pp. 344–350.

[40] A.-K. Carton et al. "Dual-energy subtraction for contrast-enhanced digital breast tomosynthesis". In: *Proceedings of SPIE* 6510 (2007), pp. 651007–651007–12.

[41] A.-K. Carton et al. "Effects of image lag and scatter for dual-energy contrast-enhanced digital breast tomosynthesis using a CsI flat-panel based system". In: *Medical Imaging: Physics of Medical Imaging*. Vol. 7961. 2011, p. 79611D.

[42] A.-K. Carton et al. "Validation of MTF measurement for digital mammography quality control". In: *Medical Physics* 32.6 (2005), pp. 1684–1695.

[43] H.-P. Chan et al. "Digital mammography: observer performance study of the effects of pixel size on the characterization of malignant and benign microcalcifications". In: *Academic Radiology* 8.6 (2001), pp. 454–466.

[44] H.-P. Chan et al. "Improvement of radiologists' characterization of mammographic masses by using computer-aided diagnosis: An ROC study". In: *Radiology* 212.3 (1999), pp. 817–827.

[45] B. Chen et al. "An anthropomorphic breast model for breast imaging simulation and optimization". In: *Academic Radiology* 18.5 (2011), pp. 536–546.

[46] F. Chen et al. "Description and characterization of a novel method for partial volume simulation in software breast phantoms". In: *IEEE Transactions on Medical Imaging* 34.10 (2015), pp. 2146–2161.

[47] L. Chen et al. "Anatomical complexity in breast parenchyma and its implications for optimal breast imaging strategies". In: *Medical Physics* 39.3 (2012), pp. 1435–1441.

[48] L. Chen et al. "Impact of subtraction and reconstruction strategies on dual-energy contrast enhanced breast tomosynthesis with interleaved acquisition". In: *SPIE Medical Imaging* 8668 (2013), 86685O.

[49] S. C. Chen et al. “Initial clinical experience with contrast-enhanced digital breast tomosynthesis.” In: *Academic Radiology* 14.2 (2007), pp. 229–238.

[50] W. Chen and F. W. Samuelson. “The average receiver operating characteristic curve in multireader multicase imaging studies”. In: *The British journal of radiology* 87.1040 (2014), p. 20140016.

[51] X. Chen et al. “High-resolution, anthropomorphic, computational breast phantom: fusion of rule-based structures with patient-based anatomy”. In: *Medical Imaging 2017: Physics of Medical Imaging*. Vol. 10132. International Society for Optics and Photonics, 2017, 101321W.

[52] Y. Chen et al. “Characterization of scatter in cone-beam CT breast imaging: comparison of experimental measurements and Monte Carlo simulation.” In: *Medical Physics* 36.3 (2009), pp. 857–69.

[53] C. P. Chou et al. “Clinical evaluation of contrast-enhanced digital mammography and contrast enhanced tomosynthesis - Comparison to contrast-enhanced breast MRI”. In: *European Journal of Radiology* 84.12 (2015), pp. 2501–2508.

[54] K.-S. Chuang and H. K. Huang. “A fast dual-energy computational method using isotransmission lines and table lookup”. In: *Medical Physics* 14.2 (1987), pp. 186–192.

[55] P. Clauser et al. “Motion artifacts, lesion type, and parenchymal enhancement in breast MRI: what does really influence diagnostic accuracy?” In: *Acta Radiologica* 60.1 (2019), pp. 19–27.

[56] M. P. Coleman et al. “Cancer survival in five continents: a worldwide population-based study (CONCORD)”. In: *The lancet oncology* 9.8 (2008), pp. 730–756.

[57] A. P. Colijn and F. J. Beekman. “Accelerated simulation of cone beam X-Ray scatter projections”. In: *IEEE Transactions on Medical Imaging* 23.5 (2004), pp. 584–590.

[58] A. Contillo et al. “A novel approach to background subtraction in contrast-enhanced dual-energy digital mammography with commercially available mammography devices: Polychromaticity correction.” In: *Medical Physics* 42.11 (2015), p. 6641.

[59] A. P. Cooper. *On the Anatomy of the Breast*. Logman, 1840.

[60] V. N. Cooper III et al. “An edge spread technique for measurement of the scatter-to-primary ratio in mammography”. In: *Medical Physics* 27.5 (2000), pp. 845–853.

[61] I. A. Cunningham. “Linear-systems modeling of parallel cascaded stochastic processes: the NPS of radiographic screens with reabsorption of characteristic x-radiation”. In: *Medical Imaging 1998: Physics of Medical Imaging* 3336 (1998), pp. 220–231.

[62] I. A. Cunningham, M. Westmore, and A Fenster. “A spatial-frequency dependent quantum accounting diagram and detective quantum efficiency model of signal and noise propagation in cascaded imaging systems”. In: *Medical Physics* 21.3 (1994), pp. 417–427.

[63] D. R. Dance and G. J. Day. “Escape probabilities for fluorescent x-rays”. In: *Physics in Medicine and Biology* 30.3 (1985), pp. 259–262.

[64] D. R. Dance and G. J. Day. “The computation of scatter in mammography by Monte Carlo methods”. In: *Physics in Medicine and Biology* 29.3 (1984), pp. 237–247.

[65] M. Daniaux et al. “Dual-energy contrast-enhanced spectral mammography (CESM)”. In: *Archives of Gynecology and Obstetrics* 292.4 (2015), pp. 739–747.

[66] B. De Man et al. "CatSim: a new computer assisted tomography simulation environment". In: *Proceedings of SPIE* 6510 (2007), 65102G.

[67] L. De Sisternes et al. "A computational model to generate simulated three-dimensional breast masses". In: *Medical Physics* 42.2 (2015), pp. 1098–1118.

[68] L. S. Del Lama, D. M. Cunha, and M. E. Poletti. "Validation of a modified PENELOPE Monte Carlo code for applications in digital and dual-energy mammography". In: *Radiation Physics and Chemistry* 137 (2017), pp. 151–156.

[69] M del Mar Travieso-Aja et al. "Factors affecting the precision of lesion sizing with contrast-enhanced spectral mammography". In: *Clinical Radiology* 73.3 (2018), pp. 296–303.

[70] E. R. DeLong, D. M. DeLong, and D. L. Clarke-Pearson. "Comparing the areas under two or more correlated receiver operating characteristic curves: a nonparametric approach." In: *Biometrics* 44.3 (1988), pp. 837–845.

[71] W. B. DeMartini et al. "Background parenchymal enhancement on breast MRI: impact on diagnostic performance". In: *American Journal of Roentgenology* 198.4 (2012), W373–W380.

[72] O Diaz et al. "Estimation of scattered radiation in digital breast tomosynthesis." In: *Physics in Medicine and Biology* 59.15 (2014), pp. 4375–4390.

[73] D. D. Dorfman and E. Alf. "Maximum-likelihood estimation of parameters of signal-detection theory and determination of confidence intervals-Rating-method data". In: *Journal of Mathematical Psychology* 6.3 (1969), pp. 487–496.

[74] D. D. Dorfman, K. S. Berbaum, and C. E. Metz. "Receiver operating characteristic rating analysis: generalization to the population of readers and patients with the jackknife method". In: *Investigative Radiology* 27.9 (1992), pp. 723–731.

[75] D. D. Dorfman et al. "Proper receiver operating characteristic analysis: the bigamma model". In: *Academic Radiology* 4.2 (1997), pp. 138–149.

[76] C. D'Orsi et al. *ACR BI-RADS Atlas: Breast Imaging Reporting and Data System*. Reston, VA: American College of Radiology, 2013.

[77] C. Dromain. "Optimisation de l'angiomammographie et de l'angiotomosynthèse double-énergie". PhD thesis. Université Paris Sud-Paris XI, 2015.

[78] C. Dromain et al. "Dual-energy contrast-enhanced digital mammography: initial clinical results". In: *European Radiology* 21.3 (2011), pp. 565–574.

[79] C. Dromain et al. "Evaluation of tumor angiogenesis of breast carcinoma using contrast-enhanced digital mammography". In: *American Journal of Roentgenology* 187.5 (2006), W528–W537.

[80] J. L. Ducote and S Molloi. "Scatter correction in digital mammography based on image deconvolution". In: *Physics in Medicine and Biology* 55.5 (2010), pp. 1295–1309.

[81] J. L. Ducote and S. Molloi. "Quantification of breast density with dual energy mammography: An experimental feasibility study". In: *Medical Physics* 37.2 (2010), pp. 793–801.

[82] J. L. Ducote, T. Xu, and S. Molloi. "Dual-energy cardiac imaging: an image quality and dose comparison for a flat-panel detector and x-ray image intensifier". In: *Physics in Medicine and Biology* 52.1 (2006), pp. 183–196.

[83] P. Elangovan et al. "Design and validation of biologically inspired spiculated breast lesion models utilizing structural tissue distortion". In: *Medical Imaging 2018: Physics of Medical Imaging*. International Society for Optics and Photonics, 2018, 105730B.

[84] P. Elangovan et al. "Design and validation of realistic breast models for use in multiple alternative forced choice virtual clinical trials". In: *Physics in Medicine and Biology* 62.7 (2017), p. 2778.

[85] P. Elangovan et al. "Development and validation of a modelling framework for simulating 2D-mammography and breast tomosynthesis images". In: *Physics in Medicine and Biology* 59.15 (2014), pp. 4275–4293.

[86] P. Elangovan et al. "Lesion detectability in 2D-mammography and digital breast tomosynthesis using different targets and observers". In: *Physics in Medicine and Biology* 63.9 (2018), p. 95014.

[87] P. Elangovan et al. "OPTIMAM image simulation toolbox-recent developments and ongoing studies". In: *International Workshop on Digital Mammography*. 2016, pp. 668–675.

[88] P. Elangovan et al. "Simulation of 3D DLA masses in digital breast tomosynthesis". In: *Medical Imaging 2013: Physics of Medical Imaging*. Vol. 8668. International Society for Optics and Photonics, 2013, 86680Y.

[89] D. L. Ergun et al. "Single-exposure dual-energy computed radiography: improved detection and processing." In: *Radiology* 174.1 (1990), pp. 243–249.

[90] E. M. Fallenberg et al. "Contrast-enhanced spectral mammography versus MRI: Initial results in the detection of breast cancer and assessment of tumour size". In: *European Radiology* 24.1 (2014), pp. 256–264.

[91] E. M. Fallenberg et al. "Contrast-enhanced spectral mammography vs. mammography and MRI – clinical performance in a multi-reader evaluation". In: *European Radiology* 27.7 (2017), pp. 2752–2764.

[92] E. M. Fallenberg et al. "Contrast-enhanced spectral mammography: does mammography provide additional clinical benefits or can some radiation exposure be avoided?" In: *Breast cancer research and treatment* 146.2 (2014), pp. 371–381.

[93] Y. Fang et al. "Monte Carlo modeling of the DQE of a-Se X-Ray detectors for breast imaging". In: *International Workshop on Digital Mammography*. 2014, pp. 387–393.

[94] Y. Fang et al. "Monte Carlo simulation of a-Se x-ray detectors for breast imaging: Effect of nearest-neighbor recombination algorithm on Swank noise". In: *Lecture Notes in Computer Science* 7361 LNCS (2012), pp. 575–582.

[95] D. Faraggi and B. Reiser. "Estimation of the area under the ROC curve". In: *Statistics in Medicine* 21.20 (2002), pp. 3093–3106.

[96] A. Farcomeni and L. Ventura. "An overview of robust methods in medical research". In: *Statistical Methods in Medical Research* 21.2 (2012), pp. 111–133.

[97] T. Fawcett. "An introduction to ROC analysis". In: *Pattern Recognition Letters* 27.8 (2006), pp. 861–874.

[98] J. Ferlay et al. "Estimates of worldwide burden of cancer in 2008: GLOBOCAN 2008". In: *International Journal of Cancer* 127.12 (2010), pp. 2893–2917.

[99] J. L. Fleiss, J. Cohen, and B. Everitt. "Large sample standard errors of kappa and weighted kappa". In: *Psychological bulletin* 72.5 (1969), p. 323.

[100] J. L. Fleiss, B. Levin, and M. C. Paik. *Statistical methods for rates and proportions*. John Wiley & Sons, 2013.

[101] J. Folkman et al. "Induction of angiogenesis during the transition from hyperplasia to neoplasia". In: *Nature* 339.Nature Publishing Group (1989), p. 58.

[102] M. Freed, S. Park, and A. Badano. "A fast, angle-dependent, analytical model of CsI detector response for optimization of 3D x-ray breast imaging systems." In: *Medical Physics* 37.6 (2010), pp. 2593–605.

[103] B. D. Gallas. "One-shot estimate of MRMC variance: AUC". In: *Academic Radiology* 13.3 (2006), pp. 353–362.

[104] B. D. Gallas et al. "A framework for random-effects ROC analysis: biases with the bootstrap and other variance estimators". In: *Communications in Statistics - Theory and Methods* 38.15 (2009), pp. 2586–2603.

[105] B. D. Gallas et al. "A framework for random-effects ROC analysis: Biases with the bootstrap and other variance estimators". In: *Communications in Statistics - Theory and Methods* 38.15 (2009), pp. 2586–2603.

[106] S. Ganan and D McClure. "Bayesian image analysis: An application to single photon emission tomography". In: *American Statistical Association* (1985), pp. 12–18.

[107] S. Gavenonis et al. "Initial Experience with Dual- Energy Contrast-Enhanced Digital Breast Tomosynthesis in the Characterization of Breast Cancer". In: *Breast Imaging. IWDM 2012. Lecture Notes in Computer Science, Vol. 7361* (2012), pp. 32–39.

[108] X. Gong et al. "A computer simulation study comparing lesion detection accuracy with digital mammography, breast tomosynthesis, and cone-beam CT breast imaging." In: *Medical Physics* 33.4 (2006), pp. 1041–1052.

[109] I. S. Gribbestad et al. "An Introduction to Dynamic Contrast-Enhanced MRI in Oncology". In: *Dynamic Contrast-Enhanced Magnetic Resonance Imaging in Oncology* (2005), pp. 3–22.

[110] L. Hadjiiski et al. "Improvement in radiologists' characterization of malignant and benign breast masses on serial mammograms with computer-aided diagnosis: An ROC Study". In: *Radiology* 233.1 (2004), pp. 255–265.

[111] A. Hadjipanteli et al. "The threshold detectable mass diameter for 2D-mammography and digital breast tomosynthesis". In: *Physica Medica* 57 (2019), pp. 25–32.

[112] J. A. Hanley. "The robustness of the binormal assumptions used in fitting ROC curves". In: *Medical decision making* 8.3 (1988), pp. 197–203.

[113] J. A. Hanley and B. J. McNeil. "A method of comparing the areas under receiver operating characteristic curves derived from the same cases." In: *Radiology* 148.3 (1983), pp. 839–843.

[114] J. A. Hanley and B. J. McNeil. "The meaning and use of the area under a Receiver Operating Curve (ROC) characteristic". In: *Radiology* 143.1 (1982), pp. 29–36.

[115] J. J. Heine et al. "On the statistical nature of mammograms". In: *Medical Physics* 26.11 (1999), pp. 2254–2265.

[116] B Heismann and M Balda. "Quantitative image-based spectral reconstruction for computed tomography." In: *Medical Physics* 36.10 (2009), pp. 4471–85.

[117] M. Helal et al. "Accuracy of CESM versus conventional mammography and ultrasound in evaluation of BI-RADS 3 and 4 breast lesions with pathological correlation". In: *Egyptian Journal of Radiology and Nuclear Medicine* 48.3 (2017), pp. 741–750.

[118] S. Heritier et al. *Robust methods in biostatistics*. Vol. 825. John Wiley & Sons, 2009.

[119] G. T. Herman. "Correction for beam hardening in computed tomography." In: *Physics in Medicine and Biology* 24.1 (1979), pp. 81–106.

[120] M. L. Hill et al. "Anatomical noise in contrast-enhanced digital mammography. Part I. Single-energy imaging." In: *Medical Physics* 40.2013 (2013), p. 051910.

[121] M. L. Hill et al. "Anatomical noise in contrast-enhanced digital mammography. Part II. Dual-energy imaging". In: *Medical Physics* 40.8 (2013).

[122] M. L. Hill et al. "Contrast-Enhanced Digital Mammography Lesion Morphology and a Phantom for Performance Evaluation". In: *International Workshop on Digital Mammography*. 2014, pp. 231–238.

[123] M. L. Hill et al. "Design and validation of a mathematical breast phantom for contrast-enhanced digital mammography". In: *Medical Imaging 2011: Physics of Medical Imaging*. Vol. 7961. 2011, 79615E.

[124] M. L. Hill et al. "Impact of image acquisition timing on image quality for dual energy contrast-enhanced breast tomosynthesis". In: *Proceedings of SPIE Medical Imaging* 8313 (2012), pp. 831308–1–9.

[125] M. L. Hill et al. "Pre-clinical Evaluation of Tumour Angiogenesis with Contrast-Enhanced Breast Tomosynthesis". In: *International Workshop on Digital Mammography* (2012), pp. 1–8.

[126] S. L. Hillis, K. S. Berbaum, and C. E. Metz. "Recent developments in the Dorfman-Berbaum-Metz procedure for multireader ROC study analysis". In: *Academic Radiology* 15.5 (2008), pp. 647–661.

[127] S. L. Hillis, N. A. Obuchowski, and K. S. Berbaum. "Power estimation for multireader ROC methods: an updated and unified approach". In: *Academic Radiology* 18.2 (2011), pp. 129–142.

[128] H Hintsala et al. "Modelling of irregular breast lesions". In: *World Congress on Medical Physics and Biomedical Engineering, September 7-12, 2009, Munich, Germany*. 2009, pp. 2024–2027.

[129] J. Hsieh, O. E. Gurmen, and K. F. King. "Recursive correction algorithm for detector decay characteristics in CT". In: *Medical Imaging 2000*. Vol. 3977. 2000, pp. 298–305.

[130] C. M. L. Hsu et al. "Generation of a suite of 3D computer-generated breast phantoms from a limited set of human subject data." In: *Medical Physics* 40.4 (2013), p. 043703.

[131] Y.-H. Hu, D. A. Scaduto, and W. Zhao. "Optimization of contrast-enhanced breast imaging: Analysis using a cascaded linear system model". In: *Medical Physics* 44.1 (2017), pp. 43–56.

[132] Y.-H. Hu and W. Zhao. "A 3D linear system model for the optimization of dual-energy contrast-enhanced digital breast tomosynthesis". In: *Proc. SPIE 7961, Medical Imaging 2011: Physics of Medical Imaging, 79611C* 7961 (2011), pp. 79611C–79611C–9.

[133] Y.-H. Hu and W. Zhao. "Experimental quantification of lesion detectability in contrast enhanced dual energy digital breast tomosynthesis". In: *Medical Imaging 2012: Physics of Medical Imaging*. Vol. 8313. 2012, 83130A.

[134] H. Huang et al. "Lesion assessment and radiation dose in contrast-enhanced digital breast tomosynthesis". In: *14th International Workshop on Breast Imaging*. Vol. 10718. 2018, 107181J.

[135] H. M. Hudson and R. S. Larkin. "Ordered subsets of projection data". In: *IEEE transactions on medical imaging* 13.4 (1994), pp. 601–609.

[136] M. Iglesias-Ham, M. Kerber, and C. Uhler. "Sphere packing with limited overlap". In: *arXiv preprint arXiv:1401.0468* (2014).

[137] D. III, J. T, and D. J. Godfrey. "Digital x-ray tomosynthesis : current state of the art". In: *Physics in Medicine and Biology* 48.19 (2003), R65.

[138] International Electrotechnical Commission. "Medical electrical equipment-characteristics of digital X-ray imaging devices-part 1-2: determination of detective quantum efficiency detectors used in mammography". In: *IEC 62220-1-2, Ed. 1.0* (2007).

[139] R. Iordache et al. "Noise reduction in dual-energy contrast enhanced digital breast tomosynthesis using regularization". In: *International Workshop on Digital Mammography*. Springer. 2010, pp. 92–99.

[140] V. Iotti et al. "Contrast-enhanced spectral mammography in neoadjuvant chemotherapy monitoring: A comparison with breast magnetic resonance imaging". In: *Breast Cancer Research* 19.1 (2017), pp. 1–13.

[141] T. Ishigaki et al. "One-shot dual-energy subtraction imaging." In: *Radiology* 161.1 (1986), pp. 271–273.

[142] M. Jasionowska, A. Przelaskowski, and R. Jóźwiak. "Characteristics of architectural distortions in mammograms-Extraction of texture orientation with Gabor filters". In: *International Conference on Computer Vision and Graphics*. Springer. 2010, pp. 420–430.

[143] M. S. Jochelson et al. "Bilateral contrast-enhanced dual-energy digital mammography: feasibility and comparison with conventional digital mammography and MR imaging in women with known breast carcinoma". In: *Radiology* 266.3 (2013), pp. 743–751.

[144] H. E. Johns and J. R. Cunningham. *Physics of Radiology, Fourth Edition*. Charles C Thomas Pub Ltd, 1983.

[145] R. C. Jones. "On the point and line spread functions of photographic images". In: *Journal of the Optical Society of America* 48.12 (2008), p. 934.

[146] R. A. Jong et al. "Contrast-enhanced digital mammography: initial clinical experience". In: *Radiology* 228.3 (2003), pp. 842–850.

[147] M. Kachelrieß, K. Sourbelle, and W. A. Kalender. "Empirical cupping correction: A first-order raw data precorrection for cone-beam computed tomography". In: *Medical Physics* 33.5 (2006), pp. 1269–1274.

[148] A. C. Kak, M. Slaney, and G. Wang. "Principles of computerized tomographic imaging. 1988". In: *Medical Physics* 29.1 (2002), pp. 107–107.

[149] W. A. Kalender et al. "Evaluation of a prototype dual energy computed tomographic apparatus. I. Phantom studies". In: *Medical Physics* 13.3 (1986), pp. 334–339.

[150] R. M. Kamal et al. "Can we apply the MRI BI-RADS lexicon morphology descriptors on contrast-enhanced spectral mammography ?" In: *The British Journal of Radiology* 89.1064 (2016), p. 20160157.

[151] Y.-H. Kao et al. "A software tool for measurement of the modulation transfer function". In: *Medical Imaging 2005: Physics of Medical Imaging* 5745 (2005), p. 1199.

[152] S. C. Kappadath and C. C. Shaw. "Dual-energy digital mammography: Calibration and inverse-mapping techniques to estimate calcification thickness and glandular-tissue ratio". In: *Medical Physics* 30.6 (2003), pp. 1110–1117.

[153] R. Karunamuni et al. "Exploring the relationship between SDNR and detectability in dual-energy breast x-ray imaging". In: *Medical Imaging 2013: Physics of Medical Imaging*. Vol. 8668. 2013, p. 866863.

[154] F Kelcz, P. M. Joseph, and S. K. Hilal. "Noise considerations in dual energy CT scanning." In: *Medical Physics* 6.5 (1979), pp. 418–25.

[155] F. Kelcz, C. A. Mistretta, and S. J. Riederer. "Spectral considerations for absorption-edge fluoroscopy". In: *Medical Physics* 4.1 (1977), pp. 26–35.

[156] F Kelcz, C. a. Mistretta, and S. J. Riederer. "Spectral considerations for absorption-edge fluoroscopy". In: *Medical Physics* 4.1 (1979), pp. 26–35.

[157] N. Kiarashi. "Towards Realizing Virtual Clinical Trials for Optimization and Evaluation of Breast". PhD thesis. 2014.

[158] N. Kiarashi et al. "Development and application of a suite of 4-D virtual breast phantoms for optimization and evaluation of breast imaging systems". In: *IEEE Transactions on Medical Imaging* 33.7 (2014), pp. 1401–1409.

[159] R Klausz et al. "Properties of a new high-ratio anti-scatter grid in digital mammography". In: *European Congress of Radiology 2018* (2018), pp. 1–21.

[160] T. Knogler et al. "Application of BI-RADS descriptors in contrast-enhanced dual-energy mammography: Comparison with MRI". In: *Breast Care* 12.4 (2017), pp. 212–216.

[161] M Koutalonis et al. "Monte Carlo studies on the influence of focal spot size and intensity distribution on spatial resolution in magnification mammography." In: *Physics in medicine and biology* 53.5 (2008), pp. 1369–84.

[162] H. Kudo, F. Noo, and M. Defrise. "Quasi-exact filtered backprojection algorithm for long-object problem in helical cone-beam tomography". In: *IEEE transactions on medical imaging* 19.9 (2000), pp. 902–921.

[163] C. K. Kuhl. "Concepts for Differential Diagnosis in Breast MR Imaging". In: *Magnetic Resonance Imaging Clinics of North America* 14.3 (2006), pp. 305–328.

[164] C. K. Kuhl. "The current status of breast MR imaging part I. Choice of technique, image interpretation, diagnostic accuracy, and transfer to clinical practice". In: *Radiology* 244.2 (2007), pp. 356–378.

[165] C. K. Kuhl et al. "Healthy premenopausal breast parenchyma in dynamic contrast-enhanced MR imaging of the breast: normal contrast medium enhancement and cyclical-phase dependency". In: *Radiology* 203.1 (1997), pp. 137–144.

[166] U. C. Lalji et al. "Evaluation of low-energy contrast-enhanced spectral mammography images by comparing them to full-field digital mammography using EUREF image quality criteria". In: *European Radiology* 25.10 (2015), pp. 2813–2820.

[167] U. Lalji et al. "Contrast-enhanced spectral mammography in recalls from the Dutch breast cancer screening program: validation of results in a large multireader, multicase study". In: *European Radiology* 26.12 (2016), pp. 4371–4379.

[168] P. M. Lams and M. L. Cocklin. "Spatial resolution requirements for digital chest radiographs: an ROC study of observer performance in selected cases." In: *Radiology* 158.1 (1986), pp. 11–19.

[169] S. J. LaRoque, E. Y. Sidky, and X. Pan. "Accurate image reconstruction from few-view and limited-angle data in diffraction tomography". In: *JOSA A* 25.7 (2008), pp. 1772–1782.

[170] B. A. Lau et al. "A statistically defined anthropomorphic software breast phantom". In: *Medical Physics* 39.6Part1 (2012), pp. 3375–3385.

[171] K. C. Lau, S. Roth, and A. D. A. Maidment. "2D and 3D registration methods for dual-energy contrast-enhanced digital breast tomosynthesis". In: *Proc. SPIE 9033, Medical Imaging 2014: Physics of Medical Imaging* 9033 (2014), 90335W–1–11.

[172] D Lazos, Z Kolisti, and N. Pallikarakis. "A software data generator for radiographic imaging investigations". In: *IEEE Transactions on Information Technology in Biomedicine* 4.1 (2000), pp. 76–79.

[173] L. A. Lehmann and R. E. Alvarez. "Energy-selective radiography a review". In: *Digital Radiography* (1986), pp. 145–188.

[174] L. A. Lehmann et al. "Generalized image combinations in dual KVP digital radiography". In: *Medical Physics* 8.5 (1981), pp. 659–667.

[175] R. Leithner, T. Knogler, and P. Homolka. "Development and production of a prototype iodine contrast phantom for CEDEM". In: *Physics in Medicine and Biology* 58.3 (2013).

[176] S. M. Leon, L. F. Brateman, and L. K. Wagner. "Characterization of scatter in digital mammography from use of Monte Carlo simulations and comparison to physical measurements". In: *Medical Physics* 41.11 (2014).

[177] J. M. Lewin et al. "Dual-energy contrast-enhanced digital subtraction mammography: feasibility." In: *Radiology* 229.1 (2003), pp. 261–268.

[178] C. M. Li et al. "Methodology for generating a 3D computerized breast phantom from empirical data." In: *Medical Physics* 36.7 (2009), pp. 3122–31.

[179] L Li et al. "Contrast-enhanced spectral mammography (CESM) versus breast magnetic resonance imaging (MRI): A retrospective comparison in 66 breast lesions". In: *Diagnostic and Interventional Imaging* 98.2 (2017), pp. 113–123.

[180] Z. Li et al. "A Novel 3D Stochastic Solid Breast Texture Model for X-Ray Breast Imaging". In: *International Workshop on Digital Mammography* 2 (2016), pp. 660–667.

[181] H. Liang et al. "Image Browsing in Slow Medical Liquid Crystal Displays". In: *Academic Radiology* 15.3 (2008), pp. 370–382.

[182] M. Lobbes, R. Prevos, and M. Smidt. "Response monitoring of breast cancer patientsreceiving neoadjuvant chemotherapy using breast MRI – a review of current knowledge". In: *Journal of Cancer Therapeutics and Research* 1.1 (2012), p. 34.

[183] M. B. Lobbes et al. "Contrast-enhanced spectral mammography in patients referred from the breast cancer screening programme". In: *European Radiology* 24.7 (2014), pp. 1668–1676.

[184] M. B. Lobbes et al. "The quality of tumor size assessment by contrast-enhanced spectral mammography and the benefit of additional breast MRI". In: *Journal of Cancer* 6.2 (2015), pp. 144–150.

[185] Y. Lu et al. “A scatter correction method for contrast-enhanced dual-energy digital breast tomosynthesis”. In: *Physics in Medicine and Biology* 60.16 (2015), pp. 6323–6354.

[186] Y. Lu et al. “Application of the ordered-subsets transmission reconstruction algorithm to contrast-enhanced dual-energy digital breast tomosynthesis”. In: *2014 IEEE Nuclear Science Symposium and Medical Imaging Conference (NSS/MIC)* (2014), pp. 1–5.

[187] G. Lubberts. “Random noise produced by X-Ray fluorescent screens”. In: *Journal of the Optical Society of America* 58.11 (1968), p. 1475.

[188] E. Łuczyńska et al. “Comparison between breast MRI and Contrast-Enhanced Spectral Mammography”. In: *Medical science monitor: international medical journal of experimental and clinical research* 21 (2015), pp. 1358–1367.

[189] E. Luczynska et al. “Comparison of the Mammography , Contrast-Enhanced Spectral Mammography and Ultrasonography in a Group of 116 patients”. In: *Anticancer Research* 36.8 (2016), pp. 4359–4366.

[190] E. Luczyńska et al. “Contrast-enhanced spectral mammography: Comparison with conventional mammography and histopathology in 152 women”. In: *Korean Journal of Radiology* 15.6 (2014), pp. 689–696.

[191] A. K. Ma, S. Gunn, and D. G. Darambara. “Introducing DeBRa: A detailed breast model for radiological studies”. In: *Physics in Medicine and Biology* 54.14 (2009), pp. 4533–4545.

[192] A. MacKenzie et al. “Conversion of mammographic images to appear with the noise and sharpness characteristics of a different detector and x-ray system”. In: *Medical Physics* 39.5 (2012), pp. 2721–2734.

[193] A. Mackenzie et al. “Image simulation and a model of noise power spectra across a range of mammographic beam qualities”. In: *Medical Physics* 41.12 (2014), p. 121901.

[194] H. MacMahon et al. “Digital radiography of subtle pulmonary abnormalities: an ROC study of the effect of pixel size on observer performance.” In: *Radiology* 158.1 (1986), pp. 21–26.

[195] A. Macovski. *Medical imaging systems*. Prentice Hall, 1983.

[196] D. M. Mahr, R. Bhargava, and M. F. Insana. “Three-dimensional in silico breast phantoms for multimodal image simulations”. In: *IEEE Transactions on Medical Imaging* 31.3 (2012), pp. 689–697.

[197] A. D. A. Maidment. “Virtual clinical trials for the assessment of novel breast screening modalities”. In: *International Workshop on Digital Mammography*. Springer. 2014, pp. 1–8.

[198] M. B. Mainiero et al. “ACR appropriateness criteria breast cancer screening”. In: *Journal of the American College of Radiology* 10.1 (2013), pp. 11–14.

[199] J. Mainprize et al. “Development of a physical 3D anthropomorphic breast texture model using selective laser sintering rapid prototype printing”. In: *Medical Imaging 2018: Physics of Medical Imaging*. Vol. 10573. International Society for Optics and Photonics, 2018, p. 9.

[200] A. Makeev et al. “Investigation of optimal parameters for penalized maximum-likelihood reconstruction applied to iodinated contrast-enhanced breast CT”. In: *Medical Imaging 2016: Physics of Medical Imaging*. Vol. 9783. 2016, p. 978327.

[201] R. M. Mann et al. "Breast MRI: Guidelines from the European Society of Breast Imaging". In: *European Radiology* 18.7 (2008), pp. 1307–1318.

[202] C. Marzban. "The ROC curve and the area under it as performance measures". In: *Weather and Forecasting* 19.6 (2004), pp. 1106–1114.

[203] G. E. Mawdsley et al. "Accurate estimation of compressed breast thickness in mammography". In: *Medical Physics* 36.2 (2009), pp. 577–586.

[204] T. Mertelmeier et al. "Optimization of tomosynthesis acquisition parameters: angular range and number of projections". In: *International Workshop on Digital Mammography*. Springer. 2008, pp. 220–227.

[205] C. E. Metz. "Some practical issues of experimental design and data analysis in radiological ROC studies." In: *Investigative Radiology* 24.3 (1989), pp. 234–245.

[206] C. E. Metz and K. Doi. "Transfer function analysis of radiographic imaging systems". In: *Physics in Medicine and Biology* 24.6 (1979), pp. 1079–1106.

[207] C. E. Metz and J.-h. Shen. "Gains in accuracy from replicated readings of diagnostic images". In: *Medical Decision Making* 12.1 (2007), pp. 60–75.

[208] P. Milioni de Carvalho. "Low-dose 3D quantitative vascular X-ray imaging of the breast". PhD thesis. Université Paris Sud-Paris XI, 2014.

[209] P. Milioni de Carvalho et al. "Spectra optimization for dual-energy contrast-enhanced breast CT". In: *Proceedings of SPIE Medical Imaging* 8668 (2013), 86681Z–86681Z–9.

[210] R. Mohamed Kamal et al. "Contrast-enhanced spectral mammography: Impact of the qualitative morphology descriptors on the diagnosis of breast lesions". In: *European Journal of Radiology* 84.6 (2015), pp. 1049–1055.

[211] P Monnin et al. "A comprehensive model for quantum noise characterization in digital mammography". In: *Physics in Medicine and Biology* 2083.February (2016), p. 2083.

[212] P Monnin et al. "Comparison of the polynomial model against explicit measurements of noise components for different mammography systems". In: *Physics in Medicine and Biology* 59.19 (2014), pp. 5741–5761.

[213] M. Mori et al. "Diagnostic accuracy of contrast-enhanced spectral mammography in comparison to conventional full-field digital mammography in a population of women with dense breasts". In: *Breast Cancer* 24.1 (2017), pp. 104–110.

[214] G. S. Muralidhar et al. "Snakules: A model-based active contour algorithm for the annotation of spicules on mammography". In: *IEEE Transactions on Medical Imaging* 29.10 (2010), pp. 1768–1780.

[215] H Neale. "Optimization and calibration of dual-energy X-ray imaging systems". PhD thesis. The University of Western Ontario London, 1996.

[216] U. Neitzel. "Grids or air gaps for scatter reduction in digital radiography: a model calculation". In: *Medical Physics* 19.2 (1992), pp. 475–481.

[217] J. von Neumann and S. Ulam. "Monte carlo method". In: *National Bureau of Standards Applied Mathematics Series* 12.1951 (1951), p. 36.

[218] T. Newton and D. G. Potts. *Radiology of the Skull and Brain*. Mosby, 1978.

[219] C. W. Niblack et al. "QBIC project: querying images by content, using color, texture, and shape". In: *Storage and retrieval for image and video databases*. Vol. 1908. International Society for Optics and Photonics. 1993, pp. 173–188.

[220] L. T. Niklason et al. "Digital tomosynthesis in breast imaging." In: *Radiology* 205.2 (1997), pp. 399–406.

[221] H. Nyquist. "Thermal agitation of electric charge in conductors". In: *Physical Review* 32.1 (1928), p. 110.

[222] N. a. Obuchowski. "Nonparametric analysis of clustered ROC curve data." In: *Biometrics* 53.2 (1997), pp. 567–578.

[223] N. A. Obuchowski, B. D. Gallas, and S. L. Hillis. "Multi-reader ROC studies with split-plot designs. A comparison of statistical methods". In: *Academic Radiology* 19.12 (2012), pp. 1508–1517.

[224] N. A. Obuchowski et al. "Multireader, multicase receiver operating characteristic analysis: An empirical comparison of five methods". In: *Academic Radiology* 11.9 (2004), pp. 980–995.

[225] T. P. et al. "In-plane visibility of lesions using breast tomosynthesis and digital mammography". In: *Medical Physics* 37.11 (2010), pp. 5618–5626.

[226] B. A. Palma et al. "Phantom study to evaluate contrast-medium-enhanced digital subtraction mammography with a full-field indirect-detection system". In: *Medical Physics* 37.2 (2010), pp. 577–589.

[227] B. K. Patel, M. B. Lobbes, and J. Lewin. "Contrast Enhanced Spectral Mammography: A Review". In: *Seminars in Ultrasound, CT and MRI* (2017), pp. 70–79.

[228] B. K. Patel et al. "Assessing tumor extent on contrast-enhanced spectral mammography versus full-field digital mammography and ultrasound". In: *Clinical Imaging* 46 (2017), pp. 78–84.

[229] B. K. Patel et al. "Contrast-Enhanced Spectral Mammography is comparable to MRI in the assessment of residual breast cancer following neoadjuvant systemic therapy". In: *Annals of Surgical Oncology* 25.5 (2018), pp. 1350–1356.

[230] J. Phillips et al. "Contrast-enhanced spectral mammography (CESM) versus MRI in the high-risk screening setting: patient preferences and attitudes". In: *Clinical Imaging* (2016).

[231] M. C. Pike and C. L. Pearce. "Mammographic density, MRI background parenchymal enhancement and breast cancer risk". In: *Annals of Oncology* 24.SUPPL.B (2013).

[232] E. D. Pisano et al. "Diagnostic accuracy of digital versus film mammography: exploratory analysis of selected population subgroups in DMIST". In: *Radiology* 246.2 (2008), pp. 376–383.

[233] D. D. Pokrajac, A. D. A. Maidment, and P. R. Bakic. "Optimized generation of high resolution breast anthropomorphic software phantoms". In: *Medical Physics* 39.4 (2012), pp. 2290–2302.

[234] S. Puong. "Imagerie du sein multispectrale avec injection de produit de contraste". PhD thesis. 2008.

[235] S. Puong et al. "Dual-energy contrast enhanced digital breast tomosynthesis: concept, method, and evaluation on phantoms". In: *Medical Imaging 2007: Physics of Medical Imaging*. Vol. 6510. International Society for Optics and Photonics. 2007, 65100U.

[236] J. Puzicha, T. Hofmann, and J. M. Buhmann. "Non-parametric similarity measures for unsupervised texture segmentation and image retrieval". In: *Proceedings of IEEE Computer Society Conference on Computer Vision and Pattern Recognition*. IEEE. 1997, pp. 267–272.

[237] M Rabbani, R Shaw, and R Van Metter. "Detective quantum efficiency of imaging systems with amplifying and scattering mechanisms". In: *Journal of the Optical Society of America A, Optics and image science* 4.5 (1987), pp. 895–901.

[238] M. Rabbani and R. Van Metter. "Analysis of signal and noise propagation for several imaging mechanisms". In: *Journal of the Optical Society of America A* 6.8 (1989), p. 1156.

[239] J Radon. "On the determination of functions from their integrals along certain manifolds". In: *IEEE transactions on medical imaging* 5.4 (1986), pp. 170–176.

[240] E. A. Rafferty et al. "Assessing radiologist performance using combined digital mammography and breast tomosynthesis compared with digital mammography alone: results of a multicenter, multireader trial". In: *Radiology* 266.1 (2013), pp. 104–113.

[241] S. Ramamurthy and C. J. D. Orsi. "X-ray scatter correction method for dedicated breast computed tomography : improvements and initial patient testing". In: *Physics in Medicine and Biology* 61.3 (2016), p. 1116.

[242] A. Rashidnasab et al. "Realistic simulation of breast mass appearance using random walk". In: *Medical Imaging 2012: Physics of Medical Imaging*. International Society for Optics and Photonics, 2012, p. 83130L.

[243] A. Rashidnasab et al. "Simulation of 3D DLA masses in digital breast tomosynthesis". In: *Medical Imaging 2013: Physics of Medical Imaging*. 2013, 86680Y.

[244] B. Razavi. *Design of analog CMOS integrated circuits*. 2005.

[245] I Reiser, A Edwards, and R. Nishikawa. "Validation of a power-law noise model for simulating small-scale breast tissue". In: *Physics in Medicine and Biology* 58.17 (2013), pp. 6011–6027.

[246] I. Reiser and S. Glick. *Tomosynthesis Imaging*. Taylor and Francis, 2014.

[247] B. Ren et al. "Design and performance of the prototype full field breast tomosynthesis system with selenium based flat panel detector". In: *Medical Imaging 2005: Physics of Medical Imaging*. International Society for Optics and Photonics, 2005, pp. 550–562.

[248] S Richard et al. "Generalized DQE analysis of dual-energy imaging using flat-panel detectors". In: *Medical Physics* 5745.5 (2005), pp. 1397–1413.

[249] S. Richard and J. H. Siewerdsen. "Cascaded systems analysis of noise reduction algorithms in dual-energy imaging". In: *Medical Physics* 35.2 (2008), pp. 586–601.

[250] S. Richard and J. H. Siewerdsen. "Comparison of model and human observer performance for detection and discrimination tasks using dual-energy x-ray images." In: *Medical Physics* 35.11 (2008), pp. 5043–5053.

[251] C. Riddell, H. Benali, and I. Buvat. "Diffusion regularization for iterative reconstruction in emission tomography". In: *IEEE Transactions on Nuclear Science* 51.3 (2004), pp. 712–718.

[252] S. J. Riederer and C. A. Mistretta. "Selective iodine imaging using K-edge energies in computerized x-ray tomography". In: *Medical Physics* 4.6 (1977), pp. 474–481.

[253] A. Rose. "The sensitivity performance of the human eye on an absolute scale". In: *JOSA* 38.2 (1948), pp. 196–208.

[254] F. Rubio, P Escobar, and C Jurado. "Contrast-enhanced spectral mammography: CESM-descriptive analysis with pathologic correlation". In: *European Congress of Radiology 2015*. 2015.

[255] Y. Rubner, C. Tomasi, and L. J. Guibas. "The Earth Mover's Distance as a metric for image retrieval". In: *International Journal of Computer Vision* 40.2 (2000), pp. 99–121.

[256] M. Ruschin et al. "Using simple mathematical functions to simulate pathological structures—Input for digital mammography clinical trial". In: *Radiation Protection Dosimetry* 114.1-3 (2005), pp. 424–431.

[257] T. Sakellaris et al. "A Monte Carlo study of the influence of focal spot size, intensity distribution, breast thickness and magnification on spatial resolution of an a-Se digital mammography system using the generalized MTF". In: *Physica Medica* 30.3 (2014), pp. 286–295.

[258] E. Salvagnini et al. "Quantification of scattered radiation in projection mammography : Four practical methods compared". In: *Medical Physics* 39.6 (2012), pp. 3167–3180.

[259] E. Samei and R. S. Saunders. "Dual-energy contrast-enhanced breast tomosynthesis: Optimization of beam quality for dose and image quality". In: *Physics in Medicine and Biology* 56.19 (2011), pp. 6359–6378.

[260] E. Samei et al. "Detector or system? Extending the concept of detective quantum efficiency to characterize the performance of digital radiographic imaging systems." In: *Radiology* 249.3 (2008), pp. 926–937.

[261] M. P. Sampat et al. "The reliability of measuring physical characteristics of spiculated masses on mammography". In: *British Journal of Radiology* 79.SPEC. ISS. 2 (2006).

[262] F. E. Satterthwaite. "An approximate distribution of estimates of variance components". In: *Biometrics bulletin* 2.6 (1946), pp. 110–114.

[263] R Saunders et al. *Optimization of dual energy contrast enhanced breast tomosynthesis for improved mammographic lesion detection and diagnosis*. 2008.

[264] R. Saunders et al. "Simulation of mammographic lesions". In: *Academic Radiology* 13.7 (2006), pp. 860–870.

[265] S. Savaridas et al. "Could parenchymal enhancement on contrast-enhanced spectral mammography (CESM) represent a new breast cancer risk factor? Correlation with known radiology risk factors". In: *Clinical Radiology* 72.12 (2017), 1085.e1–1085.e9.

[266] D. A. Scaduto et al. "Dependence of contrast-enhanced lesion detection in contrast-enhanced digital breast tomosynthesis on imaging chain design". In: *International Workshop on Digital Mammography* 9699 (2016), pp. 136–144.

[267] I. Sechopoulos. "A review of breast tomosynthesis. Part II. Image reconstruction, processing and analysis, and advanced applications." In: *Medical physics* 40.1 (2013), p. 014302.

[268] J. A. Seibert and J. M. Boone. "X-ray scatter removal by deconvolution". In: *Medical Physics* 15.4 (1988), pp. 567–575.

[269] J. A. Seibert, O Nalcioglu, and W. Roeck. "Characterization of the veiling glare PSF in x-ray image intensified fluoroscopy". In: *Medical Physics* 11.2 (1984), pp. 172–179.

[270] H. C. Shen and A. K. C. Wong. "Generalized texture representation and metric". In: *Computer vision, graphics, and image processing* 23.2 (1983), pp. 187–206.

[271] D. Shepard. "A two-dimensional interpolation function for irregularly-spaced data". In: *Proceedings of the 1968 23rd ACM national conference*. 1968, pp. 517–524.

[272] R. L. Siddon. "Fast calculation of the exact radiological path for a three-dimensional CT array". In: *Medical physics* 12.2 (1985), pp. 252–255.

[273] J. H. Siewerdsen and D. A. Jaffray. "A ghost story: Spatio-temporal response characteristics of an indirect- detection flat-panel imager". In: *Medical Physics* 26.8 (1999), pp. 1624–1641.

[274] J. H. Siewerdsen et al. "Empirical and theoretical investigation of the noise performance of indirect detection, active matrix flat-panel imagers (AMFPIs) for diagnostic radiology". In: *Medical Physics* 24.1 (1997), pp. 71–89.

[275] J. D. Silkwood, K. L. Matthews, and P. M. Shikhaliev. "Photon counting spectral breast CT: effect of adaptive filtration on CT numbers, noise, and contrast to noise ratio." In: *Medical Physics* 40.5 (2013), p. 051905.

[276] L. de Sisternes et al. "Development of a computational three-dimensional breast lesion phantom model". In: *Medical Imaging 2010: Physics of Medical Imaging*. Vol. 7622. 2010, p. 762205.

[277] M. Skarpathiotakis et al. "Development of contrast digital mammography". In: *Medical Physics* 29.10 (2002), pp. 2419–2426.

[278] J. Sogani et al. "Comparison of background parenchymal enhancement at contrast-enhanced spectral mammography and breast MR imaging". In: *Radiology* 282.1 (2016), pp. 63–73.

[279] H. H. Song. "Analysis of correlated ROC areas in diagnostic testing." In: *Biometrics* 53.1 (1997), pp. 370–382.

[280] J. Starman et al. "Investigation into the optimal linear time-invariant lag correction for radar artifact removal". In: *Medical Physics* 38.5 (2011), pp. 2398–2411.

[281] C. D. Stephen J. Glick. *A computer simulation for evaluating dual-energy contrast-enhanced breast tomosynthesis*. 2007.

[282] R. Street et al. "Comparison of PbI 2 and HgI 2 for direct detection active matrix x-ray image sensors". In: *Journal of Applied Physics* 91.5 (2002), pp. 3345–3355.

[283] M. J. Swain and D. H. Ballard. "Color indexing". In: *International journal of computer vision* 7.1 (1991), pp. 11–32.

[284] R. K. Swank. "Absorption and noise in x-ray phosphors". In: *Journal of Applied Physics* 44.9 (1973), pp. 4199–4203.

[285] J. A. Swets and R. M. Pickett. *Evaluation of diagnostic systems: methods from signal detection theory. 1982*.

[286] J. Swets. *Evaluation of diagnostic systems*. Elsevier, 2012.

[287] M. Telegrafo et al. "Breast MRI background parenchymal enhancement (BPE) correlates with the risk of breast cancer". In: *Magnetic resonance imaging* 34.2 (2016), pp. 173–176.

[288] S. L. Tennant et al. "Contrast-enhanced spectral mammography improves diagnostic accuracy in the symptomatic setting". In: *Clinical Radiology* 71.11 (2016), pp. 1148–1155.

[289] D. J. Thomson. "Random fields: Analysis and synthesis". In: *Eos, Transactions American Geophysical Union* 64.37 (1983), p. 550.

[290] A Tsigginou et al. "Adding the power of iodinated contrast media to the credibility of mammography in breast cancer diagnosis". In: *British Journal of Radiology* 89.20160397 (2016).

[291] J. Tukey. "Bias and confidence in not quite large samples". In: *The Annals of Mathematical Statistics* 29 (1958), p. 614.

[292] H Turbell and P. E. Danielsson. "Non-redundant data capture and highly efficient reconstruction for helical cone-beam CT". In: *Conf. Record of 1998 IEEE Medical Imaging Conference*. 1998, pp. 1424–1425.

[293] T. Uematsu, M. Kasami, and B. T. Nicholson. "Rim-enhancing breast masses with smooth or spiculated margins on magnetic resonance imaging: Histopathology and clinical significance". In: *Japanese Journal of Radiology* 29.9 (2011), pp. 609–614.

[294] R. Van Metter et al. "Computer simulation of radiographic screen-film images". In: *Application of Optical Instrumentation in Medicine XIV and Picture Archiving and Communication Systems*. International Society for Optics and Photonics, 1986, pp. 82–100.

[295] R. J. Warp and J. T. Dobbins III. "Quantitative evaluation of noise reduction strategies in dual-energy imaging". In: *Medical Physics* 30.2 (2003), pp. 190–198.

[296] S. M. Weis and D. A. Cheresh. "Tumor angiogenesis: Molecular pathways and therapeutic targets". In: *Nature Medicine* 17.11 (2011), pp. 1359–1370.

[297] E. W. Weisstein. *CRC concise encyclopedia of mathematics*. Chapman and Hall/CRC, 2002.

[298] H. Wieczorek. "Effects of Trapping in a-Si:H Diodes". In: *Solid State Phenomena* 44-46 (1995), pp. 957–972.

[299] F. Wilcoxon. "Individual comparisons by ranking methods". In: *Biometrics bulletin* 1.6 (1945), pp. 80–83.

[300] J. F. Williamson. "Random selection of points distributed on curved surfaces". In: *Physics in Medicine and Biology* 32.10 (1987), pp. 1311–1319.

[301] G. Wu et al. "Evaluation of scatter effects on image quality for breast tomosynthesis". In: *Medical Physics* 36.10 (2009), pp. 4425–4432.

[302] T. Wu et al. "A comparison of reconstruction algorithms for breast tomosynthesis". In: *Medical Physics* 31.9 (2004), pp. 2636–2647.

[303] B. Xie et al. "Material Decomposition in X-ray Spectral CT Using Multiple Constraints in Image Domain". In: *Journal of Nondestructive Evaluation* 38.1 (2019), p. 16.

[304] Y. Yagil et al. "Challenges in contrast-enhanced spectral mammography interpretation: Artefacts lexicon". In: *Clinical Radiology* 71.5 (2016), pp. 450–457.

[305] K. Yang, A. L. C. Kwan, and J. M. Boone. "Computer modeling of the spatial resolution properties of a dedicated breast CT system". In: *Medical Physics* 34.6 (2007), pp. 2059–2069.

[306] S. Young et al. "A virtual trial framework for quantifying the detectability of masses in breast tomosynthesis projection data". In: *Medical Physics* 40.5 (2013), pp. 1–15.

[307] S. Young et al. "A virtual trial framework for quantifying the detectability of masses in breast tomosynthesis projection data". In: *Medical Physics* 40.5 (2013), p. 051914.

[308] P. A. Yushkevich et al. "User-guided 3D active contour segmentation of anatomical structures: significantly improved efficiency and reliability". In: *Neuroimage* 31.3 (2006), pp. 1116–1128.

[309] C. Zhang, P. R. Bakic, and A. D. A. Maidment. "Development of an anthropomorphic breast software phantom based on region growing algorithm". In: *Medical Imaging 2008: Visualization, Image-Guided Procedures, and Modeling*. Vol. 6918. 2008, p. 69180V.

[310] Y. Zhang et al. "A comparative study of limited-angle cone-beam reconstruction methods for breast tomosynthesis". In: *Medical Physics* 33.10 (2006), pp. 3781–3795.

[311] B. Zhao and W. Zhao. "Three-dimensional linear system analysis for breast tomosynthesis." In: *Medical Physics* 35.12 (2008), pp. 5219–5232.

[312] B. Zhao et al. "Experimental validation of a three-dimensional linear system model for breast tomosynthesis." In: *Medical Physics* 36.1 (2009), pp. 240–51.

[313] W. Zhao, G. Ristic, and J. a. Rowlands. "X-ray imaging performance of structured cesium iodide scintillators." In: *Medical Physics* 31.9 (2004), pp. 2594–2605.

[314] W. Zhao et al. "Imaging performance of amorphous selenium based flat-panel detectors for digital mammography: Characterization of a small area prototype detector". In: *Medical Physics* 30.2 (2003), pp. 254–263.

[315] J. Zhou, B. Zhao, and W. Zhao. "A computer simulation platform for the optimization of a breast tomosynthesis system." In: *Medical Physics* 34.3 (2007), pp. 1098–1109.

[316] K. H. Zou, W. J. Hall, and D. E. Shapiro. "Smooth non-parametric receiver operating characteristic (ROC) curves for continuous diagnostic tests". In: *Statistics in medicine* 16.19 (1997), pp. 2143–2156.

[317] R. Zwiggelaar et al. "Linear structures in mammographic images: Detection and classification". In: *IEEE Transactions on Medical Imaging* 23.9 (2004), pp. 1077–1086.

université PARIS-SACLAY
ÉCOLE DOCTORALE
Sciences et technologies de l'information et de la communication (STIC)

Titre: Simulations et essais cliniques virtuels pour l'évaluation de la valeur clinique de l'angio-tomosynthèse par rapport à l'angio-mammographie

Mots clés: Imagerie médicale, simulation, angiotomosynthèse, essais cliniques virtuels.

Résumé: Contrast Enhanced Spectral Mammography (CESM) et Contrast Enhanced Digital Breast Tomosynthesis (CEDBT) sont des techniques d'imagerie par rayons X à double énergie impliquant l'injection d'un agent de contraste vasculaire. Les deux techniques fournissent des informations sur l'hypervascularisation des lésions par accumulation du produit de contraste. CESM est une application d'imagerie récemment introduite offrant un meilleur diagnostic du cancer du sein que la mammographie seule. CEDBT est une technique prometteuse fournissant des informations en trois dimensions, ce qui peut atténuer les limites du CESM. Cependant, sa valeur clinique par rapport à l'examen actuel CESM n'est toujours pas bien comprise. Notre travail vise à évaluer les performance de chaque technique afin de détecter et de caractériser les différentes absorptions de contraste apparaissant lors des examens cliniques. Cependant, une telle évaluation nécessiterait une vaste base de données de données cliniques avec une représentation complète diverses prises de contraste insérés dans différents contextes hétérogènes, ainsi que la vérité sur le terrain de chaque cas. La nouveauté de notre proposition réside dans l'évaluation des deux techniques à l'aide de données simulées réalistes. Premièrement, nous avons amélioré le réalisme d'un outil de simulation analytique d'une chaîne d'imagerie par rayons X. Ensuite, nous avons proposé un nouveau modèle d'absorption pour les prises de contraste de type masse, et pour l'accumulation du produit de contraste dans le parenchyme. Enfin, nous avons réalisé un essai clinique virtuel évaluant les performances de détectabilité et de caractérisation du CESM et de la CEDBT à l'aide des outils de simulation développés dans notre travail. Les résultats obtenus montrent que la CEDBT offre une certaine valeur ajoutée clinique par rapport au CESM. En tant que travail futur, les résultats cliniques attendus grâce à la plate-forme de simulation proposée doivent être comparés aux vraies évaluations cliniques lorsqu'un système réel sera disponible.

Title: Simulations and virtual clinical trials for the assessment of the added clinical value of angio-tomosynthesis over angio-mammography

Keywords: Medical imaging, simulation, angiotomosythesis, virtual clinical trials.

Abstract: Contrast Enhanced Spectral Mammography (CESM) and Contrast Enhanced Digital Breast Tomosynthesis (CEDBT) are dual-energy X-ray imaging techniques involving the injection of a vascular contrast agent. Both techniques provide information on hypervascularization of lesions through contrast uptake. CESM is a recently introduced imaging application providing a better diagnosis of breast cancer than diagnostic mammography. CEDBT is a promising technique providing three-dimensional information, which may alleviate the limitations of CESM. However, its incremented clinical value, compared to the current CESM exam, is still not well understood. This work aims to assess the performance of each technique to detect and accurately characterize the different contrast uptakes appearing in clinical exams. However, such an evaluation would require a large database of clinical data with a complete representation of diverse contrast uptakes. Instead, the novelty of our proposal lies on the evaluation of both techniques using realistic simulated data. First, we improved the realism of an analytic X-ray simulation tool. Then, we proposed a new model for mass-like contrast uptakes related to breast lesions and natural contrast uptake of the breast anatomy. Finally, we performed a Virtual Clinical Trial evaluating the detectability and characterization performance of CESM and CEDBT using the simulations tools developed in our work. The results obtained show that CEDBT offers a certain added clinical value compared to CESM. As a future work, the clinical results anticipated thanks to the proposed simulation platform sho compared to true clinical evaluations when a real system will be available.